APPLICATION OF NANOSTRUCTURED EMITTERS FOR HIGH EFFICIENCY LIGHTING

Andrew D. Searle

St. Cross College

Supervised by:

Prof. C.R.M. Grovenor, Prof. N. Grobert and Dr T. Doyle

A thesis submitted for the degree of Doctor of Philosophy (D.Phil.)

Trinity Term 2014

Application of Nanostructured Emitters for High Efficiency Lighting

(Abstract)

University of Oxford, St. Cross College

A thesis submitted for the degree of DPhil in Materials, Trinity Term 2014

By Andrew Searle

This is the first study comparing morphologies of CNT films on Kanthal wire, with their field emission properties, and as such offers ways to design better cylindrical emitter devices. A low turn-on field was achieved (0.35 V/μm), the field emission results have been explained using a simple model, and a fluorescent lamp was fabricated. Whilst previous work has been done on the link between "as grown" CNT films and their respective field emission properties on flat substrates, very little work has been done on linking morphology to emission performance on wire substrates, where the morphology can be very different.

Microscopic structures such as towers, ridges and clumps consisting of many aligned or entangled CNTs were grown using an aerosol chemical vapour deposition (a-CVD) technique. Hydrogen added to the carrier gas resulted in a decrease in defect density in the growth of undoped CNTs, and an increase in defect density in the growth of nitrogen doped CNTs (N-CNTs) and boron doped CNTs (B-CNTs). In-situ transmission electron microscopy (TEM) studies show that damage to CNT tips results in a significantly higher turn-on field compared to undamaged tips. This can be recovered by making the CNT emit current for several minutes which makes the tip recrystallize due to heat caused by the Nottingham effect.

The field emission properties of the "as grown" CNT films are dominated by protruding CNTs found at the edges of ridge and tower microscopic structures. The field emission properties are also related to the dimensions of these structures with the longest ridges (hence those with the longest protruding CNTs) resulting in the lowest turn-on electric field. The ridge and tower structures act to

accommodate protruding CNTs at their edges and their physical dimensions (mainly width) act to separate these emitters so that screening is minimised. This work shows that efficient emitters can be fabricated effectively from simple a-CVD techniques and microscopic structures act to improve, not degrade, field emission properties.

Acknowledgements

I would like to firstly thank my three supervisors for their support and invaluable advice over the years. I would like to thank Professor Chris Grovenor for giving general advice on my project, for proof reading my thesis, and giving me vital feedback. I would like to thank Dr Anthony Doyle for continuing support over the years in the form of lab visits, proofreading of my thesis, and advice regarding project direction. Finally, I would like to thank Professor Nicole Grobert for continuing support in meetings and proofreading my thesis.

I would like to thank the EM team at the department for all of their technical and practical support, without which this project would not be possible. Gabriella Chapman I thank for training on the electron microscopes and microscopy support. I would also like to thank Greg Cook for support and advice regarding the setting up of my field emission test rig, especially regarding vacuum systems. I am grateful to Richard Cripps for electrical advice and Peter Flaxman for the fabrication of the field emission bracket and design advice.

I would like to thank all members of the 'Nanomaterials by Design' research group for their moral and social support and making the past few years enjoyable. Last but not least I would like to thank my family and friends for emotional support.

Table of Contents

1. Literature Review

1.1. Introduction

In recent years there has been a heightened interest in energy usage, partly due to increased political anxiety regarding securing energy sources and minimising climate change. In such a consumer driven society there is increased pressure to harness energy in a clean manner, while still increasing the total supply of energy. Energy efficiency has become a government priority, and the focus of research has been towards renewable and clean alternatives to fossil fuels, with intense research into solar cells, wind power and other clean sources of energy [1]. As demand is hard to curb, products also need to be developed which consume less energy.

Developing new materials is one useful way of achieving these goals for example by; making lighter and stronger carbon-fibre composites in aircraft [2], achieving higher sunlight to electrical energy conversion in doped silicon for use in solar cells [1], designing superconductors which have zero resistance [3], and use of silicon nanorods for electronic applications [4], to name but a few.

Nanotechnology research has accelerated dramatically in the past 20 years and is at the forefront of energy efficiency research. Nanotechnology is the science of manipulating materials at the nanoscale (billionths of a metre). The two main approaches to achieving engineering at the nano scale are the 'top-down' approach and the 'bottom-up' approach. The top-down approach involves taking bulk material and processing down to smaller components. Photo-lithography and ink-jet printing are examples of top-down approaches. Bottom-up engineering involves building up nanostructures from smaller units (*e.g.* molecules or atoms) to create nanomaterials. Chemical vapour deposition (CVD) and atomic layer deposition (ALD) are examples of bottom-up approaches.

Some of the most widespread and studied nanomaterials to date are carbon nanoforms. Carbon is chemically very versatile, existing in many different forms such as graphite, diamond or nanostructured carbon nanoforms. Carbon nanoforms were first discovered in 1985 [5] with the discovery of fullerenes, followed by carbon nanotubes (CNTs) in 1991 [6], and graphene in 2004 [7]. There are also many intermediates which are a combination of two or more forms, such as nano-cones [8], nano-fibres [9], nano-horns [10], nano-ribbons [11] *etc.* There are many articles that cite such nanoforms as being very useful to increase the energy efficiency of devices such as x-ray generators [12], solar cells [13], fuel cells [14], displays [15] and lighting [16].

1.2. Traditional Lighting

Modern incandescent lights have remained virtually unchanged since Edison patented his lamp in 1880 [17]. The lamp consists of a coiled tungsten wire which is kept in the middle of a glass bulb by two support wires (Figure 1).

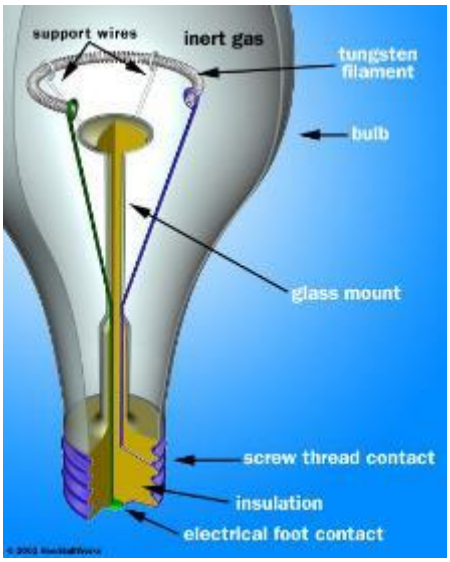

Figure 1: Schematic of incandescent light bulb, showing coiled tungsten filament inside gas filled bulb. Adapted from [18].

The bulb is filled with an inert gas (usually nitrogen) and sealed airtight. A current is passed through the tungsten filament which heats the wire *via* resistive heating. When the temperature reaches approximately 2,200 °C, visible light is emitted [18]. The

process is very inefficient as only 10% of emitted electromagnetic radiation is visible light, with the remainder consisting mainly of infrared radiation [19].

Fluorescent lights were invented in the 1950s with the intention of being more energy efficient than their incandescent counterparts. A fluorescent lamp consists of a phosphor coated glass tube, either straight or coiled, and is filled with an inert gas such as argon to a pressure of $1/75^{th}$ of an atmosphere. A potential difference is applied across two metal electrodes at either end of the tube and at a certain voltage, the gas breaks down and emits UV light. This UV light is then converted to visible light by exciting the phosphor coating.

1.3. Field-Emission Lighting

1.3.1. Basic Principle of Operation

A Direct Field Emission (DFE) lamp represents an improvement in efficiency compared to fluorescent lamps as it operates on the principle of a 'cold cathode' meaning that no heat is required to achieve emission, and hence power loss in this respect is minimised. DFE lamps consist of two parallel plates in an evacuated chamber. A potential difference is applied across these two plates and at a specific electric field (known as the 'turn on' field), electrons are emitted from the cathode and are collected at the anode. The anode is coated with a phosphor so that the collected electrons excite the phosphor and produce visible light. Very high fields are required for field emission to occur from flat cathodes and so nanostructured emitters are placed on the cathode that amplify the local electric field so that a lower average field is needed to activate electron emission.

There are two main DFE lamp arrangements, with planar or cylindrical electrodes. In the planar arrangement, both the cathode and anode are flat and the potential follows a linear

relationship with respect to distance, with the electric field (E) at any point between the two electrodes being:

$$E = V/d \qquad \textbf{Equation 1}$$

Where V is the potential difference between the two electrodes, and d is the distance between these electrodes. In a cylindrical arrangement, the electric field at the cathode surface can be expressed as:

$$E = V/(r_1 \ln\{r_1/r_2\}) \qquad [20]\ \textbf{Equation 2}$$

Where r_1 is the radius of the cylindrical cathode and r_2 is the radius of the anode. A cylindrical setup therefore enables higher fields to be obtained at larger inter-electrode displacements, making a working device more realisable.

1.3.2. DFE Figures of Merit

When considering a DFE lamp it is important to consider the figures of merit so that the best possible working lamp can be realised. The process of producing visible light in a DFE lamp is a two stage process. Firstly emitters produce electrons, and secondly these electrons are converted to photons in the phosphor screen. Therefore figures of merit must be considered for both processes.

The luminosity produced by a DFE lamp is directly related to the emitted current density from the cathode. The equation that governs the emitted current density (J) of a cathode is as follows [21]:

$$J = \eta a \frac{(\beta F)^2}{\phi} \exp\left(-b \frac{\phi^{\frac{3}{2}}}{\beta F}\right) \qquad \textbf{Equation 3}$$

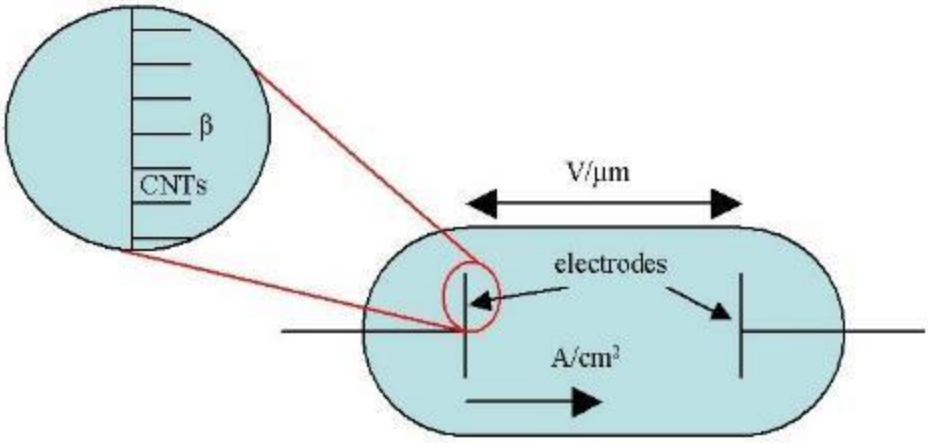

Figure 2: Schematic of a fluorescent lamp showing an electric field applied across two electrodes. The inset shows that field enhancement (β) is achieved with a non-planar surface [22].

Where a and b are constants (1.54 x10^{-6} and 6.83 x10^{7} respectively); η is the geometrical efficiency of electron emission; β is the field enhancement factor which is the ratio between the macroscopic applied field and the local field near the emitter apex; and ϕ is the work function of the electrode material. In terms of material properties, a cathode material that has a high β value and a low work function is required to maximise the emitted current density. The β value is purely geometrical and will depend on the shape (mainly the length and diameter) of the emitters; how these emitters are arranged with respect to each other; and the shape of the substrate upon which these emitters are supported. The electron to photon conversion efficiency of the phosphor will also be important, but will not be investigated in this thesis.

Before considering how to fabricate a DFE lamp, a theoretical consideration of the optimum emitter arrangement is necessary. A possible optimum morphology of emitters is shown in Figure 3. CNTs separated by an infinite displacement would represent maximum β value due to no screening. The emitters should be aligned perpendicular to the substrate and be straight so that the high aspect ratio of each CNT translate to a high field enhancement. Each emitter contributes to the emitted current and so the more

densely packed emitters are, the higher the current density. This would however, result in screening effects which lowers emitted current and so a compromise is required (in terms of spacing) to obtain an emitter array that maximises current density. An optimum distance between neighbouring CNTs could be twice the height of the CNTs [23-25] (Figure 3), where the β value becomes independent of small differences in spacing (Figure 4).

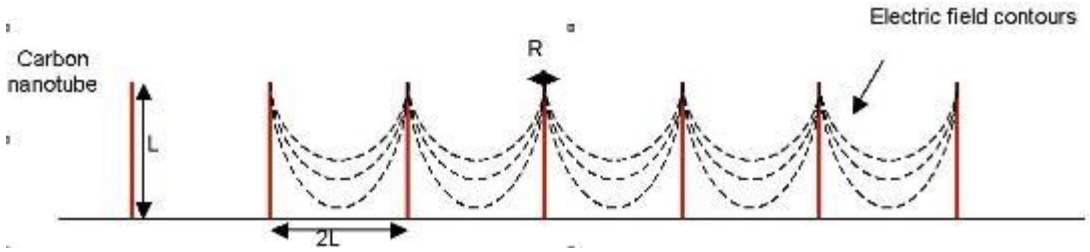

Figure 3: Schematic of a possible optimum CNT microstructure with an inter-tube displacement of 2*h*.

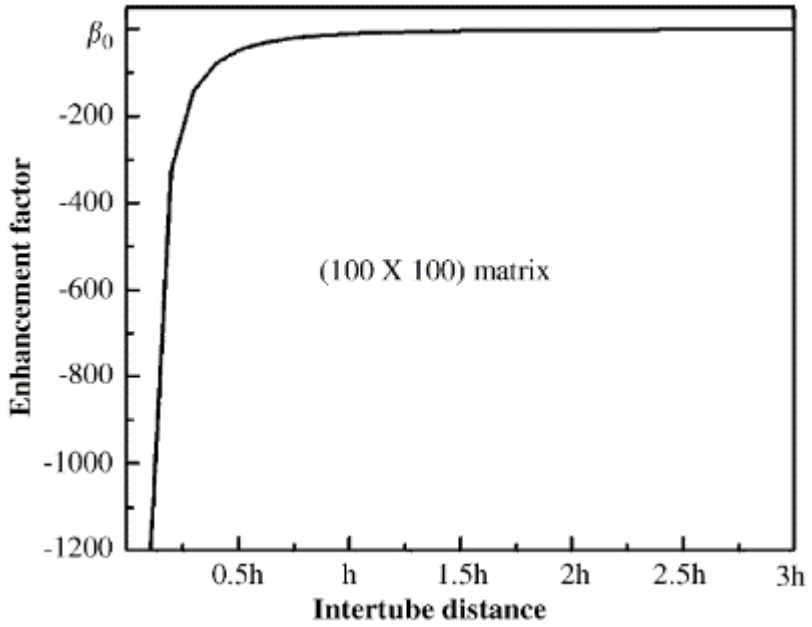

Figure 4: Graph of enhancement factor (β) against inter-tube spacing generated using a computer model [24].

The degree to which this morphology is achieved will be determined by the synthesis technique and the processing parameters used, which will be discussed in more detail in

Section 1.8 (page 33). Due to their high aspect ratios, carbon nanotubes (CNTs) could be potential materials for use as emitters on the cathode.

1.3.3. What are Carbon Nanotubes?

Single-walled CNTs (SWCNTs) consist of a single sheet of graphene rolled into a tube (Figure 5) [26-28]. The diameter varies significantly but is normally between 1 nm and 10 nm, and the length up to several microns long. Multi-walled CNTs (MWCNTs) consist of several graphene tubes inside each other, and can have up to a hundred or more walls (Figure 6). Diameters typically vary from 10 nm to 100 nm, and lengths from a few hundred nanometres to several hundred microns.

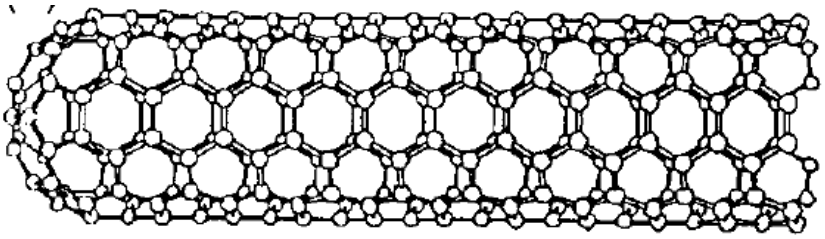

Figure 5: Schematic of a SWCNT consisting of a single rolled sheet of graphene. Taken from [29]

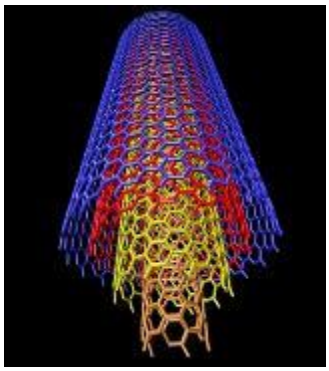

Figure 6: Schematic of a MWCNT consisting of several rolled up sheets of graphene inside one another. Taken from [30].

Experiments show that the internal structure of MWCNTs can include graphene sheets containing defects and graphitic planes aligned at an angle to the tube axis. More complicated structures, such as stacked cones, are also quite common especially if doping is introduced [31-34].

1.3.3.1. Doped Carbon Nanotubes

Since the discovery of CNTs in 1991 [6], there has been an interest almost immediately in to the effects of dopants on the electrical properties of individual CNTs, with the first synthesis of a B-C-N nanotube achieved by arc discharge in 1994 [35].

Early theoretical models showed that semi-conducting CNTs could be produced using nitrogen and/or boron as substitutional dopants [36, 37]. Nitrogen dopants produce n-type semiconducting nanotubes [38], compared to p-type for boron doping. The work function of a material is important for electronic applications and for un-doped nanotubes is often assumed to be similar to graphite (4.5 eV – 5.0 eV). Theoretical predictions predict a work function of 5.05 eV for pure, un-doped SWCNTs [37]. N-doped CNTs (N-CNTs) have a work function of ~4.8 eV for SWNTs and 4.6 eV - 4.8 eV for MWCNTs [37].

The nitrogen atom is similar in size to carbon, and so substitutional doping produces little strain in the structure. However, it is likely that nitrogen doping has an effect on defect creation as it has a co-ordination number of 3, instead of 4 and so dangling bonds will be created. N-CNTs tend to have a bamboo-like structure which is characterised by elongated internal compartments that loosely resemble bamboo stems (Figure 7). Compartments form during growth due to the nitrogen atoms periodically interrupting the diffusion of carbon to the graphitic structure [39]. The incorporation of nitrogen into the CNT walls also causes curvature, resulting in cone-like shapes [32].

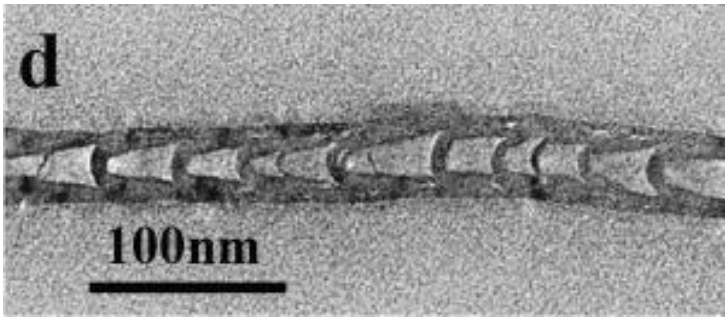

Figure 7: TEM micrograph of MWCNT showing bamboo type structure taken from [39].

1.3.4. Progress in DFE Technology

DFE lamps have only appeared relatively recently as nanostructured emitters are required to amplify the local field to an intensity significant to initiate emission. The first DFE lamp to utilise CNTs was fabricated by Saito *et al* in 2000 [40]. Since then there has been only limited literature on such devices [16, 41, 42], despite the advantages of increased efficiency (over fluorescent lamps), reduced or zero mercury content and the ability to be dimmed. Mercury is necessary in fluorescent lamps as excitation causes UV light to be emitted from the mercury vapour, which is then converted to visible light by the phosphor layer. The current maximum allowed mercury content per bulb is 4 mg [43].

Croci *et al* [16] mention some important specifications in building a prototype CNT DFE lamp if it is to compete with commercial fluorescent lamps. The main requirements are that it must have a half-life intensity of 10,000 hours, which is the average lifetime of a fluorescent light. It must also be capable of a luminosity of 10,000 cd/m^2 and output a uniform light of 5% homogeneity on the glass tube. Currently, the major challenges for integrating CNTs into such devices are obtaining large area, homogenous films of CNTs and maintaining a stable current and long lifetime. Lifetimes currently range from 150 hours [41] up to 9,000 hours [42].

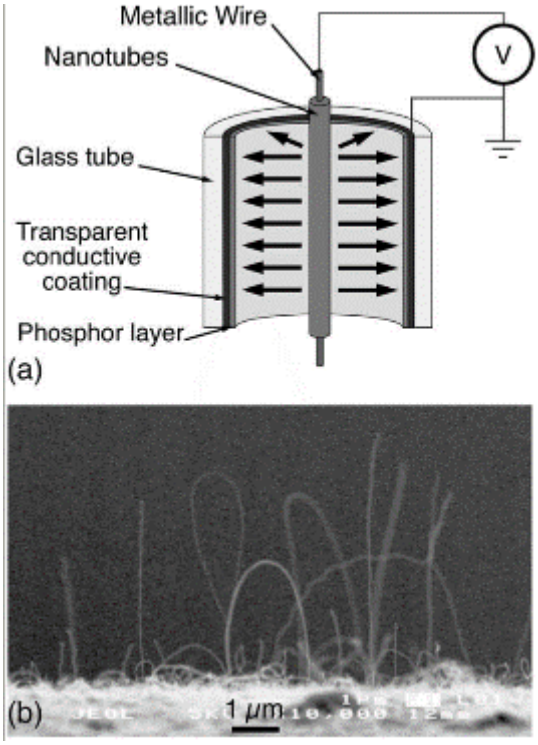

Figure 8: a) schematic of tube-shaped fluorescent light, with CNT coated metal wire and b) SEM micrograph of protruding nanotubes grown on the wire. Taken from [16].

1.3.5. Factors Contributing to DFE Efficiency

CNT degradation and current stability are important in a DFE lighting device. Ion bombardment can be an issue in field emission experiments even when in high vacuum conditions. Jonge *et al* observed that single CNT emitters can last beyond 10,000 hours in a vacuum of 2 $x10^{-10}$ mbar with very little damage sustained [21].

Other issues that need to be resolved are material factors such as substrate choice. Adhesion between CNTs and the substrate needs to be sufficient so that 'pull-off' during the large electrostatic forces experienced during operation is avoided. Most substrates used for CNT growth tend to be Si/SiO_2 or ceramic oxides due to their inertness (and hence no reaction occurs with the catalyst particles). This is unsuitable for a working, commercial device as these materials are brittle and insulating. Chapter 3 discusses substrates in more detail (see page 63).

1.4. Field Emission Mechanisms

1.4.1. The Work Function

The work function is defined as the energy required to move an electron from the Fermi Level of a material, to the vacuum (*i.e.* outside the material) (Figure 9).

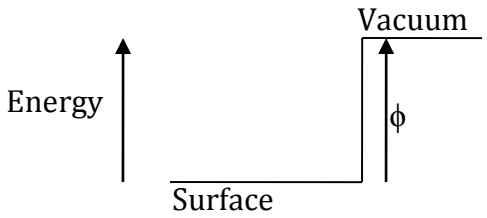

Figure 9: Schematic illustrating work function as energy required for an electron to escape a metal surface into a vacuum

The origin of the work function is complex and is related to the bonding of the material and the crystal surface presented to the vacuum. More open metallic structures tend to have lower work functions compared to densely packed metallic structures (*e.g.* aluminium has a work function of ~4 eV compared to ~5.6 eV for platinum). Changes in the surface bonding or other defects can also effect the work function of a material, as it effects how tightly electrons are bound.

1.4.2. The Fermi-Dirac Distribution

At a temperature of 0K, the probability of finding an electron in a solid with energy below the Fermi Level is 1, as there are no thermal excitations. As the temperature of the material is increased, thermal energy transferred to the electrons mean that some electrons are excited to energies higher than the Fermi Level. The probability that an electron is below the Fermi Level is no longer 1. A distribution of electrons, known as the Fermi-Dirac distribution will mean that there are a proportion of electrons above the Fermi Level (**Equation 4**).

$$f(E) = \frac{1}{e^{(E-E_f)/kT}+1} \qquad \textbf{Equation 4}$$

Where *f(E)* is the probability of an electron having energy '*E*', E_f is the Fermi Level, *k* is the Boltzmann's constant, and *T* is the temperature in Kelvin.

1.4.3. Thermionic Emission

If the temperature is increased sufficiently high, some electrons are excited and as the temperature is increased further, thermal energy is sufficient for some electrons to overcome the work function and escape into the vacuum. This process inherently involves energy to overcome the work function and is hence a less efficient process than field emission (explained in more detail in the next section). The emitted current (*J*) is related to the temperature of the emitters by the following equation:

$$J = A_G T^2 e^{-\frac{\phi}{kT}} \qquad \textbf{Equation 5}$$

Where *T* is the temperature, ϕ is the work function of the metal, *k* is Boltzmann's constant, and A_G is a material specific correction factor.

1.4.4. Fowler-Nordheim Emission

Field emission can be defined as "the emission of electrons from the surface of a condensed phase into another phase, usually a vacuum, under the action of high (0.3 – 0.6 V/Å) electrostatic fields" [22]. The potential barrier between a flat metallic surface and a vacuum is shown schematically in Figure 9. An applied electric field changes the barrier so that it becomes triangular (Figure 10). If the applied electric field is large enough, electrons will tunnel through the potential barrier and escape into the vacuum, and will accelerate towards the anode, and an emitted current will be observed. Therefore no extra energy is required to raise the electrons above the Fermi level.

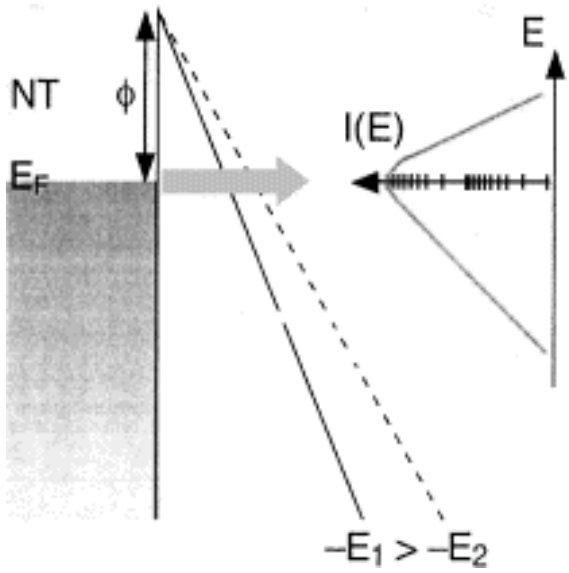

Figure 10: Schematic of altered barrier due to applied electric field. Taken from [21].

The local electric field can be enhanced at sharp tips or protrusions which will bend the potential barrier further [44, 45]. This can have a large effect on field emission, as it is the local electric field at the surface that participates in the field emission process.

1.4.5. Field Emission from Carbon Nanotubes

The mechanisms which underlie field emission have been discussed, including the importance of the work function of the emitting material, and the local field enhancement factor (β) of the emitting film.

SWCNTs are thinner (average diameter of 1.4 nm compared to multi-walled nanotubes which have diameters up to 100 nm) than MWCNTs, and if it is assumed that they are the same length and are spaced apart the same as MWCNTs, then they will have a higher β value than MWCNTS. Therefore one would expect that the former would be better performing emitters. Reports in the literature however, suggest that this is not the only factor that affects the field emission process from carbon nanotubes [21, 46-50]. It is easy to assume that MWCNTs behave as pure metallic emitters, and while it is true that the

main body of the nanotube can be considered as such, the tip of the nanotube needs more careful consideration.

Bonard *et al* [49] compared the emission characteristics from a SWCNT (average diameter 1.4 nm) film and MWCNT (diameter <14 nm) film. The CNTs were produced using an arc discharge technique. CNT films were fabricated by drawing a colloidal suspension of CNTs through a porous silica filter and coating this on to a Teflon coated metal surface. It was found that the E_{to} of the SWCNT film was comparable to that of the MWCNT film, 2.7 V/μm compared to 2.6 V/μm. Both films were processed in the same manner, and as SWCNTs are 10-100 times thinner than MWCNTs, they should have 10-100 times greater values of β. The current from the MWCNT film could be dominated by emission from a few, thin nanotubes; however this does not explain fully the disparity. Bonard *et al* concluded that the structure of the nanotube tip plays a larger role in field emission than the overall CNT morphology.

When calculating the field emission properties of CNTs, many researchers assume the work function is that of graphite (*i.e.* 5 eV) [50-55]. This is assuming that perfect hexagonal sp^2 bonding exists at the CNT tip and that curvature of the tip does not introduce strain in to the structure. However, a construction of pentagons and hexagons are needed to make a CNT tip and the creation of a cap will introduce strain.

SWNTs tend to have spherical caps, made of hexagons of carbon atoms with few or no defects and this results in SWNTs behaving as metallic emitters. MWNTs tend to have tapered, cone like tips, produced by pentagons of carbon atoms that tend to create defects as it deviates from hexagonal sp^2 bonding [21]. This results in a localised density of states (LDoS) near the Fermi level caused by topological disturbances introduced by pentagonal arrangements of carbon atoms [48]. By the same argument, defects in general should produce LDoS. De Vita states that for CNTs "…an electronic state should be localized in

the high-field regions of the structure, it should be occupied and it should be close in energy to the Fermi level" [48]. LDoS near the Fermi level will lower the effective work function of the CNT and hence the barrier to electron emission is lower. Therefore, an enhancement in field emission from tapered tips would be expected, relative to purely spherical tips.

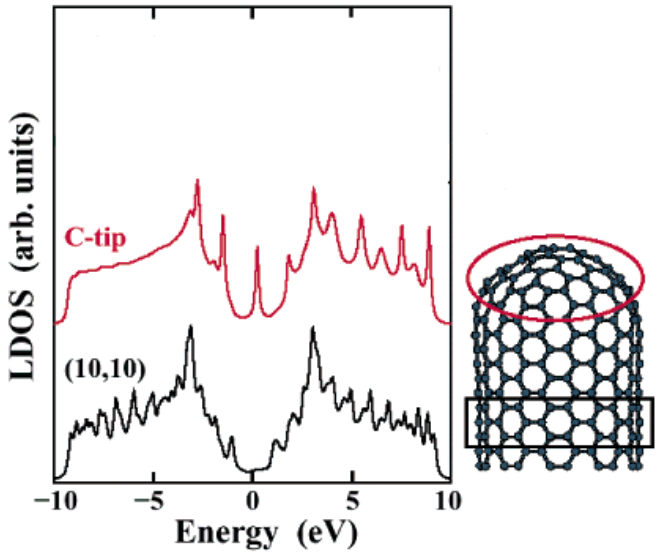

Figure 11: Density of states for an un-doped armchair (10, 10) SWNT, showing that there is a peak of localized density of states in the tip, implying improved field emission. Graph taken from [56].

The diameter at the apex of tapered tips is likely to be smaller than that of spherical tips, which would act as an electric field concentrator. Bonard *et al* [49] showed that MWCNTs produced by an arc discharge method that did not have their tips removed by acid performed far better than those that did. A turn-on electric field of 2.6 V/μm was measured compared to 4.5 V/μm for MWCNTs with tips removed. This is due to the diameter at the apex being larger for open nanotubes and, because the body of nanotubes can be considered metallic, emission is from a continuum of DoS rather than from the LDoS near the Fermi energy found in tapered tips.

While emission from CNT tips has been considered so far, field emission from the side wall of MWCNTs may be possible, especially if no protruding CNTs are present.

1.4.5.1. Emission from the sidewall of MWCNTs

Chen *et al* [46] conducted studies of plasma enhanced CVD (PECVD) grown MWCNTs orientated parallel, 45° and perpendicular to the substrate. Results showed that the MWCNTs aligned parallel to the substrate performed best (Figure 12), with those aligned perpendicular performing worse [46]

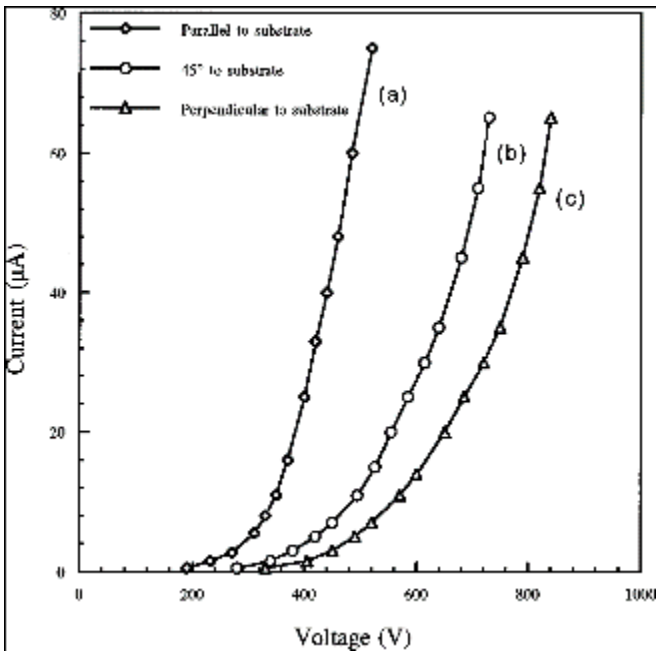

Figure 12: Graph showing emitted current versus applied voltage for differently orientated CNTs. Graph taken from [46].

They concluded that defects in the walls may be creating localised areas of field enhancement. Nevertheless, it shows that field emission is possible and significant from CNT tips and body, with the most important factor being defect position and density.

It is still desirable to have CNTs perpendicular to the substrate because this will maximize the aspect ratio (defined as the ratio between diameter and length) compared to CNTs lying flat.

1.4.5.2. Field Emission from B-CNTs

Boron can be added to CNTs to change their electrical properties. There are conflicting reports in the literature regarding the work function of B-CNTs. Qiao *et al* conducted

first-principle density-functional calculations where boron atoms were introduced in to the layers near the cap of a SWNT [37]. It was found that boron atoms inhibit the emission of electrons by increasing the work function. Qiao concludes that this is due to boron lowering the Fermi level nearer to the valence band which results in a greater barrier to electron emission. This is in direct contradiction to work carrier out by Charlier *et al* who used tight-binding and *ab-initio* calculations and found that the introduction of boron atoms coincides with the formation of LDoS near the Fermi level, which would suggest enhanced field emission [56]. This is backed up with experimental evidence, with B-CNT films produced by arc discharge having an E_{to} value of 1.4 V/μm compared to 2.8 V/μm for SWNT films and 3.0 V/μm for MWCNT films [56].

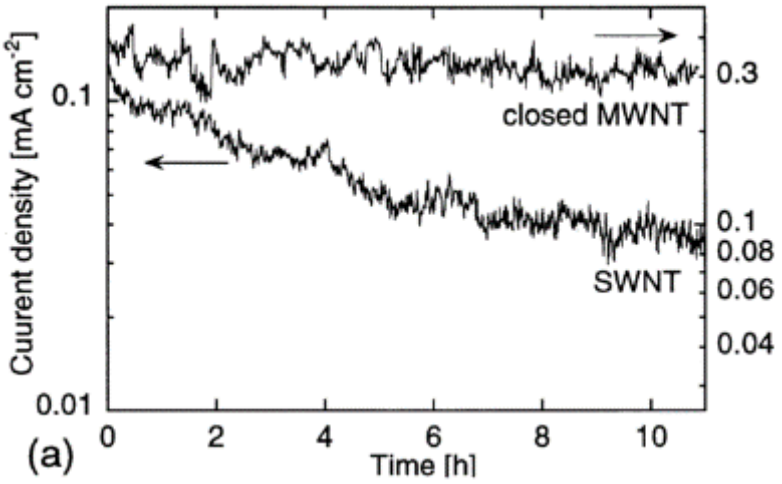

Figure 13. Graph showing that MWCNTs last ten times longer during field emission compared to SWCNTs. Taken from [45].

1.4.5.3. Field Emission from N-CNTs

Enhancement of field emission using N-CNTs has been demonstrated experimentally by a number of groups [57-60]. It was found that as the nitrogen concentration increased, the E_{TO} value of the doped CNTs decreased, with an E_{to} value of 2.3 V/μm at a nitrogen concentration of 4.08 at% [61]. These samples were produced by thermal CVD with acetylene gas on silicon substrates. Nitrogen plasma treatment was used to dope the

CNTs, with increasing nitrogen concentration resulting from increased plasma treatment times. As the dopant concentration increased, so did the defect density which is a common feature of N-CNTs as nitrogen is substitutionally incorporated in to the structure [61]. A relationship between N content and E_{TO} value was found (Figure 14) which clearly shows that increased nitrogen content results in enhanced electron emission. This is likely because of the increased density of defects which introduce LDoS near the Fermi level, lowering the work function.

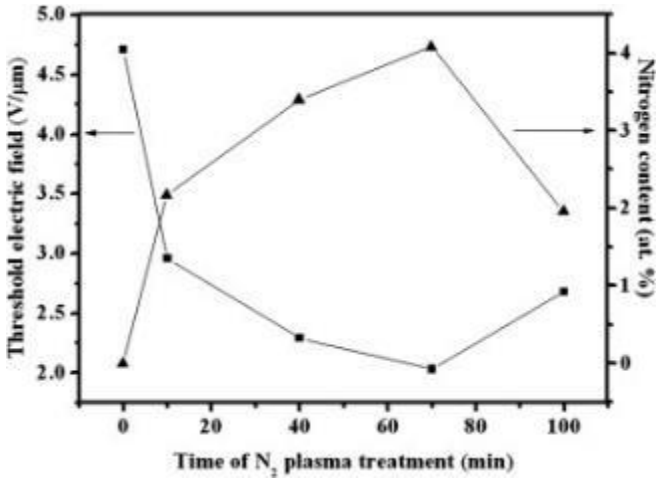

Figure 14: Graph showing the variation of threshold electric field with respect to nitrogen content, showing that increased nitrogen content results in increased field emission. Taken from [61].

1.5. Field Emission from Individual CNTs

Some work has been done on the relationship between the field emission properties of individual CNTs and that of CNT films [62]. CNTs in a film will tend to be less than twice their height apart from other CNTs and hence screening will reduce the enhancement factor, which should result in a higher 'turn on' field compared to individual emitters. However, measured CNT films tend to have lower 'turn on' fields compared to individual CNTs. Bonard *et al* [62] predicted that CNTs in the film must have a β value ~8 times higher than those they measured individually, to explain the disparity. It is possible that only a few CNTs in the film (those with highest aspect ratios) are contributing to the

emitted current and so it is the turn on field of these CNTs that dominate emission from the film as a whole. The emitting area of single CNTs is hard to define and that of the CNT films is many times more difficult due to not knowing exactly how many emitters are involved in the emission process, and how each emitter interacts with each other. Also the Fowler-Nordheim theory describes the field emission from a flat metal surface at 0K. It was not developed with CNTs in mind and does not take into account the fact that they are highly curved at apex and contain defects.

Bonard *et al*, defined turn-on as the average field necessary for a detectable current to be observed, approximately 10 pA [45]. Morihisa *et al* defined turn on as the field required to extract a current of 10 nA. It is difficult to compare between studies because of problems defining material parameters such as the field enhancement factor and work function; in addition to experimental issues such as defining the emission area, electrode geometry, and inter-electrode displacement. The inherent difficulty in dealing with such experimental issues, in addition to challenges in electrode/CNT positioning, fabrication of electrodes, and electrical measurements at such small length scales make these issues non-trivial.

When measuring the field emission properties of individual CNTs, the β value of the system becomes difficult to define due to the difficulty in obtaining a flat anode. It is important to ensure that the anode radius of curvature is significantly larger than the curvature of radius of the CNT so that it approximates a flat anode. Bonard *et al* observed that the measured β value for individual CNTs was approximately twice the actual value which, may be due to small protrusions at the CNT apex, which would increase the β value locally. At large inter-electrode displacements (*i.e.* many times larger than the height of the CNT) the β value is independent of small changes in the displacement. When the inter-electrode displacement becomes comparable to the height of the CNT, the β value is dependent

on the inter-electrode displacement. All these factors make β a difficult parameter to use in comparing emitters. Most authors use the slope of F-N plots to determine the β value of individual CNTs, but this is not necessarily the best method to calculate this. Thermionic emission can also yield linear plots. Linearity only indicates that tunnelling through a potential barrier is occurring, but as discussed in Section 1.4 (page 17), there are several mechanisms that could result in emission.

1.6. Application of CNTs to DFE Lighting

There are various important field emission properties a cathode material possesses. This study will focus on the "turn-on" electric field (E_{TO}) and the decay current (I_D). The E_{TO} encompasses both the β value and the work function of the emitting material and a high β value and low work function will result in a low E_{TO}. The decay current is important to give an indication of how long a potential device will last in operation.

1.6.1. The 'Turn On' Field

The 'turn on' field is the average field required to start field emission. Articles state different values, such as 10 nA/cm^2 [63], 1 nA [64], 0.1 μA [65], and 1 μA/cm^2 [66]. This is possibly due to the limitations of equipment in detecting sufficiently low currents but also because of the issue with differences in experimental setup and a lack of consensus on the issue as a result. Bonard *et al* uses the value for the "turn-on" field of 10μA/cm^2 from the cathode surface in an important review article [67]. Therefore this value will be used in this thesis, simply because it is used in the review article and because it appears to be a reasonable value to use.

When considering field emission properties from CNT films, it is important that the emission area under consideration is sufficiently large. This is so that the origin of the film emission current is less ambiguous as a single CNT emitter can emit a current of micro amps or more. Even when large areas (*e.g.* greater than 1 mm^2) are considered,

emission could still be from a small number of CNTs, and it is unlikely that all emitters will "turn on" at the perceived film turn on field. This is due to the fact that each CNT's environment is different from each other and the aspect ratio of each emitter is different. It is possible there are numerous emission mechanisms happening at the same time. Thermionic emission may be happening in addition to field emission as the temperature of the CNT tip will heat up during emission due to the Nottingham effect [68] and Joule heating. This should not significantly affect the turn on field as no heating has occurred up to the point of turn on and if the CNT is at room temperature, thermal excitations would be minimal.

1.6.2. Current Density

Emitted current density is calculated by taking the measured current of an emission experiment and dividing by the emission area. It is difficult to accurately measure the emission area because of several difficulties. It is mainly assumed in the literature that the emission area is that of the emitters' support (*i.e.* the substrate), and sometimes it is not even discussed. Several authors have attempted to more accurately determine the emission area by estimating the number of emitters by using a phosphor screen on the anode so that emission spots are visible. It is problematic to calculate the emission area from this however, as the electron beam spreads out from each emission site, and so the area of a 'spot' on the phosphor screen will be larger than the actual emission area [21]. Also, different regions of the emitting surface may be emitting different current densities, depending on the local work function and local fields present. All of these factors mean that an accurate measure of the emission area becomes very challenging, and all subsequent calculations based on this, also difficult.

1.6.3. Emission Current Stability

If a commercial device that utilises field emission from CNTs is to be realised, long term stability of emission current is necessary [16]. Adsorbates in the vacuum can attach to the tips of the CNTs and alter the field emission properties temporarily, resulting in a fluctuation of observed current [69]. These adsorbates can be in the form of water vapour, or other small molecules found naturally in the air and can be present in high vacuum. CNTs degrade with time under the application of high electric fields, and often the emitted current reduces down to a few "hot spots" caused by a small number of CNTs, meaning these emitters degrade faster [70]. As these emitters are destroyed, other CNTs are exposed and contribute to the emitted current. This manifests as fluctuations and a gradual decrease in emitted current. CNTs have been shown to be robust in high electric fields, due to strong covalent bonds [49]. Nevertheless, some CNTs will be more stable than others due to the presence of defects.

SWCNTs perform the worst in this respect, with MWCNTs lasting more than ten times as long [49]. This is due to the lack of multiple inner layers in the SWCNT structure, which slows degradation. CVD prepared MWCNTs do not last as long as arc discharge prepared MWCNTs as the latter are more graphitic [49]. Defects are reactive as they have dangling bonds and hence are unstable and act as weak points in the structure.

1.6.4. Erosion Factors

There are two main causes of degradation of CNT emitters which involve ion bombardment and lack of adhesion with the support. It has been reported that CNT emitters in high vacuum ($<2 \times 10^{-10}$ mbar) can emit for several hours and de Jonge *et al* [21] reported that their CNT lasted several months emitting a current of 100 nA. Pressures higher than this however, and ion bombardment occurs which can shorten the

lifetime of emitters dramatically. This manifests itself as adsorption and desorption processes on the CNT tip. Ions are very reactive and can break the carbon-carbon bonds and gradually etch the CNT. High currents can result in heating of the CNT and cause evaporation of material and hence a reduction in β value. Large fields can also rip CNTs from the substrate if it's weakly adhered. Therefore operating a DFE lamp in high vacuum and ensuring that CNTs are sufficiently adhered to the support cathode will mean that the device will last longer in operation.

1.6.5. Other Emitter Materials

CNTs are excellent field emitters due to their very high aspect ratio, which suggests that other similarly sized materials could also potentially be good emitters. Silicon nanowires and zinc oxide nanorods are also extensively researched in the literature due to their high aspect ratio and low work function.

Silicon has a low work function of 3.6 eV, lower than CNTs. Zeng *et al* [71] prepared silicon nanowires using gold coated silicon wafer substrates. Nanowires were then grown using a CVD technique at 480 °C in the presence of helium diluted silane gas. The wires that were grown had diameters of 100 nm and lengths of 100 μm. While the temperature used is less than the average temperature used for thermal CVD for growing CNTs, the diameter is larger than what is normally achieved for CNTs. The E_{TO} value is also high at 5.5 V/μm, which is higher than most similar articles on CNTs. The silicon nanowire films were annealed for 24 hours in vacuum at 550 °C, which resulted in an E_{TO} value of 2 V/μm.

ZnO has a work function of 5.3 eV, which is higher than both CNTs and Si nanowires. Despite this, they have been the topic of much field emission research. ZnO nanorods are easy to fabricate and are robust. Zhang *et al* [72] used lithographic techniques to pattern

silicon nanocrystallite substrates, and then ZnO powder and graphite powder were mixed and kept at 800°C while argon (800 sccm) was passed over. The substrate was placed downstream and after 60 minutes, ZnO nanorods of length 10μm were observed. A current density of 0.1 μA/cm^2 was achieved at an applied electric field of 3.5 V/μm.

While both silicon nanowires and ZnO nanorods show potential as good field emitters, they do not currently compete with CNTs. This is because their aspect ratio is not as high as CNTs, and the LDoS present at CNT tips may not be present in Si nanowire or ZnO nanorods tips.

1.7. Other Applications of CNTs in Energy Efficiency Applications

Due to the high aspect ratio of CNTs, upscalabilty of process, chemical and mechanical robustness, as well as beneficial electronic properties, many research groups have developed energy saving devices using CNTs.

1.7.1. Field Emission Displays

Field emission displays require a flat, large surface area of emitters to be fabricated in a triode arrangement to ensure that each pixel can be operated independently. The first article demonstrating field emission from CNTs also demonstrates how it can be used in a display environment [73, 74]. Most articles that discuss display applications use an *ex-situ* method of aligning the CNTs (*i.e.* the CNTs are grown first, and then transferred to large area flat panels) [75, 76]. Choi *et al* used an organic binder method to make a 4.5 inch flat panel display [76] and demonstrated an RGB colour display (Figure 15). The main problem with this technology is in the ability to fabricate field emitter "cells" that constitute individual pixels in the final display [15]. Lithographic techniques can be utilised to form repeating patterns for this purpose.

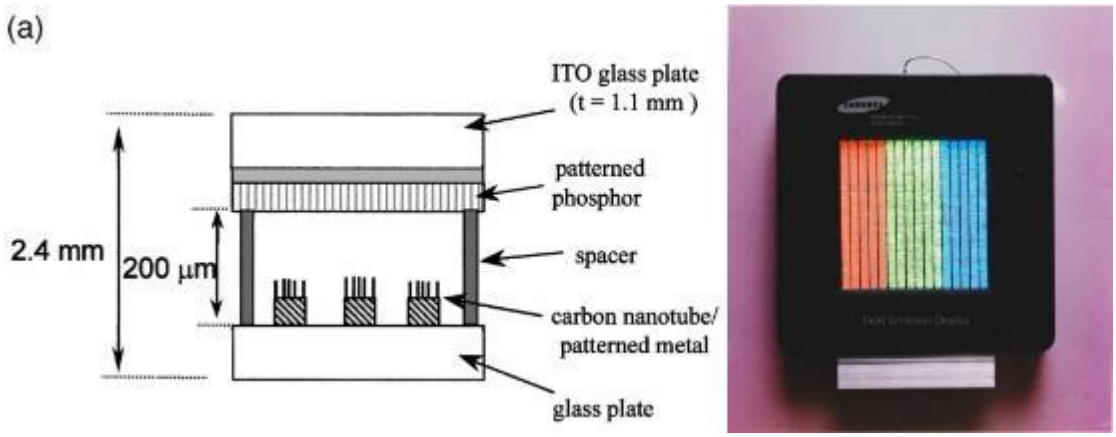

Figure 15. Schematic of field emission array (FEA) for a pixel in a flat panel display (a) and a photograph taken of the display in operation (b). Taken from [76].

1.7.2. Microwave Power Amplifiers

Microwave amplifiers consist of a triode type structure where an emitter's current is controlled *via* a gate, within a tube known as a "travelling wave tube" TWT (Figure 16) [77]. Microwave amplifiers require CNT emitters to have both long term and short term stability, high transconductance (G_m), and low capacitance [78, 79]. As G_m is the ratio of output current to input voltage, it is influenced by the work function, field enhancement factor and density of emitters. Capacitance is related to the emitter array surface area and cathode to gate spacing [78]. A maximum current of 91.4 mA at an applied voltage of 3.5 kV was achieved using a field emitter array (FEA) device based on CNTs and this represents an efficiency of 17% [80]. Field emitter array microwave power amplifiers based on CNTs have exceeded the current densities (and total current) achieved from traditional thermionic types. Higher currents at lower electric fields mean these amplifiers can be miniaturized, which has benefits for military and space applications.

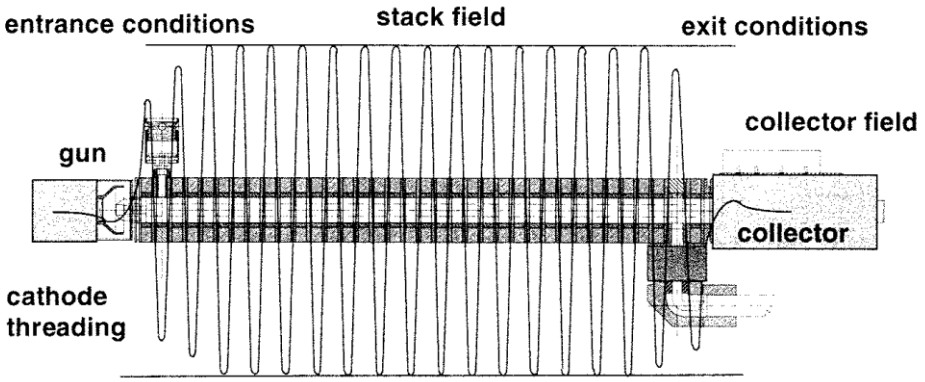

Figure 16. Schematic of a TWT microwave amplifier taken from [80]. The FEA is to be found on the cathode.

1.7.3. X-Ray Generators

X-rays are produced when high energy electrons are accelerated towards a metal target (usually tungsten, molybdenum or copper) (Figure 17). Electrons decelerate as they interact with the nuclei of the metal atoms and X-rays are emitted due to the Bremsstrahlung effect [81]. As field emitters reduce the overall energy needed to generate electrons, research has been conducted into using field emitters, in particular CNTs, for use in X-ray generators. The increased efficiency means that X-ray generators can be miniaturised to hand held spectrometers and similar medical devices [21]. Short term emission stability is vital for this application, as short acquisition times are used in medical applications [82]. Long term stability is also important and a life time of more than one year was achieved by Tolt *et al* [82].

1.7.4. Terahertz Generators

A more recent application of CNTs has been as oscillators in the terahertz range (300 GHz – 30 THz). This is due to the increased demand for faster communications and higher resolution spectroscopy [77], and a theoretical study have shown that CNTs can emit in the terahertz range [83]. Monohara *et al* [84] monolithically fabricated a nanoklystron

consisting of a coupling iris, resonating cavity and electron beam tunnel (Figure 18) and an emission current of ~0.63 mA at 3.6 V/μm was achieved.

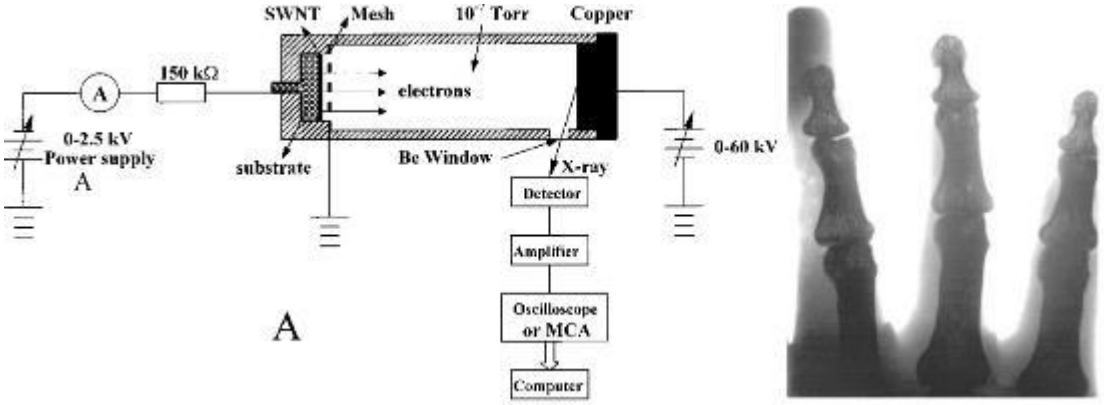

Figure 17. Schematic of X-ray generator tube where the CNT field emitters are found on the substrate (a). High quality X-ray images are produced using this method (b). Taken from [12]

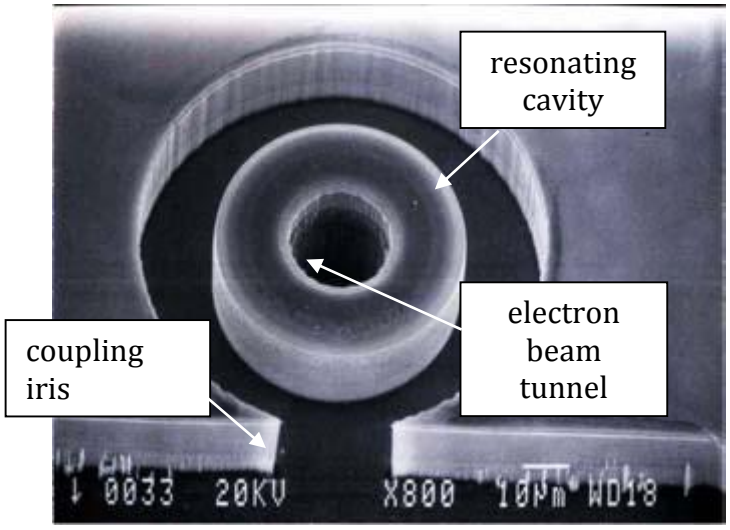

Figure 18. SEM micrograph of the nanoklystron proposed in article [84], where the CNT emitters are found in the electron beam tunnel. Taken from [84]

1.8. Processing and Growth of CNTs

There are many methods of growing CNTs, which vary between relatively simple systems such as CVD, to very novel such as inverse flame techniques [85-87].

CNTs produced by the arc discharge method tend to have fewest defects due to the high temperatures involved (>1,700 °C) [88]. Raman spectroscopy (discussed in more detail in Chapter 2, page 51) shows that the 'D' peak (an indication of the defect density) is lower

and almost absent in CNTs produced by this method. The arc discharge method of producing CNTs is performed in an inert atmosphere. Two graphite electrodes are held near each other and a voltage is applied so that an arc is produced where currents as high as 20 A are observed. The resultant CNTs have fewer defects compared to other methods of CNT production [21, 89]. However, there is less control over various CNT properties (such as diameter, length, CNT density *etc*) and it is difficult to grow CNTs directly on to substrates using this method.

CNTs are widely known for their reluctance to grow with uniform properties and often a batch of CNTs will have varying lengths, diameters and crystallinity [90]. Factors such as temperature, catalyst used, catalyst concentration, carbon source and length of growth time, and their influence on the morphology of grown CNTs, will be addressed in this section.

1.8.1. Processing Techniques

1.8.1.1. Chemical Vapour Deposition (CVD)

CVD is one of the most popular methods of producing large quantities of CNTs due to its versatility, ease of scaling and relatively low temperatures (<1,000 °C) [27]. For the production of CNTs, a carbon containing compound (the precursor), normally in the gas phase, is diluted in a carrier gas, usually argon or nitrogen, and in the presence of a catalyst decomposes at elevated temperatures to produce CNTs.

The carrier gas often contains H_2 (from 10% up to 100%) [50, 53, 91] which is believed to remove amorphous carbon *via* an etching process [92]. Water vapour is sometimes used to remove amorphous carbon because it is a weak oxidiser [93]. Water vapour was also found to increase catalytic activity. Catalysts used are usually iron [94, 95], nickel [96], cobalt [97, 98] or a combination of the three, and can be either pre-fabricated onto

a substrate (supported catalyst) or as an organometallic compound that decomposes with the carbon precursor at elevated temperatures (floating catalyst) [97, 99-101].

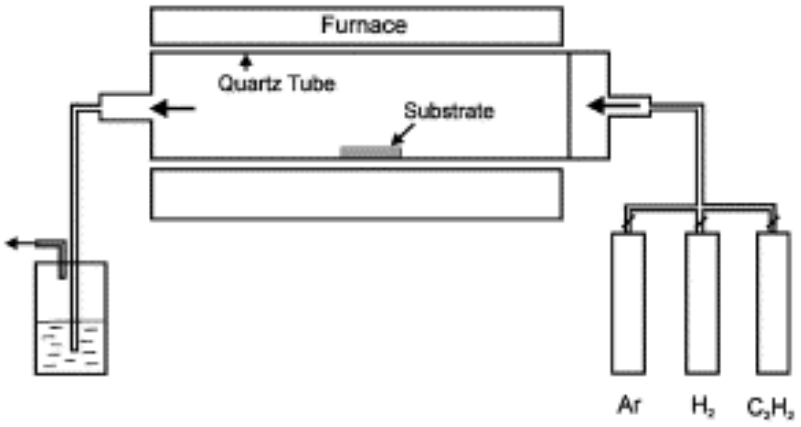

Figure 19: Schematic of CVD arrangement. Taken from [102].

Vertically aligned CNTs are possible with the CVD technique, due to a crowding effect [103]. Versatility, scalability, ease of producing CNTs, and the possibility of producing vertically aligned CNTs are the main advantages of using CVD for field emission applications.

1.8.1.2. Plasma Enhanced CVD (PECVD)

Plasma enhanced CVD (PECVD) is usually carried out at lower temperatures or even room temperature [103], whereas growth does not occur below 550 °C for catalytic CVD [101]. In the case of RF-PECVD, the plasma chamber is filled with the carbon precursor, which is diluted with argon, hydrogen or ammonia to a pressure between 1 and 20 Torr [103] (Figure 20). An electric field is applied between two coils which causes a breakdown of the gases and a plasma is formed. The substrate is placed on either the anode or cathode. As the temperatures used are relatively low, CNTs can be grown on glass substrates [104], and potentially on polymer substrates [103].

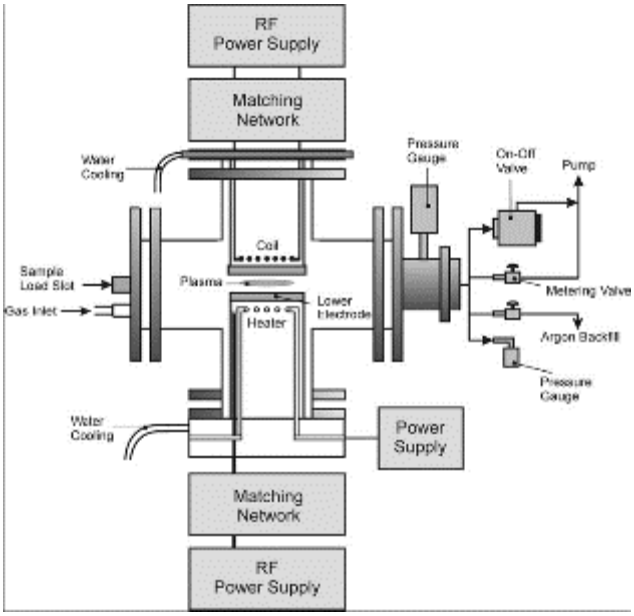

Figure 20: Schematic of PECVD system taken from [103].

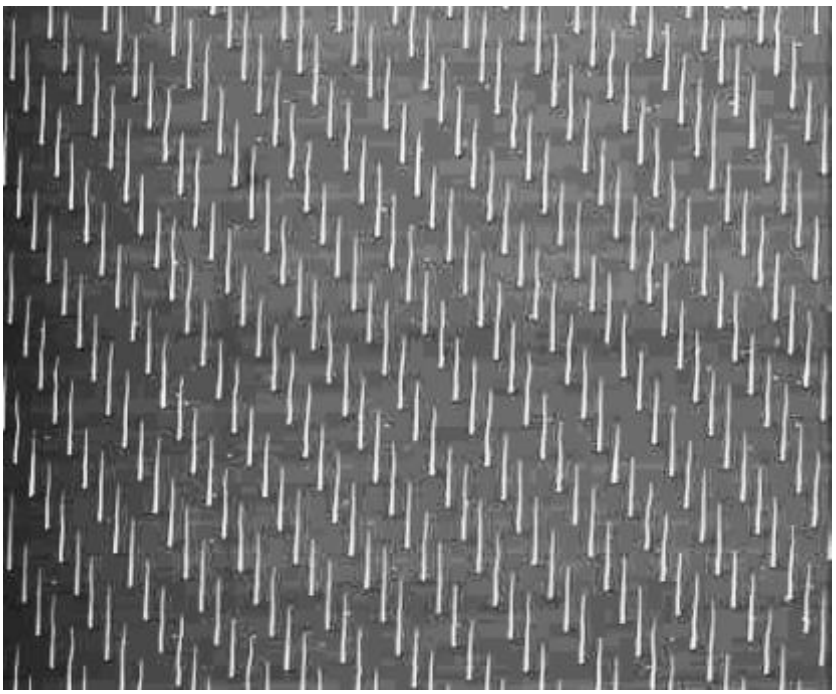

Figure 21: SEM micrograph of free standing spaced CNTs, produced using PECVD. Taken from [21].

Tu *et al* demonstrated how the density of free standing CNTs would be controlled from 10^5 CNTs per cm^2 to 10^8 per cm^2 [105]. Using pulse-current electrochemical deposition to achieve a varying density of Ni catalyst particles from a 0.01 M solution of $NiSO_4$ and 0.01 M of H_3BO_3 in water. Another way of creating isolated catalyst particles Li *et al*

deposited a thin film (100 nm) of Fe on a Si substrate and a hydrogen plasma was used to create catalyst particles at a pressure of 225 Pa and an etching time of 10 minutes [106]. Spaced, free standing and vertically aligned CNTs can be grown using PECVD, due to the electric field influencing the growth direction (Figure 21). This is the main advantage of using PECVD for field emission applications [105].

1.8.2. Catalyst Preparation

There are two main methods of delivering catalyst particles into the reaction chamber for CNT growth. Either the catalyst particles are prepared and deposited on to the substrate prior to CNT growth *ex-situ,* or an organic-metallic compound can be used that decomposes in the reaction chamber to produce particles *in-situ*.

1.8.2.1. Supported Catalyst

Catalyst nanoparticles are pre-fabricated on substrates before growth of CNTs (*ex-situ*). The advantage of this method is that catalyst particle morphology can be controlled more easily, and characterised before CNT growth. Catalyst particles can be deposited by suspending in a solution. A catalyst solution can be used where it is spin coated on the substrate or where the substrate is dipped into the solution. Once dried, the substrate is left with a deposit of catalyst particles [107, 108].

Another technique relies on initially depositing a thin layer (<10nm) of catalyst metal and after reduction small nanosized islands of catalyst metal are formed. The agglomeration is driven by surface and elastic energy minimisation and higher temperatures increases surface mobility. Reduction can occur from treatment in hydrogen at elevated temperatures, annealing in vacuum, or etching in plasma [106]. The main techniques for depositing the thin metal layer are magnetron sputtering [79, 94, 109], electron beam

evaporation [110, 111], or application of a metal containing solution [112, 113]. These nano-islands act as catalyst particles for CNT growth.

In all supported catalyst techniques, greater control of CNT density is achieved by adjusting the catalyst concentration in a "wet chemistry" technique, or depositing a thinner catalyst layer in sputtering technique. The supported catalyst method can be time consuming as it is a two-step process and often several hours are needed to reduce the layers to form nano-islands. More control over the size and distribution of nanoparticles however, is obtained in comparison to other methods [114].

1.8.2.2. Floating Catalyst

The floating catalyst technique involves the dissolution of the catalyst in the carbon precursor so that catalyst particles are generated *in-situ*. This technique offers a higher density of CNTs and vertical alignment which is essential for field emission applications. No pre-treatment of the substrate is necessary as the catalyst containing compound is gaseous and mixed with the gaseous carbon-precursor. Ferrocene is commonly used as it is solid at room temperature (*i.e.* easy to handle) and sublimes at about 250 °C. Within the furnace ferrocene decomposes and iron particles are deposited and adhere to the substrate and act as the catalyst for CNT growth [115]. This method is simpler than the supported catalyst method as particles are produced *in-situ*. Nanoparticle size and distribution can be controlled by changing the ratio of ferrocene to precursor [116].

Aerosol CVD uses liquids instead of gases for the carbon precursor. Ferrocene is also used in this method as it dissolves in a wide range of organic compounds. The aerosol is produced using an ultrasonic unit which produces a mist of small liquid droplets containing the precursor/catalyst solution. The mist is then passed through the furnace at elevated temperatures using a carrier gas where it decomposes and CNT growth occurs.

The ideal morphology for lighting applications are nanotubes that are less than 100nm in diameter and are several tens of microns long, perpendicular to the substrate surface and separated from each other (see page10). This is necessary so that field enhancement can be maximised. It is very difficult to produce free standing, vertically aligned CNTs using the CVD method. Zakhidov *et al* [117] observed that when an electric field is applied to a CNT yarn, the emitters align in the electric field. This in turn will affect the β value of the CNT such that it will be higher than before alignment. CNTs therefore can be lying parallel to the substrate as it is likely they will align in an applied field. If CNTs are entangled too much, alignment of them during emission maybe limited. By changing the processing parameters of the CVD method, these properties can be controlled [107, 118].

1.8.3. Kinetics *vs.* Thermodynamics

A fundamental understanding of both the thermodynamics and kinetics of nanotube growth is necessary if nanotubes are to be produced in a controlled and predictable manner [27, 90, 92, 119]. For this project, control over the thickness, length and density of CNTs is most important. Catalytic methods of producing nanotubes involve the decomposition of hydrocarbons (or similar compounds) over catalytic particles. It has been shown that if a metal foil is used as a catalyst for the decomposition of hydrocarbons, a thin film of graphite is grown [120]. If micron sized particles are used, carbon filaments of similar diameter are grown [121]. Clearly, the size of the particles and not just the thermodynamics and kinetics play an important role in determining the type of nanotube produced too.

The process of carbon nanotube growth can be split into 4 mechanisms. Firstly, the carbon precursor is adsorbed onto the catalyst particle surface, then the precursor molecule dissociates. Next, carbon is diffused through or on the surface of the particle

and finally carbon is incorporated into the growing structure [92, 103, 122] which results in lengthening of the tube (Figure 22).

Studies by Hofmann *et al* [122] show that the activation energy for dissociation of C_2H_2 over Ni catalyst particles used for CNT growth is 0.23 eV when using the PECVD technique. This compares to 1.21 eV for thermal CVD [123]. The hydrocarbons need to be dissociated so that carbon can diffuse on the surface of the catalyst particle and growth can occur. The plasma lowers the activation energy required for hydrocarbon dissociation and hence growth can occur at a lower temperature. This means that CNTs can be grown directly onto polymer substrates. Merkulov *et al* state that the primary parameter that affects CNT growth rate is the carbon concentration in the catalyst particle, which is determined by the diffusion coefficient of carbon in the catalyst metal [92]. Therefore the adsorption of carbon species on the catalyst surface, surface reactions, or diffusion of carbon through the catalyst could all be rate limiting factors in CNT growth [124].

It is widely believed that the size of the catalyst particles not only determines the width of the CNTs grown, but also the type of filament produced. If the particles are large, of the order of a few microns, then carbon filaments are produced that consist of stacked graphene layers [121]. As the size of the particles decreases, the curvature of the graphene layers increases (and strain increases) until it is more favourable to form a continuous graphene layer perpendicular to the particle surface (*i.e.* MWCNT produced instead of carbon nanofiber) [116]. Controlling particle size and size distribution is therefore important to obtain nanotubes with uniform properties.

1.8.4. Processing Parameters

1.8.4.1. Growth of CNTs on various substrates

CNTs have been grown on several different substrates ranging from quartz to glass to carbon fibre and ceramics. For field emission applications, it is important that the substrate is electrically conducting, adheres well to the grown CNTs, is mechanically robust and does not poison the catalyst.

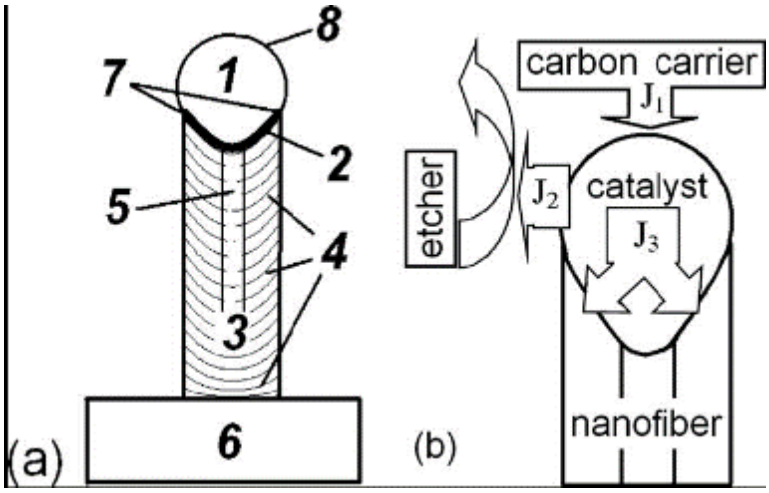

Figure 22: Schematic of CNT growth, showing the different processes that occur. a) CNT during growth 1. catalyst particle, 2. particle/CNT interface, 3. growing CNT structure, 4. graphene layers, 5. hollow central tube, 6. substrate, 7. gas/particle/CNT interface and 8. particle/gas interface. b) schematic of carbon diffusion process that occurs during growth. J1 is diffusion of carbon from precursor to particle surface, J3 is diffusion through catalyst and into growing structure and J2 is removal of excess carbon. Taken from [92].

1.8.4.2. Growth on Metal Substrates

Talapatra *et al* have shown that CNTs can be grown on Inconel *via* injection CVD with ferrocene-xylene solutions at 770 °C [125]. The nanotubes show good adhesion to the substrate, similar to CNTs grown on SiC. Inconel can be made into various shapes, including small disks and wires, and also deposited (*via* magnetron sputtering) onto other metal substrates, resulting in various novel lighting elements.

Other metals that have been used as substrates have been stainless steel and Kanthal wire, to name but a few [85, 126, 127]. If using stainless steel, treatment prior to deposition to roughen the surface and to remove the chromium layer that is often found at the surface of stainless steel is necessary as chromium is known to prevent CNT growth [128, 129]. Etches and various oxidation and reduction techniques can be used to remove the chromium layer and dense carpets were grown using stainless steel itself as the catalyst [128].

Kanthal wire has been shown to catalyse nanotube growth without the addition of another catalyst. This is due to the Fe-Cr particles in the alloy acting as nucleation sites for growth. While this simplifies the process of the CVD technique, it is more difficult to control CNT size and density as there are no catalyst particles that can be manipulated. Annealing Kanthal wire in air for several hours' results in an oxidised surface, this therefore means that catalyst particles can be used in the usual way as the surface is now inert.

1.8.4.3. Temperature effects

When the CVD reaction temperature increases, the nanotube diameter tends to also increase. With toluene, nanotubes of diameter 10 nm were produced by the injection CVD method at 550 °C [101]. The diameter was increased to an average of 75 nm at 850 °C and the diameter range was also increased. When acetylene was used, the diameter of CNTs grown was 20 nm at 750 °C [20]. The diameter doubled when the growth temperature was increased to 1,050 °C. Noury *et al* show that an increase in temperature results in both thicker and longer CNTs using acetylene on silicon substrates [112]. Whilst it is difficult to compare results between different research groups, an increase in growth temperature seems to coincide with an increase in both diameter and diameter range.

1.8.4.4. Catalyst effects

When the catalyst concentration was increased, the nanotube diameter also increased as well as the diameter range [101, 116]. A tenfold increase in ferrocene concentration (0.2% to 2%) increased the average outer diameter from 7.7 nm to 28.4 nm when toluene was used as the carbon source [101]. With xylene, a similar increase in ferrocene concentration resulted in an average diameter increase from 28.3 nm at 0.075% (Fe/C) to 33.6 nm at 0.75% (Fe/C) [116].

As the concentration of the floating catalyst increases, larger metal particles are formed. In smaller concentrations, metal atoms on the substrate surface are further apart, and hence agglomeration and coalescence into larger particles is more difficult. Therefore, anything that increases the mobility of metal atoms (*e.g.* elevated temperature, substrates that promote metal atom mobility, *etc*) would result in carbon nanotubes of larger diameter, because of the increased size of the metal particles [116].

Using different metals as catalysts could also influence CNT properties as the growth rate is determined by the concentration of carbon in the catalyst. Cobalt has the slowest diffusion rate and results in CNTs that are thinner, less dense and shorter than iron, with nickel having the fastest carbon diffusion rate and hence the thickest CNTs [20, 130].

1.8.4.5. Boron-Doped Carbon Nanotubes

The growth techniques used to fabricate doped nanotubes are similar to those used for un-doped carbon nanotubes *i.e.* CVD, laser ablation and arc discharge. For the CVD method the boron is usually contained in the carbon source precursor (typically a hydrocarbon) so that the dopant atoms become integrated into the growing structure *in-situ* [131]. Common precursors are diborane and boroazine [131, 132]. While we might expect this to result in a doped nanotube with a homogenous distribution of boron atoms, this is not the case, and instead high concentrations of boron atoms are found at the tips

of doped nanotubes [56]. Boron acts as both a catalyst and a surfactant during growth, which explains the very high growth rates observed in comparison to un-doped nanotubes [56]. Local concentrations of boron can be as high as 20% which implies that boron clusters form [133].

There are some problems with the production of B-doped nanotubes. There are very few stable B/C precursors available and those that are tend to be toxic. In addition, the CVD growth of B-CNTs is made more difficult as the processing 'window' is narrower, due to the tendency of the boron to segregate in to clusters [27] as C-C bonds are more stable than C-B bonds [134].

1.8.4.6. Nitrogen-Doped Carbon Nanotubes

More work has been conducted on N-CNTs in comparison to B-CNTs as there are more stable nitrogen-containing precursor hydrocarbons than boron compounds. Again, the most common methods of production are arc discharge, laser ablation and CVD. Ammonia is popular as a N precursor, and is normally mixed with a carbon precursor such as acetylene or sometimes an inert gas and ferrocene [135]. Nitrogen is incorporated into the CNT structure substitutionally, either directly replacing a carbon atom or by being positioned next to an atom vacancy (pyridinic nitrogen) (Figure 23), with concentrations as high as 13% when using high pressure processing techniques [136], but lower (2 at% - 9 at%) using the CVD method [135].

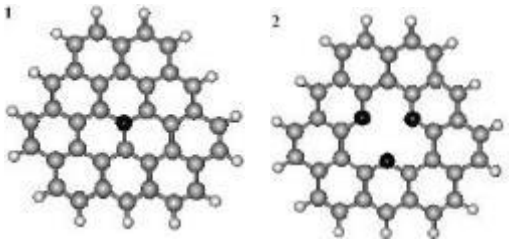

Figure 23: Schematics of how nitrogen can be incorporated into graphitic structures a) direct substitution of carbon atom and b) pyridinic nitrogen. Taken from [137]

Studies by Koos *et al.* show that nitrogen slows the growth of N-CNTs [32] as confirmed by Liu *et al* [135]. This is possibly due to nitrogen being adsorbed on the surface of the catalyst particles which in turn limits the rate of surface diffusion of carbon *i.e.* excess nitrogen needs to be removed before carbon is incorporated into the growing CNT structure.

1.9. Conclusions

CNTs synthesised by CVD, have been chosen for further study in this project as field emitters due to their high aspect ratio in comparison to other nanostructured emitters, such as ZnO and Si. Previous research has shown that CNTs can emit for many hours in vacuum and are also chemically/mechanically robust and are hence well suited for operating in the harsh environment of high electric fields. The work function of CNTs can be tailored relatively simply by introducing dopants into the structure (*e.g.* nitrogen or boron) which introduce LDoS near the Fermi Level. The relative ease of producing CNTs with desired properties and the up-scalability of CVD growth techniques makes the prospect of implementing CNTs in a commercial DFE lamp more viable.

The numerous issues in the literature with regard to field emission from CNTs have been discussed. The main problem is a lack of consensus on how to measure and define the figures of merit, in addition to the inherent difficulty in reproducing experimental setups. This latter point is due to the equation that governs field emission being an exponential term, hence a small change in material properties can have a large impact on emitted current. For example, a change in the geometry of a CNT tip can drastically alter its β value. This issue is exaggerated when measuring the field emitted current from individual CNTs because the inter-electrode gap is typically shorter when compared to measuring CNT films. There are also issues when considering the field emission properties of CNT films and DFE lamps. It is difficult to compare the results from various

articles due to the lack of similarity in the experimental setup. Previous work appears to focus on the demonstration of a DFE lamp but does not consider optimisation of such a lamp through controlling the processing parameters (and hence CNT film morphology) to achieve improved field emission results.

The work contained in this thesis attempts to address these problems by comprehensively studying the link between the 'as grown' CNT film morphology and their corresponding field emission properties, towards a DFE lamp application. The hope is that, by conducting these experiments in one study, results can be compared between differing morphologies and therefore a better understanding of how to produce better field emitter CNT films for DFE lamp applications achieved.

The field emission properties of individual CNTs will also be investigated. A very large number of CNTs would need to be studied in order to produce a statistically significant result, in terms of the field emission properties of individual CNTs and comparing between them. That is not the aim in this thesis, instead only a handful of CNTs shall be studied. The hope is that by studying individual CNTs *in-situ* and, for example, measuring a CNT before and after irradiation damage, clues to the role of defects (dopants, bonding *etc*) will help facilitate the optimisation of such emitters.

There are several questions that are beyond the scope of this project. It is unlikely that a detailed understanding of how the work function of the 'as grown' CNT films will vary with the film morphology as it is difficult to know the contribution of emitted current from each emitter. Also it is difficult to determine in detail the states at the cap of a CNT and what mechanism is contributing during field emission. These problems may be answered sometime in the future when *in situ* analysis of CNTs during field emission and over a whole CNT film ensure that a statistical comparison can be made.

2. Experimental Techniques

2.1 Growth of MWCNT Films

The cathode component that will make up the DFE lamp consists of a film of CNT emitters supported by a substrate. CNT films on wire substrates were grown using an aerosol chemical vapour deposition (a-CVD) technique. Various wire substrates were prepared prior to deposition of CNTs *in-situ*. To determine the best material for the project, various substrates were investigated; carbon fibre ribbon, Kanthal wire, and tungsten filament coil.

The Kanthal wire is an Fe alloy with composition: Fe, Cr (20.5-23.5%), Al (4.8%), Mn (0.5%), C (0.08%) and Si (0.07%). The carbon fibre ribbon used (supplied by Goodfellows) was a continuous multi-filament ribbon yarn consisting of carbon fibre strands approximately 10 μm in diameter each. These samples were used to investigate the morphology of CNT samples so that optimum processing parameters could be established.

2.1.1. Substrate Preparation

Wires were firstly cleaned in acetone, and placed into the furnace using a steel substrate holder that was fabricated to support the wire substrates so that they were exposed to the highest aerosol concentration (Figure 24). Using the holder, wire substrates can be mounted either parallel to the carrier gas flow or perpendicular, as the flow direction could be an important factor in CVD CNT deposition [138].

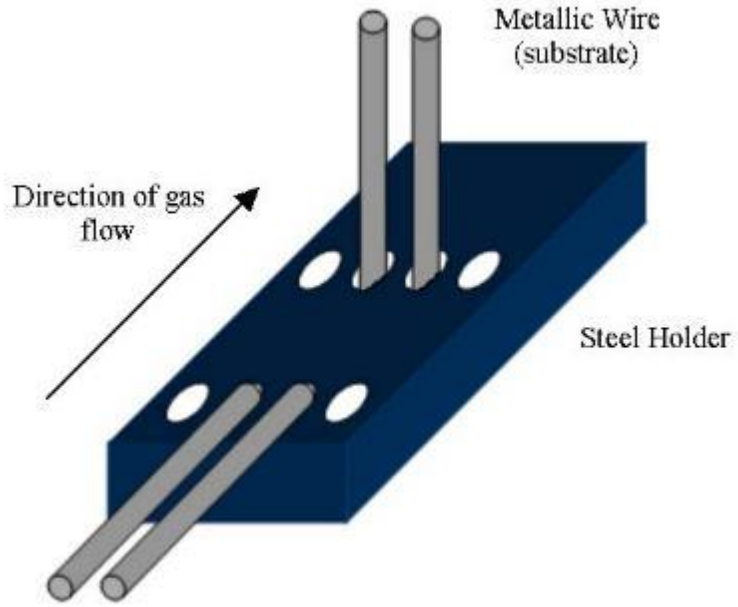

Figure 24. Steel holder used to hold horizontal and vertical wires in the furnace, so that they are placed in region of maximum flow (*i.e.* near the central axis of symmetry of the quartz tube).

To investigate the difference in CNT morphology with respect to the displacement along the furnace, long wires (<50 cm) were placed parallel to the gas flow. A steel holder was also made to align 5 cm wires parallel to the gas flow to produce suitably sized samples for macroscopic testing of field emission properties of CNT films.

2.1.2. a-CVD growth of CNTs on substrates

A quartz tube was placed running through a tubular furnace (Figure 25). The wires that were to have CNTs grown on them were mounted in one of the steel wire holders and placed using a long spatula, in the quartz tube approximately 10 cm from the furnace entrance [139]. Previous work in the group has found this distance to be beneficial to CNT growth [140]. For long wires (<50 cm), the wire was placed within the furnace with the start of the holder coinciding with the front face of the furnace.

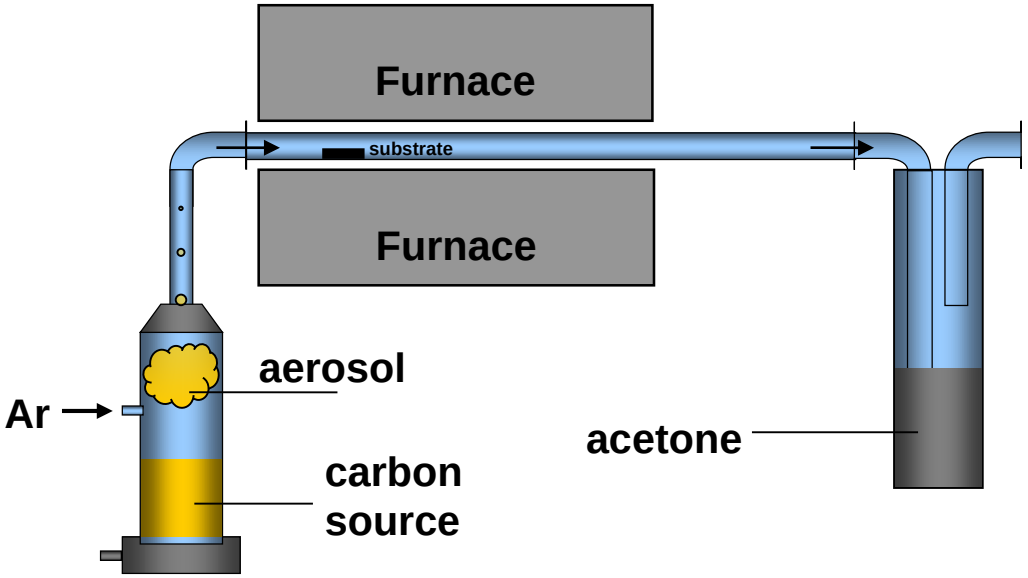

Figure 25. Schematic of experimental setup used to grow CNTs on various substrates. A mist consisting of a solution of carbon precursor and dissolved catalyst is passed through the furnace using a carrier gas, usually argon. The exhaust gases exit the furnace and are bubbled through the acetone to remove harmful particulates in it before leaving the system.

The apparatus was set up as shown in Figure 25 and the atomiser filled with either a toluene ($C_6H_5CH_3$) solution, benzylamine ($C_6H_5CH_2NH_2$) solution, or a 1 M solution of triethylborane (TEB) in hexane to grow undoped, N-doped or B-doped CNTs respectively. The solution contained either 1 wt% or 5 wt% ferrocene. Ferrocene decomposes to form iron particles in the 'hot zone' of the furnace, which then catalyse CNT growth. The atomiser was set to a known amplitude and frequency, which were often changed before each experiment to ensure that a dense mist was produced. For benzylamine, the viscosity was too high to produce a mist of the same density as with toluene. Often a thinner, translucent mist was formed that took up to 4 minutes to reach the furnace entrance.

Argon was used as the carrier gas at a flow rate of 1 SLM (standard litre per minute) and H_2 was added to the carrier gas (between 0 and 0.2 SLM) to control the defect density [141, 142]. For the toluene and benzylamine experiments, the furnace was set to between

700 °C and 900 °C for a time period of 10 minutes. In the case of TEB, the growth temperature was between 900 °C and 1,000 °C, for a time period of 10 minutes (Table 1) as previous work in the group indicates these parameters to be optimum [31]. After deposition, and when the quartz tube had cooled to less than 150°C, the substrate, or wire holder, was carefully removed using a metal spatula.

Important Growth Parameters

Precursor Solution	Catalyst (dissolved in precursor)	t (mins)	T (°C)	Carrier gas
Toluene	1-5wt% ferrocene	10-30	800-900	1SLM Ar + 0-0.2SLM H_2
Benzylamine	1-5wt% ferrocene	10-30	800-900	1SLM Ar + 0-0.2SLM H_2
1M TEB in hexane	1-5wt% ferrocene	10	900-1,000	1SLM Ar + 0-0.2SLM H_2

Table 1. Table showing the various growth parameters that can be manipulated to grow optimum CNT film microstructures.

2.2. Characterisation Techniques

Material properties, such as CNT length, diameter, and defect density, in addition to the overall arrangement and inter-tube interaction (such as entanglement and bundling), were characterised using scanning electron microscopy (SEM), transmission electron microscopy (TEM), and Raman scattering spectroscopy. SEM and energy-dispersive X-ray (EDX) were also used to characterise the surface of substrates prior to CNT growth.

2.2.1 Sample Preparation

For SEM and Raman investigation, films of "as grown" CNTs on wire substrates were sectioned into 1 cm lengths. A carbon sticky pad was attached to an SEM stub and the wire sections were adhered to the pad.

For TEM analysis, CNTs were removed from wire substrates by placing them in vials of ethanol and sonication for 30 minutes in an ultrasonic bath, or until a uniform grey/black solution was formed. A copper TEM grid was placed on filter paper and a pipette was used to dispense droplets of the solution on to the grid. The grid was then left to dry overnight leaving a deposit of CNTs on its surface.

2.2.2. Raman Scattering Spectroscopy

Raman scattering spectroscopy is a common method used to establish the vibrational and rotational modes of bonding present within individual CNTs. A laser beam is focussed onto the sample using an optical microscope. The monochromatic photons emitted by the laser interact with phonons and molecular vibrations within the CNT structure. This results in a shift in the wavelength of light being scattered. Resonance of the Raman shift intensity produces characteristic peaks which indicate how dominant certain types of bonding are within the sample. This information can give an indication of the "quality" of the CNTs produced (*i.e.* good quality implies low defect density, or a high degree of sp^2 bonding). The 'G' peak (found at ~1580 cm^{-1}) corresponds to tangential vibrational modes of carbon atoms in sp^2 graphitic bonding. The 'D' peak (found at ~1350 cm^{-1}) corresponds to scattering from defects of the graphitic sp^2 bonding that corresponds to breaking of the bonding symmetry [143]. Therefore any defects (*e.g.* breaking C-C bonds, dopant atoms, strain *etc*) will contribute to this peak. The ratio between these two peaks gives an indication of the defect density of the CNTs. An I_D/I_G ratio less than 1 indicates

that the CNT is mainly graphitic with defects found within the structure. An I_D/I_G ratio near unity and above indicates that the CNT is not graphitic in nature and is considerably disordered.

A JY Horiba Labram Aramis imaging confocal Raman microscope was used to examine the Raman shift of CNT samples. Scan ranges were made from 500 cm^{-1} up to 3,000 cm^{-1}.

2.2.3. Scanning Electron Microscopy (SEM)

SEM was used to determine the microstructure of CNT films. A beam of electrons was accelerated towards the sample through an array of apertures and lenses, which are used to focus and stigmate the electron beam, thus altering the resolution and depth of field of the corresponding image. The beam was focused onto the sample with a spot size as small as 3nm and scanned across the chosen field of view. The secondary electron signal generates an image where the contrast is mainly due to surface topography.

An SEM has superior depth of field and an increased lateral resolution compared to an optical microscope. In addition, minimal sample preparation is involved and so it is very convenient for the study of CNT samples, which tend to be fragile.

A JEOL FEG 840F SEM was used in this work, with an acceleration voltage of 5 kV, a probe current of 2 $x10^{-11}$ A, and a working distance of 14 or 15 mm at various magnifications.

Problems can arise when the sample is non-conducting, as charge builds up that distorts the resultant image. CNT films have a reasonable conductivity and so no gold or carbon coating is required to image these samples.

2.2.4. Energy-Dispersive X-ray Microanalysis (EDX)

An EDX detector is attached to the main column of an SEM. Qualitative and semi-quantitative data regarding the elemental composition of a material is achieved by collecting the X-rays produced when the electron beam hits the surface of the material.

The electron beam interacts with the surface and the bulk of the sample, and X-rays are generated in the interaction volume of the sample which is roughly 1 μm^3. Electrons from the incident beam excite the inner-shell electrons of atoms within this interaction volume. Outer shell electrons then drop down to fill the vacant shell, emitting X-rays of an energy that is specific to the element from which it originated. These X-rays interact with the EDX detector (usually a silicon drift detector) and a characteristic set of peaks are observed which can be analysed to determine the elements present in the material.

EDX was carried out in a JEOL 840A SEM at a working distance of 20 mm and an acceleration voltage of 20 kV. A beam current of $\sim 10^{-9}$ A was used and this was changed whilst taking an initial spectrum to achieve an optimum deadtime in the EDX detector.

2.2.5. Transmission Electron Microscopy (TEM)

TEM is used to determine the internal structure of CNTs as well as the diameter distribution of "as-grown" samples. An electron beam was accelerated at 200 kV towards a sample which was up to several hundred nanometres in thickness. Condenser and objective lenses act to align and focus the electron beam onto the sample, which must be thin enough to allow electrons through (*i.e.* "electron transparent"). To obtain bright field images, a selected area aperture was introduced to block all diffracted beams so that only the transmitted beam was allowed through the aperture (giving strong diffraction contrast). To increase contrast, the image was focussed, and was then slightly under focussed, so that graphitic planes were seen as black (*i.e.* phase contrast). "As grown" samples cannot be studied in a TEM, as the substrate is too thick to be electron transparent. A JEOL 2000FX was used to study dispersed samples, while a JEOL 2010 TEM was used to characterise individual CNTs while conducting field emission experiments in a specially adapted NanoFactory TEM holder (Figure 26) (see page 54).

Figure 26. NanoFactory TEM holder used to test the field emission properties of individual CNTs.

2.3. Field Emission Property Characterisation

The NanoFactory TEM holder allowed the investigation of the FE characteristics of individual nanotubes *in-situ,* while a dedicated ultra-high vacuum (UHV) system was utilised to measure these same properties in films of CNTs. The films of CNTs were characterised using SEM, TEM and Raman both prior to and after FE testing.

2.3.1. *In-situ* field emission testing of individual CNTs

A carbon SEM pad was used to attach adhesive to the end of an STM tip (the cathode) which was then brought into contact with a previously made sample, so that individual CNTs were transferred from the "as-grown" sample and stuck to the surface of the STM tip.

The STM tip with the CNTs attached was then mounted in the NanoFactory holder, which in turn was placed inside a TEM. Another STM tip (the anode), which is part of the NanoFactory holder setup (Figure 27), was brought into contact with the CNT under investigation, and a stepped, ranged bias was applied to assess the quality of contact (*i.e.* to measure the contact resistance) between the CNT and substrate. The bias started at -500 mV, and was then stepped with 100 points over a time of 100 ms (*i.e.* one reading every millisecond), up to 500 mV. Field emission experiments were only conducted on

nanotubes that had a linear current-voltage response. The STM tip was then moved a measurable distance away from the CNT apex, typically between 100 nm and 200 nm, and a bias from 0 V up to 140 V was applied, again in a stepped fashion. Data took 100 ms to acquire, with 100 points taken (*i.e.* one reading every millisecond). The corresponding current *vs.* voltage data was plotted in a graph (Figure 28).

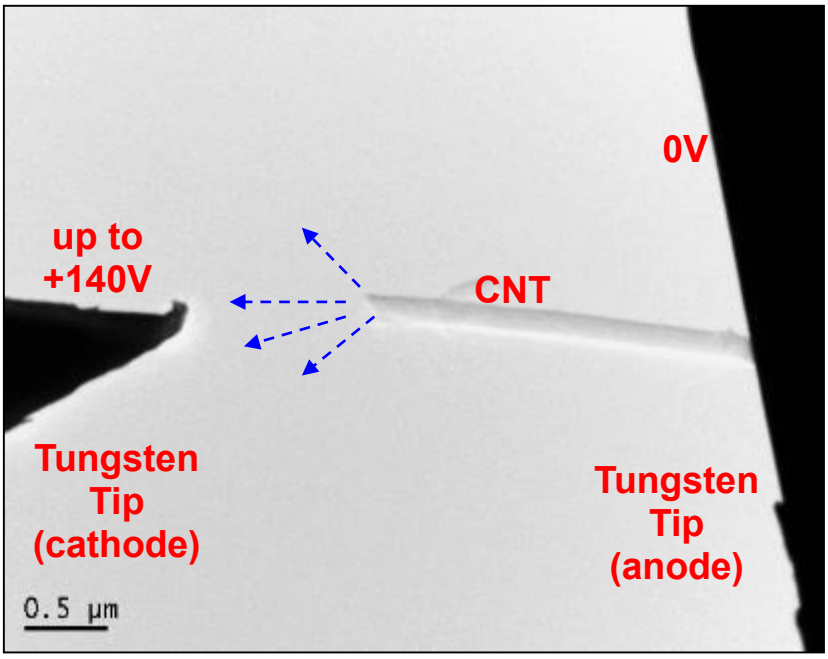

Figure 27. TEM micrograph of a typical experimental setup inside TEM chamber. Measurements are made *in-situ*.

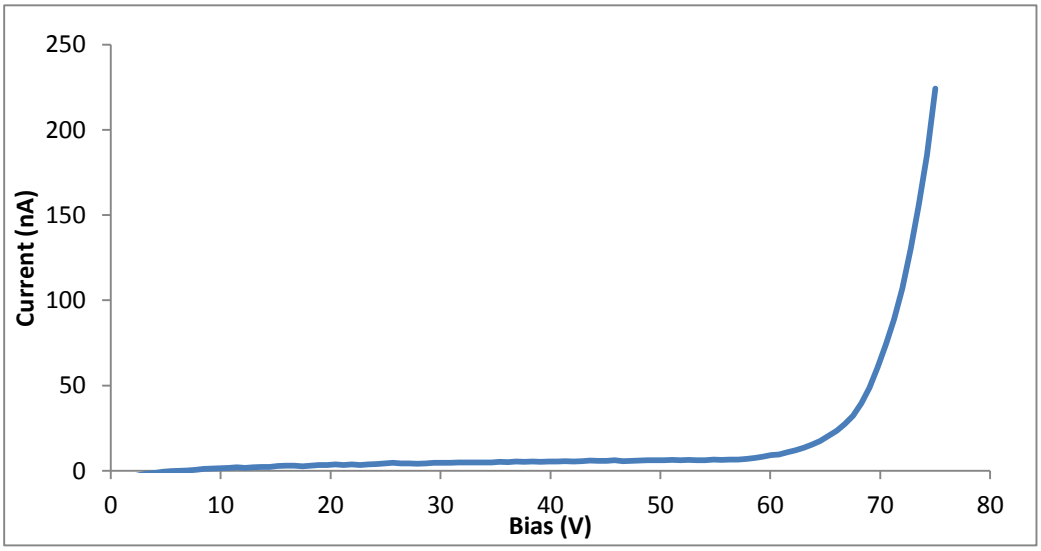

Figure 28. A typical 'current vs. voltage' graph plotted from the data obtained from the NanoFactory experiment.

2.3.2. Macroscopic field emission properties of CNT films

An ultra high vacuum (UHV) system was utilised to conduct field emission experiments on 5 cm long "as-grown" CNT wire samples (Figure 29). The wires were fixed in the centre of a 2 cm diameter aluminium cylindrical anode, in a diode arrangement (Figure 30). This arrangement was supported by a plastic bracket fixed to the underside of the UHV lid.

A potentiometer was used to control the high voltage supply between 0 V and 5,000 V applied to the anode (Figure 31). The cathode was grounded and a NI USB 6211 data logger recorded the voltage across the sample and the current flowing. The corresponding data was plotted on a computer using Labview Signal Express 2009 (version 3.5.0.).

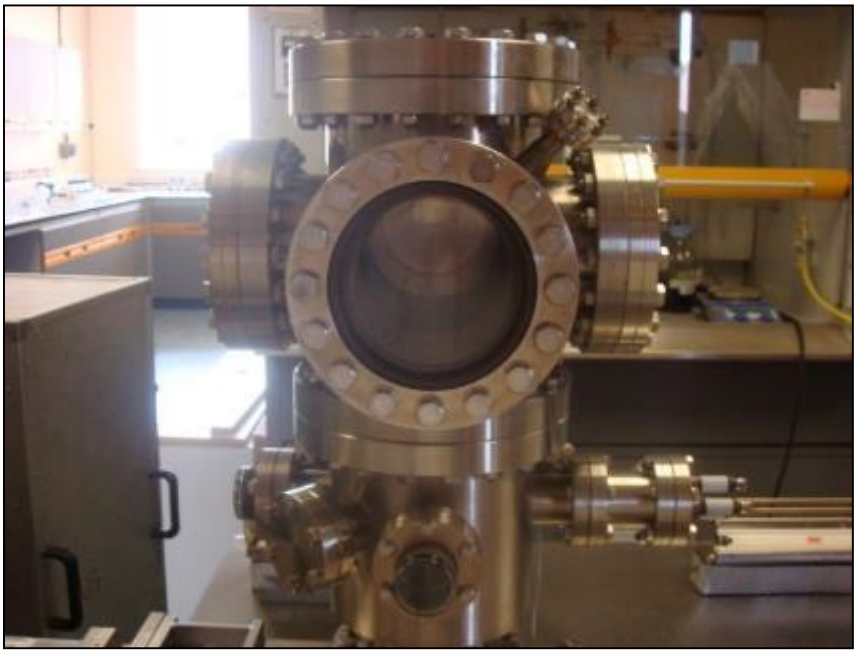

Figure 29. The UHV system used to conduct FE experiments of whole samples.

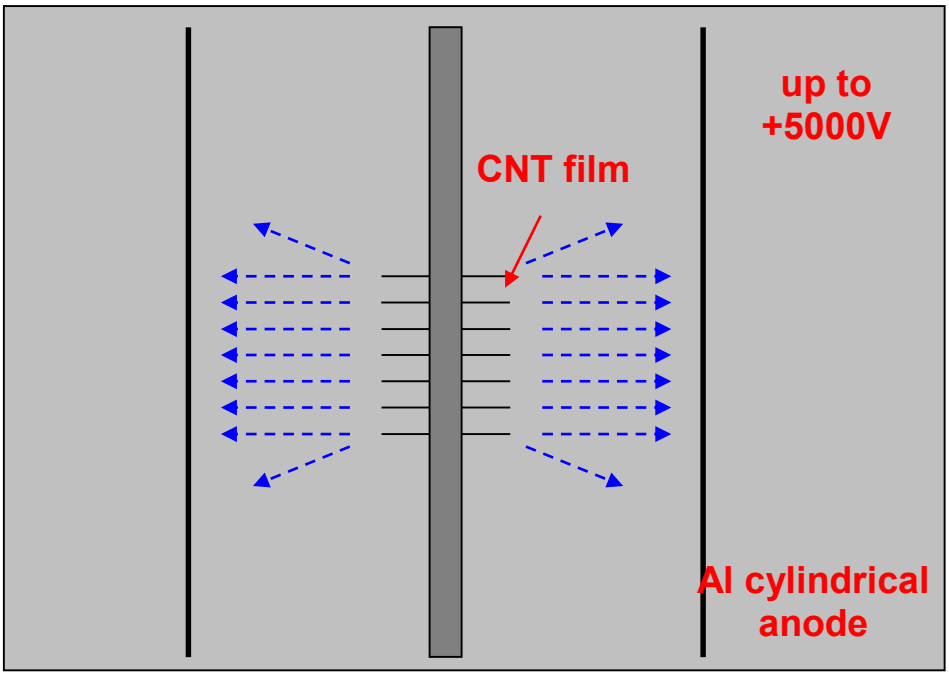

Figure 30. Schematic of experimental setup inside the UHV system. A varying DC high voltage is applied to the anode, while the cathode is grounded

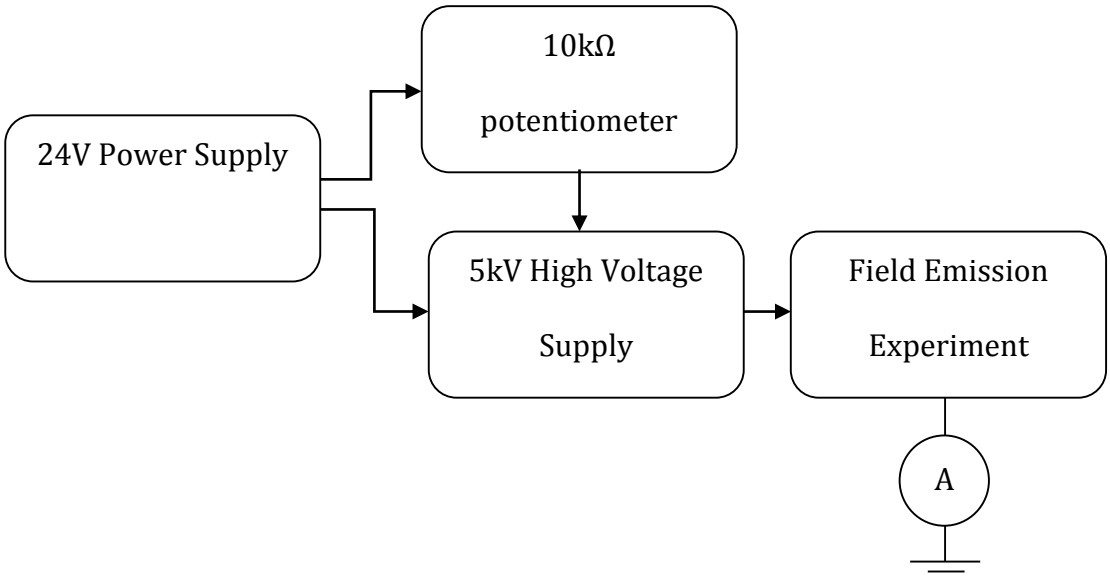

Figure 31. Block diagram of experimental setup to test macroscopic field emission properties of CNT films. The 24V power supply supplies power to both the potentiometer and the high voltage supply. The potentiometer controls how much voltage the HV system supplies to the sample.

3. Growth and Processing of CNT-wire composites

3.1. Introduction

As CNTs have high aspect ratios [6, 67, 144], and are chemically stable in the expected application environment in addition to being mechanically stable [40, 145], they are a suitable material to use for field emission applications (Chapter 1, page 26). There are several techniques used to grow CNTs and these were discussed in more detail in Chapter 1 (see page 33).

3.1.1. Growth of CNTs using the CVD technique

CVD is the process of depositing solid material on a substrate using a chemical reaction in the vapour phase. The physical vapour can either be transported to the substrate in the gas phase (g-CVD) [146, 147] or *via* an aerosol (a-CVD) [31, 32, 148].

In the g-CVD technique, the carbon precursor is usually a hydrocarbon and the catalyst is deposited on to the substrate prior to CNT growth. The substrate is usually dipped into a pre-prepared suspension of catalyst nanoparticles and then the solution is evaporated leaving these particles on the surface. The main advantage of this technique compared to a-CVD is the level of control of catalyst particle size and distribution. The process of optimising the nanoparticle size and analysis can all be done independent of (and prior to) CNT growth. The density of catalyst particles, and hence CNTs, can be more easily controlled by simply controlling the concentration of the nanoparticle suspension.

In the a-CVD technique, the precursor and catalyst are dissolved in a solution which is vapourised using an ultrasonic generator which is introduced in to the furnace *via* a carrier gas [140]. The main advantage of this technique is that of simplicity, especially when doping is used as all the precursors and catalysts are dissolved into one solution [149]. Another advantage is that it does not require a volatile precursor [150].

Growth parameters such as temperature and catalyst concentration affect the diameter, length and morphology of the CNT films grown and were discussed in more detail in Chapter 1 (see page 41). Therefore, it is important to determine which processing parameters create what morphologies. In turn, it is important to verify whether these morphologies are actually favourable for field emission, and this is discussed in more detail in Chapter 4 (see page 141). Knowledge of the field emission properties of the grown CNT films were used to provide feedback to further improve the growth parameters.

As discussed in Chapter 1 (see page10), the optimum morphology would consist of an array of emitters aligned perpendicular to the surface of the substrate and spaced at a separation twice the height of the emitters. This morphology however, is difficult if not impossible to achieve using CVD techniques due to its inherent chaotic nature. A compromise must be met where a morphology that closely resembles the ideal case is grown, whilst using realistic and practical CVD techniques.

To this end, the following important morphological parameters should be considered: a) CNTs should be separated from each other so that the full benefit of the high aspect ratio of each CNT can be realised [151]. Vertically aligned "bundles" can be formed when aligned CNTs group together and should be avoided, unless stray CNTs protrude from the edges of these bundles (Figure 32). b) CNTs should be aligned perpendicular to the substrate surface, which would increase the probability of the CNT tips, the part of the CNT that is most likely to emit electrons, being aligned towards the anode [61]. c) There should be a high density of CNTs so that a high current density is achieved [152]. Even if only a small percentage of CNTs contribute to the emission current, a high density of CNTs will ensure that a large overall emission current is observed. d) Homogeneity of the film surface is important to ensure that homogenous light emission is produced in the final

device. e) A large emitting surface should be available so that a high maximum current is achieved. f) The geometry of individual CNTs is important and should be as long and thin as possible to ensure a high aspect ratio and hence high field enhancement factor [67]. g) The CNTs should be as graphitic as possible [153], as the overall work function is affected mainly by the defect density of the CNTs [56]. This last point is a matter of debate as the literature suggests that defects either play a beneficial [37, 154, 155] or detrimental [70, 156] role in field emission from CNTs.

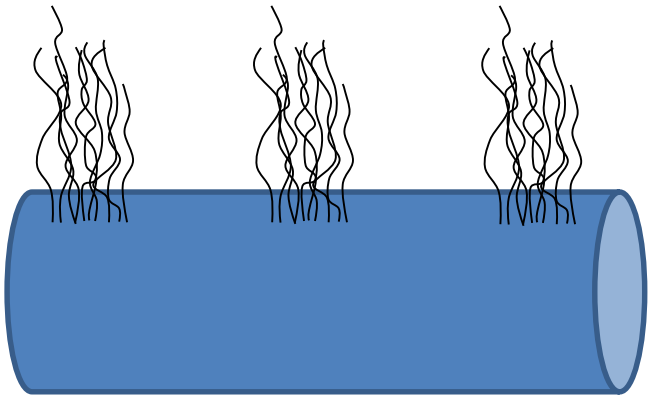

Figure 32. Groups of aligned adjacent CNTs grown perpendicular to the substrate to form "bundles".

In addition to bundles, entanglement of CNTs can also occur which result in agglomerates of CNTs resembling "clumps" (Figure 33), often found when a rough surface, such as a metal wire, is used (Figure 34). The entanglement of the CNTs can be attributed to the fact that the catalyst particle density is low, and hence there are few nearby CNTs that can support each other to create an aligned carpet [118, 157]. On rough surfaces such as metal wires, CNTs will not grow as closely together as would be the case on atomically smooth substrates and hence there is less chance of CNTs growing vertically together.

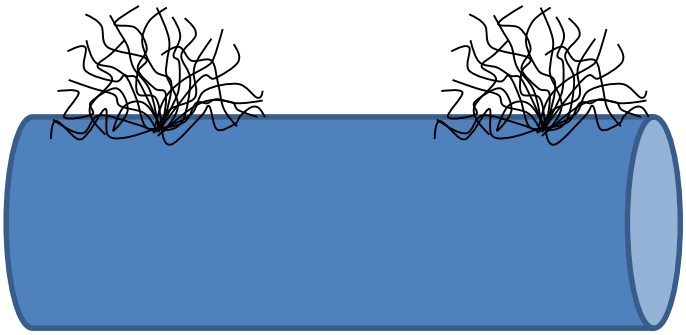

Figure 33. Schematic of "clump" morphology found on the surface of a wire after CNT growth. Clumps consist of entangled CNT agglomerates that resemble grass-clumps.

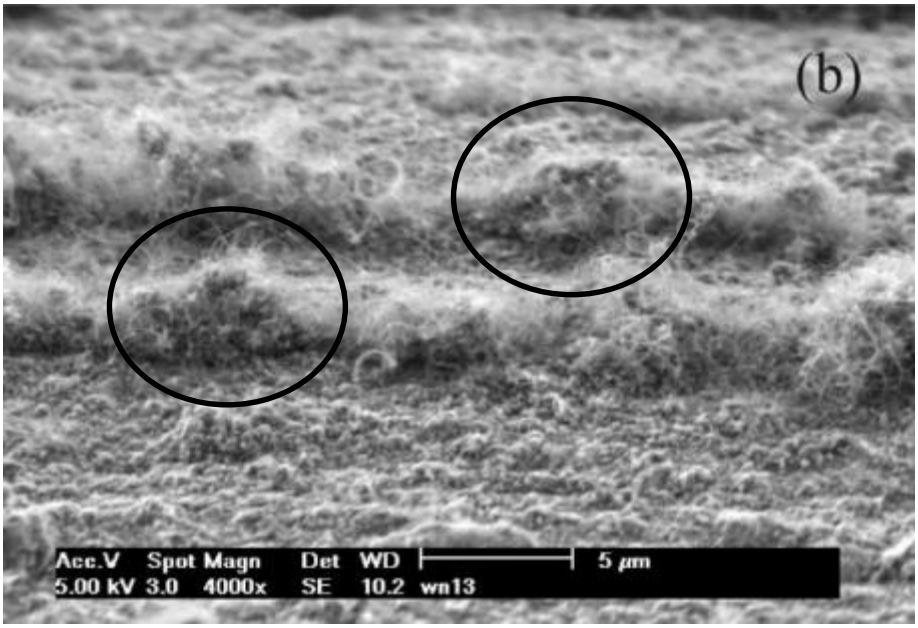

Figure 34. SEM micrograph of CNTs grown on Kanthal wire using a g-CVD technique. Circled in black are agglomerated and entangled CNTs resembling "clump" type morphology. Taken from [20].

Densely packed vertically aligned CNTs that resemble forests or carpets, have been shown to grow on flat substrates by many groups using CVD [32, 140, 148, 158, 159]. When grown on cylindrical substrates with a small radius of curvature, these carpets break up along the length of the cylindrical substrate and Van der Waals and other attractive forces ensure that these form ridges (Figure 35 and Figure 36) [125] as the CNTs try to grow perpendicular to the wire surface.

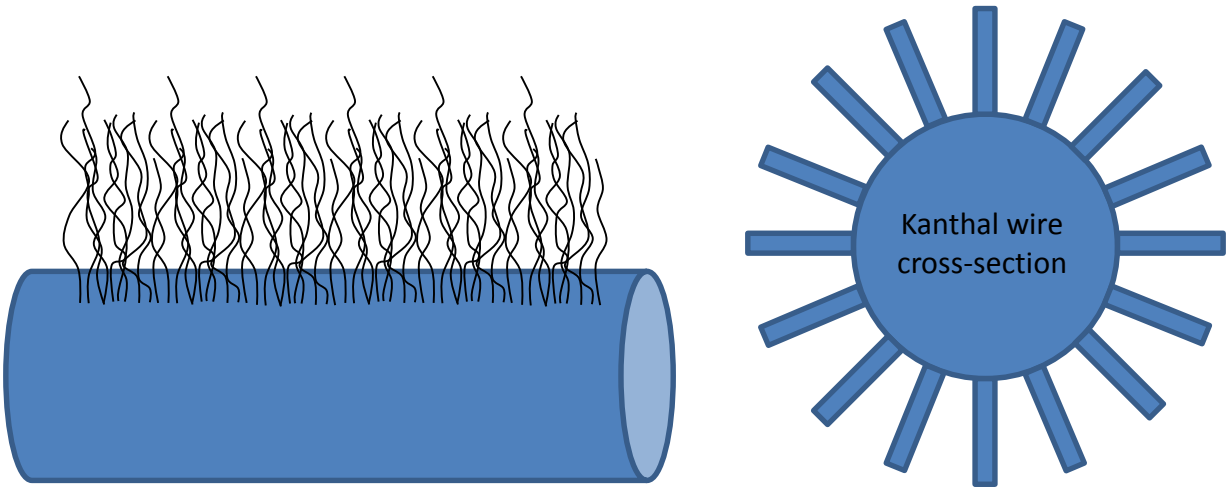

Figure 35. Schematic diagram showing (a) how CNTs align when in a "ridge" type morphology and (b) how the ridges grow out radially when looked at in cross section.

Figure 36. SEM micrograph of CNTs "ridges" on 50 µm diameter Inconel wire. A schematic is inset showing the brush type structure. Taken from [125].

3.1.2. Growth of CNTs on Various Substrates

The final component will consist of an array of emitters supported by a substrate. The substrate must be chosen carefully if the final device is to function properly and the following considerations should be taken into account.

The substrate must be able to transfer power to each emitter. Therefore it must be electrically conducting. To minimise contact resistance, the contact should be ohmic. The adhesion of the CNTs on the substrate must also be strong to prevent the loss of emitters during operation in strong electric fields [67]. Therefore, the substrate must be chemically and mechanically stable to withstand the harsh environment of field emission and ion bombardment from the gas phase. The substrate geometry is also important as the field enhancement factor (β) of the overall system is a product of β of the emitters and of the substrate [63].

Due to a lack of a supporting shaft, a floating sphere represents a completely curved surface, which would imply that it could have a high β value compared to flatter substrates. However, despite the number of emitters per unit area on a sphere being the same as on a cylinder of the same curvature, the total number of emitters one can fit on a sphere would be limited, and a cylinder can be made as long as is needed. Therefore the maximum current would not be as high using a spherical substrate compared to using a cylindrical substrate. Furthermore, a sphere cannot be floating in a real device and would need to be attached to the system in some way. A cylindrical substrate therefore is the favoured geometry as it has a higher β value than a planar surface but can contain a larger total number of emitters than a spherical substrate. A roughened cylinder will have a higher field enhancement factor than a smooth cylinder as the protrusions on the surface will provide areas which experience higher localised electric fields. When considering hierarchical structures, such as CNTs on a substrate, the field enhancement factors of the individual components multiply. So in the hypothetical case of a CNT, on top of a fibre, on top of a cylinder, then the final field enhancement factor of the system is the product of the individual field enhancement factors. This approximation only holds if the half width of the macroprotusion the CNT is sitting on, is less than the height of the CNT.

3.1.2.1. Growth of CNTs on Carbon Fibre Ribbon

Carbon fibre is robust and chemically inert [9, 14, 63, 160] and hence is a suitable support for carbon nanotube growth. Homogenous CNT coverage of entire carbon fibres have been achieved by Jo *et al* [63] and the CNTs were entangled within the film (Figure 37). 30 nm of Stainless steel was sputtered onto the carbon cloth and treated in a 10% hydrogen atmosphere at elevated temperature to create nanoislands for CNT growth. g-CVD was used to grow the CNTs shown in Figure 37.

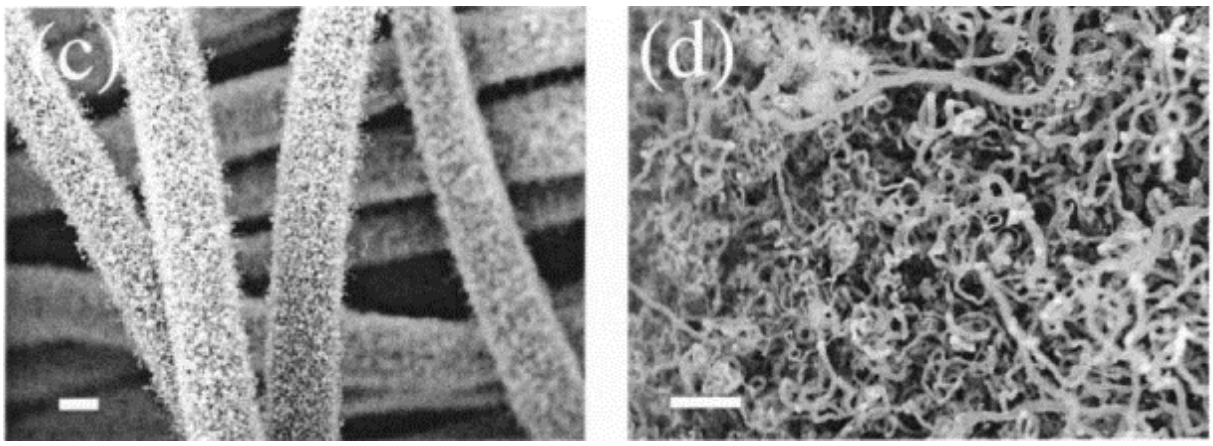

Figure 37. SEM micrographs showing the coverage of carbon fibres with grown CNTs (left) and showing the entangled nature of the CNTs (right). Taken from Figure 2 of [63].

3.1.2.2. Growth of CNTs on Tungsten

Thin tungsten coils are in common use as elements in incandescent lamps and as heated electrodes in fluorescent lights and are abundant and cheap. A highly coiled and thin metallic wire could provide an additional field enhancement factor in comparison to CNTs on a flat surface due to the inherent field enhancement from the filament itself.

CNTs have been grown on tungsten tips in the past using plasma assisted CVD [109, 161] but the literature is limited compared to other substrates, possibly due to issues with catalyst particles interacting with tungsten, limiting diffusion of carbon. Buffer layers (usually TiN) are deposited on the tungsten tips prior to growth of CNTs to increase the adhesion between the CNTs and tungsten substrate [65]. Grown CNTs are entangled and

many tips exposed, which may prove beneficial for field emission applications (Figure 38).

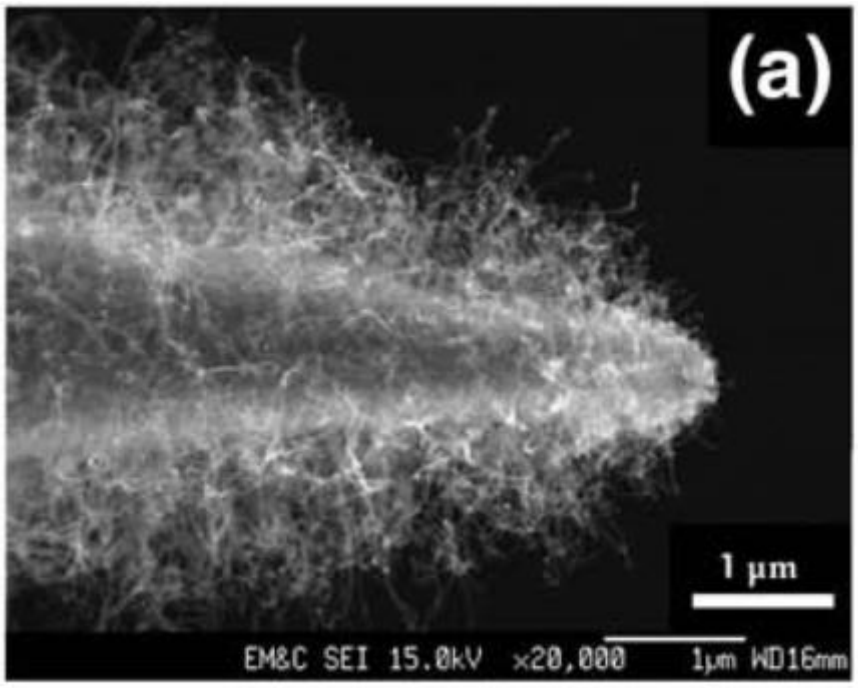

Figure 38. SEM Micrograph of CNTs grown on a tungsten tip using plasma assisted CVD with C_2H_2/NH_3 (125:200 sccm) at RF power of 200 W at 700 °C at a pressure of 400 mTorr [65].

3.1.2.3. Growth of CNT films on Kanthal wire

Kanthal wire is used in furnaces for heating coils, and several research groups have grown CNTs on its surface as it is chemically inert [162-165]. Gomer *et al* reported homogenous coverage of CNTs along both the length and circumference of the wire [162] and Kanthal supports the growth of thinner CNTs compared with the same growth technique on other metal wires [165]. Growth of CNTs on Kanthal wire and metals in general was discussed also in Chapter 1 (see page 41).

3.2. Growth of CNTs using a gas-CVD Technique

In this study, a gas CVD technique was initially used to grow CNTs on Kanthal wire. Knowledge of the composition of the Kanthal wire surface is important to determine any possible contamination with the iron catalyst particles. EDX was used in an SEM to determine the near *surface* composition. Figure 39 shows as expected large quantities of

iron and chromium on the surface (see page 47). It should be noted that there is also a significant quantity of aluminium, which is considered to deactivate iron catalyst particles [166].

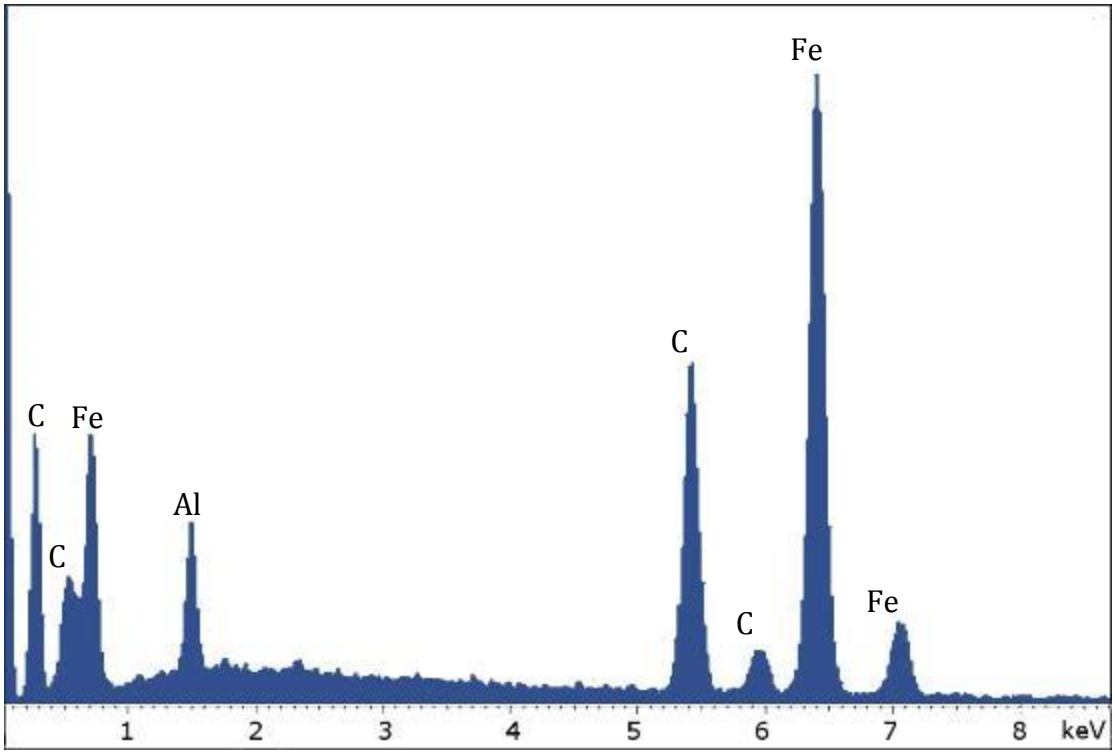

Figure 39. EDX spectrum of the "as received" Kanthal wire surface showing a large amount of iron, chromium and aluminium on the surface.

A suspension of iron nanoparticles in hexane was obtained and Kanthal wire was placed in the suspension for 24 hours. The wire was removed, dried and placed in the furnace so that a growth experiment could be conducted and the iron nanoparticles act as the catalyst for CNT growth. The carrier gas used was 0.2:0.2 SLM (Ar:H_2). Acetylene (0.05 SLM) was used as the carbon precursor and a growth temperature of 650 °C was used for 30 minutes as previous work in the group suggested that these processing parameters produced CNTs that are graphitic (*i.e.* they have lower I_D/I_G ratios when compared to CNTs grown at different temperatures and flow rates).

Figure 40 shows separated CNTs that were produced after the g-CVD growth experiment. The I_D/I_G is 1.04 which is higher than CNTs grown using an a-CVD technique [140]. This

experiment was repeated 4 times and Figure 40 is representative of the morphology found in these samples. In all samples adhesion with the substrate was weak as CNTs were sparse and easily fell off the wire.

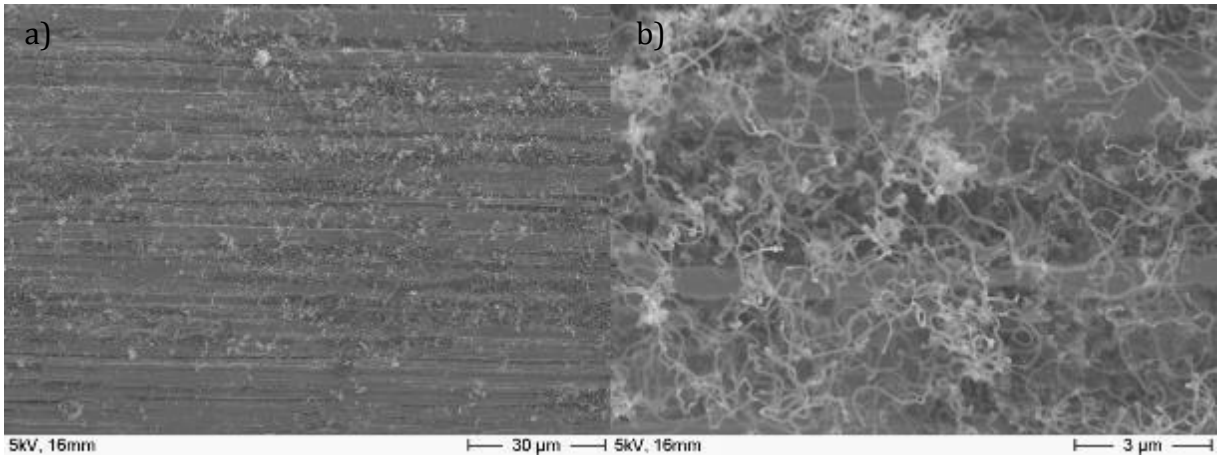

Figure 40. SEM micrograph showing individual CNTs on a Kanthal wire substrate (a) and higher magnification confirms separated CNTs have been achieved (b).

3.3. Growth of CNTs using an aerosol-CVD Technique

A-CVD was used to make CNT films as it is cheap, simple, easy to scale, versatile and can produce high quality CNTs [32, 158, 167]. In this project, CNTs were grown at a temperature of 800 °C for 10 minutes as previous work in the group has shown that these are the best starting parameters for this system [31, 32]. Argon was used as the carrier gas with a precursor solution of 5 wt% ferrocene in toluene and the substrate (Kanthal wire) was placed approximately 8 cm inside the furnace. The overall microstructure of CNTs grown on Kanthal wire using these conditions consists of clumps of CNTs (Figure 41).

3.3.1. Reproducibility of Growth Experiments

Experiments using these conditions were repeated six times to examine the reproducibility of the morphology of samples produced. No noticeable difference between growth runs were observed during characterisation of these samples.

Experiments were also carried out to investigate if any morphological variation occurred dependent on the *x* and *y* position of the substrate wire inside the furnace. A stainless steel block with drilled holes (Figure 42c) was used to hold 8 wires vertically inside the furnace and Figure 42a and Figure 42b shows that the CNT morphologies remain constant at the different positions.

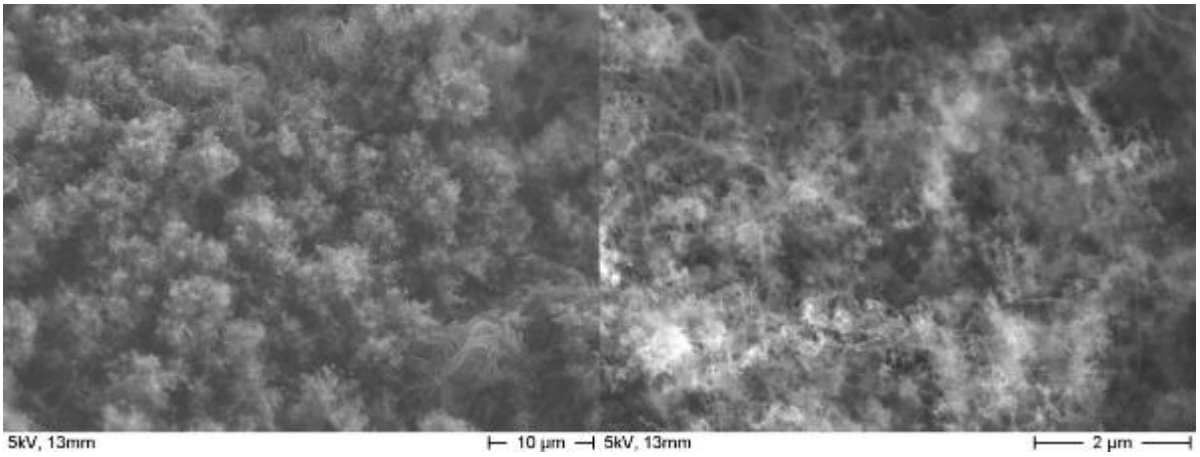

Figure 41. SEM micrographs of the overall microstructure of CNTs found on Kanthal wire (a) and higher magnification (b).

It should be noted that the SEM is operated at 5 kV so that minimum damage was inflicted on the CNTs. The electron beam diameter (and hence resolution) is determined by the accelerating voltage of the electrons, amongst other factors such as aperture diameter and aberrations *etc*. The resolution therefore would be better with a higher accelerating voltage however, there was no notable difference when a sample was examined with 10 kV. The typical resolution for an SEM ranges between 2-10 nm for a thermionic tungsten emitter, however for a field emission emitter (used in this study), the resolution is nearer to 2nm. Hence it may be difficult to observe the thinnest of CNTs (<5 nm diameter), but should still be possible. The main purpose of using the SEM in this study is to get an idea of the topological differences between various 'as grown' CNT film morphologies.

3.3.2. Growth of CNTs with respect to displacement

The displacement along the furnace was initially investigated using a standard set of parameters which was established in Section 3.3 (see page 68). There is a range of positions inside the furnace in which CNTs will grow. Before and after this region, it is unfavourable for CNT growth, due to the temperature being too low to facilitate the catalytic cracking of toluene, and even within this region the morphology of CNTs grown can be quite different. A Kanthal wire was used that was as long as the furnace (in this case 50 cm) and was sectioned after CNT growth for characterisation.

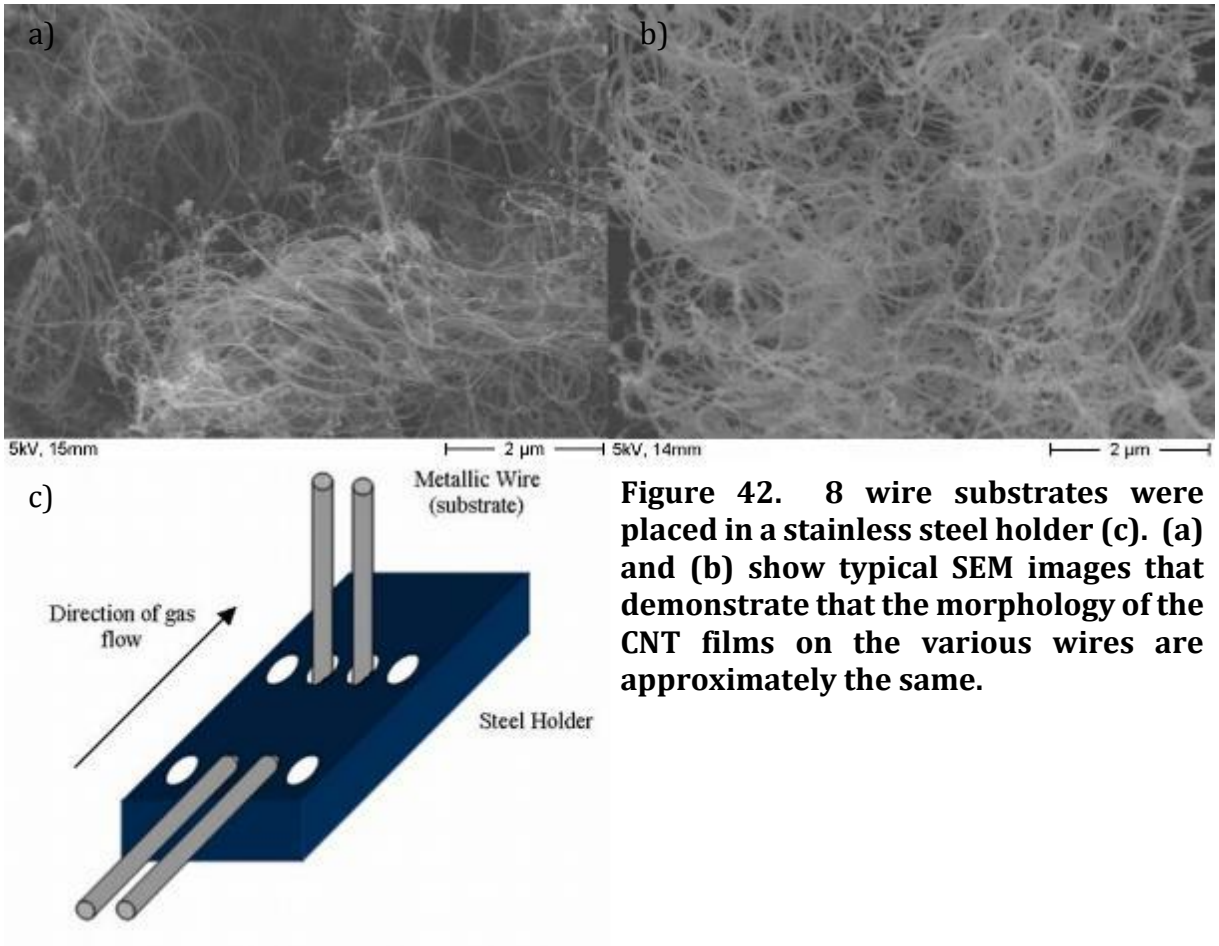

Figure 42. 8 wire substrates were placed in a stainless steel holder (c). (a) and (b) show typical SEM images that demonstrate that the morphology of the CNT films on the various wires are approximately the same.

Despite the furnace control unit being set to a certain temperature, the actual temperature is a function of the displacement along the furnace. The furnace entrance and exit act as heat sinks, so the temperature is lower at either end. Insulation is inserted around the quartz tube at the entrance and exit of the furnace to mitigate this effect.

However, as it is impossible to insulate inside the quartz tube without disturbing the gas flow, heat escapes from the entrance and exit of the furnace.

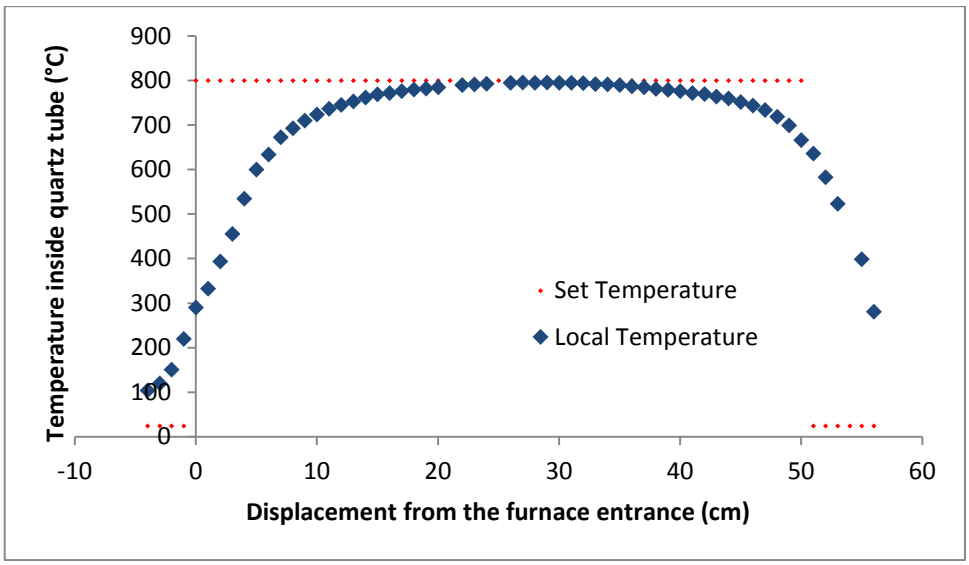

Figure 43. Graph showing the local and set temperature inside the CNT growth furnace.

Figure 43 shows the *local* temperature profile as a function of the displacement inside the furnace when the controller was set to 800 °C and at a flow rate of 1 SLM argon. The set temperature, the temperature in a perfectly insulated scenario, is represented by the red data points. It is interesting to note that at a displacement of 9 cm inside the furnace, the temperature is only 710 °C and reaches a maximum of 796 °C after 26 cm.

After CNT growth has occurred, and the furnace has cooled to room temperature, the wire is removed. Figure 44 is a schematic of how the wire appeared to the naked eye after the experiment. A white colour indicates that the wire looks the same after the experiment as it did before. A black colour refers to a black deposit on the surface of the wire.

The start of the schematic coincides with the entrance of the furnace. The first centimetre of the wire appeared just as it did before the experiment (*i.e.* a dullish grey). Beyond this region, there appears a black deposit that extends to 39 cm, beyond which there is a region of grey before the wire is again black from 43 cm to 50 cm. The wire was sectioned into several 1 cm sections and the "as-grown" morphology was investigated by SEM.

Figure 44. Schematic of what the Kanthal wire looked like to the naked eye after the experiment.

Figure 45a and Figure 45b are low and high magnification SEM micrographs respectively of the area 1 cm from the entrance of the furnace. Large, faceted particles that range from ~210 nm to ~590 nm were found on the Kanthal wire and no CNTs grow at this position. This is most likely due to a combined effect of the temperature being lower than the toluene cracking temperature [168], the precursor not having enough time to decompose, and the catalyst particles being too large.

Thus it can be concluded that CNT growth begins somewhere between 1cm and 8cm inside the furnace. Figure 45c shows that the CNTs found at approximately 8cm inside the furnace form clumps on top of a carpet of CNTs and Figure 45d shows those CNTs at a higher magnification. The average diameter of the clumps at 8 cm was found to be 11.5 μm and repeated experiments conducted at this displacement grew clumps of average diameter between 8 μm and 14 μm (Figure 48). The size of the CNT clumps decreases as the displacement from the furnace entrance increases from 8 cm to 16 cm (Figure 45e) and clumps are not present after 38 cm. Further along the furnace, the amount of carbon and the number of catalyst particles decreases so that less and less material is deposited, resulting in smaller clumps.

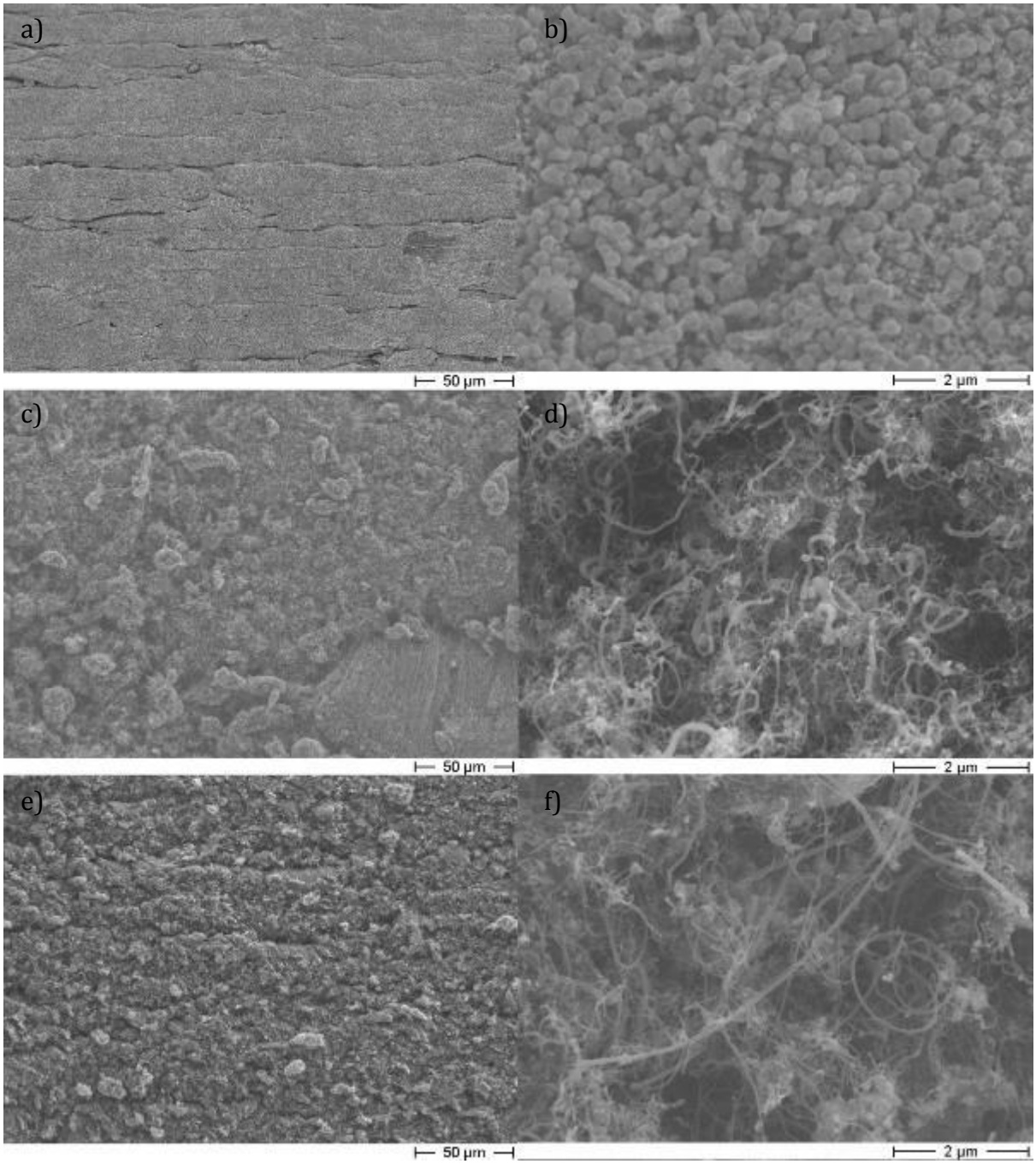

Figure 45. SEM micrographs of CNTs grown on Kanthal wire at a set temperature of 800 °C for 10 minutes, using a precursor solution of 5 wt% ferrocene in toluene with 1 SLM Ar flow rate. No CNTs grow 1cm into the furnace (a) and high magnification reveals faceted particles between ~210 nm and ~590 nm in diameter (b). At 8 cm clumps of CNTs sitting on top of a carpet of CNTs are observed at 8 cm (c and d) and a similar structure at 16 cm (e and f).

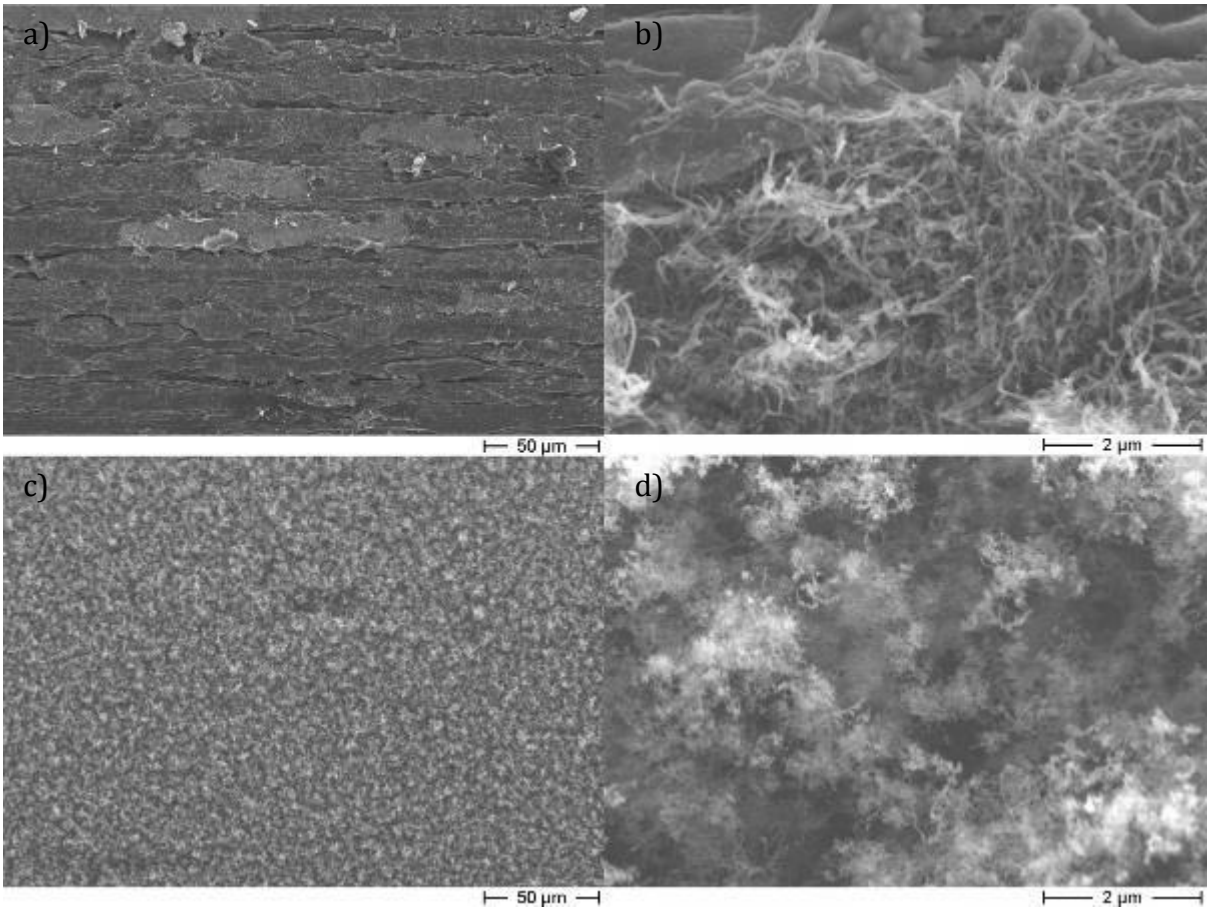

Figure 46. SEM micrographs of CNTs grown on Kanthal wire at a set temperature of 800 °C for 10 minutes, using a precursor solution of 5 wt% ferrocene in toluene with 1 SLM Ar flow rate. CNT coverage becomes more sporadic at 42 cm (a and b), and at 50 cm (c and d) there is a lot of amorphous carbon coating the CNTs.

As displacement from the furnace entrance increases, the amount of amorphous carbon decorating the CNTs (see schematic, Figure 47) remains low, as shown in Figure 45d, Figure 45f and Figure 46b. The I_D/I_G ratio however, gradually increases with displacement (Figure 49) which indicates an increase in defect density. As the amount of amorphous carbon decorating the CNTs remains low, this indicates that it is the CNTs themselves that are becoming more defective.

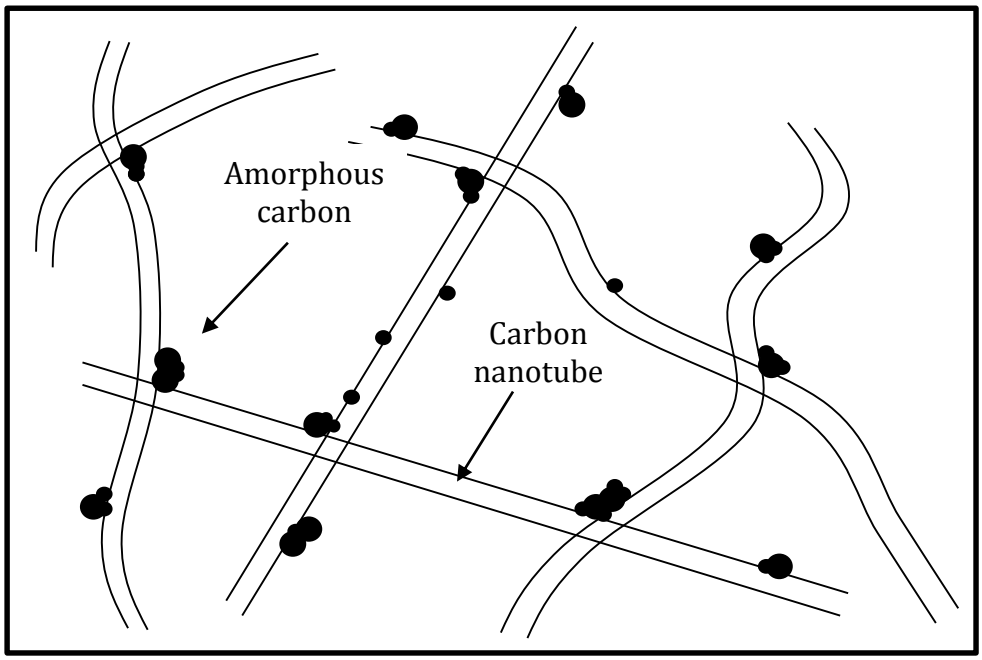

Figure 47. Schematic of amorphous carbon coating carbon nanotubes.

A continuous coverage of CNTs on the Kanthal wire is observed between positions 8 cm and 38 cm (Figure 45c to Figure 45f). This coincides with the black deposit found on the wire. There is a change in morphology after 39cm where a continuous coverage of CNTs is no longer observed. Figure 46b reveals CNTs grown at 42 cm that are considerably shorter and thicker (<120 nm diameter) than at other positions during the same experiment, and these CNTs do not form a homogenous film at this position (Figure 46a). The concentration of thick fibres decreases as the displacement from the furnace entrance increases.

Other authors [140, 169] also reported that the diameter of CNTs decreases with increasing distance from the furnace entrance due to the catalyst particle size decreasing with increasing distance. Near the furnace entrance, iron particles agglomerate into larger clusters that catalyse CNTs with larger diameters as the concentration of iron is highest in this region. Further along the furnace, the iron concentration decreases and so iron clusters are further apart and do not coalesce into larger particles which results in thinner CNTs [169].

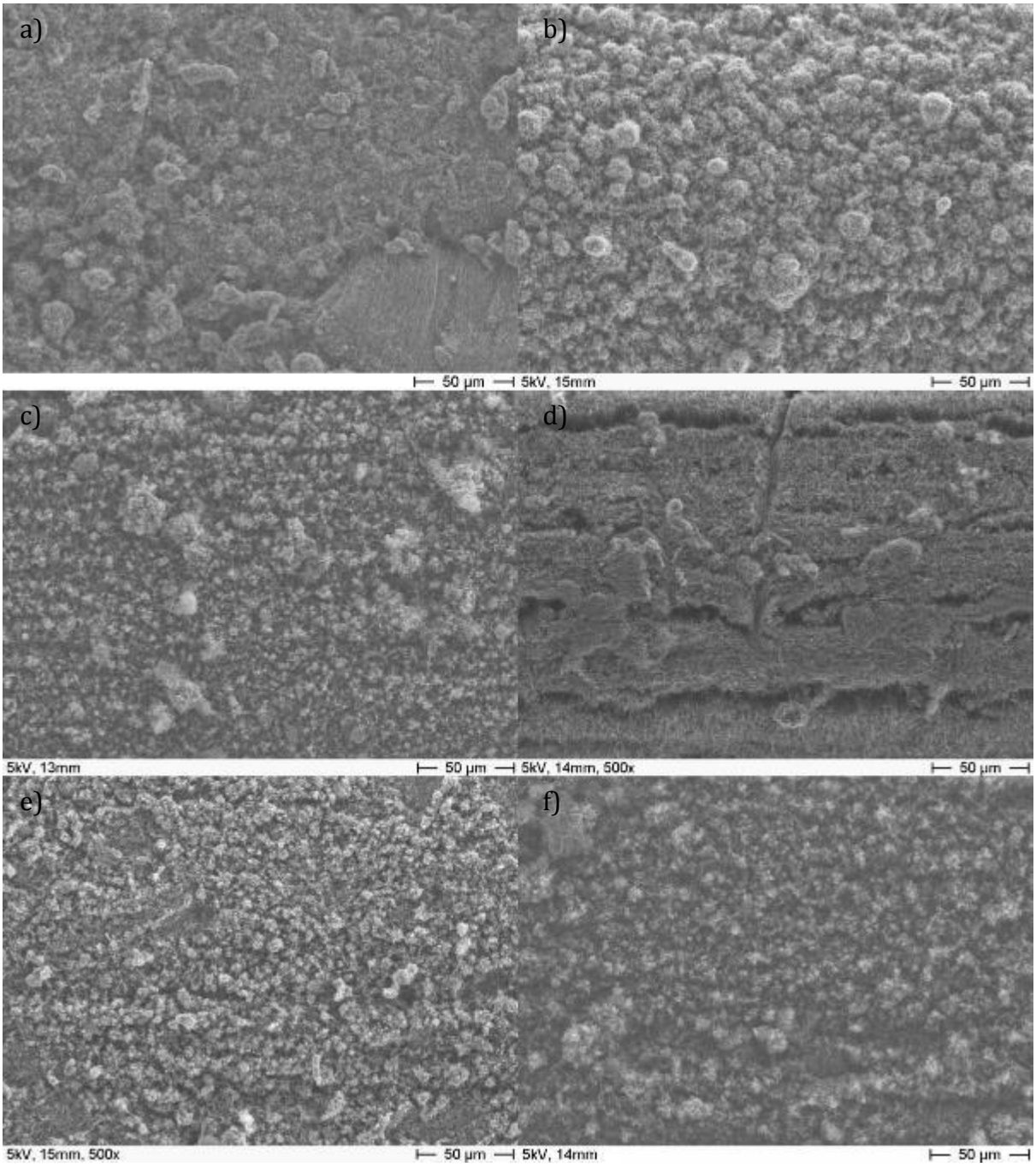

Figure 48. SEM micrographs of (a) original experiment and the same experiment repeated five times (b to f). All samples consist of clumps sitting on top of a thick carpet. The size of the clumps varies slightly between each sample.

There is a second region after 43 cm where CNTs grow (Figure 46c and Figure 46d), but there is visibly more amorphous carbon present (Figure 46d) and this is confirmed by the increase in I_D/I_G ratio shown in Figure 49.

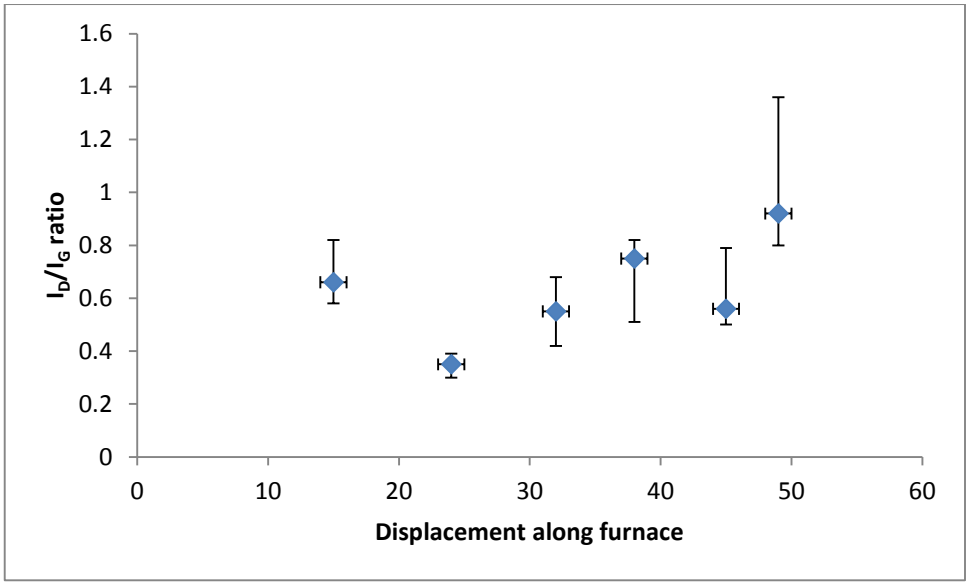

Figure 49. Graph showing the relationship between defect density and displacement along the furnace. The defect density gradually increases with displacement after a minimum near the centre of the furnace.

Nearer the furnace exit, CNT growth diminishes. This is due to the catalyst particles being used up in the earlier parts of the furnace and the temperature being too low to facilitate CNT growth. There are several types of carbonaceous structures on the surface of the Kanthal wire (Figure 46d), but there are a few thin CNTs in samples produced in this region. The temperature here is too low to facilitate CNT growth and it is likely that the CNTs found in this part of the furnace were actually grown in the hotter regions of the furnace and blown by the carrier gas along the Kanthal wire. The CNTs therefore may not be strongly adhered to the substrate and hence would be unsuitable for field emission devices.

Clearly distinguishable, separated CNTs are grown from 8 cm upto 43 cm (Figure 45c to Figure 45f and Figure 46a and Figure 46b), after which the CNTs become significantly coated with amorphous carbon (Figure 46d). CNTs at the surface of the film are mainly in the form of clumps and hence there will not be many CNTs that are aligned perpendicular to the surface as they tend to be entangled. Between 8 cm and 39 cm, the CNTs films are homogenous in nature and contain a high density of CNTs. Beyond this

displacement the nature of the CNT film becomes more sporadic and the density of CNTs becomes lower, and hence CNTs do not align perpendicular to the surface because CNTs need to be closely packed in order to support each other for vertically aligned growth.

3.3.3. The Effect of Hydrogen in the Carrier Gas on the Growth of CNTs

Hydrogen can be added to the carrier gas to manipulate the defect density of the "as-grown" CNT films [170]. These experiments are interesting because defects play an important role in the field emission properties of CNTs as discussed in more detail in Chapter 1 (see page19).

Hydrogen was added to the argon carrier gas in a preliminary experiment but with overall gas flow of 1SLM and it was seen that the opaque aerosol failed to rise due to the hydrogen being too light to lift the aerosol droplets. Hydrogen was therefore added to the argon so that the carrier gas is 1:0.2 SLM argon:hydrogen. Argon must be maintained at 1 SLM as it is considerably denser than hydrogen and is responsible for lifting the aerosol upwards into the furnace.

Toluene decomposes over a wider range of positions inside the furnace and as furnace temperature is a function of position, this implies that hydrogen has lowered the toluene decomposition temperature. This is evident in the schematic below, which shows a thin grey deposit observed up to 4cm inside the furnace, which then turns black up to 50 cm (Figure 50). The average I_D/I_G ratio in this experiment ranges between 0.33 and 0.73 and appears to not be a function of displacement until approximately 30cm after which I_D/I_G decreases as displacement increases. Figure 51 shows that near the exit of the furnace, the range in I_D/I_G ratio increases, indicating that there are a wider range of CNTs with varying defect densities.

Figure 50. Schematic of what the wire looked like after CNT growth in Ar/H_2.

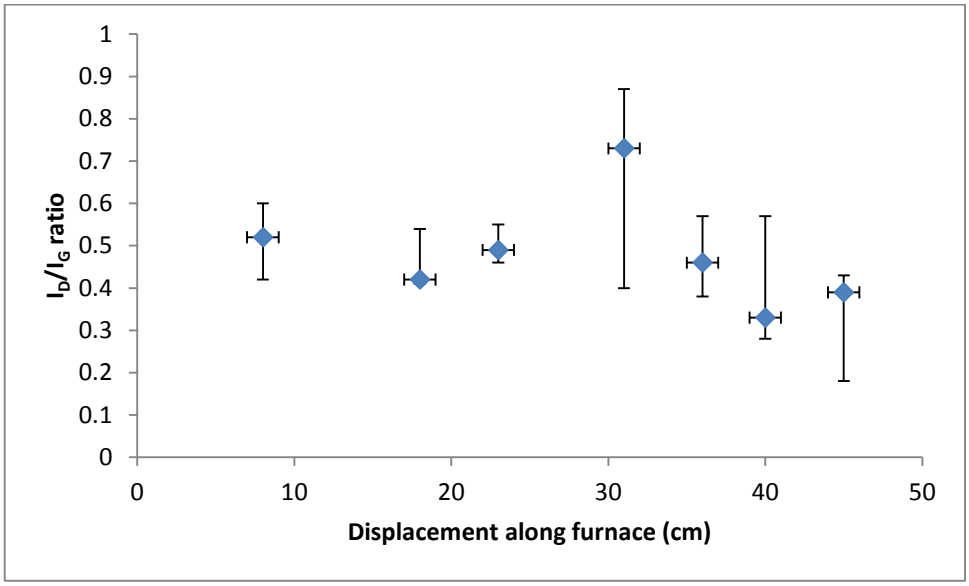

Figure 51. Graph showing the defect density with respect to displacement when hydrogen is introduced to the carrier gas mix.

There is visibly less amorphous carbon coating the CNTs where arrows in Figure 52d show CNTs free of amorphous carbon, compared to when no hydrogen is used and this is reflected in the lower I_D/I_G ratio obtained. Hydrogen acts as an etchant and preferentially reacts with amorphous carbon due to its dangling bonds to create hydrocarbons which are removed by the carrier gas [138].

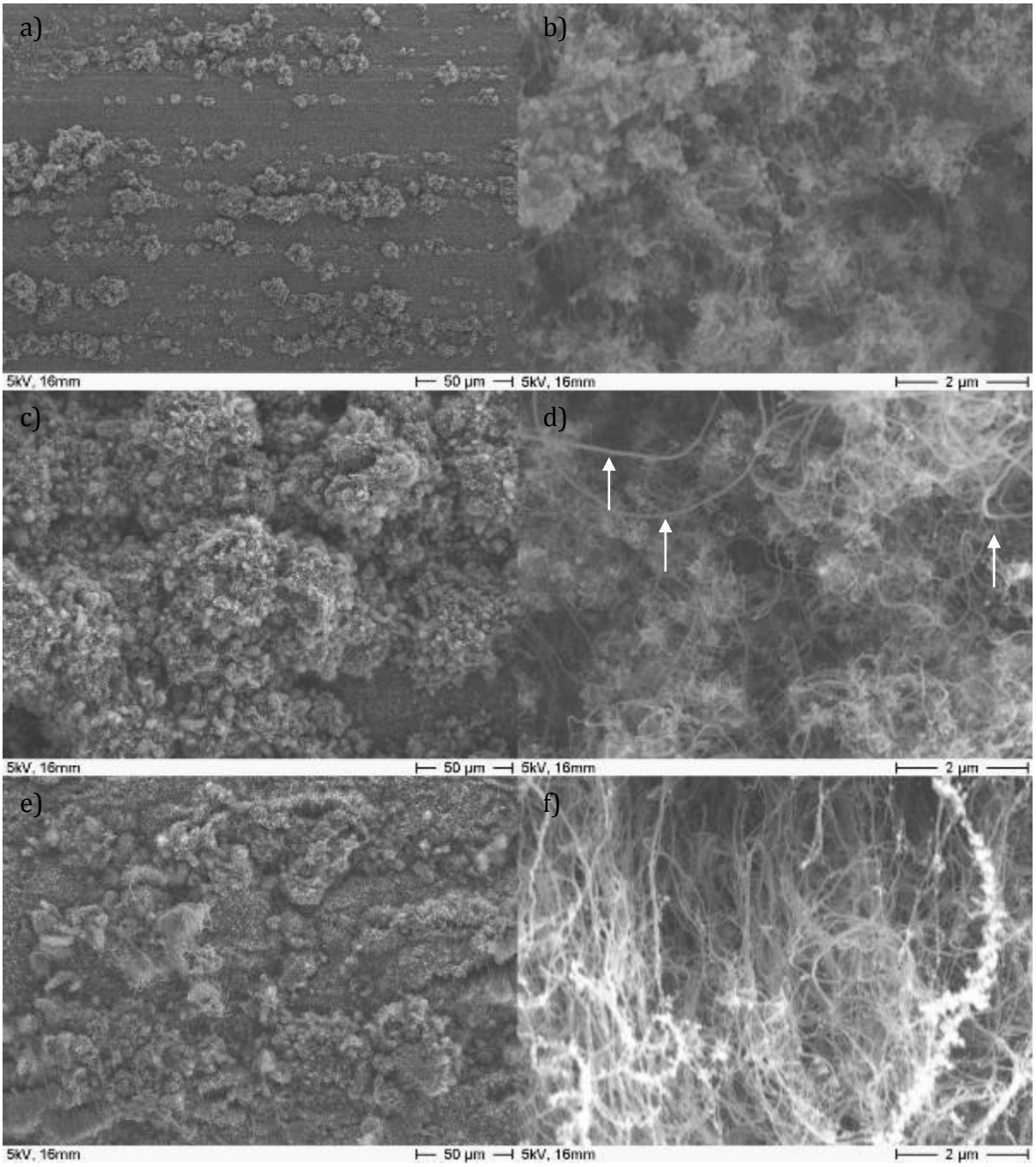

Figure 52. SEM micrographs of CNTs grown on Kanthal wire when hydrogen is introduced into the carrier gas. The CNTs form agglomerates (a) and are short at the beginning (~2 cm) of the furnace (b). For displacements between 10 cm and 36 cm, larger agglomerates have formed (c) and the CNTs are free of amorphous carbon coating, and are similar in terms of morphology (d). CNTs found at the rear of the furnace (43 cm) have amorphous carbon decorating the CNTs (e and f).

The homogeneity of the CNT film is less when hydrogen is added. Large clumps of CNTs can be seen growing along the length of the wire, and they appear to grow along the pre-existing extrusion lines of the underlying metal substrate (Figure 52a). These clumps are

seen to be considerably larger at 10 cm inside the furnace, and become smaller again towards the end of the furnace (Figure 52e). When this experiment was repeated, the same clump-like morphology was observed to grow (Figure 53). Carbonaceous material forms methane in hydrogen rich environments in a process called methanation. Iron is a known catalyst, which is necessary for methanation to occur and so it is possible that the iron used to catalyse CNT growth is also acting as a catalyst for methanation in hydrogen rich environments which would result in the loss of carbonaceous material, and hence would result in inhomogeneity.

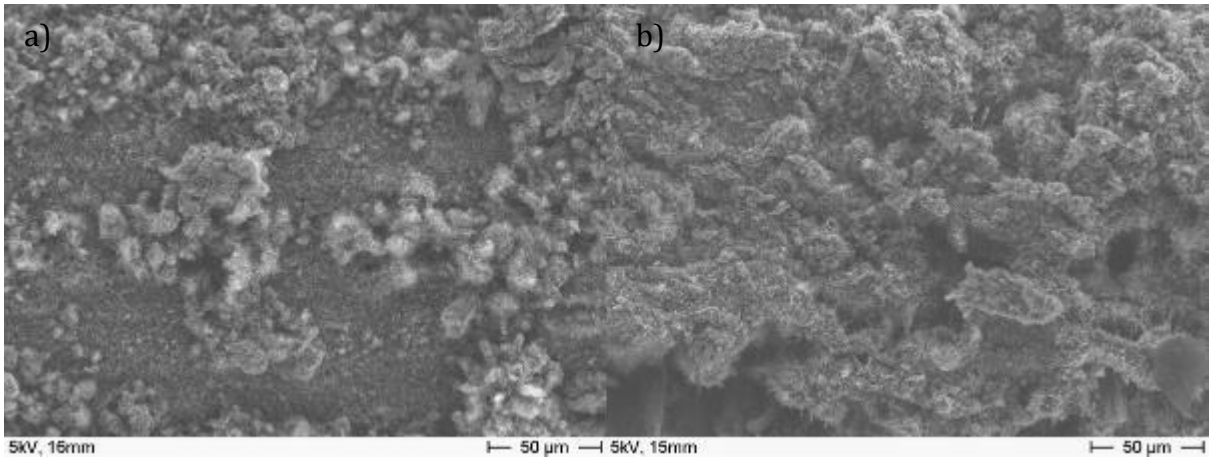

Figure 53. SEM micrographs of (a) original experiment from Figure 52 and a repeated experiment showing consistency in CNT morphology produced (b).

3.3.4. The effect of furnace temperature on the growth of CNTs

The furnace was set to 900 °C to investigate the effects of an elevated temperature on the growth of CNTs. The schematic below (Figure 54

Figure 54) shows that there are regions only near the entrance and exit of the furnace that support CNT growth. This is due to the temperature at the centre of the furnace being too high to facilitate CNT growth. At high temperatures iron particles coalesces to form larger iron agglomerates that are too large to catalyse CNT growth [169].

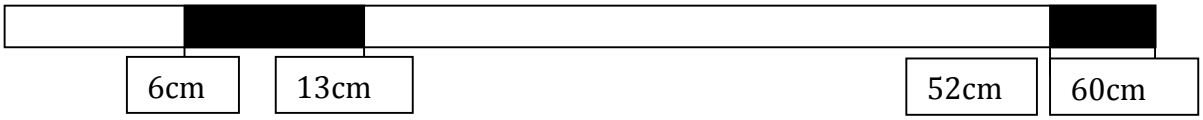

Figure 54. Schematic the appearance of the Kanthal wire after the attempt to grow CNTs at 900 °C.

There is generally less disorder in CNTs grown at a higher temperature near the furnace entrance than those grown at 800 °C, with I_D/I_G values for CNTs found in the first black deposit zone ranging between 0.58 and 0.79 (Figure 55). The I_D/I_G ratio of CNTs found near the furnace exit is above 1, which indicates that the CNTs are more disordered than those grown at 800°C.

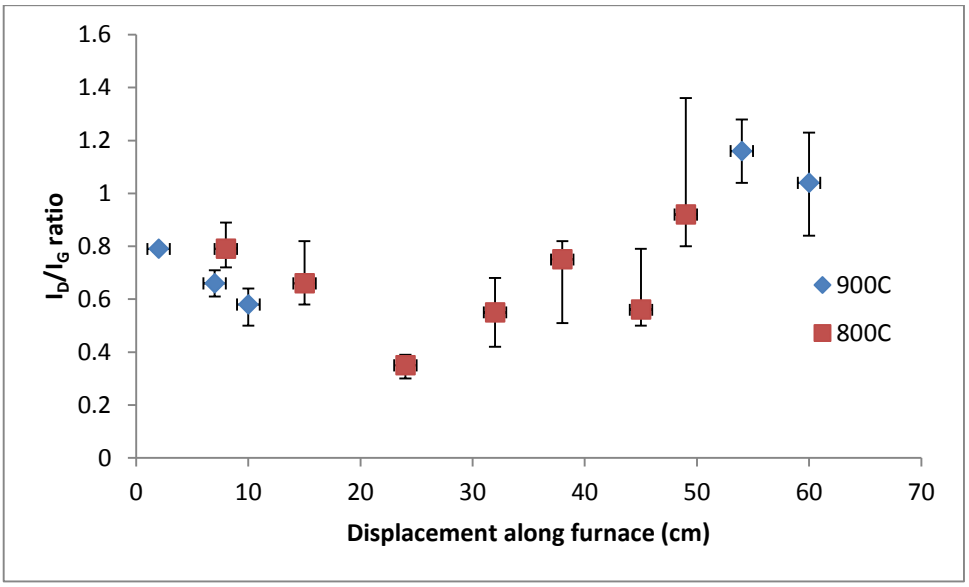

Figure 55. Graph showing the relationship between I_D/I_G ratio and displacement along the furnace for CNTs grown when the controller is set to 900°C. Data for CNTs grown at 800°C from Figure 22 is also added for comparison purposes.

Near the furnace entrance (7 cm), CNTs grow in clumps (Figure 56a), and large particles are visible (Figure 56b). Thick aligned carpets of CNTs grow 10 cm inside the furnace that form ridges because as CNTs grow radially from the substrate wire surface, they get further apart (Figure 56c and Figure 56d). A repeat experiment using the same parameters showed that ridges were consistently produced both times (Figure 57).

Towards the exit of the furnace the overall CNT density is lower and the CNTs are not aligned perpendicular to the substrate. Large faceted particles were found near the furnace exit and thin CNTs can be seen interconnecting these particles (Figure 56f). As reported in the literature [140, 169, 171], the quantity of the precursor and catalyst fall at the end of the furnace. This means that a combination of thin CNTs and amorphous carbon will be present. The thin CNTs are a result of some nanoparticles retaining their original small size and the amorphous carbon is a result of the larger iron particles losing their catalytic potential by coalescing into large faceted particles, hence graphitic carbon is more difficult to grow.

3.3.5. The Effect of Catalyst Concentration on Growth of CNTs

The catalyst concentration in the precursor was reduced to 1 wt% ferrocene to investigate if this would result in the catalyst particles being further apart and not coalescing [148]. This in turn would mean that the CNTs grown will have thinner diameters, which will result in a higher field enhancement factor provided there is sufficient separation between the CNTs. Hydrogen was introduced in to the carrier gas (1:0.2 SLM) to investigate if this encouraged the growth of CNTs [172], as no hydrogen resulted in no growth.

Figure 58 shows CNTs grown using these conditions. The sample is more defective than previously, as the I_D/I_G ratio has increased to 0.83 from 0.56, compared to when 5 wt% ferrocene solution was used. This is despite there being little amorphous carbon present coating the CNTs (Figure 58b).

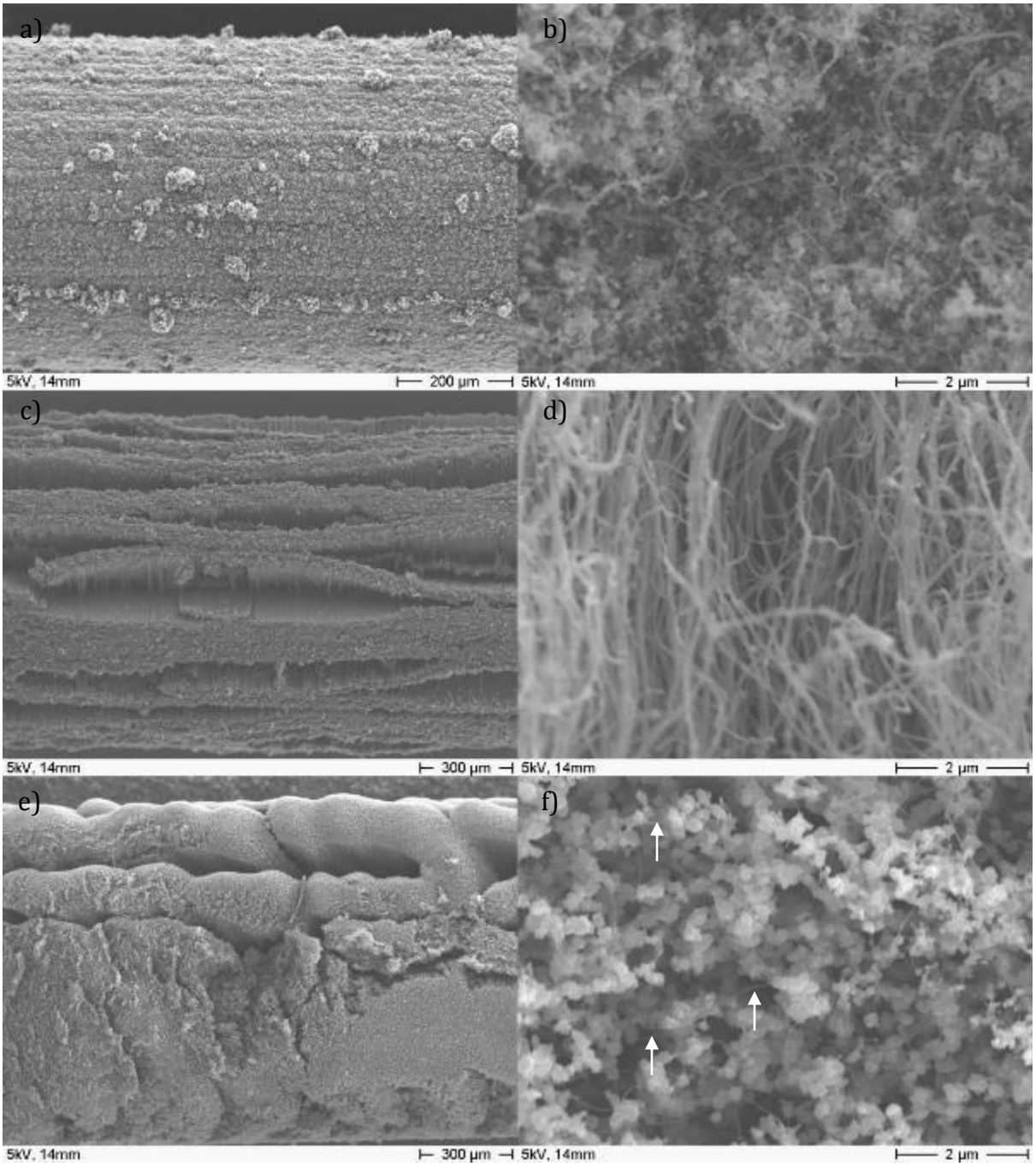

Figure 56. SEM micrographs of CNTs grown at a furnace temperature of 900°C. CNTs grow only near the furnace entrance and exit. 7cm inside the furnace, CNT agglomerates are visible along extrusion lines (a) and a limited number of CNTs are grown along with particles (b). 10cm inside the furnace, ridges of CNT carpets are formed (c) which contain CNTs aligned perpendicular to the substrate surface (d). Near the exit, particles are observed with thin CNTs interconnecting the particles (indicated by arrows) (f).

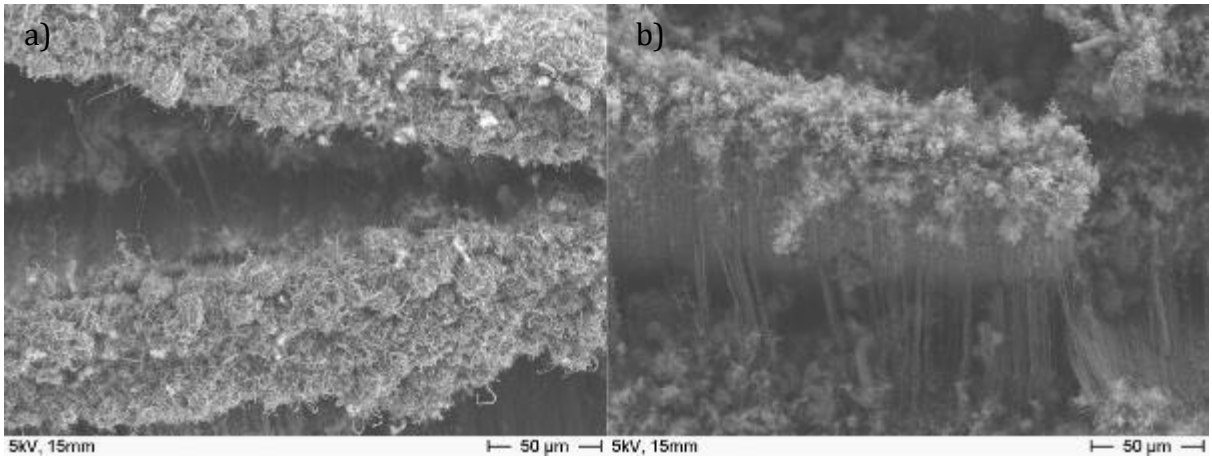

Figure 57. SEM micrographs of an original experiment from Figure 56 (a) and a repeated experiment (b) with the same parameters. The same ridge-like morphology is produced in both cases.

The CNTs tended to grow in bundles and carpets which means that emitters are not separated from each other. However, the CNTs grow perpendicular to the substrate surface and are hence aligned in a favourable position for field emission, if there are protruding CNTs present at bundle edges. The growth is not homogenous however, and there are areas where no CNTs grow and other areas where CNT carpets are present (see Figure 58). This has resulted in an overall CNT film that has a high surface roughness in comparison to other samples.

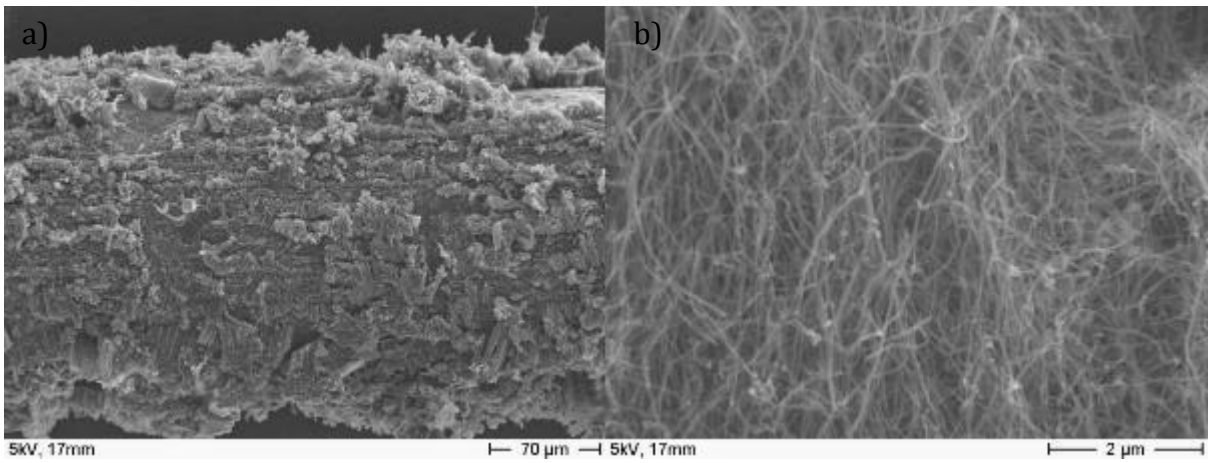

Figure 58. SEM micrographs of CNTs grown using 1wt% ferrocene in toluene. Low magnification reveals the rough nature of the surface (a) and higher magnification shows that these CNTs are aligned in bundled carpets (b).

The introduction of hydrogen into the carrier gas etches the iron particles so that larger agglomerates are broken down and hence CNT growth can occur [106, 173]. However, these CNTs are more defective than CNTs grown using 5 wt% ferrocene. Figure 58b shows particles encapsulated in the CNTs which is the cause of the higher defective densities observed as the particles have introduced strain into the structure.

3.3.6. Summary of Growth of Undoped CNTs

In this section the processing parameters used to control the growth of CNTs on Kanthal wires were manipulated and the resultant morphologies characterised. These material parameters are important to understand how a final field emission device will function. Table 2 shows the relationship between the a-CVD growth parameters used to grow CNT films and the resultant morphology. The CNT morphology is highly position sensitive, *i.e.* it matters where inside the furnace the CNTs are grown. The highest quality CNTs, those with the lowest I_D/I_G ratio, are found in the first half of the furnace. Amorphous carbon coating the CNTs appears close to the front of the furnace.

It has been reported that CNTs grown further inside a tube furnace will contain fewer defects than those grown closer to the entrance due to the precursor requiring a longer time to decompose [140]. Growth on Kanthal wire shown in this thesis however, show an increase in the defect density of CNTs as displacement along the furnace increases. A possible explanation is that as displacement along the furnace is increased, CNT growth on the inside of the quartz tube is increasingly more efficient and yields more mass than at the beginning of the furnace [140] due to an increase in the efficiency of the catalyst graphitising the carbon precursor [169].

Processing parameter	I_D/I_G ratio	Separated?	Vertically aligned?	Length	Morphology
Displacement (5 samples)	Increases with displacement	Yes, but within clumps	No, tend to entangle	<40μm at 32cm	Increasing size of clumps. sparse at end
Hydrogen (4 samples)	Flattens with displacement	yes, but within clumps	No, tend to entangle		little effect
Temperature (4 samples)	Increases with T	Yes, near entrance	Yes, near entrance	<230μm at 900°C	formation of ridges
Catalyst Conc. (4 samples)	Decreases with increasing conc.	partially	Yes	<25μm	little effect

Table 2. Table summarising the various effects growth parameters have on CNT material parameters.

On the Kanthal wire however, increased temperature may result in the catalyst particle interacting more strongly with the substrate, thus limiting the diffusion of carbon through the catalyst and hence producing more defective CNTs [174]. This increase in the defect density with displacement is reversed when hydrogen is added to the carrier gas. Not only does hydrogen etch away amorphous carbon that sometimes decorates the outside of CNTs, but it also reduces the increase in defect density normally visible in the back half of the furnace and prevents the formation of thick (above 100 nm diameter) CNTs. Hydrogen is known for changing the chemical state of iron [172, 175] and it is possibly reducing the catalyst particles to a state more preferably for CNT growth or ensuring they

do not interact strongly with the Kanthal wire and hence carbon can diffuse through the catalyst.

Towards the end of the furnace the range in I_D/I_G ratio, and hence defect density, increases. This is because the catalyst efficiency decreases with displacement as the temperature decreases [169] which means that the catalyst cannot dissociate and dissolve the carbon effectively and so CNTs with more defects are created. In addition to these more defective CNTs, higher quality CNTs (*i.e.* CNTs with fewer defects) which were created earlier in the furnace are blown on to the Kanthal wire resulting in a wider range of defect densities in CNTs towards the end of the furnace.

Using a growth temperature of 900 °C for 10 minutes, 5 wt% ferrocene in toluene solution as the precursor, and a carrier gas flow rate of 1SLM Ar, it was possible to grow thick carpets of CNTs that grow perpendicular to the substrate surface, creating ridge type structures. This is a step towards realising an effective field emitting film as the CNT tips are pointed towards the anode. Also, the formation of these ridges means that there is a high density of CNTs which will increase the probability of a high current density.

Another important material property of a field emitter is the work function. A decreased work function will extract a higher current for the same electric field. As discussed in Section 1.4.5. (page19), defects can introduce LDoS near the Fermi Level which lowers the effective work function. Therefore doping the CNTs with nitrogen [58] or boron [56] represents another way of lowering the work function and hence improve field emission properties.

3.4. Growth of N-doped CNTs using an Aerosol CVD Technique

N-doped CNTs were grown using benzylamine as the precursor instead of toluene [32]. Benzylamine has the chemical formula $C_6H_5CH_2NH_2$, and in the presence of ferrocene at an elevated temperature, fragments into H_2, N_2 and CN_x species to grow N-doped CNTs

[115]. Instead of clumps of entangled CNTs, bundles of vertically aligned N-CNTs ranging in diameter from 3 μm up to 12 μm form (Figure 59). These bundles align along the length of the Kanthal wire along pre-existing extrusion lines. Bundling is common in N-doped CNTs, and is caused by N-N bonding between neighbouring N-CNTs [155].

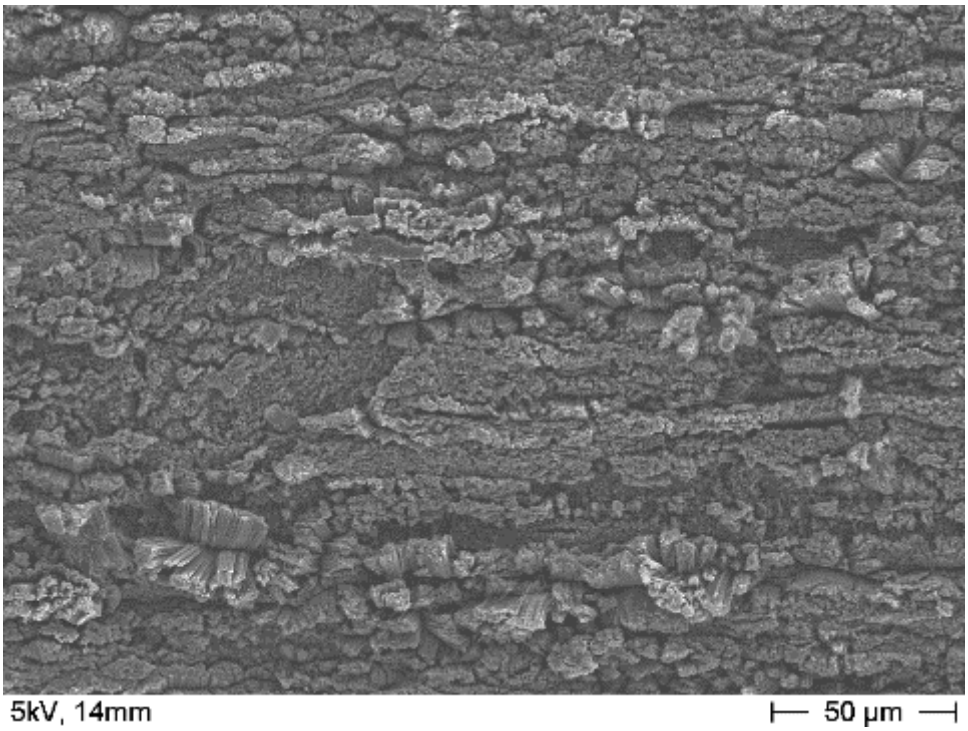

Figure 59. Low magnification SEM micrograph of N-doped CNTs showing the presence of bundles that grow along the length of the wire.

3.4.1. Growth of N-CNTs with respect to displacement

Figure 60 shows that a black deposit begins to appear 8cm inside the furnace, which is in contrast to 1cm in the case of toluene. The aerosol produced by the ultrasonic generator was not opaque (*i.e.* the density of aerosol particles was less than with toluene), and it took longer to lift the aerosol into the furnace compared to toluene. This is due to the difference in viscosity between toluene and benzylamine, where the latter is more viscous, hence the formation of an aerosol is more difficult.

Figure 60. Schematic of the deposit found on the Kanthal wire after growth of N-doped CNTs.

N-doped CNTs are intrinsically more defective than their undoped counterparts [176, 177]. The dopant atom introduces strain into the structure and changes the bonding of nearby atoms [178, 179]. This results in an increased number of defects and hence a higher I_D/I_G ratio when compared to undoped CNTs (Figure 61) [32].

8cm inside the furnace, low magnification SEM reveals little deposited material (Figure 62a). Short CNTs, of the order of a few hundred nanometres, were present at this position (Figure 62b). The temperature in this part of the furnace is in fact 700 °C as shown by the temperature profile in Figure 43. At this temperature, decomposition of benzylamine is possible, but becomes more effective at higher temperatures [180]. This explains why the start of the black deposit is closer to the furnace entrance when toluene is used as it can decompose (and hence grow CNTs) at a lower temperature.

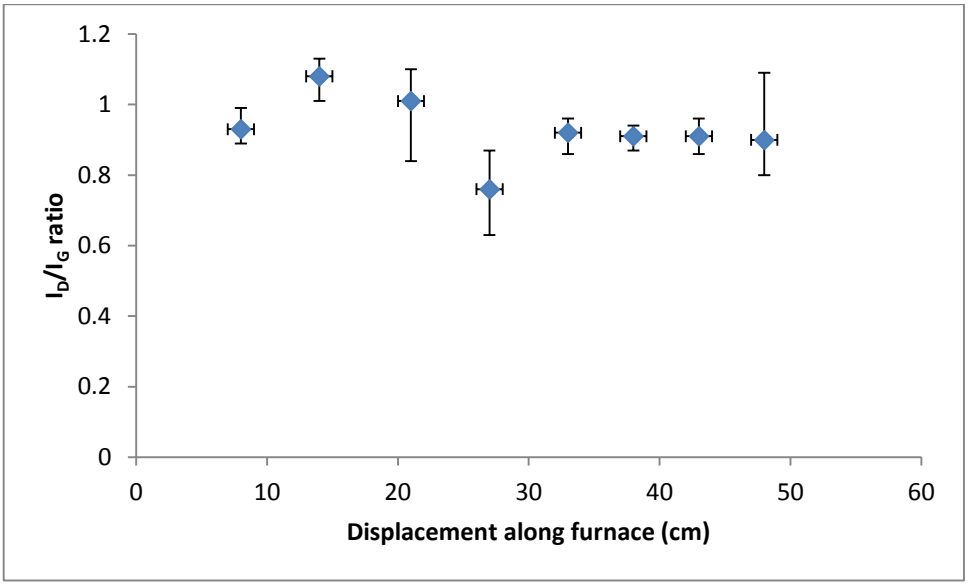

Figure 61. Graph showing the relationship between I_D/I_G ratio and displacement along the furnace for N-doped CNTs.

CNTs are found throughout the furnace as shown by the high magnification SEM micrographs at 8 cm (Figure 62b), 14 cm (Figure 62d), 27 cm (Figure 63b) and 33 cm (Figure 63d). Whilst the CNT film thickness is at a maximum at approximately 14 cm (Figure 62c), the CNTs found at this displacement are decorated with amorphous carbon (Figure 62d). Beyond 33 cm, CNT coverage is not continuous (Figure 63c). N-CNTs lie parallel to the Kanthal wire surface both near the entrance of the furnace and after 33 cm due to the lower density of N-CNTs present in these regions. Therefore the N-CNTs harvested from these regions potentially do not offer significant field enhancement. Towards the end of the furnace (after 33 cm), very little amorphous carbon can be seen in the SEM image despite very little change in I_D/I_G ratio (Figure 63b and Figure 63d). Between 14 cm and 27 cm, ridge like structures are found that run parallel to the length of the Kanthal wire, but these are not as well defined as is the case of undoped CNTs grown at 900 °C (Figure 56c) *i.e.* they are not as tall. The process of adding nitrogen into CNTs slows the growth because nitrogen needs to be removed from the surface of the catalyst particles so that carbon can diffuse [32].

3.4.2. The effects of hydrogen in the carrier gas on N-doped CNTs

Hydrogen was added in 20% ratio with argon (1:0.2 SLM) and the displacement over which CNT growth occurs has increased compared to the growth without hydrogen, from 41 cm to 44 cm (Figure 60 and Figure 65). The I_D/I_G ratio has increased, ranging between 0.93 upto 1.07 (Figure 66). There is visibly less amorphous carbon surrounding N-CNTs compared with no hydrogen (Figure 67b and Figure 67d). Therefore, the increase in I_D/I_G ratio implies an increase in defect density inside the CNT structure. This increase in defect density with hydrogen is contradictory to when growing undoped CNTs. It is possible that the hydrogen reacts preferentially with the nitrogen found in the structure

of NCNTs as it is known that the addition of nitrogen into the CNT structure increases its reactivity [181]. When this nitrogen atom is removed, point defects are introduced into the CNT structure.

3.4.3. The Effect of Catalyst Concentration in the Precursor on Growth of N-CNTs

When a 1 wt% ferrocene in benzylamine solution was used, bundles of N-CNTs are observed on the surface of a carpet of N-CNTs (Figure 68a). The I_D/I_G ratio of 0.97 is approximately the same as with 5 wt% ferrocene in benzylamine solution. Whilst N-CNTs grow perpendicular to the surface, they have formed bundles which means that N-CNTs are not individually separated from each other.

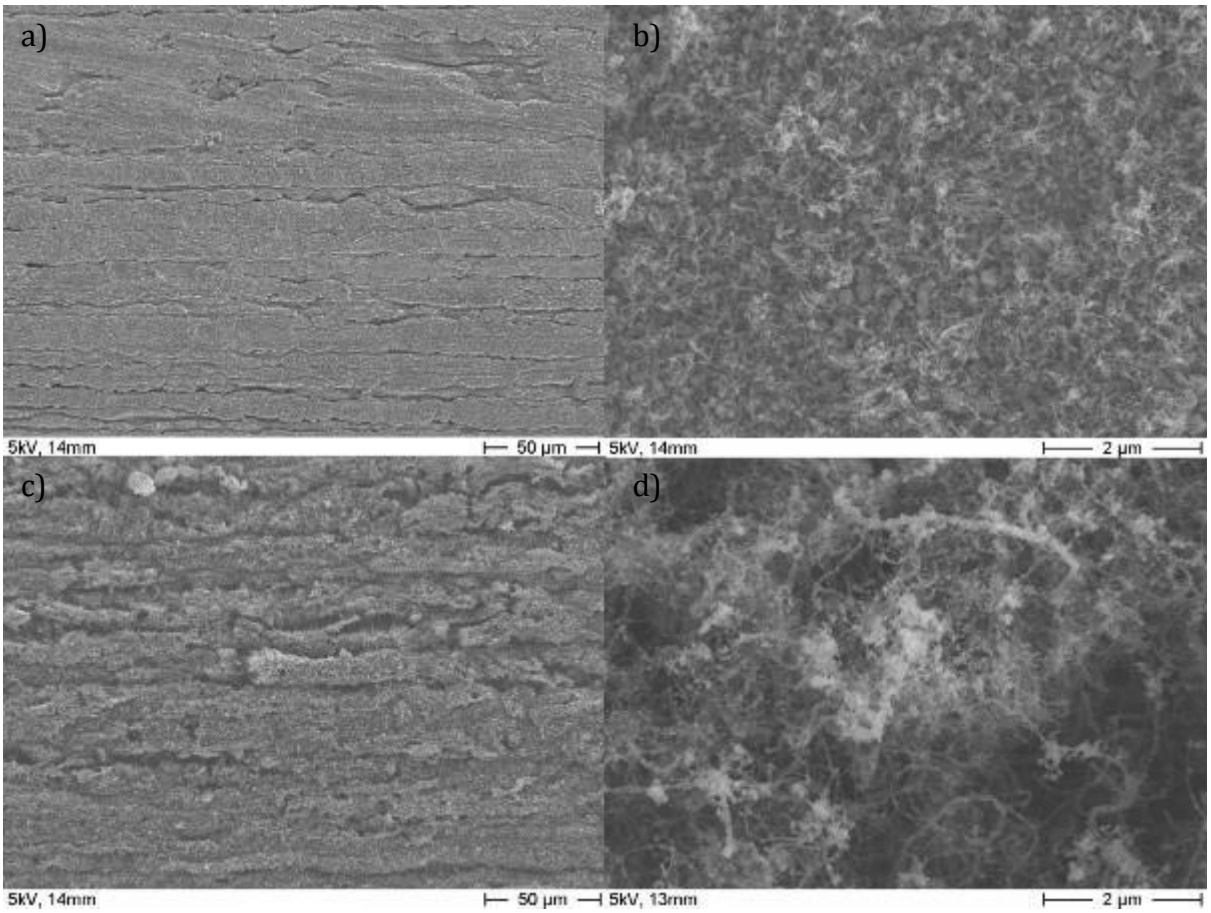

Figure 62. SEM micrographs of N-CNTs grown using the standard growth parameters but with a precursor solution of benzylamine. Little deposited material is observed 8 cm inside the furnace (a) and short CNTs are present (b). More material is deposited 14 cm inside the furnace (c) and the only CNTs are longer but decorated with amorphous carbon (d).

3.4.4. The Effect of Furnace Temperature on the Growth of N-CNTs

When 700 °C was used as the furnace temperature no CNTs were observed to have grown on the Kanthal wire. At 900 °C, the defect density is roughly the same as previous experiments, growing N-CNTs with an I_D/I_G ratio of 0.89. Bundles are found to run parallel along the length of the Kanthal wire and do not form a continuous film (Figure 69) and there are areas of the sample where no bundles exist.

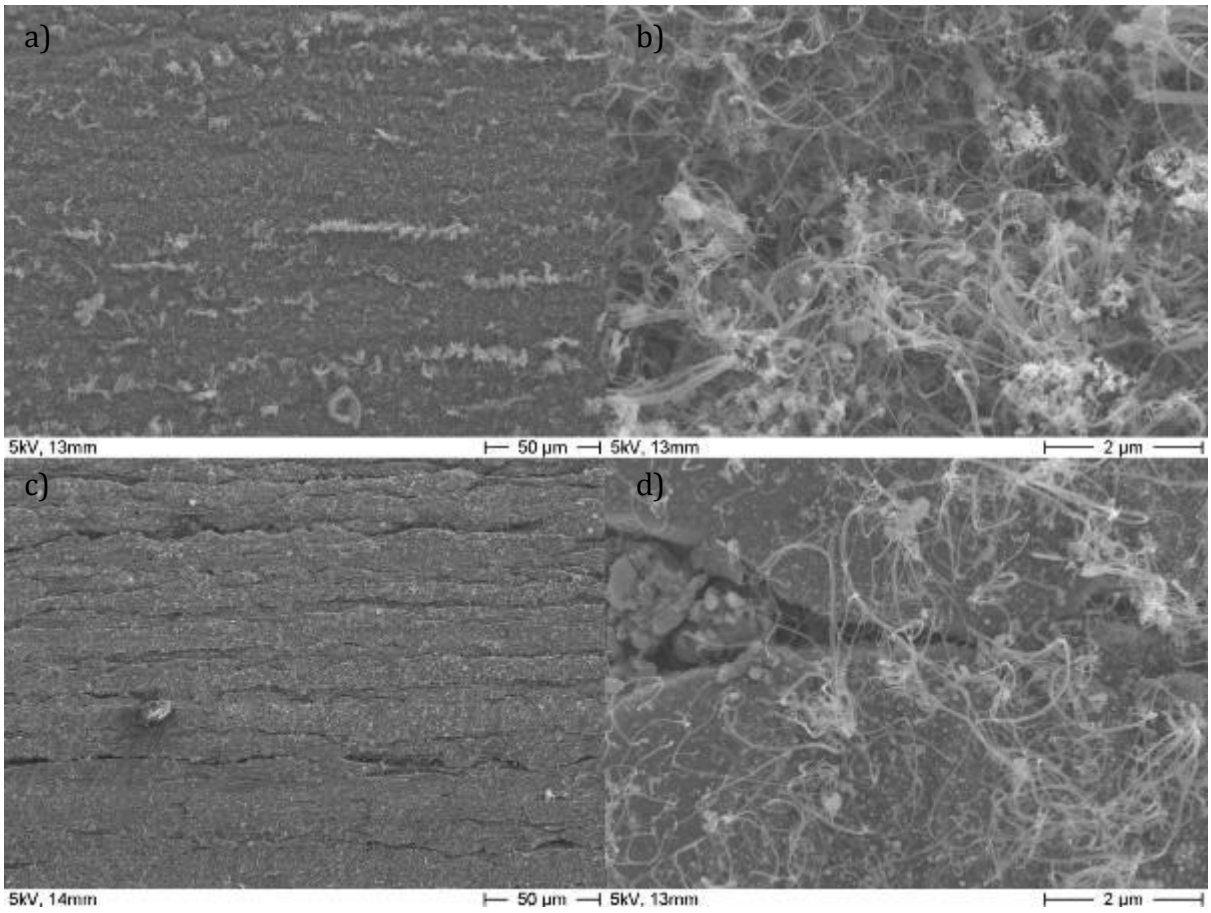

Figure 63. SEM micrographs of N-CNTs grown using the standard growth parameters but with a precursor solution of benzylamine. N-CNTs form along the length of the wire (e) and become thicker above 27 cm (f) and become more sporadic above 33 cm (g and h)

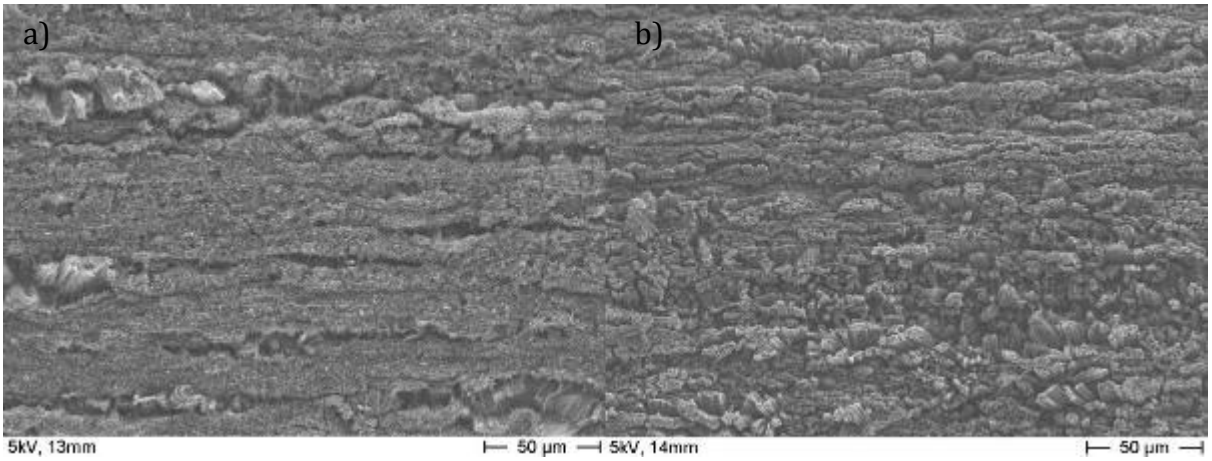

Figure 64. SEM micrographs of the repeat experiment from Figure 36, showing that the original (a) and the repeated morphology (b) is similar in both cases.

Figure 65. Schematic diagram of deposit found on Kanthal wire after an experiment which used 5wt% ferrocene in benzylamine solution, at a furnace temperature of 800 °C for 10 minutes using an Ar:H_2 flow rate of 1:0.2 SLM as the carrier gas.

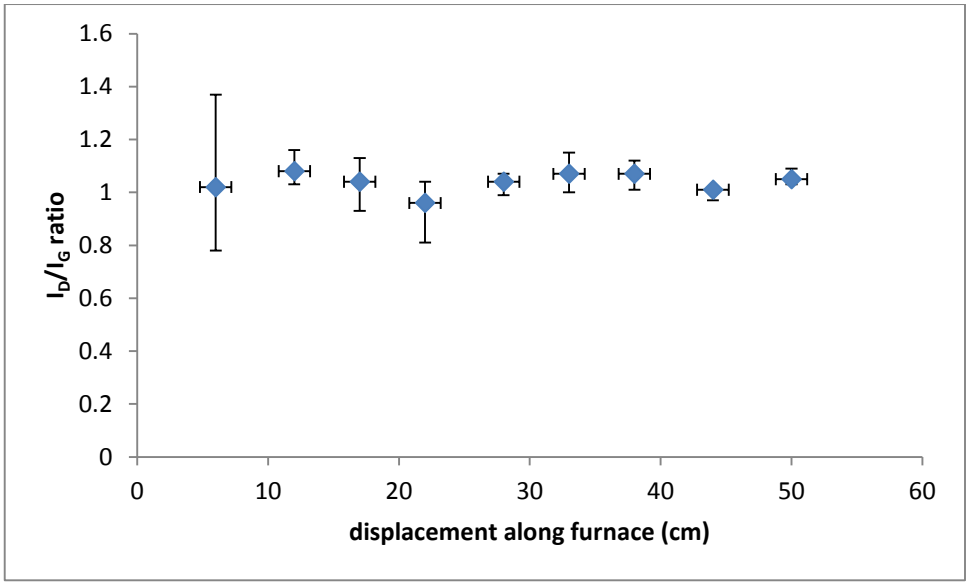

Figure 66. Graph showing no significant variation of I_D/I_G ratio with displacement along the furnace when hydrogen is introduced to the carrier gas.

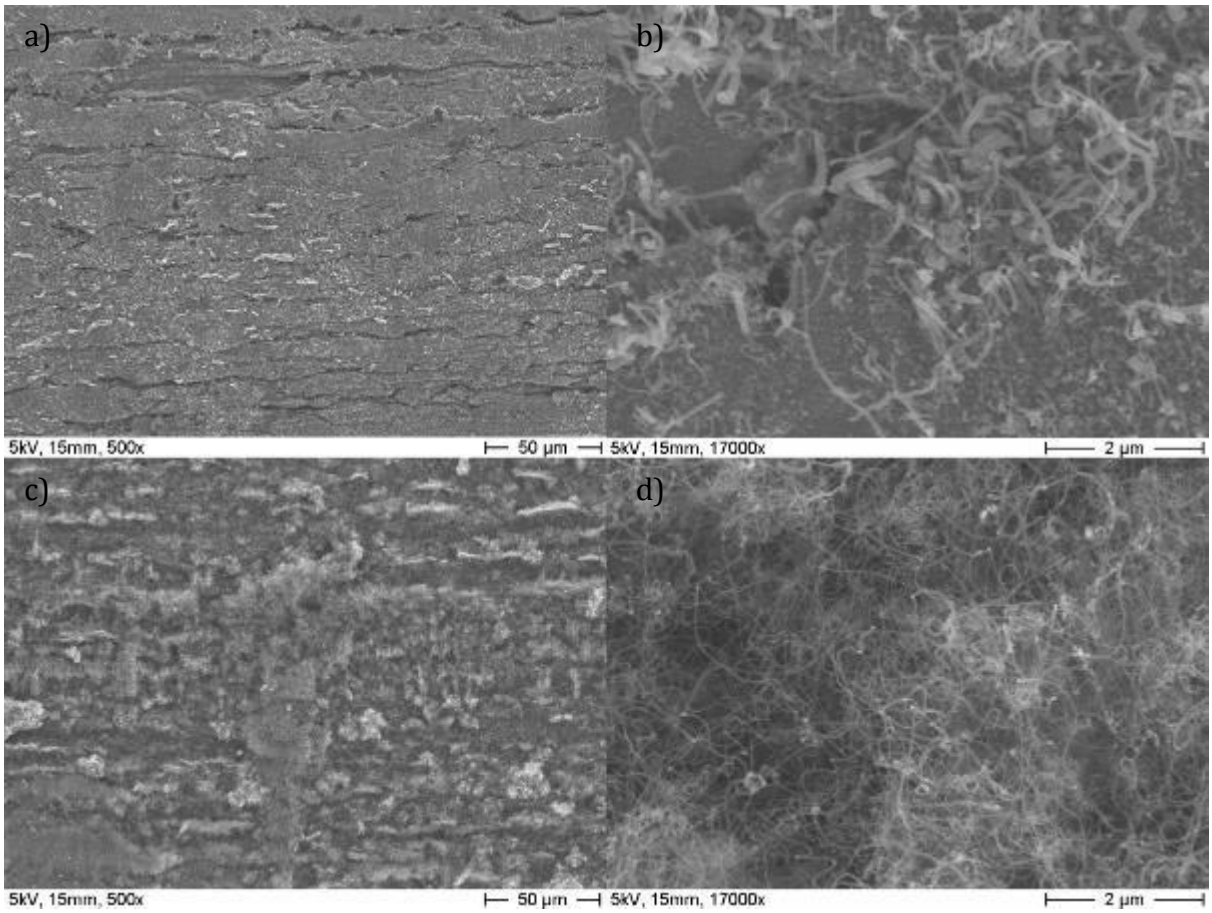

Figure 67. SEM micrographs of N-CNTs grown on Kanthal wire when H_2 is added to Ar. Near the furnace entrance little material is deposited as N-CNTs have not covered the entirety of the surface (a) and thick (<150nm) N-CNTs are observed (b). From 12 cm to 50 cm, thin continuous films of N-CNTs are grown (c) and are visibly thinner and longer (d). p54 N11

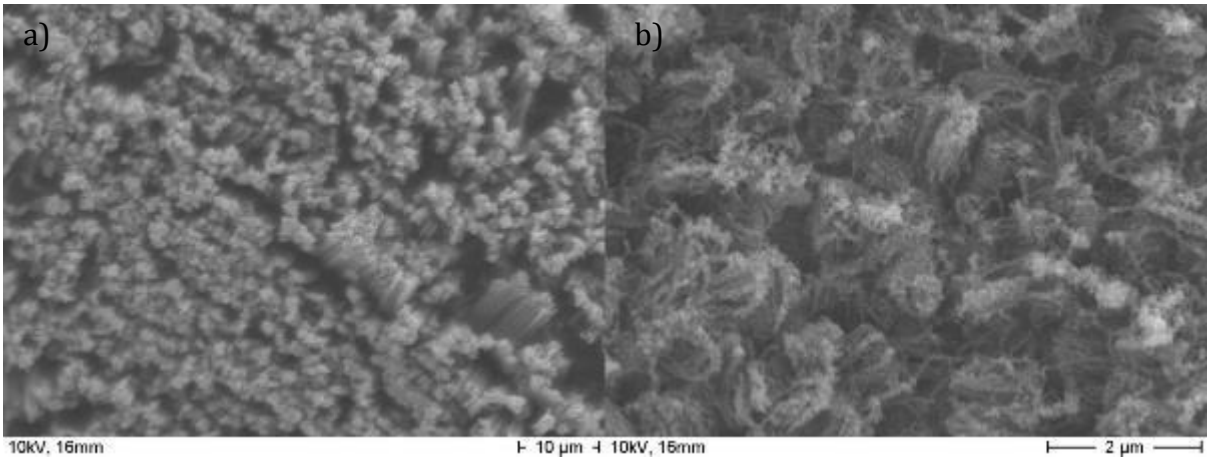

Figure 68. SEM micrographs of N-CNTs grown on Kanthal wire using 1wt% ferrocene in benzylamine solution. Bundles have formed (a) and higher magnification reveals the random alignment of these bundles (b).

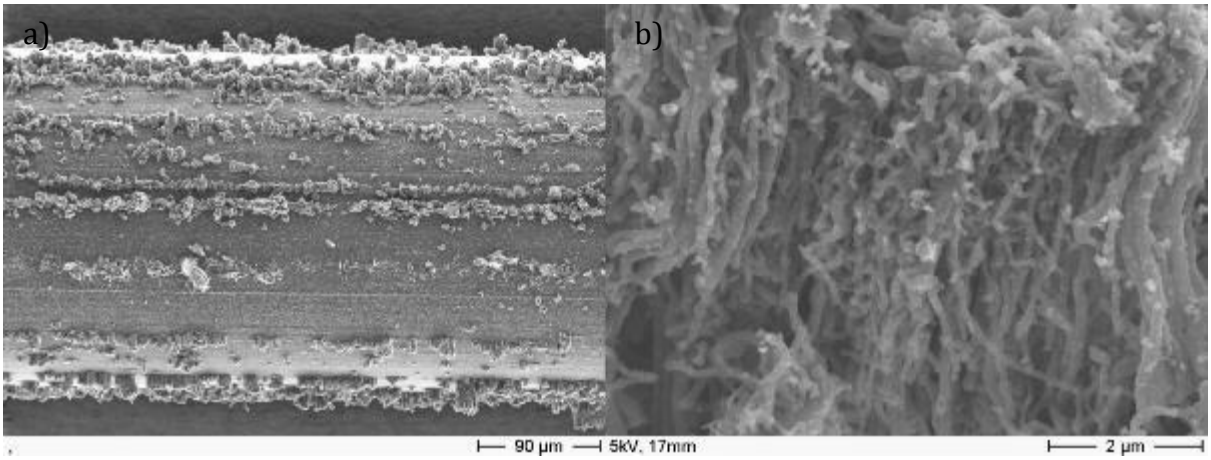

Figure 69. SEM micrographs of bundles of N-CNTs grown at 900°C that run parallel to the length of the Kanthal wire (a). High magnification reveals the N-CNTs that make up these bundles (b).

3.4.5. Summary of the Growth of N-CNTs

After investigating the growth of undoped CNTs on Kanthal wire in Section 3.3, the growth parameters of N-CNTs have now been investigated. Unlike undoped CNTs, N-CNTs tend to more readily form vertically aligned bundles due to the inherent N-N bonding. As the CNTs grow from the catalyst particles, nitrogen found in the walls of the N-CNTs form N-N bonds with neighbouring N-CNTs and they effectively 'stick' together as they grow. These bundles were not continuous however (*i.e.* ridges were not formed) and at 900 °C, their density dropped.

Baddour *et al* [127] grew similar CNT bundles on stainless steel. They achieved this by using stainless steel as the catalyst and using HCl to etch the surface. This roughens the surface of the stainless steel and CNTs grow from these protrusions that catalyse growth [127]. Whilst this is different to this study because the substrate is being used as the catalyst too, similar bundles have been grown. This must be because there are areas of the surface of the Kanthal wire, potentially along extrusion lines, where the catalyst particle has reacted so that carbon diffusion is limited. This happened at 900 °C and so it may be that the higher temperature resulted in this catalyst-surface reaction to proceed.

Processing Parameter	I_D/I_G ratio	Separated?	Vertically aligned?	Length	Morphology
Displacement (5 samples)	slightly decreases with displacement	Yes	No, entangled	<20µm at 14cm. <10µm at 27cm	Bundles, then sparse CNTs
Hydrogen (5 samples)	Increases with H_2	Yes	No, entangled	<20µm at 12cm	bundled carpets
Temperature (5 samples)	Unchanged	No	Yes	<25µm	CNT bundles
Catalyst Conc. (4 samples)	Unchanged	No	Yes	<10µm	CNT bundles

Table 3. Table summarising the various effects processing parameters have on the growth of N-CNTs.

Continuous films of N-CNTs are possible up to 33 cm into the furnace, beyond which N-CNTs are sporadically found. The I_D/I_G ratio varies to a lesser extent than for undoped

CNTs, but this is because N-CNTs are generally more defective than undoped CNTs and there is a limit to how defective a CNT can be. The defect density decreases with distance from the furnace entrance, instead of increasing as for undoped CNTs.

The addition of hydrogen results in the defect density increasing, due to the hydrogen preferentially reacting with the nitrogen due to its increase in reactivity. This affect is weak in comparison to the reduction of defect density in undoped CNTs and this is because of the already relatively defective nature of N-CNTs.

3.5. Growth of B-doped CNTs Using an Aerosol CVD Technique

Boron doped CNTs were grown using the same standard processing parameters as for undoped and N-doped CNTs, except the growth temperature was changed to 1,000°C and the precursor used was 10% 1 M triethylborane (TEB) in hexane solution. This is because past work in the group found this growth temperature to be optimum for producing B-CNTs [31].

3.5.1. Growth of B-CNTs with respect to displacement along the furnace

The schematic below (Figure 70) shows that growth over the length of the furnace is not homogenous. Large spongy black deposits were found to grow at approximately 8cm inside the furnace and they were approximately 8mm to 10mm in height and 10mm in length. There were also regions inside the quartz tube where a silvery material was found and this is denoted as a grey colour in Figure 70. The rest of the Kanthal wire had a black deposit similar to that found with undoped and N-doped experiments (Figure 65). SEM reveals that in the initial region of the furnace the B-CNTs are coated in a thick material (Figure 72b). There are very few clean B-CNTs visible at this displacement, and those that are visible are very large, ranging in diameter between 70nm and 190nm.

The "as grown" B-CNTs are highly defective with an I_D/I_G ratio ranging from 0.87 to 1.07 (Figure 71). This indicates that the material produced near the furnace exit is more disordered in nature than graphitic.

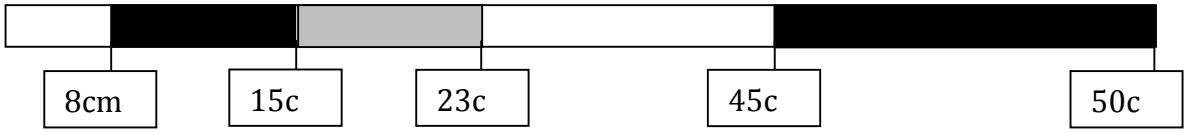

Figure 70. Schematic of the Kanthal wire after an experiment to grow B-CNTs.

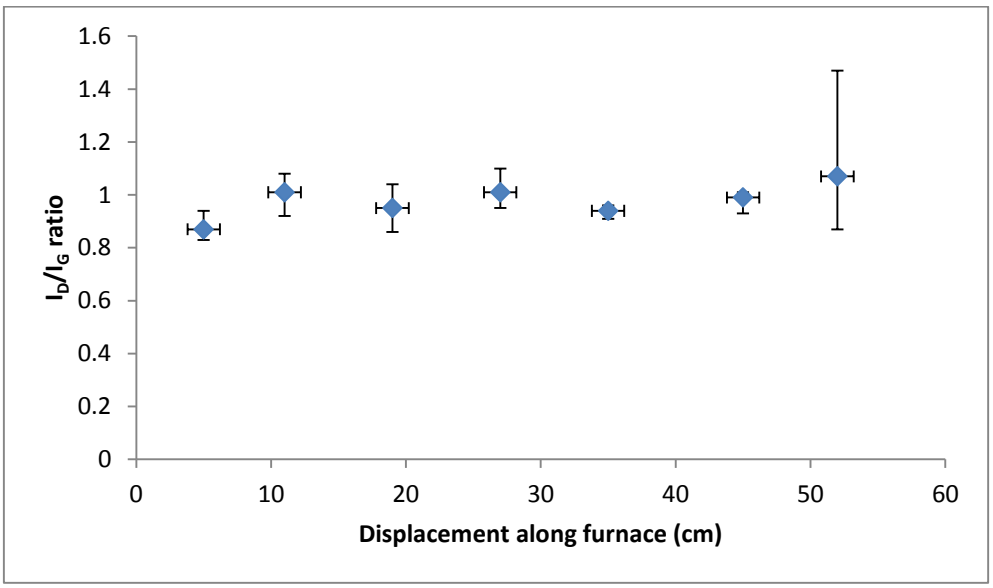

Figure 71. Graph showing the relationship between I_D/I_G ratios and position along the furnace for B-CNTs.

Near the middle and the exit of the furnace, carbonaceous spheres are grown instead of CNTs and are several micrometers in diameter (Figure 72c and Figure 72d). Short nano-fibres of diameter ~40nm and lengths ranging from several hundreds of nanometres up to 1µm are found on the spheres grown at 27 cm. These fibres however, lie parallel to the surface of the spheres and hence would not offer significant field enhancement.

3.5.2. The effect of hydrogen in the carrier gas on the growth of B-doped CNTs

Hydrogen was added to the carrier gas with partial pressures of 0.9:0.1 Ar:H_2 to determine if it had an effect on defect density. A sample wire was placed 15cm inside the

furnace for this experiment. No large spongy material appeared in the furnace after this experiment. The I_D/I_G ratio is 0.99 and is approximately the same as for the initial B-CNT experiment. Also, the morphology has remained unchanged and large nanofibres of diameters ranging between 120 nm and 200 nm are found that are coated in an unknown material (Figure 73).

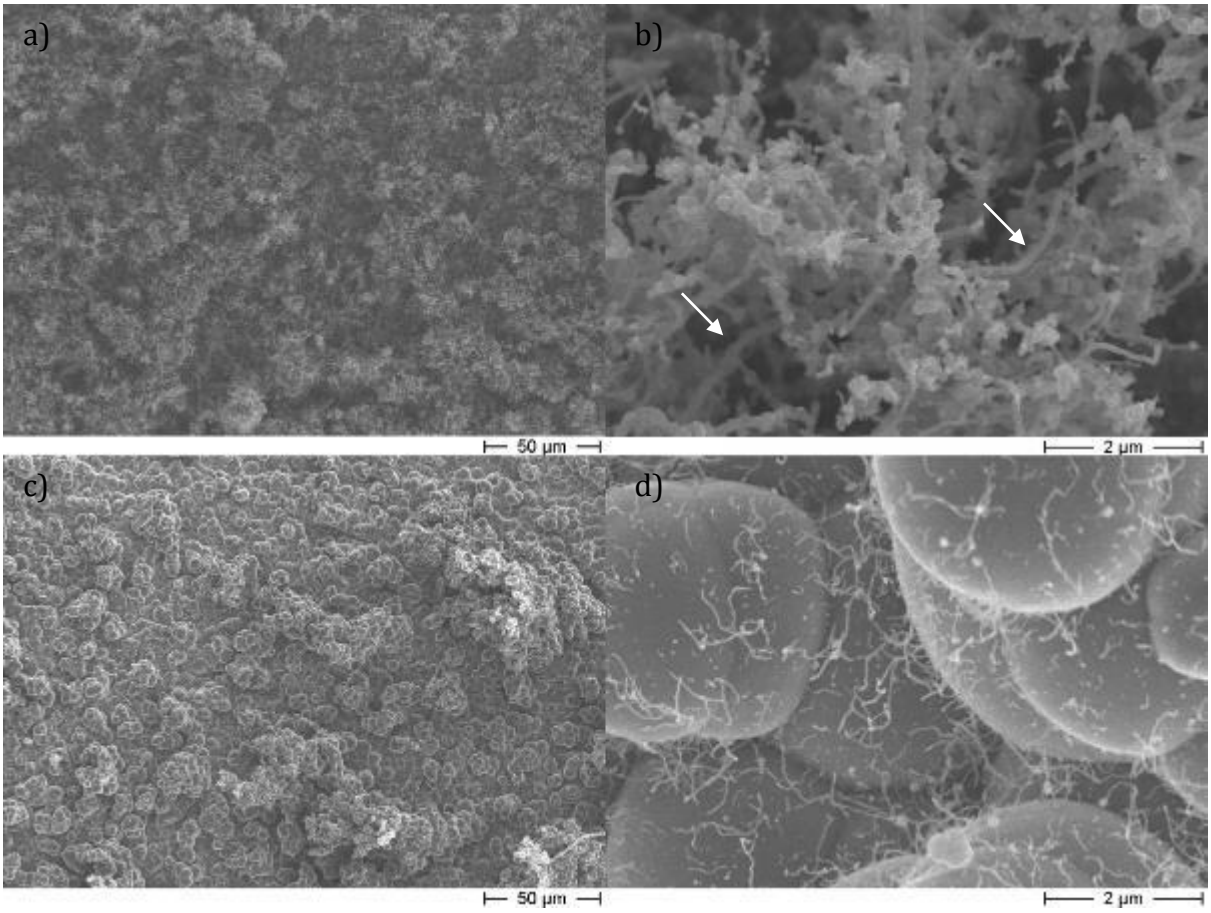

Figure 72. SEM micrographs of morphologies produced by using a boron based precursor. B-CNTs coated in a material are observed near the furnace entrance (a and b) and spheres are observed from 27 cm (c and d). White arrows indicate the presence of thick (>70 nm) B-CNTs.

3.5.3. The effect of temperature on growth of B-CNTs

Two further experiments were conducted, one at 900 °C and one at 800 °C, to investigate the effect of growth temperature on the morphology of B-CNTs. Both were on samples placed 15 cm inside the furnace. Figure 74 shows that B-CNTs grown at 900 °C form a similar morphology to those grown at 1,000 °C *i.e.* very thick tubes with a coating.

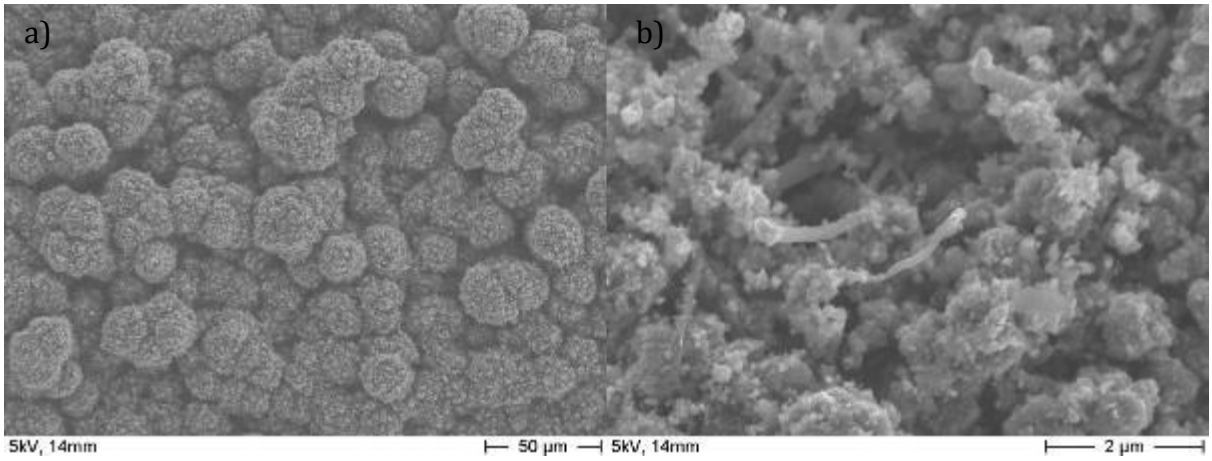

Figure 73. SEM micrographs of coated B-CNTs on a Kanthal wire. Large spheres are observed at low magnification (a) which consist of thick fibres coated in an unknown material (b).

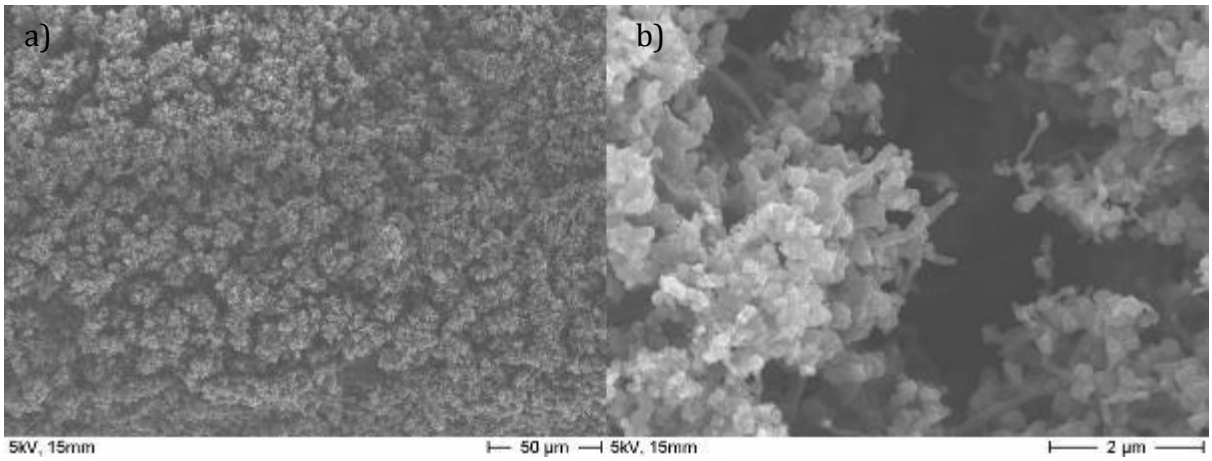

Figure 74. SEM micrographs showing coated B-CNTs produced at a growth temperature of 900°C for 10 minutes, using a 10% 1M triethylborane (TEB) in hexane solution as precursor and a flow rate of 1SLM Ar. Spheres are not present at low magnification (a) and higher magnification reveals thick coated fibres (b).

When a growth temperature of 800 °C is used however, B-CNT clumps aligned along extrusion lines are grown (Figure 75). This is the first instance of B-doping experiments in this study which has produced anything that could be considered a "nanotube".

3.5.4. Summary of the Growth of B-CNTs

Growth of B-CNTs on Kanthal wire was attempted. Most experimental conditions produced either carbonaceous spheres or fibres that were coated in a thick unknown material. 1wt% ferrocene solution was also used but failed to produce any deposit.

Only one experiment was successful in making B-CNTs, using experimental conditions of 800°C, 5wt% ferrocene TEB in hexane solution, 1SLM argon, and for 10 minutes. However, these B-CNTs were larger in diameter than most of the undoped or N-doped CNTs produced earlier in this study.

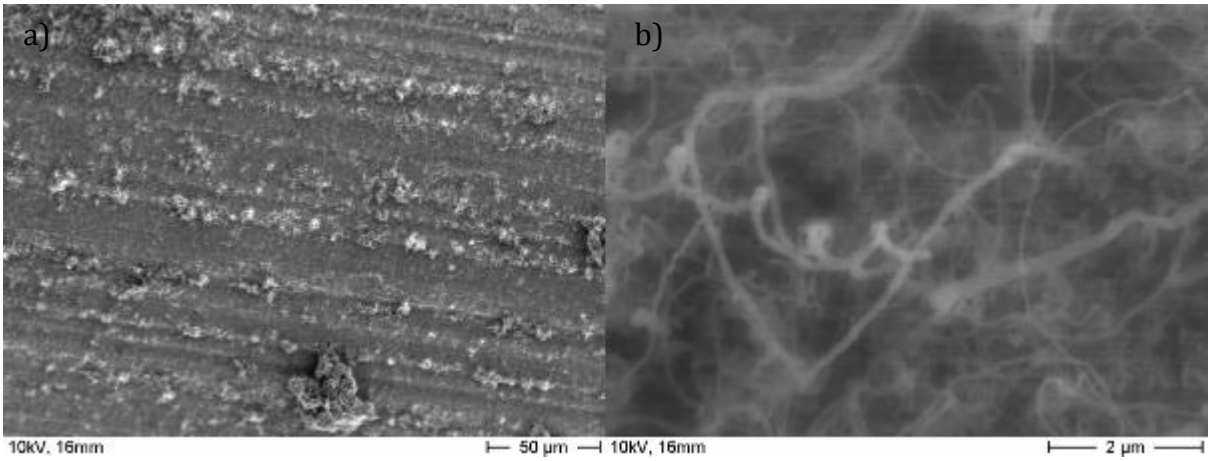

Figure 75. SEM micrographs showing small clumps of B-CNTs aligned along the length of the Kanthal wire (a) and higher magnification reveals separated B-CNTs (b). p71 – B5

The iron-boron-carbon system is known to stop the diffusion of carbon and this would explain why it is so difficult to produce B-CNTs as the boron in TEB may react strongly with the Kanthal wire surface and hence would inhibit CNT growth [31]. B-CNTs were only produced at 800 °C and this is possibly because the interaction between boron and Kanthal wire is minimised at this lower temperature. There are many other elements present on the Kanthal surface and some other undesirable compound may be formed with the addition of boron.

3.6. Growth of CNTs on Various Substrates

CNT growth on quartz, carbon fibre ribbon, and tungsten filament was investigated as alternatives to Kanthal wire.

3.6.1. Comparison between Kanthal wire and Quartz

A comparison was made between growth of CNTs on Kanthal wire and on quartz. The morphology of CNTs grown on quartz is quite different: a thick, carpet-like morphology is grown, where all the CNTs are aligned perpendicular to the substrate (Figure 76c). As CNTs are so close to each other, screening effects may make this sample a bad emitter. Enhancement is only possible if there are stray CNTs protruding from the surface of the carpet.

As quartz is very smooth in comparison to Kanthal wire, each catalyst particle that nucleates on its surface will be on the same plane as each other and growth of CNTs will be perpendicular to the surface, resulting in very dense and vertically aligned carpets [182]. On a rough surface (*e.g.* Kanthal wire), each catalyst particle that nucleates will grow CNTs at different angles and heights and so entangled CNTs that resemble clumps are more likely.

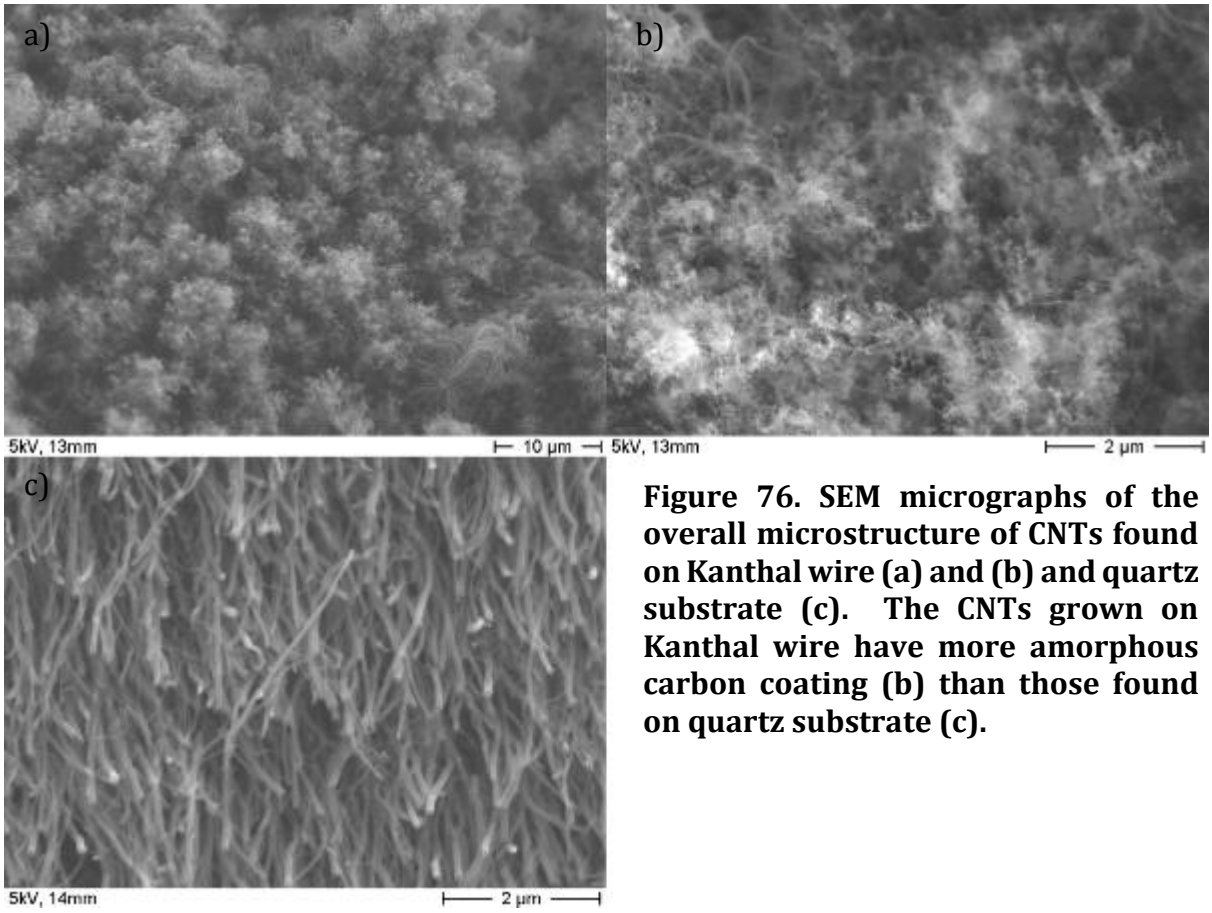

Figure 76. SEM micrographs of the overall microstructure of CNTs found on Kanthal wire (a) and (b) and quartz substrate (c). The CNTs grown on Kanthal wire have more amorphous carbon coating (b) than those found on quartz substrate (c).

CNTs grown on Kanthal wire had more amorphous carbon coating (Figure 76b) than on CNTs found on the quartz tube wall for identical conditions, which were virtually free of amorphous carbon (Figure 76c). This is confirmed by Raman scattering spectroscopy, which shows an increase in I_D/I_G ratio from 0.57 to 0.76 on the quartz and Kanthal substrates respectively, indicating an increase in defect density (Figure 77).

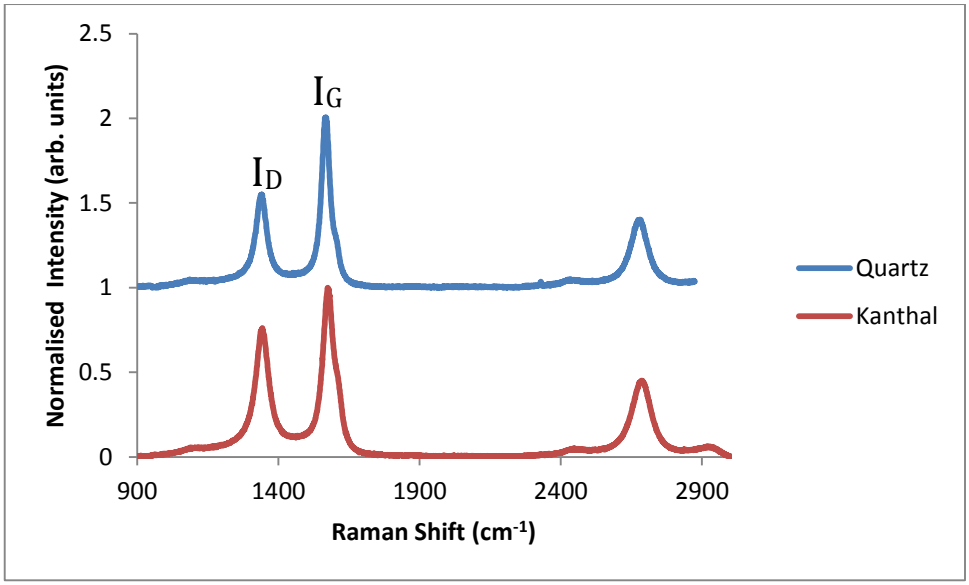

Figure 77. Raman shift spectra of undoped CNTs grown on Kanthal wire and quartz. The CNTs grown on Kanthal wire are more defective indicated by the higher I_D peak with respect to the I_G peak.

The decrease in the defect density of CNTs grown on quartz is due to the inertness of quartz, meaning that the iron particles are able to dissolve carbon more efficiently in comparison to when the catalyst particles are deposited on Kanthal wire.

3.6.2. Growth of CNTs on Annealed Kanthal Wire

It is well known that the catalyst-substrate interaction can prevent the growth of CNTs– a phrase known in the field as "catalyst poisoning" by restricting the dissolution of carbon in the catalyst [183]. For example, iron catalyst particles on a silicon substrate react chemically with the silicon to produce iron silicate and other compounds [184]. Iron silicate compounds do not facilitate the diffusion of carbon and hence cannot act as catalysts for CNT growth. Therefore a substrate is required that will be inert in relation to the iron catalyst particles so that no chemical reaction occurs and the probability of catalyst poisoning is minimised. Simple oxides, such as silicon oxide and aluminium oxide are inert and do not react with iron particles [184-186].

As shown by EDX in Figure 39 there is a significant amount of aluminium on the surface of Kanthal wire and reports in the literature suggests that annealing in air will produce an aluminium oxide layer [165]. Therefore Kanthal wire was annealed in air at 1,000°C for 12 hours to see whether the Kanthal wire oxidised and to see if there was an improvement in the quality of the CNTs.

Figure 78 shows that there has been in an increase in aluminium and oxygen on the surface of the Kanthal wire compared to the other elements (mainly iron and chromium) prior to oxidation observed in Figure 39 and it is likely that an aluminium oxide layer has formed on the surface. Figure 79 shows the surface after oxidation and shows that the surface morphology changes from one that is aligned along extrusion lines, to a morphology that is characterised by angular platelets on the surface which are oxide grains [187].

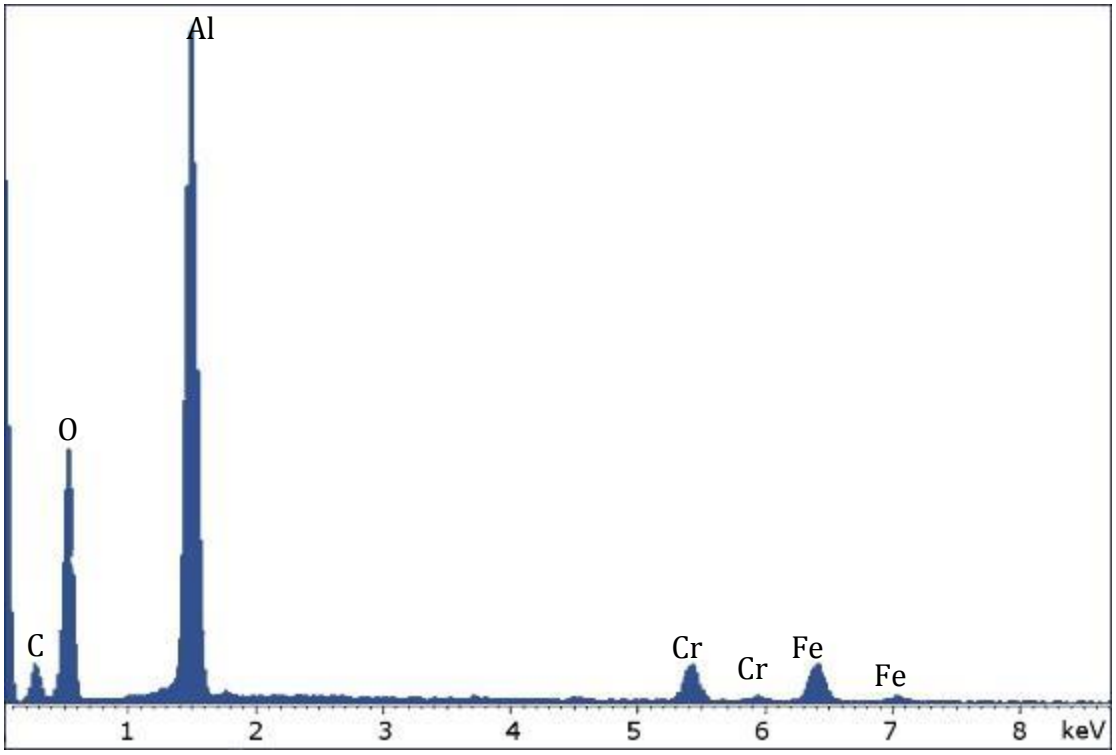

Figure 78: EDX spectrum of the Kanthal wire surface after oxidation in air for 12 hours at 1,000°C. There is a high concentration of aluminium and oxygen after oxidation in comparison to the other elements shown on the surface of bare Kanthal wire indicating that an aluminium oxide layer may have formed.

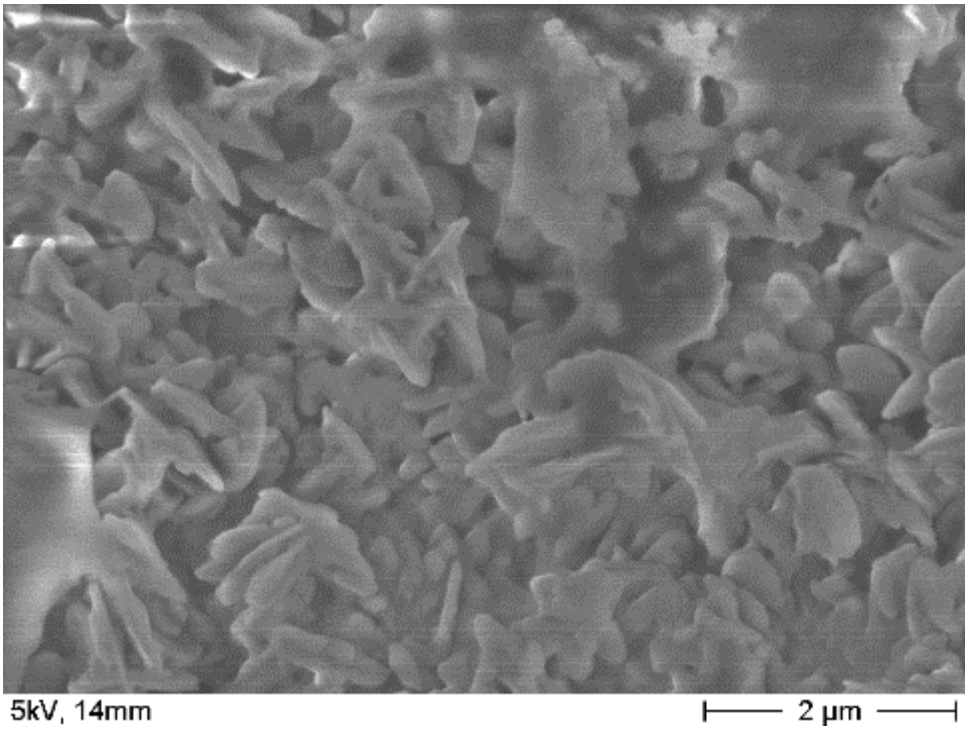

Figure 79. SEM micrograph of the surface of a Kanthal wire after annealing in air for 12 hours at 1,000°C.

CNTs were grown on this surface and Figure 80 shows that, whilst at lower magnifications, the morphology appears similar to CNTs grown on "as received" Kanthal wire (Figure 80a and Figure 76a); fewer CNTs are actually grown (Figure 80b and Figure 76b). Whilst the CNTs are entangled, they are mainly aligned parallel to the surface of the wire, and are not in a 3-dimensional clump type structure. CNTs need to be aligned perpendicular to the substrate surface of the Kanthal wire in order to maximise the field enhancement factor. However, CNTs need to be spaced somehow and not packed closely together in a carpet as this would reduce the field enhancement factor of the CNTs. The I_D/I_G ratio is lower than that on un-annealed Kanthal wire (0.61 compared to 0.76) (Figure 81), confirming that the inertness of the surface has resulted in CNTs that are slightly higher "quality" (i.e. more graphitic as indicated by a lower I_D/I_G ratio in Raman spectroscopy).

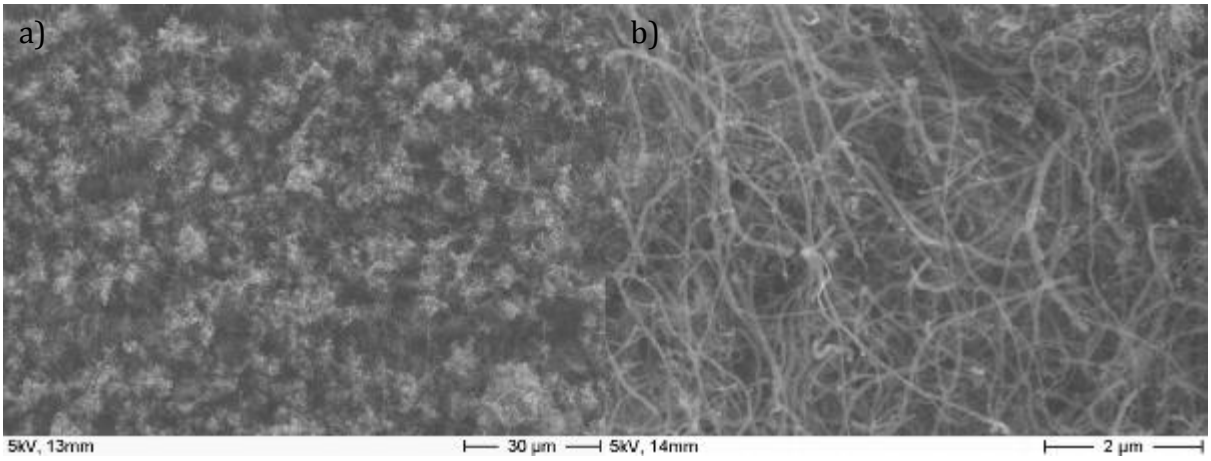

Figure 80. SEM micrographs showing (a) the overall microstructure of CNTs grown on oxidised Kanthal wire taken at low magnification, and a high magnification SEM micrograph (b) of those same CNTs.

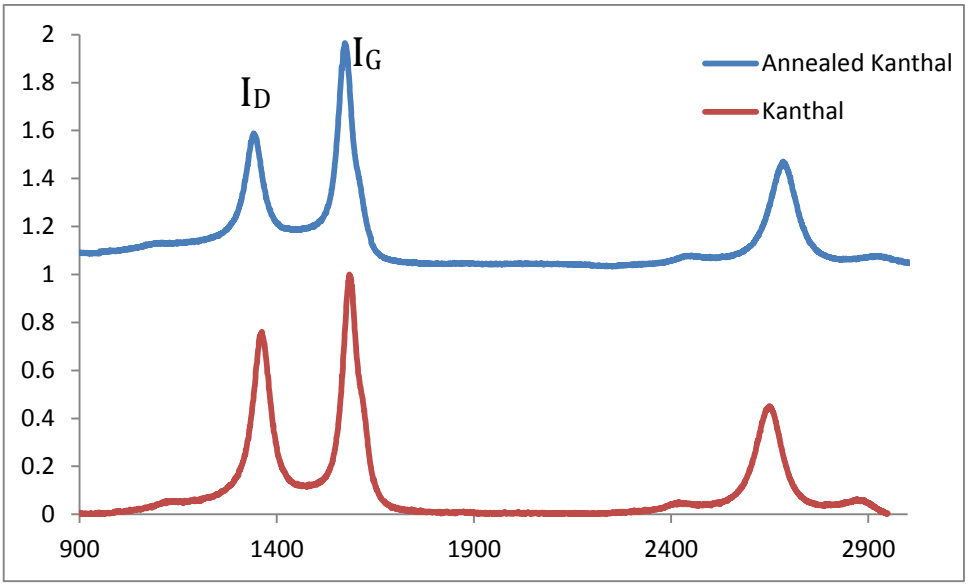

Figure 81. Raman shift spectrum of CNTs grown on annealed Kanthal wire showing a decrease in defect density compared to CNTs grown on "as-received" Kanthal wire.

3.6.3. Growth of CNTs on Carbon Fibre Ribbon

Figure 82 shows a typical SEM micrograph of the growth of CNTs on continuous multi-filament carbon fibre ribbon (high modulus grade supplied by Goodfellow). Unlike growth on metals [125], and indeed quartz [184], a continuous film of CNTs has not formed. Growth of CNTs varied between adjacent carbon fibres (Figure 82a) with some fibres supporting no CNT growth and others supporting almost continuous growth. The

density of "clumps" varies significantly, from 0.02 clumps per μm^2 up to a semi-continuous film with clumps closely packed together.

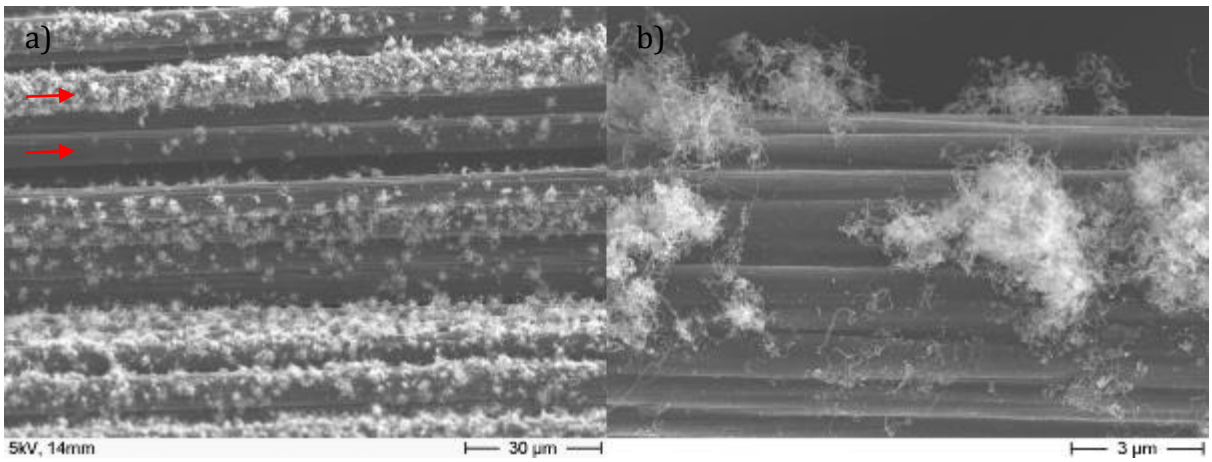

Figure 82. SEM micrographs showing the inhomogeneous nature of CNT growth on carbon fibre. Adjacent fibres support different levels of CNT coverage (a) and higher magnification (b) reveals that CNTs tend to form agglomerates (clumps) on the surface. The arrows in (a) indicate two adjacent carbon fibres that have drastically different CNT densities.

Higher magnification images (Figure 82b) reveal sparse clumps on the surface of individual carbon fibres. Carbon fibres that lie near the surface of the carbon fibre ribbon tend to facilitate CNT growth more than those found deeper inside (Figure 82a). The carrier gas, and hence the catalyst and carbon precursor, cannot penetrate deep in to the carbon fibre ribbon. This means that for a given length of time, carbon fibres near the surface of the ribbon experience a faster flow rate and hence will result in a higher total number of catalyst particles being deposited, and hence a higher density of CNTs grown. Therefore areas which are exposed to higher local carrier gas flow rates will result in a higher density of CNTs grown. The catalyst is unable to penetrate the entire depth of the fibre ribbon, and hence there is a reduced supply of catalyst and carbon precursor. This explains the inhomogeneous nature of CNT growth on carbon fibre ribbon in this study.

Jo *et al* [63] grew CNTs on carbon cloth by firstly sputtering a stainless steel catalyst layer and then using C_2H_2 as the carbon precursor. Uniform coverage of the fibres was achieved

however as the catalyst was deposited via a "line of sight" method, this would be limited to the top surface.

3.6.4. Growth of CNTs on Tungsten Filaments

Two tungsten filaments were placed inside the furnace for CNT growth, one near the furnace entrance (approximately 8cm from the entrance) and another was placed near the furnace exit (approximately 45cm from the entrance). Figure 83a shows the surface of the tungsten filament prior to CNT growth and extrusion lines less than 2μm wide are clearly visible.

Figure 83b shows CNTs deposited on the surface of the tungsten filament at a displacement of 8cm. Growth is not homogenous, and there are preferential regions where large clumps of CNTs form. These are probably areas which are exposed to the most mobile carrier gas flow and hence have experienced the highest concentration of precursor. There are regions where large agglomerates of particles have grown which were not present prior to CNT growth (Figure 83c and Figure 83d). Within these structures, a few CNTs can be seen protruding from the surface in between the particles. The EDX spectrum prior to CNT growth shows a small amount of calcium and barium present. Calcium and barium carbides are sometimes used during the manufacture of tungsten filaments to increase the mechanical stability of the tungsten by pinning grain boundaries and barium is also used as a getter to absorb water molecules that may be present [188]. After CNT growth, Figure 84 shows an increase in calcium and barium and also oxygen is present which suggests that these particles are a combination of calcium oxide and barium oxide.

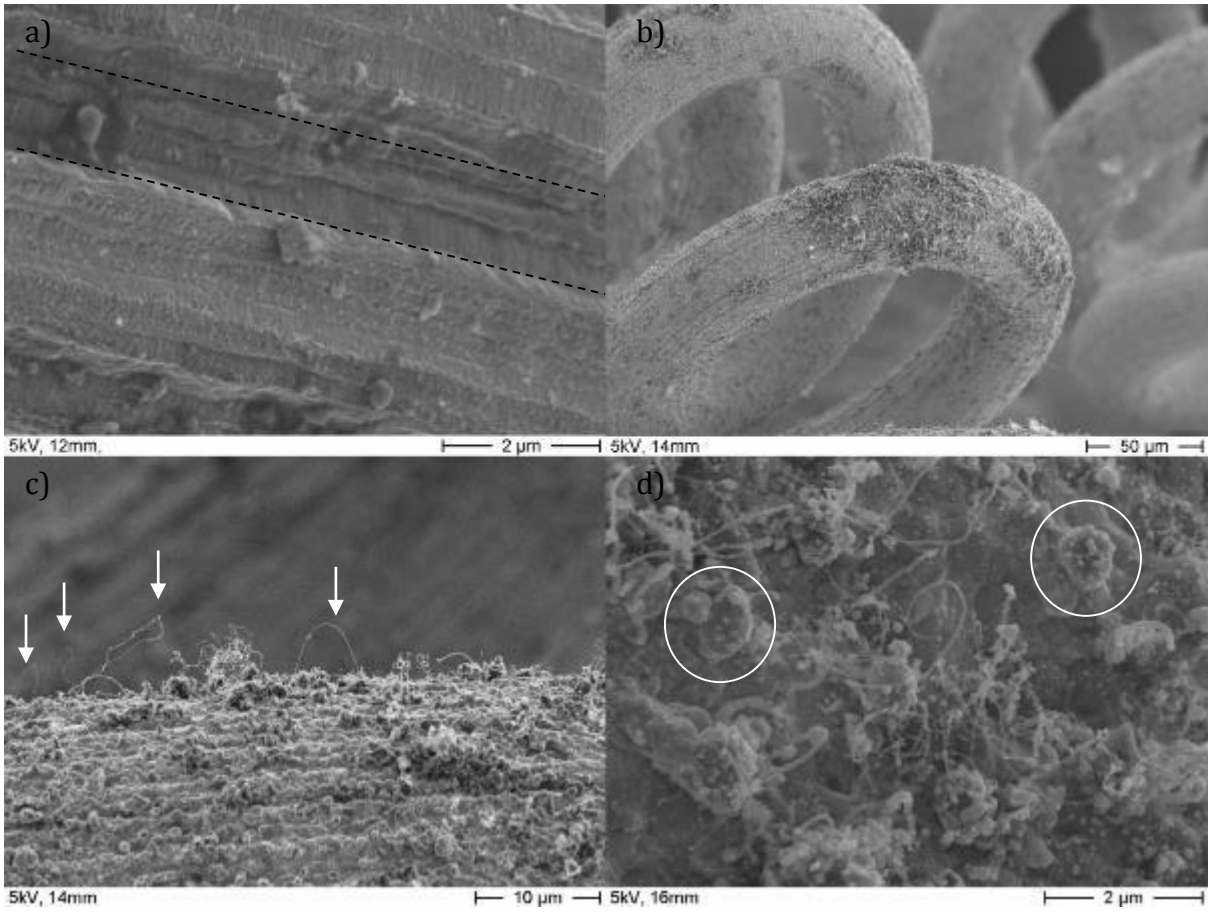

Figure 83. SEM micrographs of tungsten coil wire. (a) shows the "as received" tungsten coil with the clearly visible extrusion lines highlighted by dashed lines. (b) shows a low magnification micrograph of the general microstructure when normal CNT growth parameters are used, (c) shows some CNTs that are protruding (indicated by arrows) and (d) shows the presence of particles (circled in white).

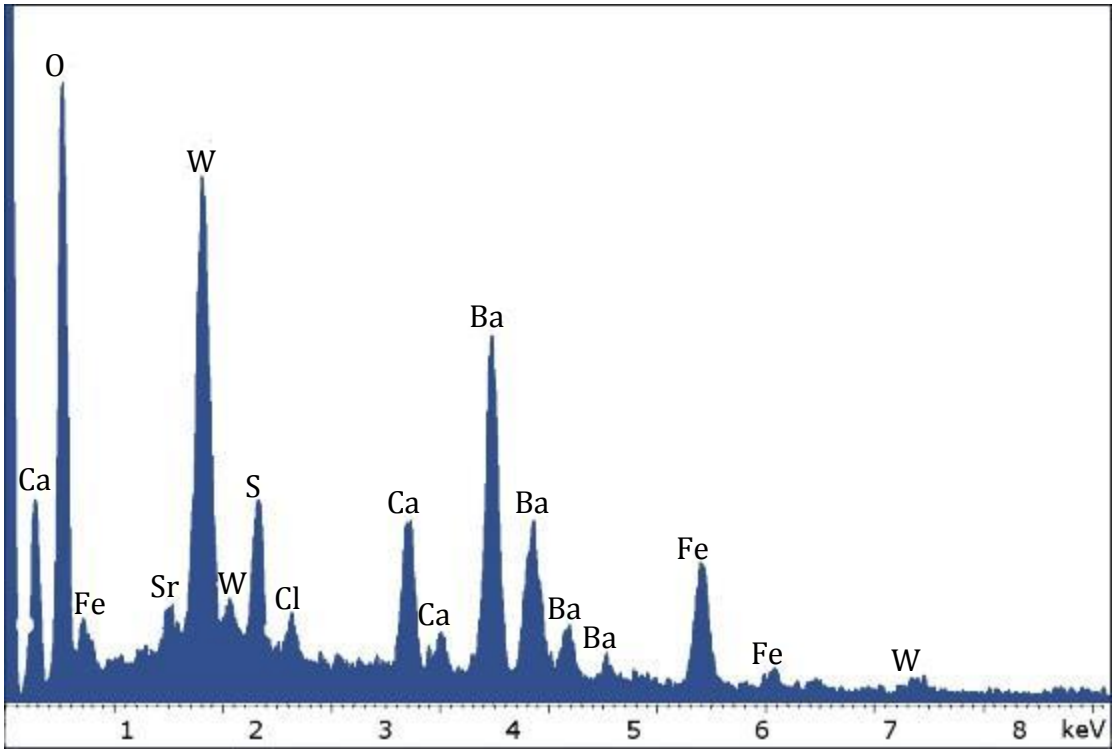

Figure 84. EDX spectrum of area of sample containing particles as shown in Figure 83c and Figure 83d.

CNTs were more numerous and more were protruding on the tungsten filament placed 45cm inside the furnace (Figure 85). By analysing SEM micrographs, it was found that there was roughly 1 protruding CNT per 10μm of tungsten coil length at 8cm, compared to about 2.5 CNTs per 10μm at 45cm. The latter CNTs did however have more amorphous carbon decorating them, and this is confirmed by Raman scattering spectroscopy (Figure 86) with an I_D/I_G ratio of 0.59 at 8cm and 0.87 at 45cm.

Growth on tungsten filaments in this thesis show an increase in defect density of CNTs grown at 45cm inside the furnace compared to those grown 8cm inside. This is consistent with the results presented earlier with growth on Kanthal wire using toluene (see page 70). Figure 85 shows that the CNTs grown at 45cm have particles visible along the length of protruding CNTs. This is likely the cause of the increase in defect density of CNTs grown at this displacement. The particles may have been produced towards the beginning of the furnace and blown on to the tungsten filament at 45cm. Another possible

explanation is that at this displacement, CNT growth on the inside of the quartz tube is most efficient and yields more CNT mass than towards the entrance [140]. This increases the probability of CNT flakes and other debris detaching from the quartz and attaching to the tungsten. Large agglomerates of CNTs can be seen in Figure 85a which could have been flakes that have fallen onto the tungsten. Debris from earlier in the furnace could have also been blown on to the tungsten filament as growth occurs and becomes encapsulated in the CNT structure, thus increasing the defect density.

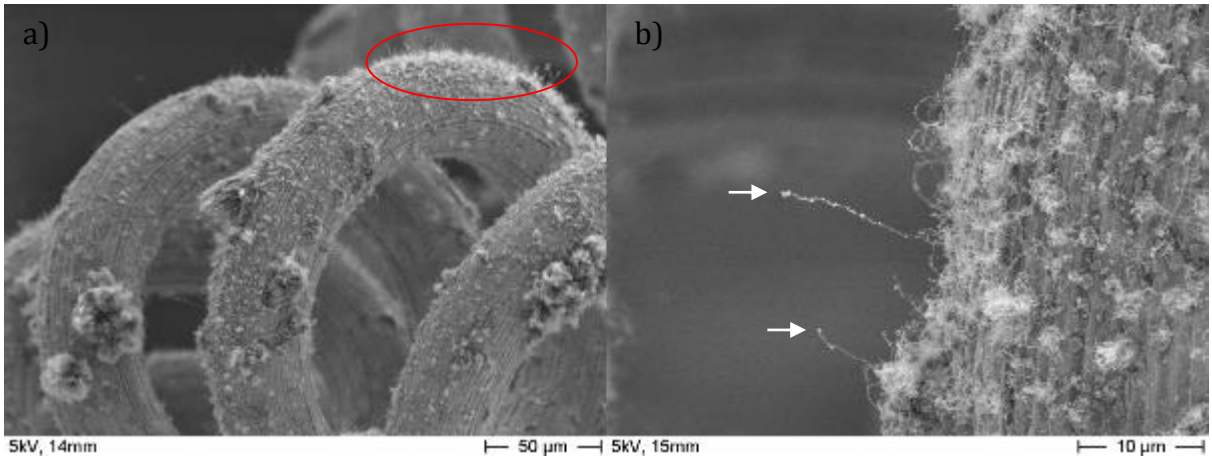

Figure 85. Low magnification SEM micrograph (a) of CNTs deposited on tungsten coil placed 45cm inside the furnace. Area of protruding CNTs is circled. Protruding CNTs that could enhance β are found on the coil surface (b) indicated by arrows.

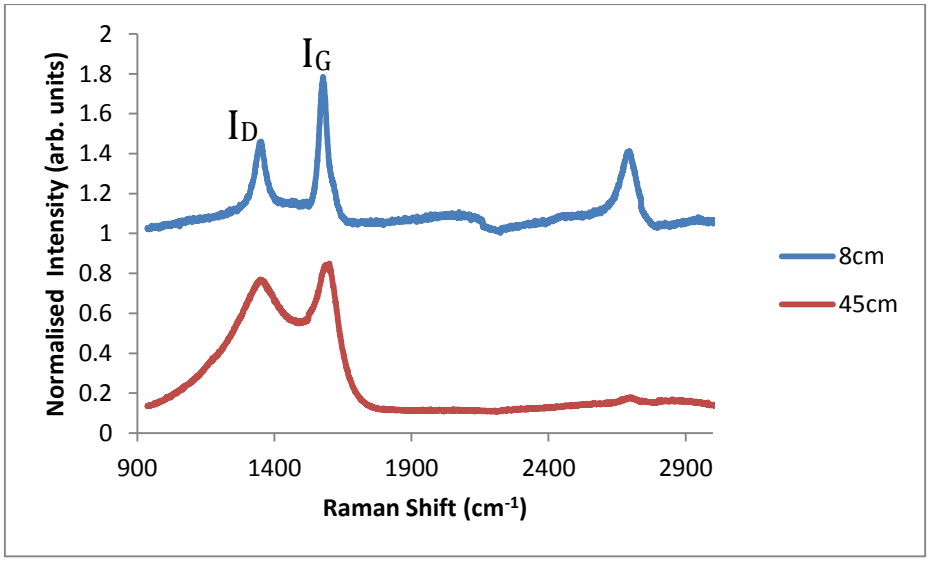

Figure 86. Raman Scattering Shift spectra for CNTs grown on tungsten coils placed 8cm and 45cm inside the furnace. CNTs grown further into the furnace are more defective.

3.2.6. Summary of the Growth of CNTs on Various Substrates

Carbon fibre ribbon, tungsten filament, annealed and "as received" Kanthal wire, and quartz were all investigated for their suitability as support substrates for CNT growth for field emission cathodes. Table 4 summarises the substrates investigated and the length, I_D/I_G ratio and general morphology of the grown CNTs.

Quartz produced CNTs of the highest quality (*i.e.* the lowest I_D/I_G ratio, and hence the lowest defect density). However, thick carpets of CNTs were produced that would potentially offer very little field enhancement due to electrostatic screening [62]. Furthermore, it is very difficult to manufacture quartz wires of the same dimensions as metals, and quartz is also highly resistive. For these reasons, it would be unsuitable for field emission applications.

Carbon fibre ribbon supported growth of CNTs. However, the CNTs formed clumps that are separated from each other in some fibres and growth on carbon fibres is unreliable (*i.e.* neighbouring fibres may, or may not, have CNTs on their surface). Whilst separation of emitters is beneficial for field emission as it reduces screening, too much separation can reduce the overall current density as there will be too low a density of emitters.

CNT films grown on tungsten filaments were inhomogeneous, with some regions containing CNTs and other regions containing no CNTs. Due to the geometry of the coils, many CNTs were protruding.

Kanthal wire was annealed to produce an oxidised surface. This was to increase the quality (*i.e.* the graphitisation) of the "as grown" CNTs. Whilst this was the case, the CNT "film" that was produced is inhomogeneous and, furthermore, the CNTs lie parallel to the surface of the substrate in most cases which would not enhance the local electric field significantly.

Substrate	length	I_D/I_G	Morphology	Further Comments
Carbon Fibre	<2.5µm	N/A	entangled agglomerates	decreased β due to entanglement
Tungsten Coil at 8cm	<7µm	0.59	~1 protruding CNT per 10µm	random coverage
Tungsten Coil at 45cm	<15µm	0.87	~2.5 protruding CNTs per 10µm	random coverage
Kanthal Wire	<40µm	0.76	fluffy carpets	increased β due to non-smooth surface
Annealed Kanthal Wire	<40µm	0.61	fluffy carpets	random coverage of CNTs
Quartz Tube	<90µm	0.57	carpets	low β due to smooth surface

Table 4. Table summarising the various affects on certain CNT material properties when different support substrates are used.

3.7. Chapter Summary

CNTs were grown on various wire materials using the CVD technique and control over the different morphologies of CNT films was obtained by manipulating the growth parameters. Precursors that contained nitrogen or boron enabled the growth of doped CNTs which could potentially be beneficial for field emission devices.

The substrate-catalyst interaction is very important and governs the adhesion of CNTs to the wire, in addition to the catalyst particle poisoning, which stops CNT growth. This interaction was controlled by growing CNTs on annealed Kanthal wire, which produced CNTs of higher quality compared to unannealed Kanthal wire due to the inertness of the

oxide, limiting the catalyst poisoning. Oxidised metal wires however are not conducting and hence will hinder the final device as a significant portion of the potential drop would be over the oxidised metal and would result in power loss. It is believed that the growth of B-CNTs proved challenging because of the strong substrate-catalyst interaction due to the boron reacting with the catalyst particles to create compounds which do not dissolve carbon effectively.

The I_D/I_G ratio ranged from 0.35 (at 800°C and 24cm displacement) upto 1.08 with benzylamine and using 0.2SLM hydrogen in the carrier gas. When using toluene, the introduction of hydrogen resulted in a lower I_D/I_G ratio due to the removal of amorphous carbon. When using benzylamine for the growth of N-doped CNTs, the introduction of hydrogen resulted in a higher I_D/I_G ratio due to the removal of nitrogen in the structure leaving point defects behind.

There is a region of the furnace where the most homogenous of CNT films are produced and the longest CNTs which is approximately between 10cm and 35cm. Before this region, it is more likely that no CNTs are formed and after this region, fewer CNTs are formed and are more defective.

Growth of CNT bundles and ridges have been achieved by using benzylamine or a growth temperature of 900°C. Bundles and ridges could offer a way of achieving beneficial field emission properties if there are protruding CNTs found at the corners of the bundles.

3.7.1. Chapter Conclusions

Kanthal wire is the best substrate of choice for the final field emission device due to the homogenous growth and high density of CNTs grown on its surface, which is needed for uniform emission. Various morphologies were created and ridges and towers were most likely to create CNTs where the tips are aligned towards the anode. 900°C and longer

growth times are desirable because this will create longer CNTs and are more likely to create ridges. Further optimisation of the process parameters will be required to achieve more control over the type of ridges and bundles that are formed to produce the most beneficial field emission properties.

Displacement inside the furnace and the presence of hydrogen in the carrier gas have the strongest effect on the growth of CNTs in terms of morphology produced and defect density, which are the most important material properties for field emission applications. Introducing dopants into the precursor introduces a more challenging growth environment and needs to be optimised further to obtain the same level of control as with toluene.

4. Field Emission Properties of Individual CNTs

4.1. Introduction

Chapter 3 was concerned with the growth of CNT films and Chapter 4 will be regarding the field emission properties of those films. This chapter is concerned with the field emission properties of *individual* CNTs (both undoped and doped), which were obtained from the samples grown in Chapter 3.

The purposes of investigating the field emission properties of individual CNTs are two-fold. Firstly, an understanding of the *stability* of emission from individual CNTs could provide a better understanding of the stability of the overall device. By studying the field emission properties of individual CNTs, and comparing the results with field emission properties of CNT films in Chapter 4, this process should become clearer.

Secondly, to investigate the role of defects in the field emission process as the literature is divided over whether defects decrease the work function (by introducing LDoS near the Fermi Level) or whether it increases the work function. Individual CNTs were subjected to varying degrees of damage to introduce varying levels of defect density so that their role in field emission could be better understood.

4.2. Experimental Methodology

There are many issues in testing the field emission properties of individual CNTs due to the small lengths involved. Measuring the inter-electrode displacement is challenging as the CNTs and anode need to be at the same height. As the viewing screen in a TEM is two dimensional, setting this up can be tricky. Using the 'wobbler' function on the TEM, where the focus function is made to oscillate, the same height can be established. The wobbler functions by making the image focus oscillate between two positions either side of the rest position if the objective lens is not focused to the same plane as the CNT. When the

objective lens is focussed on the same plane as the sample, the wobbler does not change the image.

Finally isolating a single CNT for investigation is difficult because there are normally many CNTs clustered together and therefore emitted current would potentially be from all or some of these CNTs. Isolation of one CNT can be achieved by making contact with nearby CNTs and passing a large current which destroys the CNTs that are not of interest.

4.3. Field Emission Properties of Individual CNTs

4.3.1. Field Emission Properties of Undoped CNTs

Firstly undoped individual CNTs were tested for their field emission properties. 6 CNTs were isolated from sample C18 using the method outlined previously in Chapter 2 (see page 54). The STM tip was moved approximately 2μm from the CNT tip and a stepped voltage up to 140V over a time interval of 100ms was applied in 100μs steps and the emission current recorded. I-V Acquisitions were repeated five times to remove adsorbents and other contaminants on the surface of the CNT that can cause emission instability [189]. Heating the CNT tip during these initial acquisitions removes undesirable absorbents, such as water [21]. If no field emission is detected at 2μm separation, the STM tip is brought closer to the CNT tip until field emission is detected. In practise a separation less than 500nm is required in most cases.

E_{TO} in this case is defined as the local electric field (*i.e.* the electric field near the CNT tip) required to extract a current of 100nA [190] and hence is different to E_{TO} defined in Chapter 4 which is the *average* electric field near the cathode required to extract 10 $\mu A/cm^2$. The local turn-on electric field in this case shall be named as E_{LTO} to avoid confusion with E_{TO} as defined in Chapter 4. Smith *et al* calculated E_{LTO} from I-V curve data for several individual CNTs [190]. Firstly the β value for the CNT in question is calculated

from the corresponding F-N plot. Then this value is used to calculate E_{LTO} using the following equation:

$$E_{LTO} = \beta E_{TO}$$

Where:

$$E_{TO} = V_{TO}/(D - h)$$

and V_{TO} is the potential difference applied to the system at turn-on, D is the distance between the STM tip (anode) and the STM tip that the CNT is attached to (Cathode), and h is the height of the CNT. A schematic of this setup is illustrated in Figure 87.

The field enhancement factor (β) is constant at large interelectrode displacements. When the interelectrode displacement is reduced to less than $3h$, β reduces. This is because at very small interelectrode displacements ($h<D<3h$), the system approximates two parallel plates, and a significant proportion of the field enhancement is lost. This is why the turn-on *local* field is considered as this will not change with respect to interelectrode displacement as reported by Smith *et al* [190].

The field emission properties of each CNT varies dramatically within sample C18, and Figure 88 shows that there is a variation of ~3 V/nm in E_{LTO} values of these 6 CNTs. There appears to be no correlation between CNT diameter and local turn on field (Table 5). This is probably because of the reduction in field enhancement due to the small interelectrode displacement and hence diameter becomes irrelevant as the system approaches a parallel plate situation.

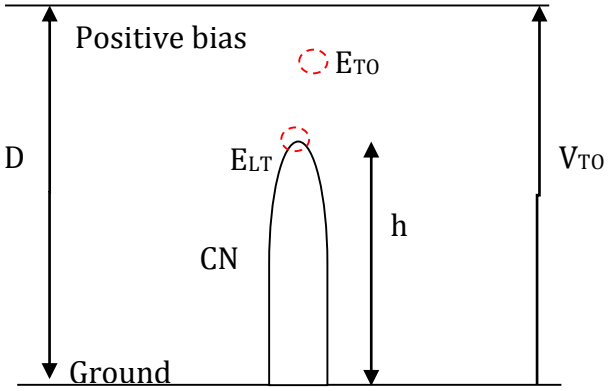

Figure 87. Schematic of the experimental setup for testing the field emission properties of individual CNTs. D is the interelectrode displacement, V_{TO} is the voltage immediately after field emission starts, h is the length of the CNT, E_{TO} is the average electric field far from the CNT immediately after field emission starts and E_{LTO} is the local electric field near the CNT tip immediately after field emission starts.

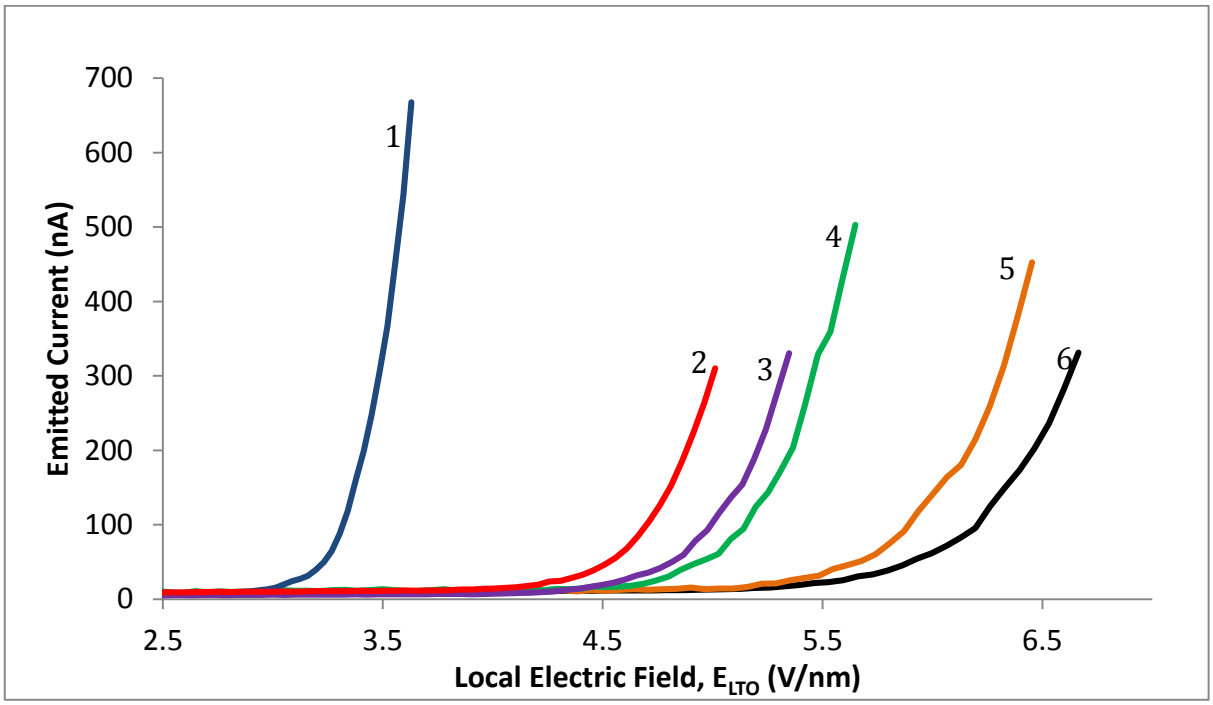

Figure 88. Graph showing the current density vs. local electric field curves for 6 CNTs taken from sample C18. There is a wide range in the E_{LTO} values of the CNTs.

Figure 89 shows TEM images of these 6 CNTs that were subjected to I-V sweeps. The CNTs have different diameters and structures yet there is no correlation between thinner CNTs and lower turn on fields. It is difficult to determine the cause of the difference in field emission properties as CNTs vary so greatly between each other, even when grown

in the same process run. A very small change in the geometry of a CNT tip can drastically change its enhancement factor. A small protrusion may double β, for example [21].

The CNT tip state (*i.e.* the presence of defects) is likely to be important as this will control the work function. It is possible that it is mainly the CNT tip that is responsible for the apparent difference in local turn on fields.

4.3.2. Field Emission Properties of Doped CNTs

The process of testing individual CNTs was repeated for more samples of both undoped and doped CNTs. Again, there was found to be no correlation between E_{LTO} and CNT diameter. This is to be expected as the distance between the anode and the CNT tip under investigation is less than three times the height of the CNT. This means that the field enhancement factor is a function of the interelectrode displacement, which in this case is the distance between the anode and the CNT tip [190]. Figure 91 shows that there is a linear trend of increasing field enhancement factor with increasing interelectrode displacement and this is consistent with the literature [62, 190]. The trendline of Figure 91is set to intercept the y-axis at a value of 1 corresponding to no field enhancement when the interelectrode displacement is zero. This is a reasonable assumption because, as the interelectrode displacement approaches zero, the system approximates two parallel plates in which no field enhancement would be observed. As the field enhancement factor (β) is related to the local electric field by $E_{loc} = \beta E$, where E is the macroscopic electric field and is given by $E = V/D$ in a parallel plate setup, a β value of 1 would therefore correspond to no field enhancement.

CNT Number	E_{Lto} (V/nm)	Diameter (nm)
1	3.3	50
2	4.6	100
3	4.9	45
4	5.1	40
5	5.9	63
6	6.3	55

Table 5. Table summarising 6 CNTs tested from sample C18 and their corresponding local turn on field and diameter. There is no correlation between diameter and E_{LTO}

There are slightly more CNTs with lower than expected field enhancement factors (Figure 91). It should be noted that a majority of these CNTs were produced with pure toluene and hence are undoped. Figure 90 shows examples of typical N-doped CNTs. The main difference compared to undoped CNTs is that their internal structure is characterised by compartments resembling a bamboo-type structure. For field emission applications however, it is the CNT tip that is important. For each CNT, F-N plots were constructed and it was assumed that the work function of each CNT was 4.82 eV [191] regardless of the level of doping when calculating β using the following equation: $M = \frac{-6.83\phi^{\frac{2}{3}}}{\beta}$ where M is the gradient of the F-N plot. This is because it is very difficult to measure accurately the level of doping near the CNT tip as the dopant is unlikely to be distributed homogenously throughout the CNT. If there are dopants near the CNT tip, then it is likely to result in a lowering of the work function due to LDoS being introduced near the Fermi Level [192]. This will manifest itself as an increase in apparent β in Figure 91. This could explain why the β values of doped CNTs tend to be nearer the trendline in Figure 91.

Point A and point B in Figure 91 are where E_{LTO} values of CNTs lie far from the trendline. The inset for point A shows the relevant TEM image of the CNT and shows that the CNT walls are parallel to the anode and this is perhaps why the field enhancement is lower. The inset for point B does not show anything that indicates that β value should be higher than the trendline. The average diameter of CNTs is 42nm and the CNT for point B has a diameter of 46nm and therefore the geometry of the CNTs seems to play an insignificant role in β value. A more detailed consideration of the CNT tip state is required.

4.4. Investigation of the effect of CNT Tip State on Field Emission Properties of CNTs

4.4.1. Field Emission Properties of CNTs Damaged by a Low Intensity Electron Irradiation

Varying degrees of electron irradiation of undoped and N doped CNT tips were induced to study the effects of CNT tip state on their field emission properties. Electron energy loss spectroscopy (EELS) was used to determine the level of dopant in the CNT tip. The level of graphitisation (and hence the level of defects) can also be extrapolated qualitatively using this method.

When a CNT is doped it is unlikely that the dopant atoms are found homogenously throughout the tube. It is desirable for the dopant atoms to be at the CNT tip so that localized density of states (LDoS) are introduced near the Fermi Level. This has the effect of lowering the work function and hence reduces E_{LTO}.

Only a few CNTs were investigated in this damage inducing study. Outer diameters ranged between 25nm and 35nm, and they were several μm in length. EELS analysis was used for two purposes: 1) to irradiate a CNT tip by converging the incident electron beam to a small area, and 2) to determine the N content in an individual N-CNT.

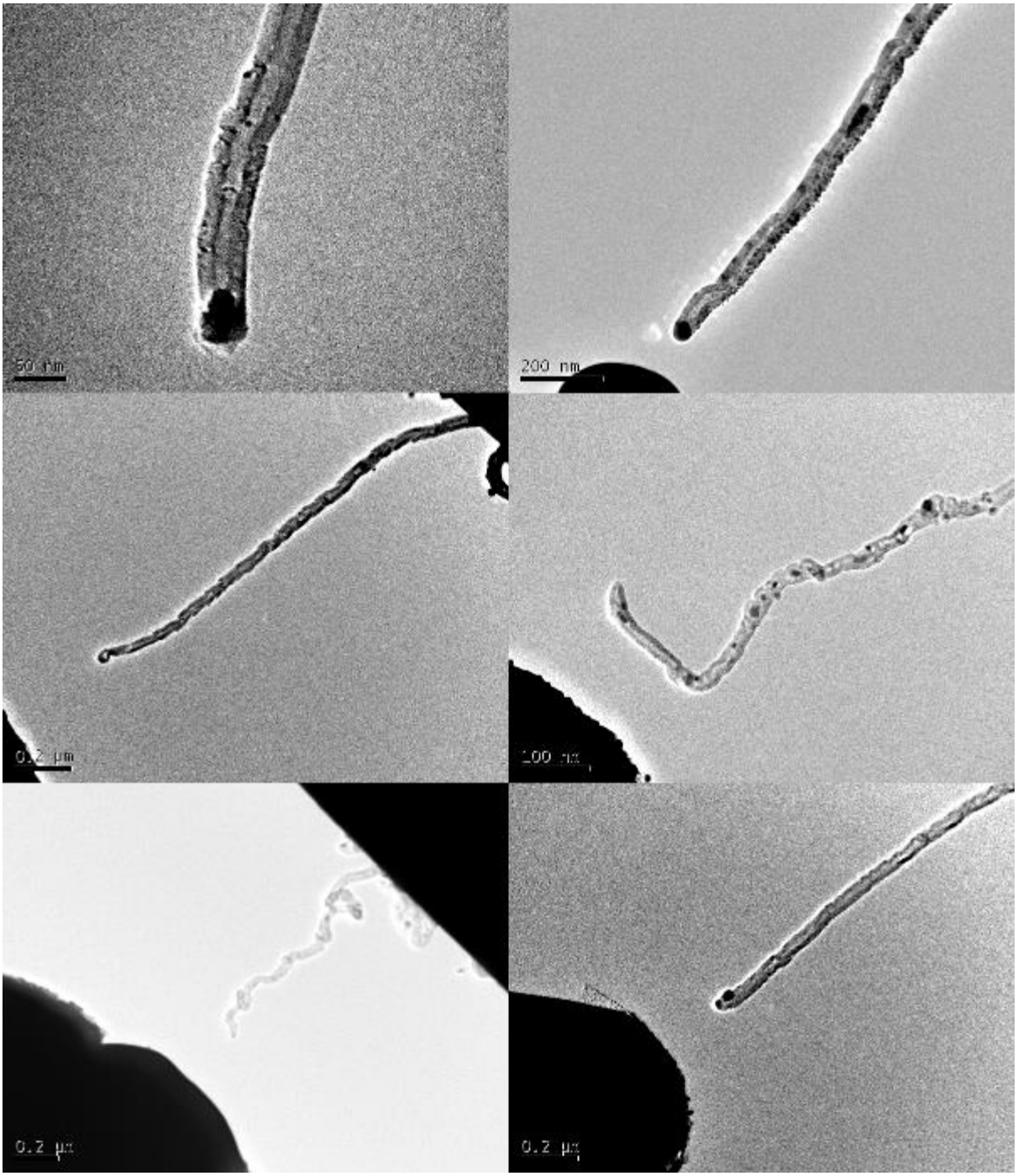

Figure 89. TEM micrographs of the undoped CNTs obtained from sample C18 and subjected to I-V sweeps. Starting with the TEM micrograph top right, CNT1 to CNT6 moving right then down as described in Table 9. The structure varies between CNTs however the exact nature of the CNT tip is hard to determine.

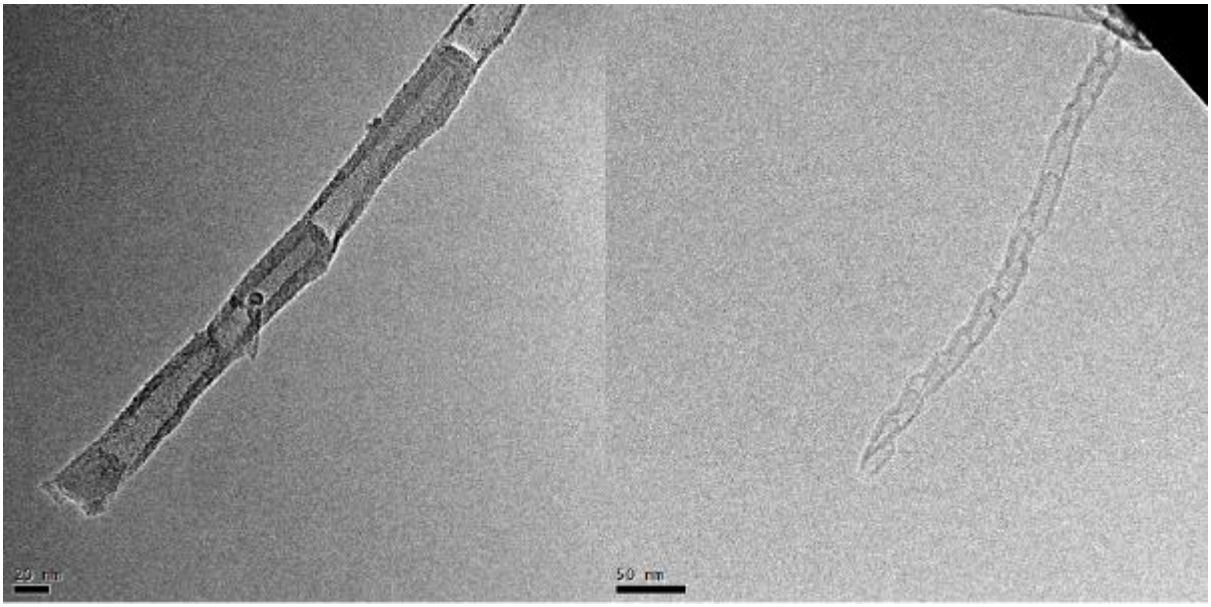

Figure 90. Examples of N-doped CNTs that investigated in this study. They differ in structure compared to undoped CNTs with visible internal compartments which resembles a bamboo-type structure.

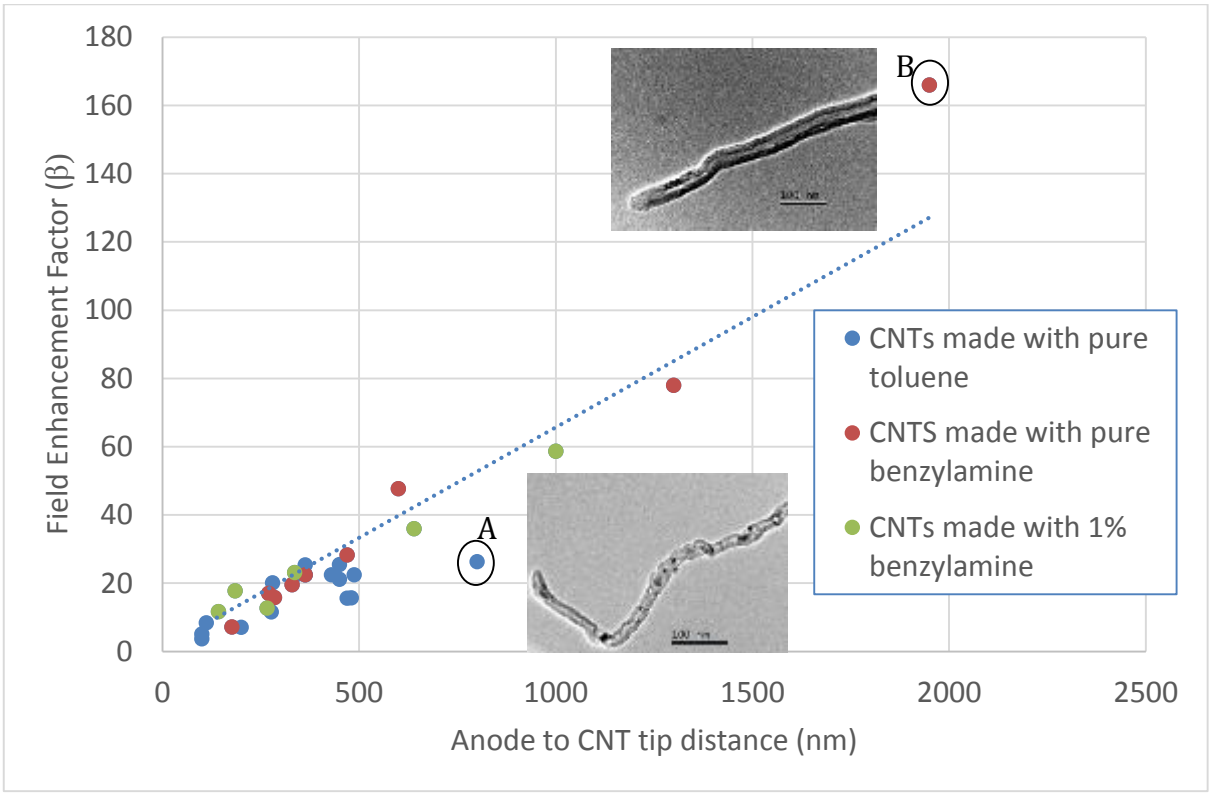

Figure 91. Graph of CNTs tested in this study. There is a linear relationship between increasing interelectrode displacement and increasing β value.

An open ended N-CNT containing 3.5at% N (determined by EELS) is shown in Figure 92a. On acquiring EEL spectra, the graphitized walls were damaged by the electron beam and have become more disordered, whilst the overall structure of the CNT remains unchanged (Figure 92b). A subsequent EEL spectrum recorded after a few I-V sweeps showed that there is no change in dopant level, or to any type of bonding, within the structure. An I-V curve was acquired and the process of taking an I-V curve and then taking an EELS spectrum was repeated several times on the same N-CNT. Figure 93 shows that repeated acquisitions resulted in no change in E_{LTO}. However, F-N plots (Figure 94) show that the gradient of the fitted line has increased after the second acquisition of the EEL spectrum. As Figure 92 shows no visible signs of geometrical changes, and the inter-electrode distance is the same, one can assume that β remains constant. Using $M = \frac{-6.83\phi^{\frac{2}{3}}}{\beta}$, where M is the gradient of the fitted line in the F-N plot; the work function of the new CNT tip is ~3.8eV, if it is assumed that the original CNT tip had a work function of 4.82eV . This is reflected by the slight increase in steepness of the curve in Figure 93, and the increased maximum current. This implies that a slight increase in defect density induced by damage caused by the low intensity electron irradiation during EELS analysis, results in slightly improved field emission properties.

4.4.2. Field Emission Properties of N-CNTs Damaged by High Intensity Electron Irradiation

High intensity electron irradiation was also carried out to investigate the effects of a more disorderly CNT structure on field emission properties. This was achieved by converging the TEM imaging beam on the tip of individual N-CNTs for approximately 30 seconds. Figure 92c shows that the inner core near the CNT tip, to a length of approximately 80

nm, has been damaged (the walls and the inner core have changed). Due to irradiation, the graphitic structure has turned amorphous at the CNT tip. EELS reveals that beam damage has resulted in a relative increase in N-doping (Figure 95). Carbon atoms are removed from the surface as a result of the convergent beam, resulting in an apparent increase (54%) in N concentration. Electron irradiation causes atoms to be sputtered, due to high energy electron knock-on collisions, which cause atoms to be ejected from the CNT [193]. As nitrogen atoms are only slightly heavier than carbon atoms, it is surprising that there is an apparent increase in N concentration. A possible explanation is that nitrogen is not homogenously distributed inside the CNT.

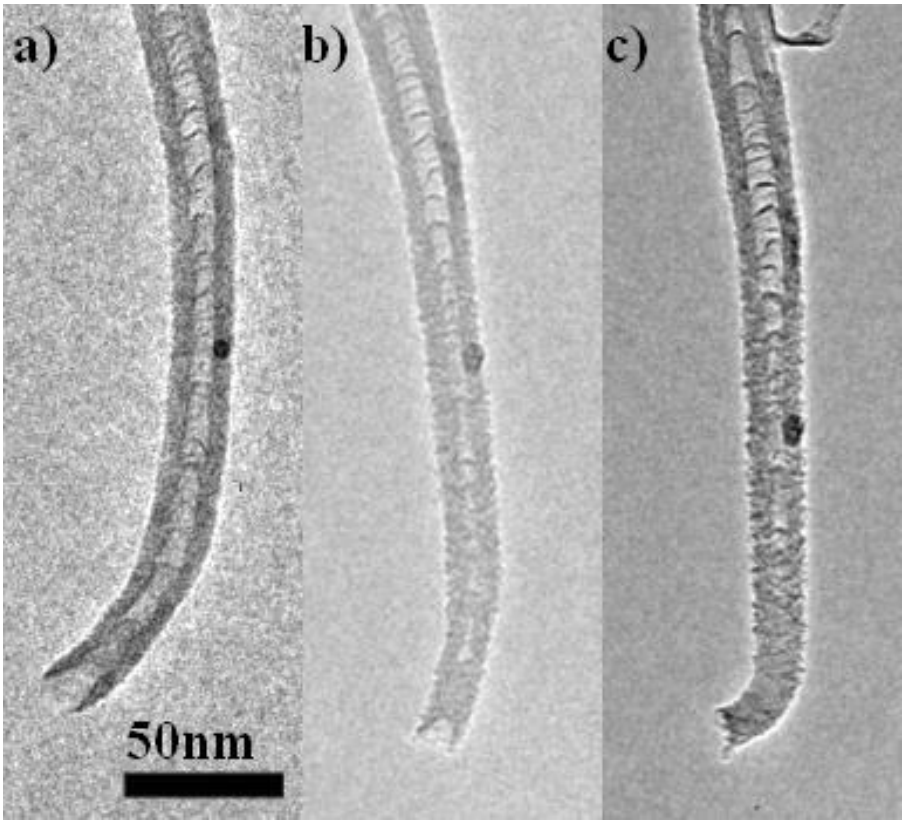

Figure 92. TEM micrographs of a pristine N-CNT (a), N-CNT after several acquisitions of EELS (b) and after irradiation damage of CNT tip (c). The CNT walls become more disordered after EELS measurements (b) and the tip becomes completely amorphous due to irradiation damage (c).

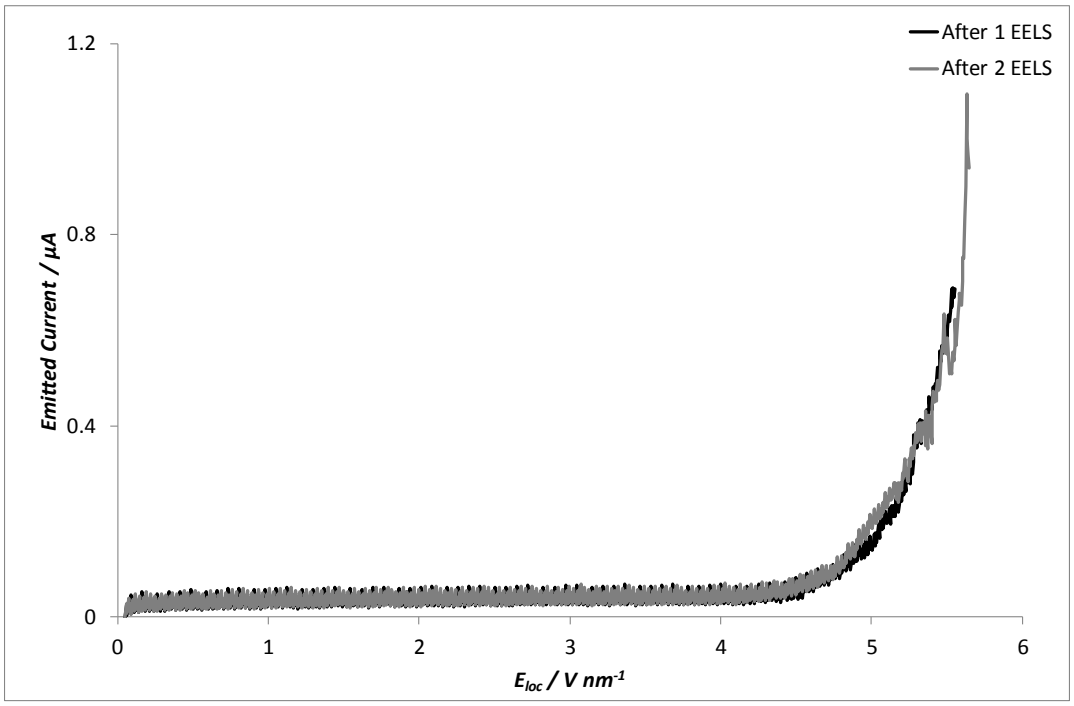

Figure 93. Graph showing the I-E_{loc} for a pristine N-CNT and the same nanotube after several aquisitions of EELS. There is no increase in the EL_{TO}.

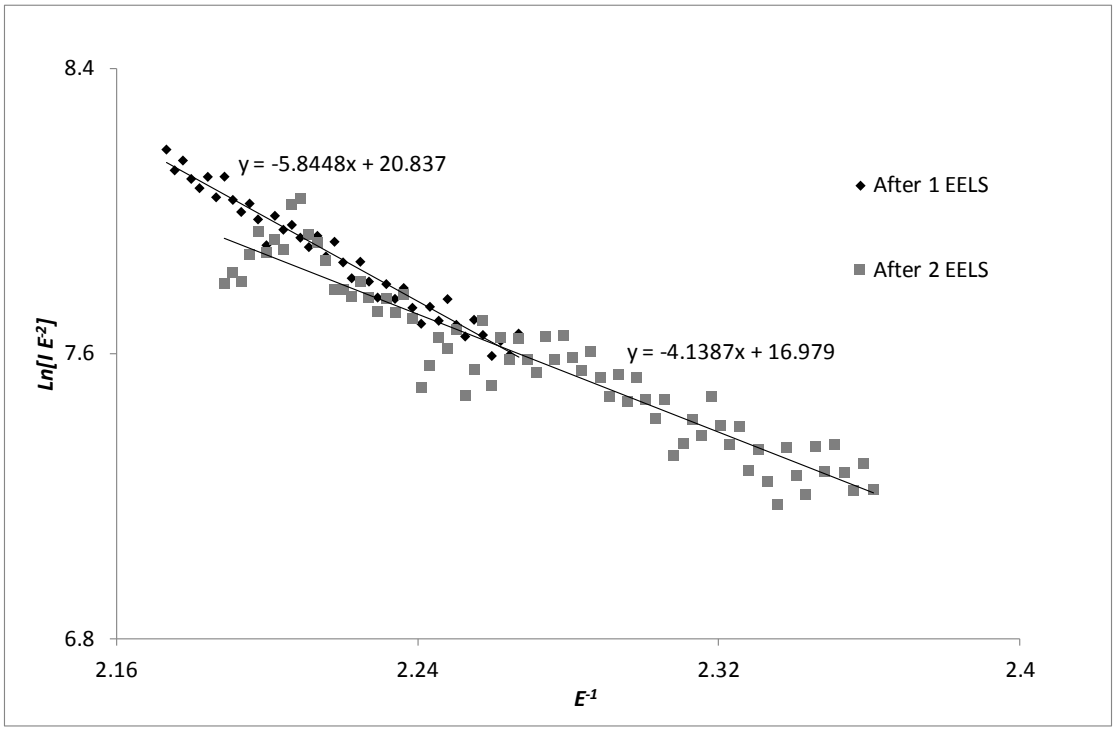

Figure 94. F-N plot showing the change in gradient upon several EEL spectra. This implies a slight decrease in work function as β has remained constant.

Another N-CNT was investigated for reliability of results (Figure 96a). Several acquisitions of current-voltage data are obtained before and after high intensity irradiation. Upon irradiation, the structure at the tip is destroyed and the tip became rounded and larger in diameter (Figure 96b). This would imply that a reduction in emitted current should be observed, as β has decreased. The methodology set out by Smith *et al* cannot be used, as both β and the work function have changed. It appears however, that electron irradiation has had a detrimental effect on field emission, as no emission current was observed with the anode at the same distance used preceding irradiation. The inter-electrode distance was therefore reduced from 1.3 μm to 400 nm upon irradiation. E_{LTO} has increased from 87 V μm^{-1} to 338 V μm^{-1} (Figure 97). It is unclear if this dramatic reduction in field emission properties is solely caused by a reduction in β, or by a combination of lowered β and increased work function.

Undoped CNTs were also investigated with outer diameters ranged from 37nm to 51nm and lengths of several μm (Figure 98). Several CNTs were examined and all were found to have higher E_{LTO} after high intensity irradiation and lower maximum emitted current.

4.4.3. Change in Field Enhancement Factor Due to Irradiation Damage

Geometry is important in the field emission process as the value of β determines the emitted current. It is possible that irradiated damaged material increases the work function as the work shown in this chapter reveals an increase in E_{LTO} upon damage. Figure 99 shows an N-CNT that has been irradiated. Its tip geometry has altered so that it has a smaller radius of curvature. Despite this, the emitted current is significantly less after damage (Figure 100). The negative effects of beam damage are not compensated by the positive effects of the more highly curved surface thereby implying an increase in

work function. It is impossible to verify the value of the work function using F-N plots however, as β has also changed.

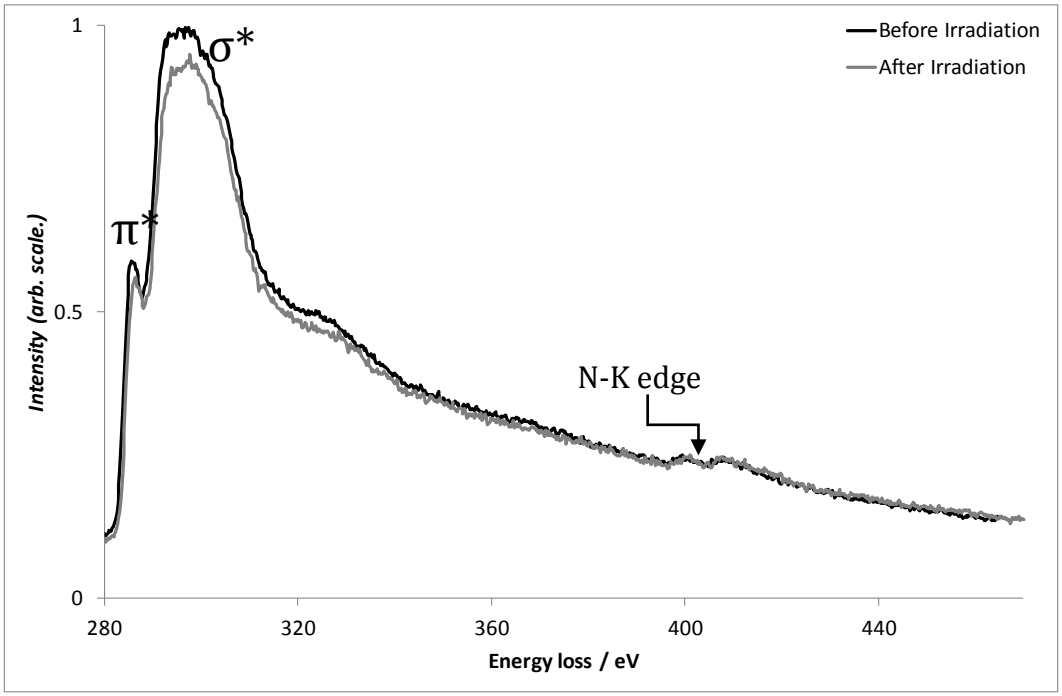

Figure 95. EEL spectra for a pristine N-CNT, before and after high intensity irradiation damage. A π* peak is present, which corresponds to inter-plane bonding of graphitic planes. The σ* peak is a measure of the sp^2 bonding [194]. There is a relative increase of N content after damage.

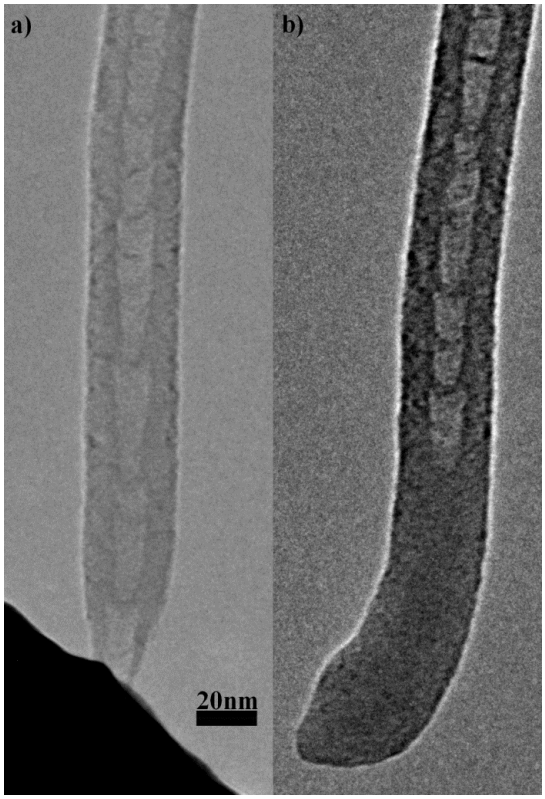

Figure 96. TEM micrographs of a N-CNT showing typical bamboo type structure (a). (b) shows structure after irradiation has become amorphous at the tip and has become rounded and larger in diameter.

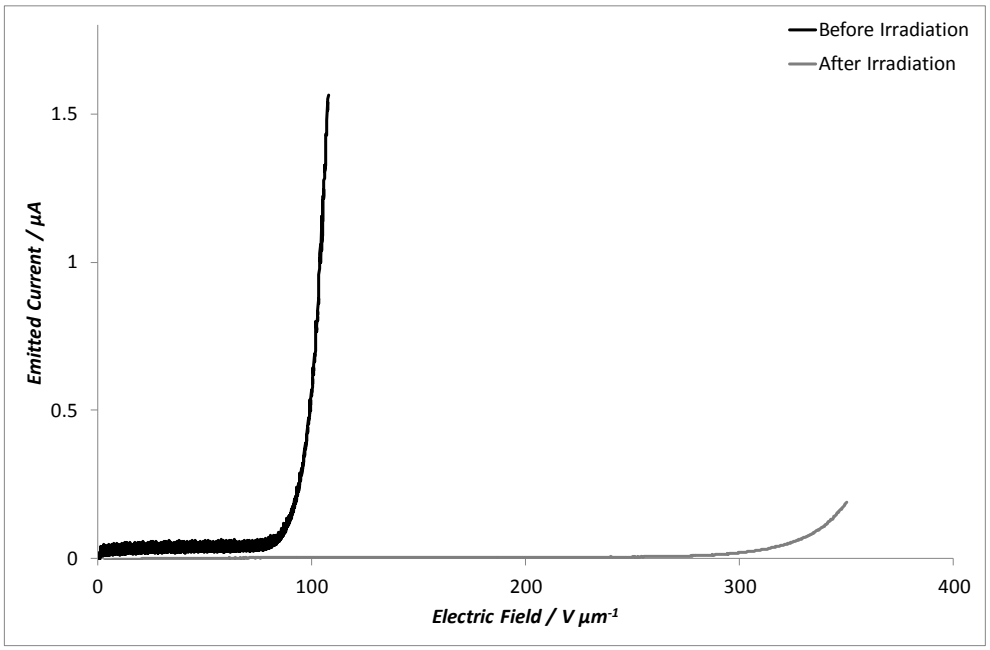

Figure 97. Graph showing a dramatic reduction in emitted current upon application of high intensity irradiation.

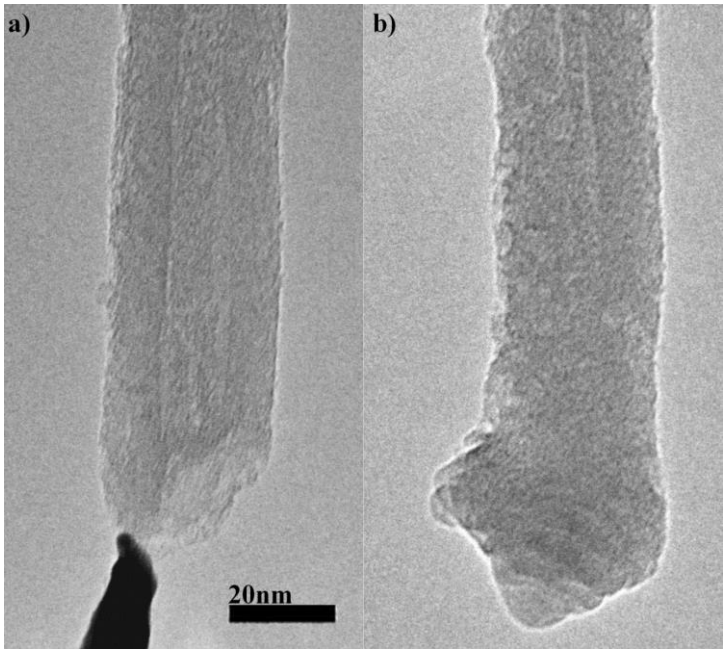

Figure 98. TEM micrograph of a typical undoped CNT before (a) and after (b) high intensity electron irradiation. The CNT tip has become amorphous and resulted in detrimental field emission properties.

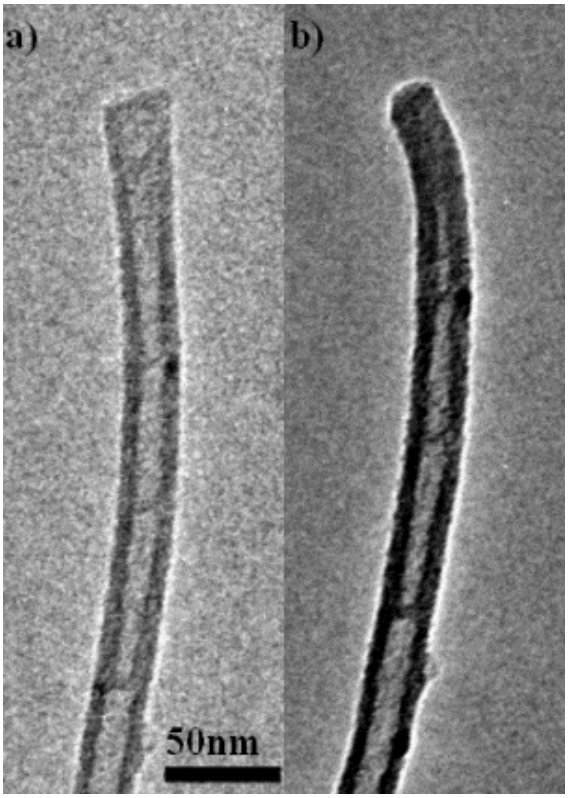

Figure 99. TEM micrograph of N-CNT before (a) and after (b) irradiation damage. The CNT tip has become sharper, and hence should have an increased field enhancement factor.

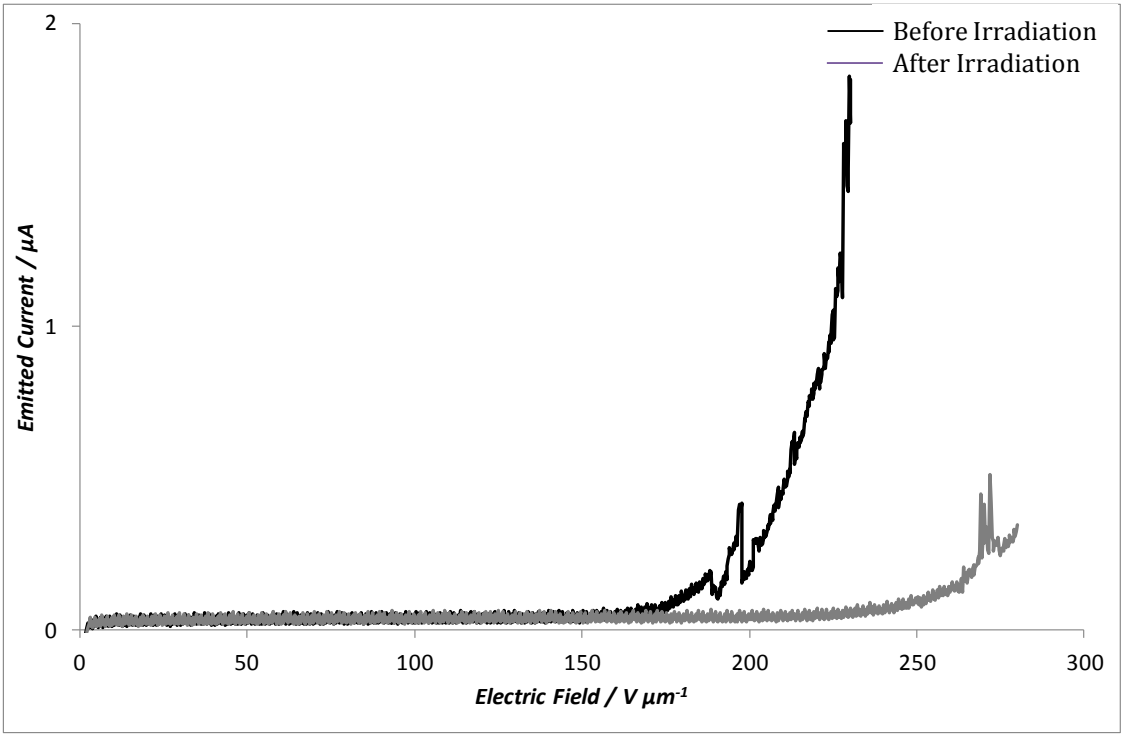

Figure 100. Graph of emitted current and E_{loc} for the N-CNT shown in Figure 99 before (black line) and after (grey line) irradiation damage.

4.5. Recrystallization of Amorphous Material at CNT Tips

Recrystallization of the damaged amorphous CNT tips was achieved by an extended period of emission. A voltage was applied to the damaged tips and held constant whilst the corresponding emission current was logged. EELS was acquired for a single N-CNT and the N-K edge reveals that it contained 1.7at% N. The EELS C-K edge reveals that there is graphitization prior to damage, indicated by the σ* peak (Figure 101). After damage, the graphitic structure at the tip is destroyed, and amorphous carbon has replaced it. This is confirmed by the decreased π^* peak, corresponding to a decrease in inter-plane graphitic bonding. The σ^* peak has been greatly reduced, which indicates that sp^2 bonding has become less prevalent.

A fixed voltage was maintained while the current was logged for almost six minutes (Figure 103). The emitted current starts at approximately 100 nA and fluctuates between this and 500 nA for a duration of 40 s. The current gradually increases to 5 μA over 170 s, after which there is a jump to 10 μA. Thereafter, the current fluctuation is greater, oscillating over a 4 μA range whilst reaching a peak of 20 μA, and then dropping to an oscillating level of about 8 μA.

EELS shows that some recrystallization has occurred confirmed by a peak in the σ^* region reappearing (Figure 101). This coincides with a decrease in E_{TO} of 1.1V nm^{-1} (from 5.7V nm^{-1} to 4.6V nm^{-1}) and a dramatic increase in maximum current emitted, from 0.1μA to 4.1μA (Figure 102).

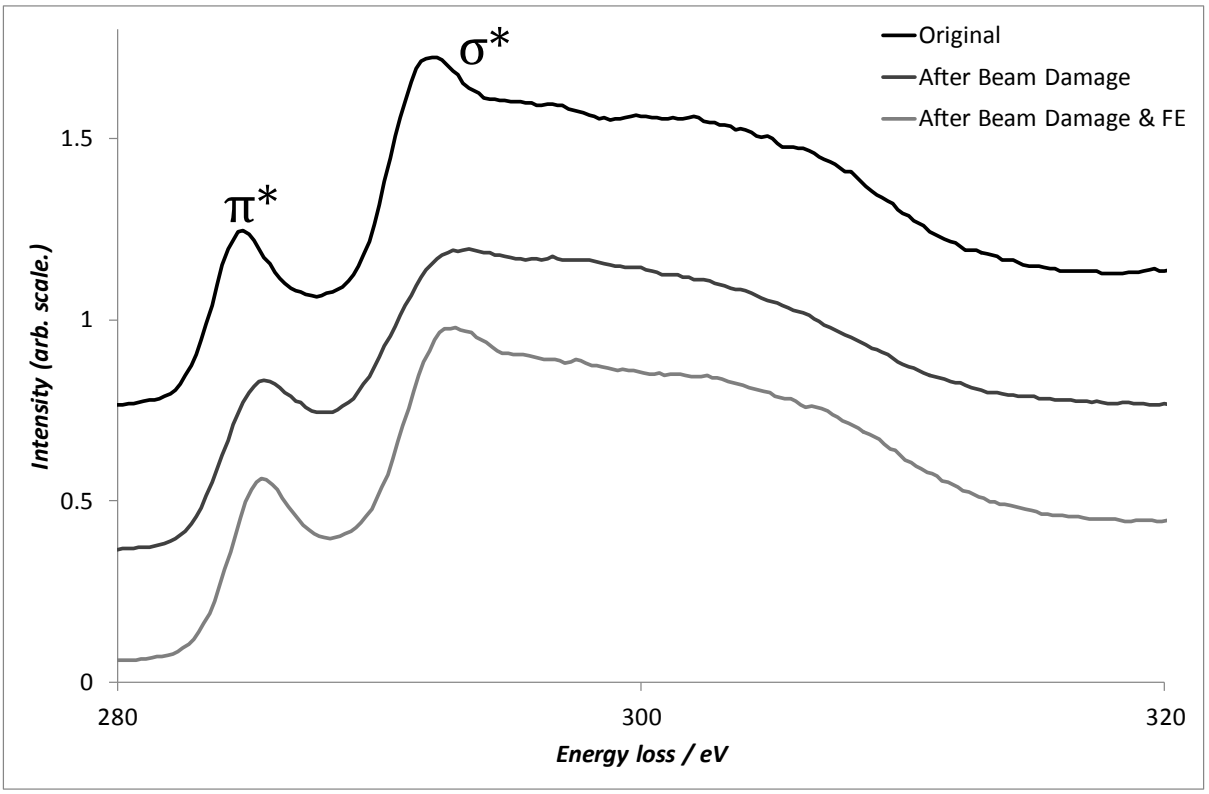

Figure 101. EELS spectra of a N-CNT. A peak is visible in the σ^* region, indicating that there is significant sp^2 type bonding [194]. After irradiation damage, the peak almost disappears, but reappears upon recrystallization.

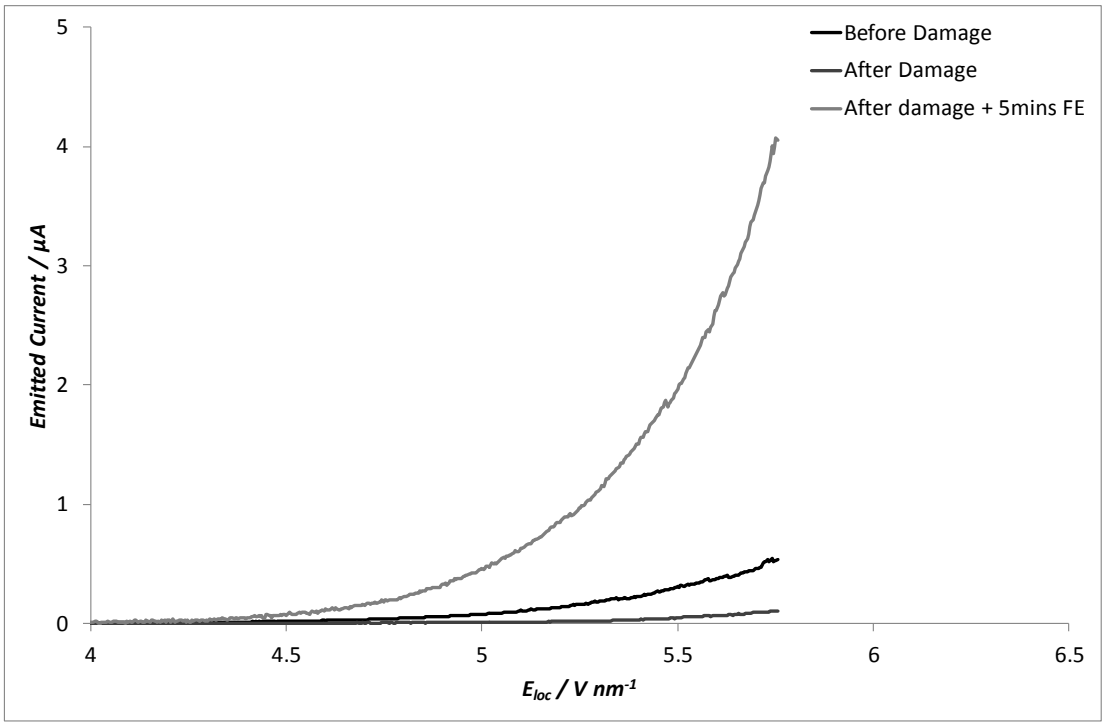

Figure 102. Graph showing the I-V characteristics of a N-CNT subjected to irradiation damage and recrystallization. E_{LTO} is depressed by the onset of irradiation damage, and is drastically improved when the tip is recrystallized.

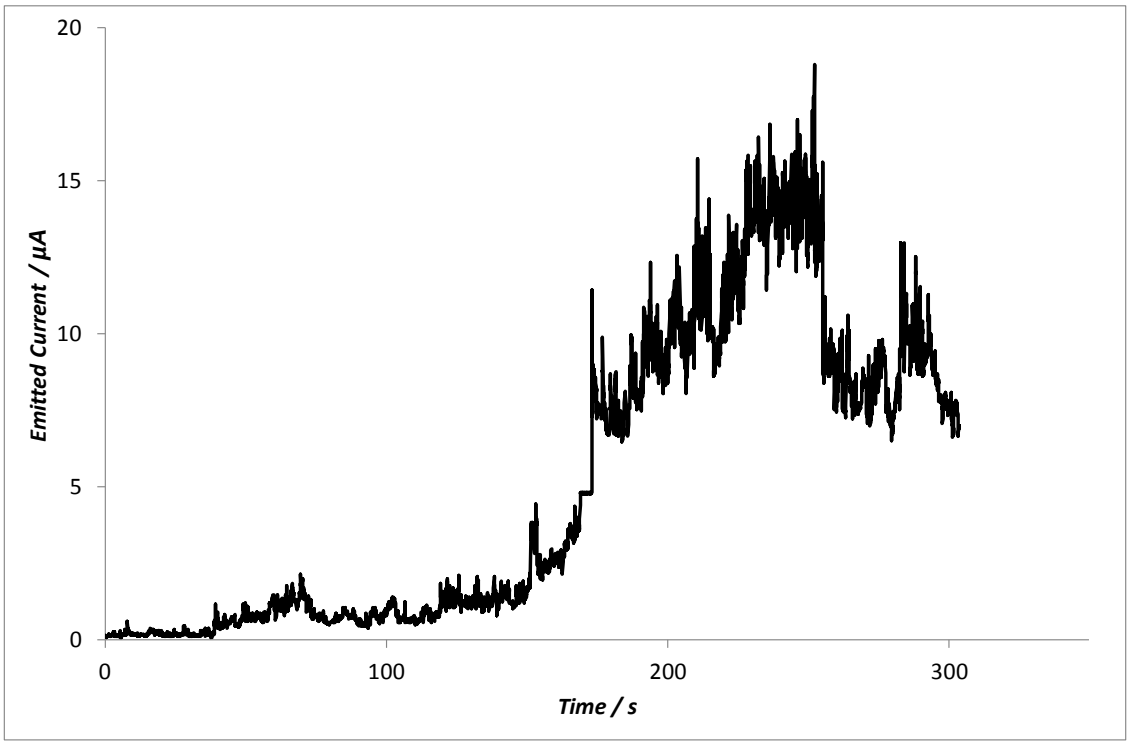

Figure 103. Graph showing current vs. time for experiment whereby voltage is held constant. There is a large current fluctuation caused by structural changes in the CNT.

Recrystallization also occurs in pure CNT samples that have been damaged. Figure 104 shows that the current from damaged undoped CNTs also increases with time suggesting recrystallization is occurring.

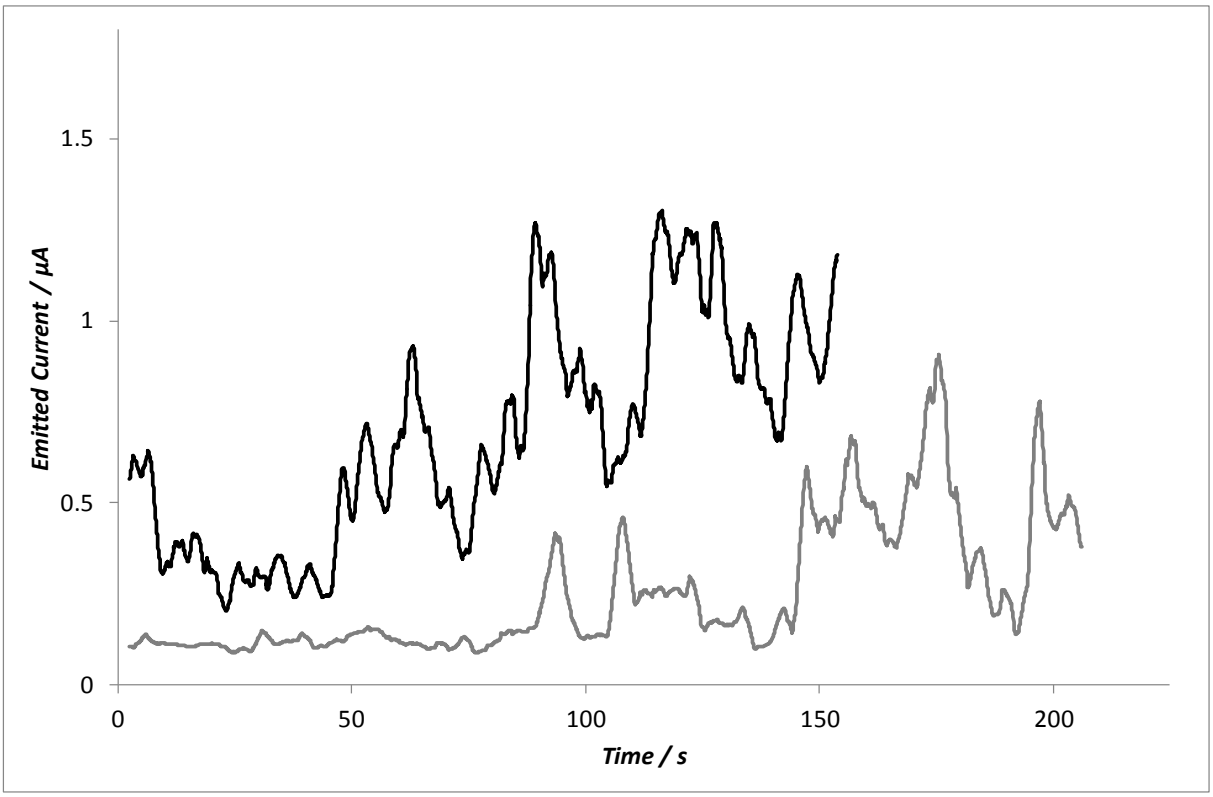

Figure 104. Graph showing current vs. time for two undoped CNTs that have damaged tips. The increase in current and current fluctuation suggests recrystallization has occurred.

4.6. Chapter Summary

The field emission properties of individual CNTs were investigated in an attempt to better understand the field emission properties of CNT films, specifically the role of defects and current stability.

Pure and N-doped CNTs were subjected to varying degrees of electron irradiation to investigate the effects of defects on the field emission properties of individual CNT emitters. Low energy electron irradiation, induced by EELS measurements, resulted in a slight decrease in the work function from 4.82 eV to 3.8 eV. High energy electron irradiation, caused by a convergent electron beam, caused a dramatic decrease in field emission properties, notably, an increase in E_{LTO} and a reduction, typically by an order of magnitude, in the maximum emitted current. This effect is so strong that even a decrease in CNT tip diameter, and increase in radius of curvature, caused by irradiation damage

resulted in degraded field emission properties. These large reductions in field emission properties can be attributed to an increase in the work function. This damage is recovered by allowing the damaged CNT to emit current for five minutes, decreasing the E_{LTO} by 1.1 V nm^{-1} (from 5.7 V nm^{-1} to 4.6 V nm^{-1}).

A possible explanation for these results is that low intensity irradiation only partially damages the graphitic sp^2 bonding found in CNTs. Incident electrons break a small number of C-C bonds so that there are several dangling bonds available. These dangling bonds produce additional states that could potentially sit near the Fermi Level, and hence lower the work function of the CNT tip. When a high intensity electron beam is focused on a CNT tip, there are more incident electrons per unit area, and hence more energy is transmitted. This results in high energy collisions so that atoms are ejected and most of the sp^2 bonds break. It is possible that diamond like bonding (*i.e.* sp^3 bonding) is created in the process as EELS reveals that sp^2 bonding has diminished. There are no delocalized electrons in sp^3 bonding as they are used in creating bonds. In fact, diamond is considered a wide band gap insulator and hence has the equivalent of a high work function. This explains why damage induced by high intensity electron irradiation can result in a significant increase in E_{LTO}. As current is passed through the CNT during extended emission, heating at the CNT tip results in recrystallization so that sp^2 bonding is restored and hence E_{LTO} has been lowered again.

4.7. Chapter Conclusions

The handful of CNTs studied in this chapter does not constitute a statistical study, but by comparing the same CNTs before and after various irradiation damage experiments, the significant variability between CNTs becomes less important because results are compared with the same CNT. This way the role of defects in the field emission properties of CNT films can be elucidated. The nature of the defect density at CNT tips is important

in determining the onset of field emission. It is likely that when the I_D/I_G ratio is high for a given CNT film (for example, 1 or over), it corresponds to many individual CNT emitters where the sp^2 bonding is severely disturbed. This would indicate that the CNT may be similar in terms of bonding to individual CNTs damaged using high intensity irradiation. Introducing a small number of defects, representing CNT films that have relatively low I_D/I_G values, the field emission properties can be enhanced due to the work function decreasing. This could potentially explain why Bonard *et al* [62] did not observe any benefit from using SWCNTs as field emitters, compared to MWCNTS, because the structure perhaps did not contain as many defects as would be the case for MWCNTs.

By recrystallising the damaged CNT tip after emitting current for several minutes, the structure is partially restored. This has implications for post treatment of CNT films deposited that have relatively high I_D/I_G ratios so that their field emission properties can be improved.

5. Field emission properties of CNT films on Kanthal wire

5.1 Introduction

This project is concerned with the fabrication and electrical testing of a high efficiency field emission lighting device using a CNT-Kanthal wire cathode. As discussed in Chapter 1, the field emission properties of emitters control the light emitting properties of the lamp (see page16). Chapter 3 was concerned with the fabrication of the composite cathode component; this chapter is concerned with the field emission properties of the "as-fabricated" cathode component consisting of CNT films on Kanthal wire.

The final lighting device will consist of a CNT film-Kanthal wire acting as the cathode and a phosphor tube acting as the anode in a diode arrangement. Kanthal was chosen as the substrate material as it facilitated the growth of a homogenous coverage of CNTs and a wide range of different film morphologies was achieved which may provide beneficial field emission properties. The Kanthal wire should be thinner than the diameter of the tube, so that a gap exists radially between the wire and the inside surface of the evacuated tube (Figure 105). Electrons are accelerated from the CNTs to the phosphor screen upon the application of a high voltage. The screen emits photons as the electrons interact with the phosphor to emit light. For the purposes of studying the field emission properties of the fabricated cathodes, the phosphor tube is replaced by an aluminium tube of the same dimensions so that the resistance of the anode can be ignored.

The electric field in-between, but far from both electrodes (F), is defined as $F = V/d$ where V is the applied voltage and d is the inter-electrode distance in a planar experimental setup. As already described in Chapter 1 (see page10), emitted current density is governed by the following equation:

$$J = \eta a \frac{(\beta F)^2}{\phi} \exp\left(-b \frac{\phi^{\frac{3}{2}}}{\beta F}\right) \qquad \textbf{Equation 6}$$

Where a, b and η are constants; a is defined as $e^3/8\pi h_p$ (where e is the elementary electronic charge and h_p is Plank's constant), b is defined as $(8\pi/3)(2m_e)^{1/2}/eh_p$ where m_e is the electron mass and η is the geometrical efficiency of electron emission.

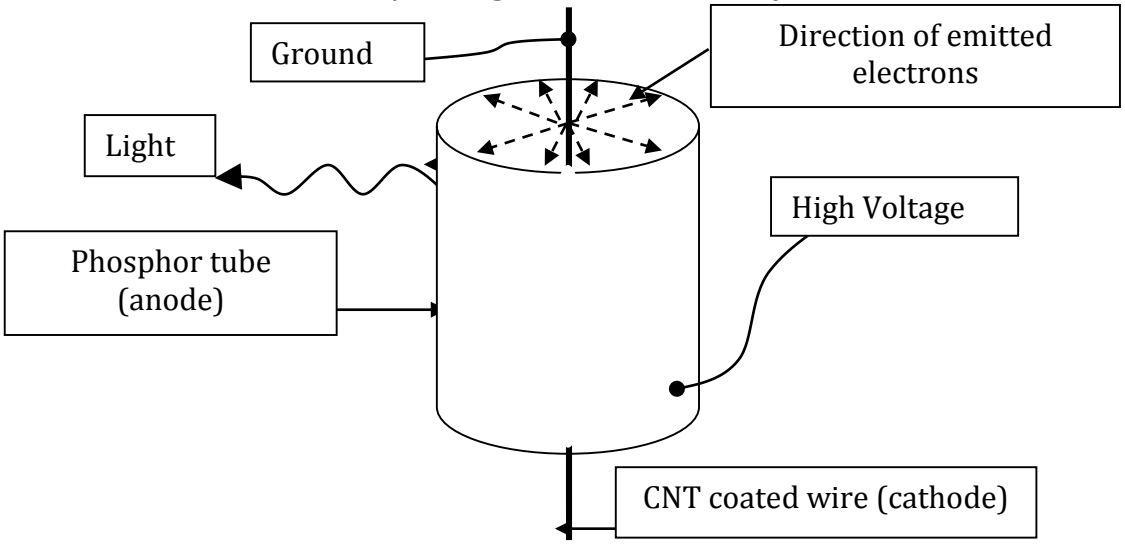

Figure 105. Schematic showing the experimental setup of a field emission based lamp used in this study.

Real emitters experience a decay of current over a prolonged period of emission time and this current decay is defined as the reduction of current observed over a fixed period of time at a fixed electric field. Normally, the starting current is chosen to be the same value when comparing samples. This is an important parameter in real devices that need to function for long periods of time.

Most groups working on the application of CNT field emitters have been working on CNT films on flat substrates and over large areas [15, 67, 73, 104] as there is a high demand for highly efficient displays. The majority of work has concentrated on a two stage *ex-situ* technique of using a mixture of CNTs and an organic binder which is printed onto a flat substrate [26, 76, 195, 196]. "As printed" films tend to have CNTs that lie parallel to the substrate surface, making them non ideal for field emission applications. Sticky tape or a brushing technique can be used to make the CNTs protrude from the CNT film that

increases the probability of a CNT acting as an emitter. Indeed Samsung have created a display using this technique [197]. Other ex-situ techniques involve CNT-polymer composites where the field emission properties are directly related to the volume fraction of CNTs present in the polymer [198]. As the volume fraction is increased above 1%, E_{TO} gradually decreases and is minimum at 15% volume fraction, presumably because as more CNTs are introduced in to the polymer, more protruding CNTs are present which contribute to the lower E_{TO} value observed.

Lithographic techniques have also been used to create patterns of CNT carpets that could potentially be used in microelectronic applications. Firstly, the catalyst is dissolved in a solvent and this 'ink' is patterned on to silicon substrate and then growth of CNTs is achieved using CVD of acetylene [199]. Varying the concentration of catalyst in the ink results in CNT films of different CNT density and it was found that a medium density film achieved the lowest E_{TO} due to the presence of protruding CNTs.

Work has also been done on the field emission properties of CNT films on wire substrates for application in lamps [20, 138, 162, 163]. It is more difficult to pattern on these substrates due to their curved geometries. Lamps which match luminosities of those available on the market have however been produced [163] using a simple CVD technique.

In this chapter the field emission properties of various CNT morphologies, as defined in Chapter 3, will be characterised with respect to E_{TO} and current decay, and this knowledge will be used to create better field emission devices.

5.1.1. Simulations of Tower Geometries on Field Emission Properties

COMSOL was used to model the maximum local electric field at the top surface of various tower configurations. COMSOL is a finite element analysis (FEA) method of solving

partial differential equations in a given mesh. The electrostatics module was implemented in these calculations to determine the electric field in the area in-between electrodes and around geometries by applying a mesh structure over the outline of the geometry to be investigated. Each element is solved using Maxwell's Equations to determine the electric field strength at that particular point in space.

5.2. Experimental Methodology

A cylindrical setup was used for field emission experiments in this study because the field enhancement factor of the system will be increased due to the inherent field enhancement factor of the cylindrical wire substrate; and other benefits as discussed in Chapter 3 (page 63). The average electric field near the cathode surface in this case is defined as $F = V/(r_s * \mathrm{Ln}(r_a/r_s))$ where r_s is the radius of the cathode (125 μm – 650 μm) and r_a is the radius of the anode (10,000 μm) (Figure 106). As the cathode consists of a film of CNTs on a Kanthal wire, r_s is defined as the sum of the radius of the wire (r_w = 125 μm) and the average height of the CNT film (h_{cnt} upto 525 μm) so that $r_s = r_w + h_{cnt}$. As CNTs vary between hundreds of nanometres and hundreds of microns in this study, r_s will always be significantly smaller than r_a (~ 2 orders of magnitude). This means that it can be assumed that the average electric field (at a given voltage) near the CNTs is the same with all samples.

For the purposes of simplifying the current density calculation, it is assumed that the current is emitted homogenously across the surface of the cathode. This could be a source of error as the surface of the sample may not be homogenous and would therefore not produce a homogenous current density. For the purposes of simplicity, the surface of the

composite will be assumed to be a perfect cylinder and its area calculated using $A_{surface}$ = $2\pi r_s.L_s$ where L_s is the sample length.

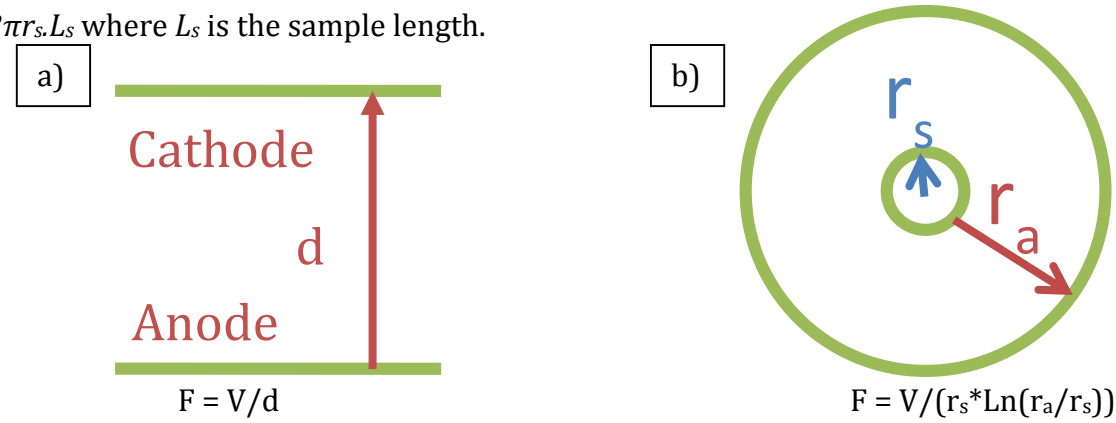

Figure 106. Schematics showing the calculation of the average electric field in a planar setup (a) and the average electric field at the surface of the cathode in a cylindrical setup (b).

5.2.1. Preliminary Experiments

Field emission experiments were undertaken to produce current-voltage (I-V) curves which in turn were converted to current density-electric field (J-E) curves by using the equations described in Section 5.2. These J-E curves were used to calculate $E_{TO,}$ which is the electric field at the cathode surface required to extract an emission current of 10 $\mu A/cm^2$. Preliminary experiments investigated what experimental conditions should be used to obtain reproducible I-V curves. An undoped CNT sample, produced using a toluene precursor, was placed in the UHV chamber for field emission testing and the pressure was ~ 10^{-6} mbar at the beginning of the experiment. A turbo pump, backed up by a rotary pump, was used to reach this pressure. The voltage was stepped up 100 V every ten seconds and the emitted current recorded at each voltage step. A second reading was measured at the same voltage after the ten seconds had lapsed. For each experiment two sets of data points were plotted; the first being the initial current reading (The Upper Limit) for a given voltage and the second the reading recorded 10 seconds later at the same voltage (The Lower Limit) (Figure 107).

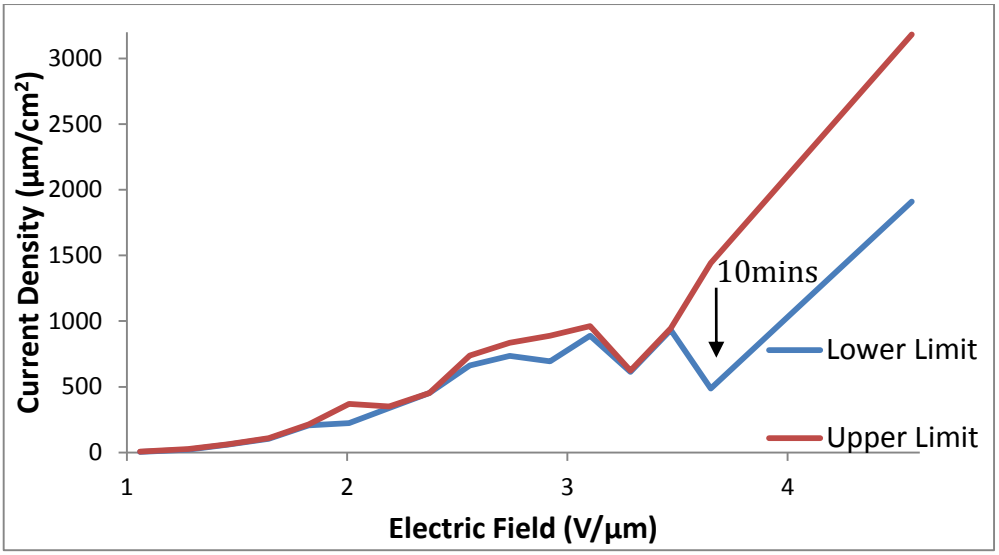

Figure 107. Graph showing the upper and lower limits of current density when the voltage is increased in 100V steps. The arrow represents the current degradation after the sample is held at that particular voltage for 10 minutes. Equations from Section 5.2 were used to calculate current density and electric field.

In this experiment there is no degradation of emitted current up to 1,100V (2.01V/µm), merely small fluctuations. At 1,700V (3.10 V/µm), the pressure started to increase to 3 x10^{-6} mbar, and there was a further increase to 1 x10^{-5} mbar at 3,000V (5.48 V/µm). When a current of 453µA was reached at 2,000V (3.65 V/µm), the voltage was kept at this level for 10 minutes and the current degraded to 153 µA over this period of time (shown in the graph as a fall in current from the upper limit to lower limit at ~3.65 V/µm). After this point, the rate of degradation increased compared to lower fields and the normal protocol of a second data point taken 10 seconds after each initial reading, commenced.

Three samples were tested in this manner, and the results are shown in Figure 108. All curves have a characteristic shape, where the curve becomes less steep and plateaus as the voltage is increased. This is not a physical characteristic of field emission, instead it is because of the relatively long delays between acquiring data points which produces a time-dependent degradation of current (probably gas discharge or ion bombardment). At low voltages there is no degradation of current, and emission obeys the F-N equation, confirmed by linearity in the F-N plots (Figure 109). The gradient of the plots is related

to the work function and field enhancement factor of those respective films. At a threshold electric field, which seems to be different for each sample, current degradation begins (from around 3 mA/cm^2 for all samples) and the apparent increase in current with voltage slows down (Figure 108). At a second threshold electric field, the degradation in current equals the increase in current and the curve plateaus at a current density between 4 mA/cm^2 and 6 mA/cm^2. This is accompanied by an increase in pressure, which is probably due to the evaporation of material from CNT tips when high current flows during field emission [200].

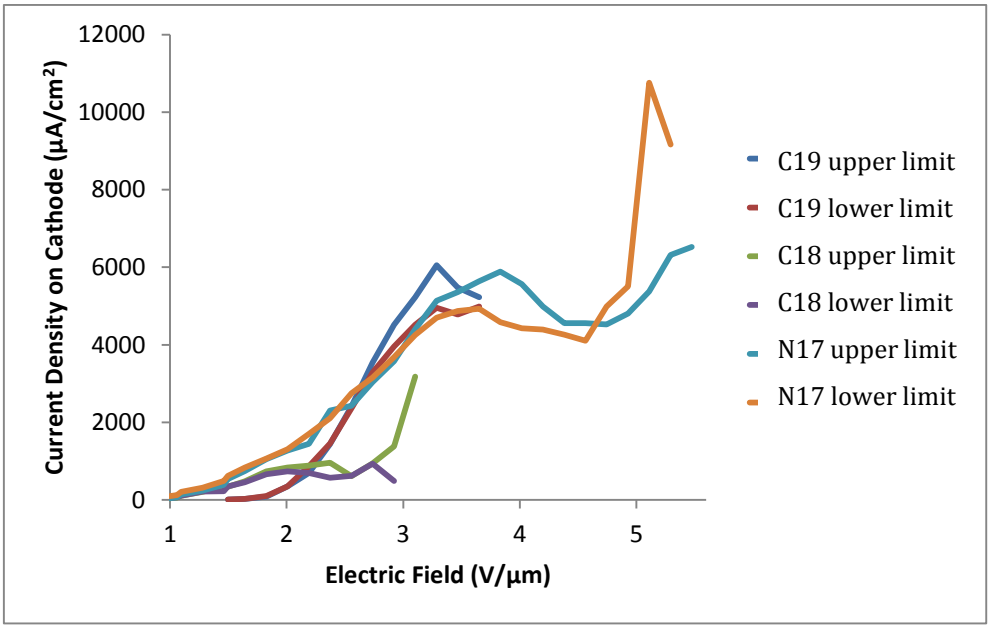

Figure 108. Graph showing several samples tested in preliminary experiments. Note the plateau in the current density values above 4mA/cm^2.

In sample N17, the voltage was increased beyond the plateau region (Figure 108). The current increases exponentially with virtually no increase in voltage in this region. The experiment was stopped once this occurred to prevent any potential damage to the equipment.

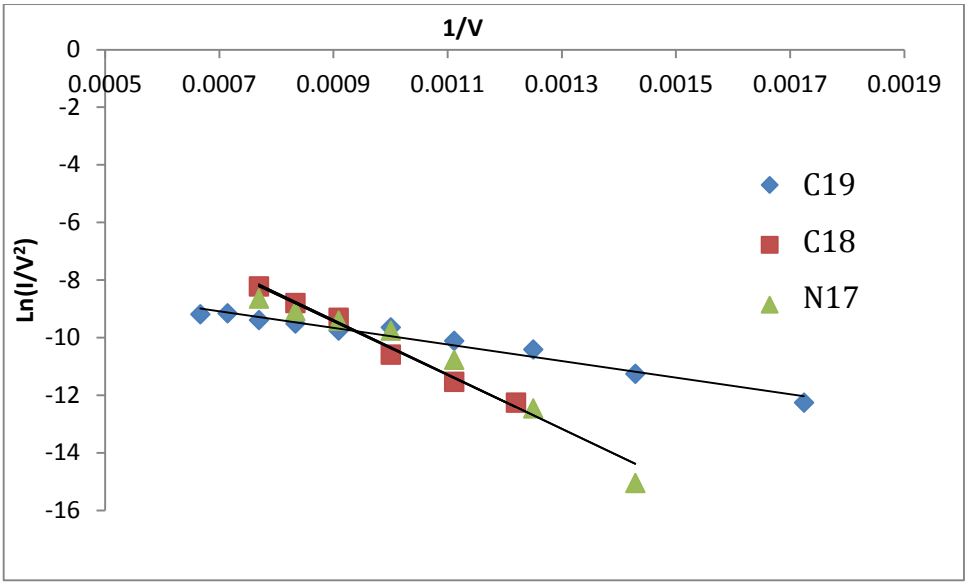

Figure 109. F-N Plots of the initial rise in current from the data shown in Figure 108 showing linearity in preliminary experiments which indicates that the samples follow the F-N equation for field emission. The gradient of the plots is related to the work function and field enhancement factor of those respective films.

Figure 110a and Figure 110b below show SEM micrographs of sample N17 before and after the experiment respectively. After the experiment there are craters that contain re-solidified metal on the surface of the Kanthal wire where CNT bundles once stood (Figure 110c). Thermal runaway has occurred where local Joule heating from the contact resistance between the CNT bundle and the Kanthal wire surface causes the underlying metal to heat and melt, destroying the bundle [201] and leaving a crater of re-solidified metal behind.

After these preliminary experiments, a data logger (National Instruments USB-9215A) was added so that the voltage could be recorded typically a thousand times a second. This means that the voltage could be increased and decreased quickly to avoid the onset of any time-dependent current degradation during an I-V acquisition. The pressure was monitored in these subsequent experiments to ensure this was the case.

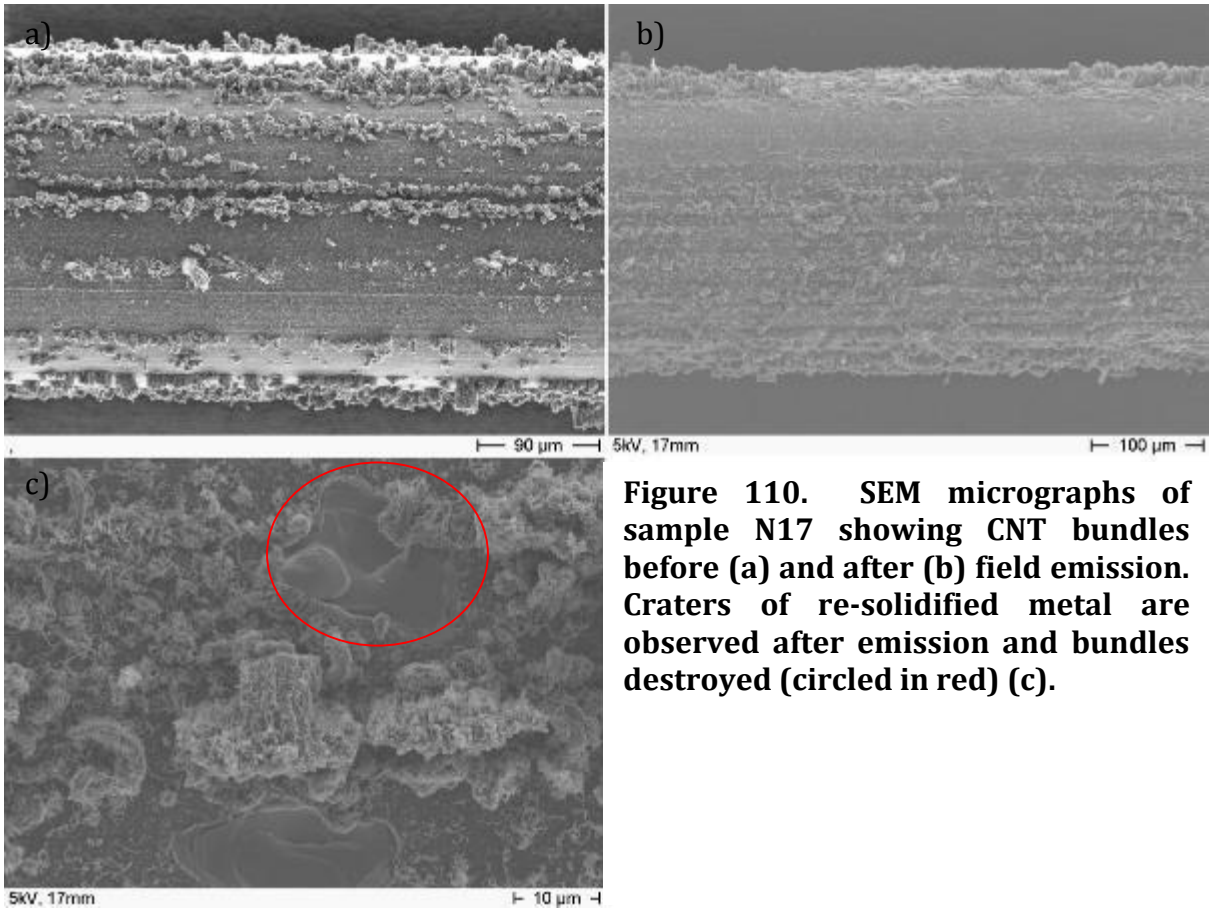

Figure 110. SEM micrographs of sample N17 showing CNT bundles before (a) and after (b) field emission. Craters of re-solidified metal are observed after emission and bundles destroyed (circled in red) (c).

The maximum allowed current was set to 1mA so that the heating of the sample is kept to a minimum; pressure was kept constant and no damage occurred to the acquisition equipment. Five runs of I-V data were obtained per sample so that an average E_{TO} value could be obtained.

5.3. Field emission of undoped and doped CNT films on Kanthal wire substrates

5.3.1. Effects of various morphologies on field emission properties

As field emission properties are linked to the geometry of the emitters and only indirectly to the processing parameters used to make that geometry, field emission properties of various morphologies were studied, rather than simply using a matrix of processing parameters. The previous chapter demonstrated that manipulation of the processing parameters created an array of differing CNT morphologies, whose different geometries could affect β.

5.3.1.1. Thin films of CNTs

Firstly, smooth samples were investigated such that as close a match to an ideal cylinder is achieved. The idea being that as other structures and morphologies are investigated, this deviates more and more from a smooth cylinder and the field enhancement factor increases. Table 6 summarises the growth parameters used for this initial study.

Firstly, two samples were considered which satisfy the morphological requirements for this study *i.e.* they approximate flat surfaces. The first (N22) was grown using a pure benzylamine precursor, whilst the second (N25) was grown using a 1% benzylamine precursor (Table 6). The reduced concentration of nitrogen-containing precursor should produce CNTs with lower N content. This was to compare samples with different nitrogen content and hence varying levels of defect density. The introduction of defects is due to the incorporation of nitrogen into the CNT structure [202] and the I_D/I_G ratio values given in Table 6 shows that lower defect concentration is achieved when using a 1% benzylamine solution.

Figure 111 shows that both morphologies are similar in nature and comprise entangled CNTs. N25 has a lower E_{TO} value than N22 (2.09V/μm compared to 2.75V/μm) and this cannot be attributed to the presence of random individual emitters that cause "hot spots" [67, 145], as the J-E curve does not show significant instability (Figure 112). Repeated I-V acquisition runs show that the E_{TO} of N25 fluctuates by less than 3%, indicating that individual CNTs are not responsible for the improved field emission properties. If individual CNTs were responsible for the improved field emission properties, then as each emitter is destroyed due to the current being too high, a new emitter (with a different E_{TO} value) becomes active and this manifests as instability in the I-V curve.

Sample ID	Precursor	Cat. %	T (°C)	t (mins)	Carrier gas flow (Ar:H_2 SLM)	I_D/I_G	E_{TO} (V/μm)
N22	Benzylamine	1	900	2	1:0.2	1.00	2.75
N25	1% Benzylamine 99% toluene	5	900	2	1:0.2	0.54	2.09
C22	Toluene	1	900	10	1:0.2	0.73	1.74
C25	Toluene	1	900	30	1:0.2	0.70	1.80
AC4	50sccm acetylene	-	650	30	0.2:0.2	1.04	3.00
N38b	1% Benzylamine 99% toluene	5	900	20	1:0.2	1.01	1.09

Table 6. A table summarising the processing parameters used to grow thin CNT films on Kanthal wire for field emission testing.

Samples N22 and N25 represent the shortest CNTs studied in this set (<10μm). N22 contains CNTs that are shorter than N25 and hence the possibility of entanglement is reduced. However, the CNTs appear more 'curled' than for N25 and hence fewer tips per unit area will be exposed and aligned perpendicular to the surface (Figure 111b). The shortness of the CNTs reduces the aspect ratio, and hence the β values for the emitters, which should result in a smaller emission current.

Furthermore, the I_D/I_G ratio of N22 is double that of N25, implying a higher defect density for the carbonaceous material found in N22. Amorphous carbon is sometimes found on the outside of CNTs, in the form of small particles. The SEM image in Figure 111b (N22) shows little amorphous carbon coating the CNTs in comparison to Figure 111d (N25). One would expect to see more amorphous carbon in sample N22 because it has a higher

I_D/I_G ratio. Most of the defects in N22 could therefore be in the CNT structure itself, whereas most of the defects in N25 could be found in the amorphous carbon coating. This hypothesis would also explain why sample N25 has a lower E_{TO} than N22, as it is the CNT tips themselves that are more likely to participate in the field emission process. It is possibly a combination of lower I_D/I_G ratio and a higher aspect ratio of the CNTs on N25 compared to N22 that is the cause of the improved field emission properties.

5.3.1.2. Growth of separated CNTs using a gas CVD technique

It was shown that individually separated CNTs could be grown if a gas CVD technique is used (see Section 3.2, page 66) (Figure 113). This is potentially beneficial for field emission, as the full field enhancement factor of individual CNTs could contribute to field emission. However, as shown in Table 5, sample AC4 had an E_{TO} value of 3.00V/μm, which is higher than any other sample. The adhesion between the catalyst particles and the wire substrate may be weak, due to the *ex situ* method of depositing the particles. This would not result in a higher E_{TO} value however, as at turn on the current is very small (*i.e.* high resistance). As the current increases, the voltage drop across the contact would increase but this would translate to a large electric field as the contact is of the order of a nanometre or less., hence it would breakdown and conduct. Clearly contact resistance would not have an effect on the E_{TO} value of the sample. AC4 has the highest ID/IG ratio (Table 6) which indicates it is very defective and may hinder field emission.

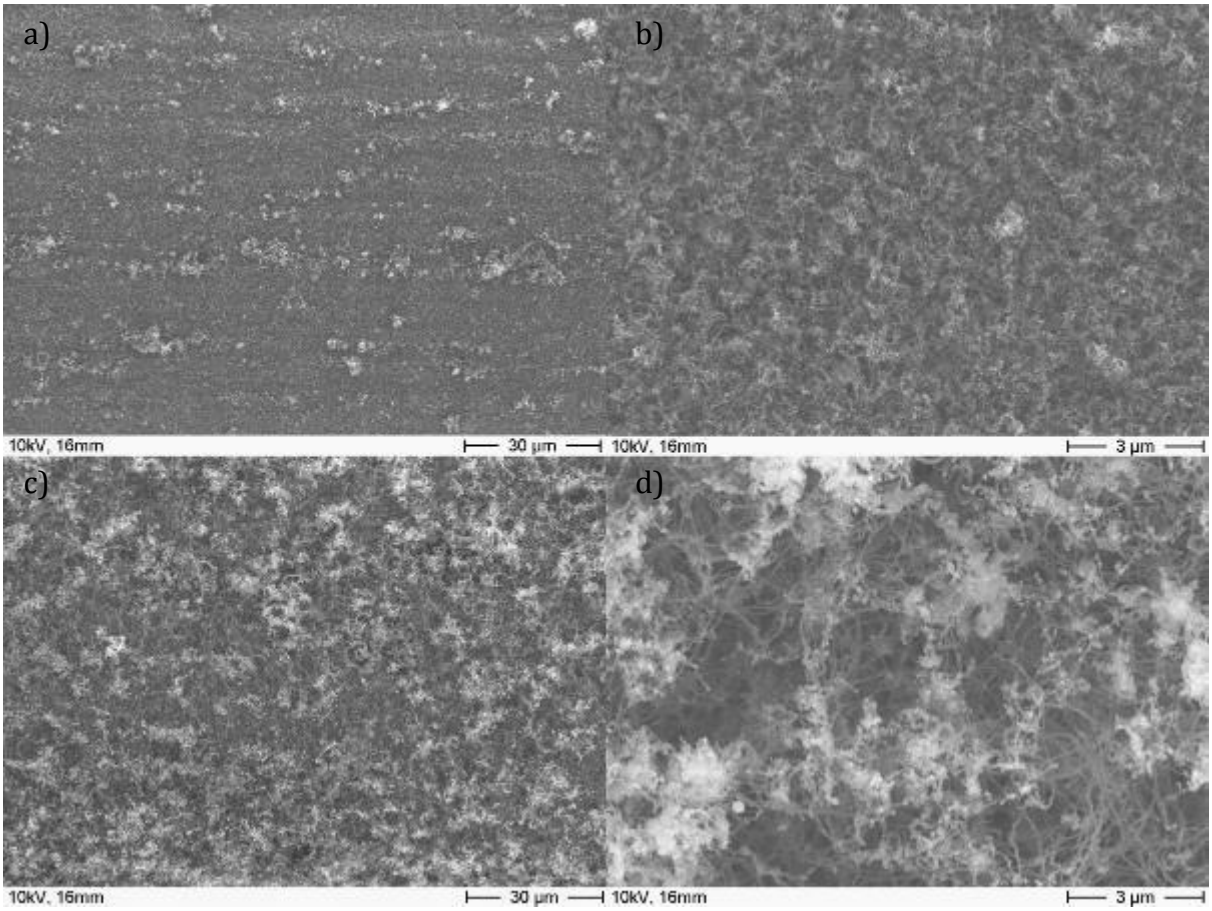

Figure 111. SEM micrographs of samples N22 (a and b) and N25 (c and d).

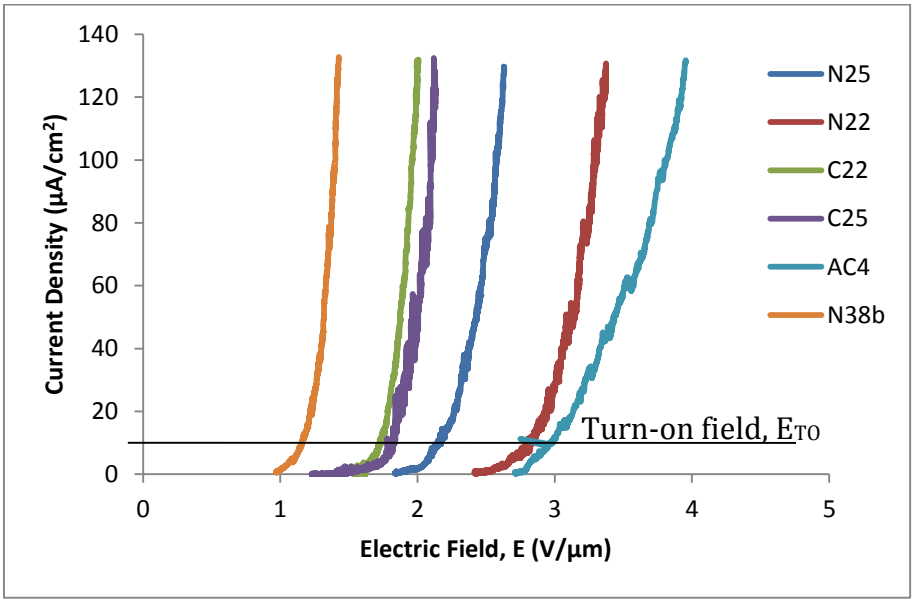

Figure 112. J-E curve of N25, N22, C22, C25, AC4 and N38b showing stability in emission.

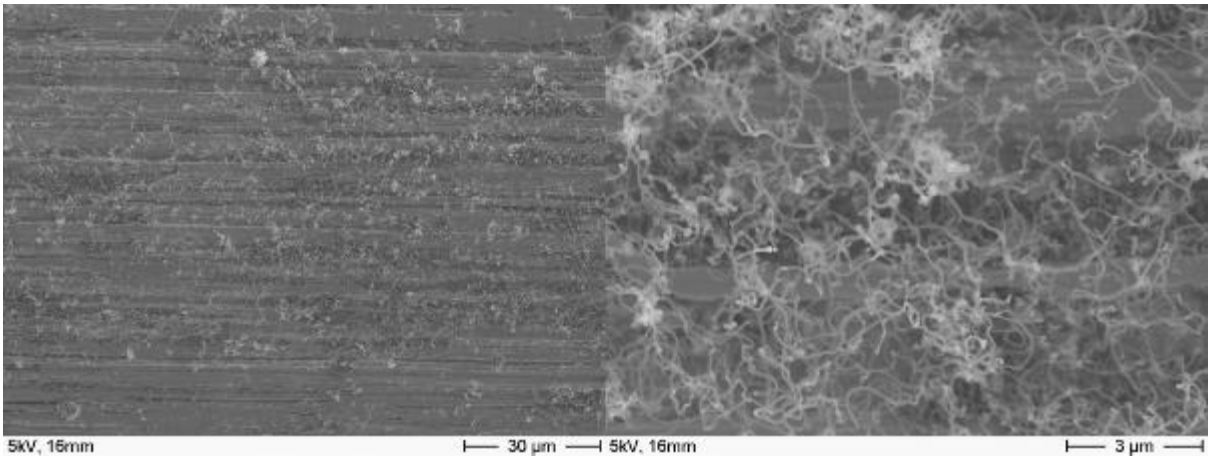

Figure 113. SEM micrographs of separated CNTs grown using a gas-CVD technique. Low magnification reveals the bare substrate underneath, indicating low density of CNTs (a).

5.3.1.3. Separated protruding CNTs using a "pull off" technique

Whilst separated CNTs were achieved using a gas CVD technique, they were not aligned perpendicular to the substrate surface and had poor contact resistance. To investigate the role of protruding CNTs on the field emission properties of CNT films, a sample of protruding CNTs was prepared. This was achieved by preparing a ridge sample of CNTs on Kanthal wire and subsequently removing these ridges by using a small spatula and scraping this along the length of the wire. As the ridges are pulled away, the CNTs on the Kanthal wire surface are pulled into a protruding position (Figure 114). Figure 114c shows the sparse arrangement of these protruding CNTs (sample N38b).

The E_{TO} is the lowest so far, with a value of 1.09V μm^{-1} (Table 6). There are far more protruding CNTs on the surface of the Kanthal wire compared to sample AC4, N22 and N25. This has resulted in the decreased E_{TO} presumably because there is less screening, as CNTs are more separated.

5.3.1.4. CNT towers on Kanthal wire

In some samples prepared with benzylamine, towers of bundles (as defined in Section 3.1.1., page 59) of CNTs are visible. These towers stand perpendicular to the surface of

the Kanthal wire and sit upon an entangled mat of CNTs (Figure 115). A summary of the processing properties used for this investigation can be found in Table 7.

The first sample (N31) was grown using pure benzylamine with 1% ferrocene at a growth temperature of 900 °C for 2 minutes with carrier gas Ar:H_2 (1:1 SLM) and its E_{TO} value was 2.49 V/μm, which is lower than N22 but not as low as N25 (Table 6 and Table 7). The towers are aligned perpendicular to the substrate surface and the I_D/I_G ratio is ~1, which is higher than that of samples with lower E_{TO} values.

Previous work in the group reveals that samples produced using a 5% benzylamine (95% toluene) precursor contain an average nitrogen content of 0.28% and using pure benzylamine, an average N content of 2.2% [32]. Sample N25 which is grown using 1% benzylamine is therefore likely to have an N content of below 0.28% and sample N28 of approximately 2.2%.

Sample N32 has taller which was achieved by mixing no hydrogen with the carrier gas during the growth experiment. The E_{TO} value of 1.81 V/μm is lower than that for N25.

Samples N31, N48, N47a and N47b have similar average tower heights (Figure 116a, Figure 116c, Figure 116d, and Figure 116e respectively) and also similar E_{TO} values. Sample N23 has significantly shorter towers (Figure 116g) and has a significantly higher E_{TO} value.

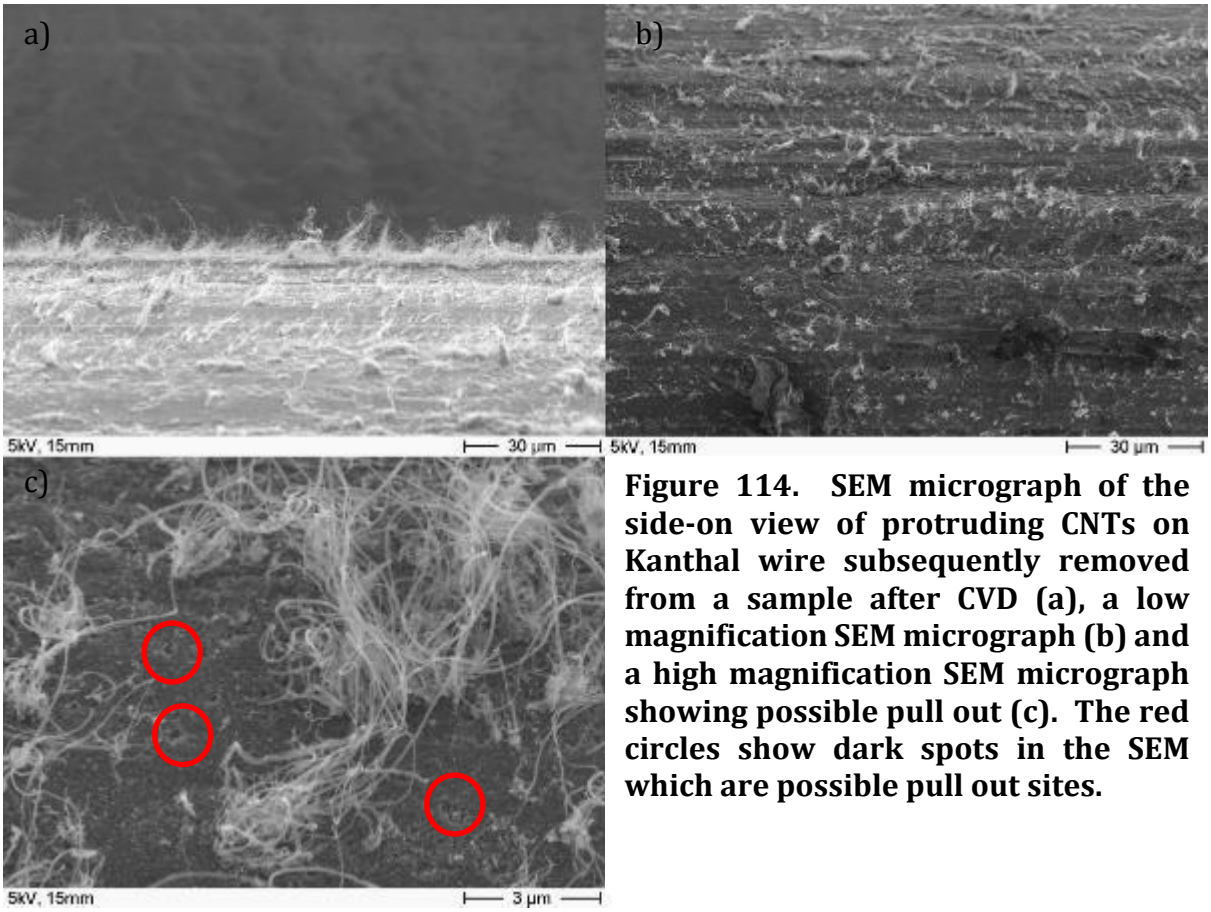

Figure 114. SEM micrograph of the side-on view of protruding CNTs on Kanthal wire subsequently removed from a sample after CVD (a), a low magnification SEM micrograph (b) and a high magnification SEM micrograph showing possible pull out (c). The red circles show dark spots in the SEM which are possible pull out sites.

Sample ID	Precursor	Cat. %	T (°C)	t (mins)	Carrier gas flow (Ar:H_2 SLM)	I_D/I_G	E_{TO} (V/µm)
N31	Benzylamine	1	900	2	1:1	1.01	2.49
N32	Benzylamine	1	900	2	1:0	0.99	1.81
N48	Benzylamine	1	900	2	1:1	1.11	2.88
N47a	Benzylamine	1	900	2	1:0.2	1.11	2.62
N47b	Benzylamine	1	900	2	1:0.2	1.11	2.62
N35	1% Benzylamine	1	900	10	1:0.2	0.62	1.91
N23	Benzylamine	1	900	2	1:0.2	1.19	3.69

Table 7. Summary of the processing parameters used to grow CNT towers on Kanthal.

Figure 118 below shows a simple 'tower' like geometry and the corresponding electric field intensity around such a structure calculated using COMSOL. Three separate electric field intensity regimes are observed. Firstly, the area around the base of the tower experiences shielding effects from the tower itself (marker 1 in Figure 118). Secondly the top surface of the tower will experience a similar field as the substrate, far from the tower. This is because the local electric field at the top surface away from the corners is governed simply by $E_{loc} = V/(d-h)$ where h is the height of the tower. As h is several orders of magnitude smaller than d, the electric field will change by ~0.1 V/μm at most due to the height of the towers. Thirdly the corners of the top surface of the towers will experience the highest localised electric fields due to the geometry of corners (marker 3 in Figure 118).

Figure 117 shows the inverse linear relationship between average tower height in a given sample and E_{TO} value. Field enhancement must be from CNTs protruding from the corners of the towers as β value is the product of the beta value of the tower corners, and the β value of the CNTs found there.

Clearly the results presented in Figure 117 are not due to the difference in the average tower height as that will only show a change of ~0.1 V/μm. The tower height range also has an inverse relationship to E_{TO}. The change in tower height range was simulated using COMSOL. A planar diode arrangement was assumed and a cathode-anode displacement of 550 μm was used (this is the separation needed to produce an equivalent planar electric field intensity, as that seen in the real cylindrical setup).

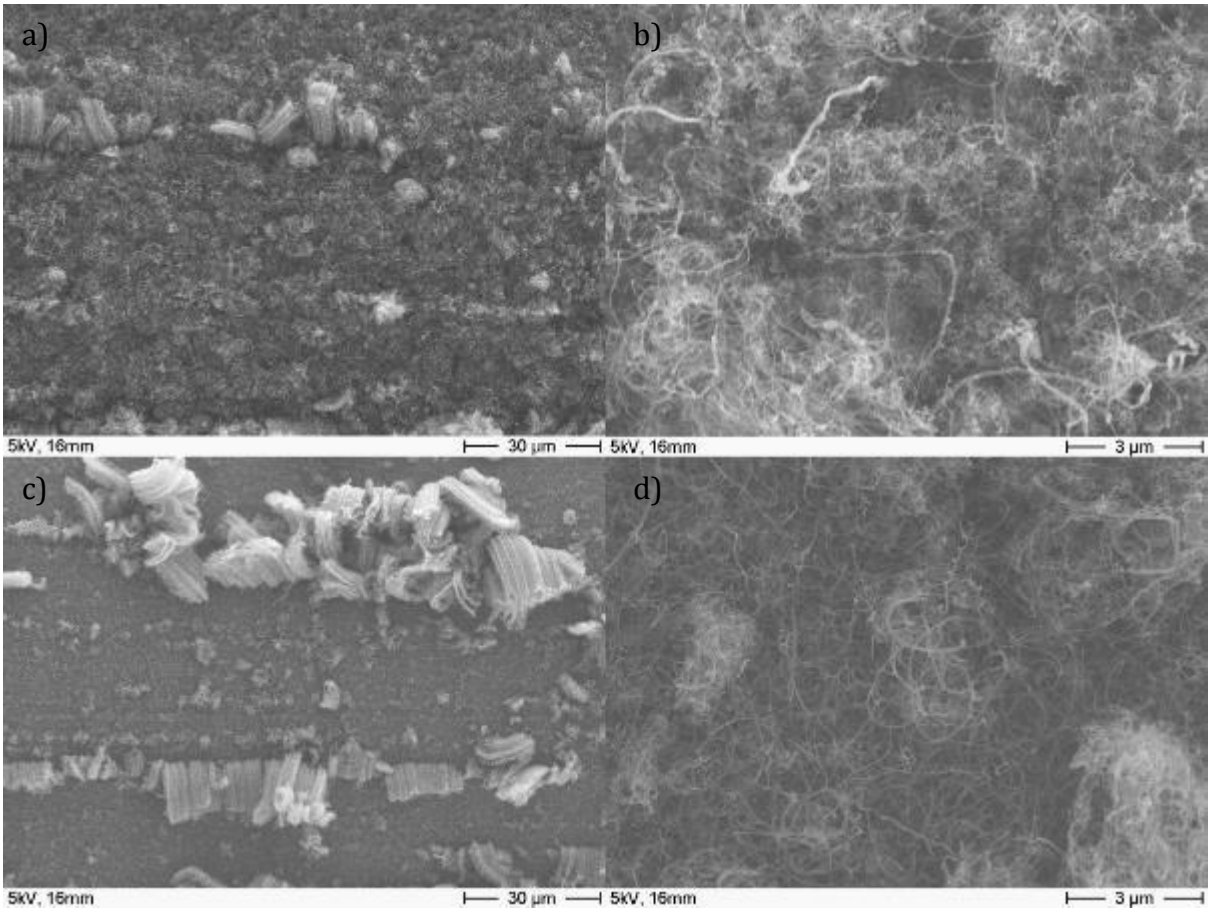

Figure 115. SEM micrograph of N31 showing towers of CNTs (a) that sit on entangled CNTs (b). N32 has taller towers compared to N31 (c) and also sit upon entangled CNTs (d).

Sample N23 was simulated by using a value for L of 3µm and an inter-tower spacing of 2L. It was found that the local electric field achieves a maximum value of ~3.8V/µm near the tower corners due to local edge effects, when an external voltage of 1,000V is applied. This value is reduced dramatically to ~2 V/µm when the inter-tower spacing is significantly less than 2L. As samples N31, N48, N47a and N47b are similar in terms of average tower height, a value for L of 10 µm with an inter-tower spacing of 2L was used to represent these samples. A maximum value of ~4 V/µm at 1,000 V was achieved at the corners of the towers which is only slightly higher than that for sample N23. When the inter-tower spacing was reduced to significantly less than 2L and the range in the height of towers adjusted to that of the real sample, the maximum electric field intensity is ~4.2

V/μm for the same applied voltage. This is double the value for sample N23 at a similar spacing, and this is reflected in Figure 117 where measured data shows that sample N23 has an E_{TO} value almost double that of samples N31, N48, N47a and N47b.

If the range of height in the towers is very small (*i.e.* they are all the same height), then closely spaced towers will shield each other from the external electric field and the overall field enhancement will be reduced compared to a single isolated tower of the same height. If the range is very large and the inter-tower spacing very small, we would get taller towers next to shorter towers. This setup can be thought of as equivalent to larger spacing between taller towers. This was confirmed by simulation which showed a significant difference in the E_{TO} values found at the corners of the towers in these scenarios. Therefore it is feasible that the reduction in E_{TO} value seen in Figure 117 is mainly due to the increase in the *range* of tower heights, not the *average* tower height.

Sample N38b achieved an E_{TO} value of 1.09 V/μm, which is lower than any tower sample. This is because CNTs are vertically aligned, and are separated from each other. Clearly this scenario is the closest yet to the optimum array structure described in Chapter 1 (see page10). There is room for improvement however, as the CNTs are spaced less than 2L apart and the CNT length could be extended.

5.3.1.5. CNT clumps on Kanthal wire

A summary of clump samples investigated for their field emission properties can be found in Table 8. All samples had a similar morphology when observed by SEM (Figure 122 and Figure 123). Most samples have clumps that are approximately 10μm in average diameter. Thick fibres can be seen on the surface of samples N34 (Figure 122b) and N35 (Figure 122c). As thinner CNTs have higher aspect ratios compared to thicker fibres, it is

more likely that the thinner CNTs found in a sample will contribute most to the overall field emission current and so these thick fibres can be ignored.

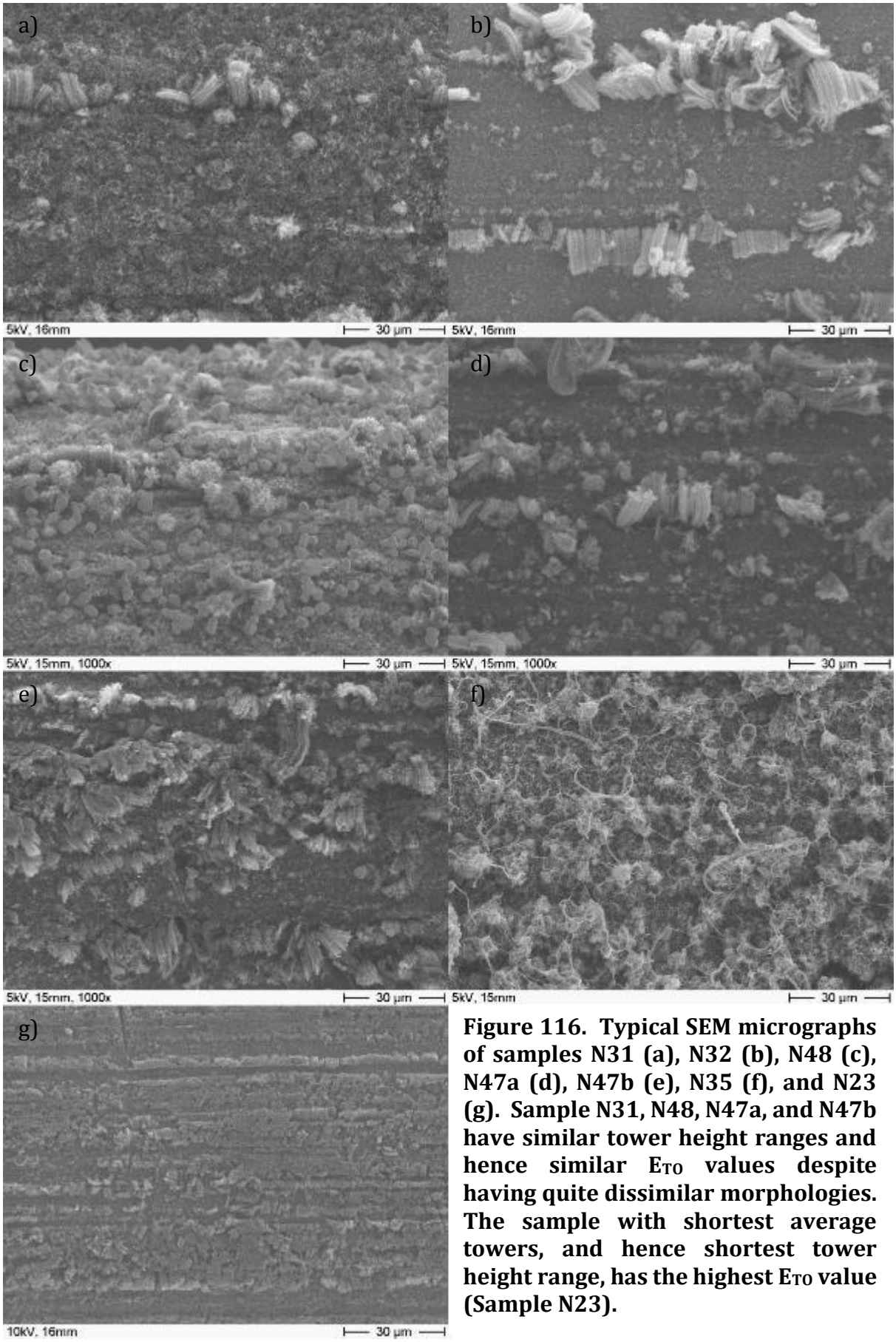

Figure 116. Typical SEM micrographs of samples N31 (a), N32 (b), N48 (c), N47a (d), N47b (e), N35 (f), and N23 (g). Sample N31, N48, N47a, and N47b have similar tower height ranges and hence similar E_{TO} values despite having quite dissimilar morphologies. The sample with shortest average towers, and hence shortest tower height range, has the highest E_{TO} value (Sample N23).

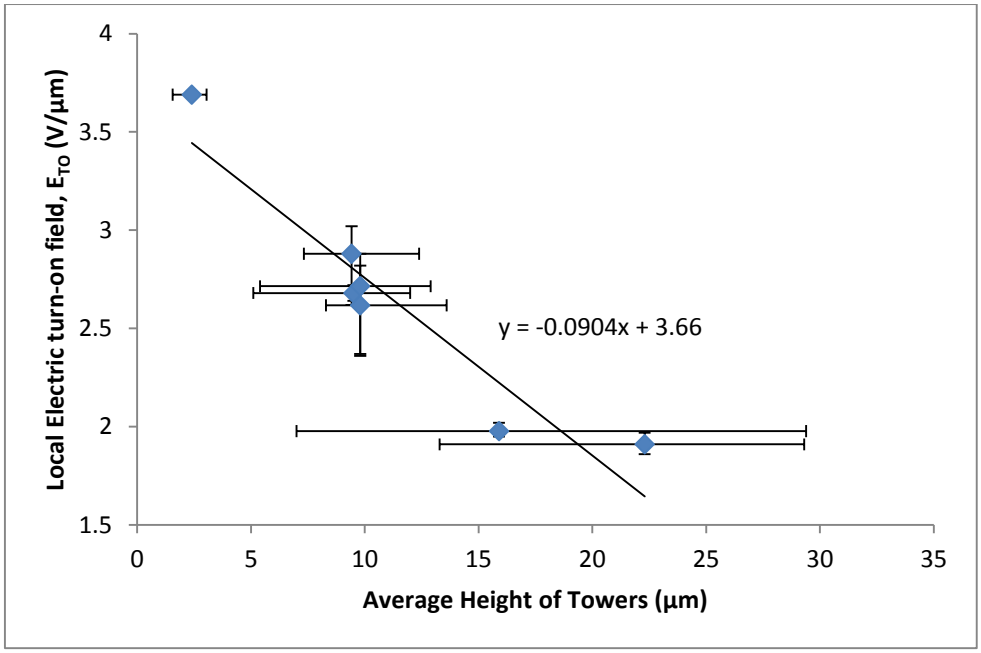

Figure 117. Graph of the inverse relationship between average tower height and E_{TO}.

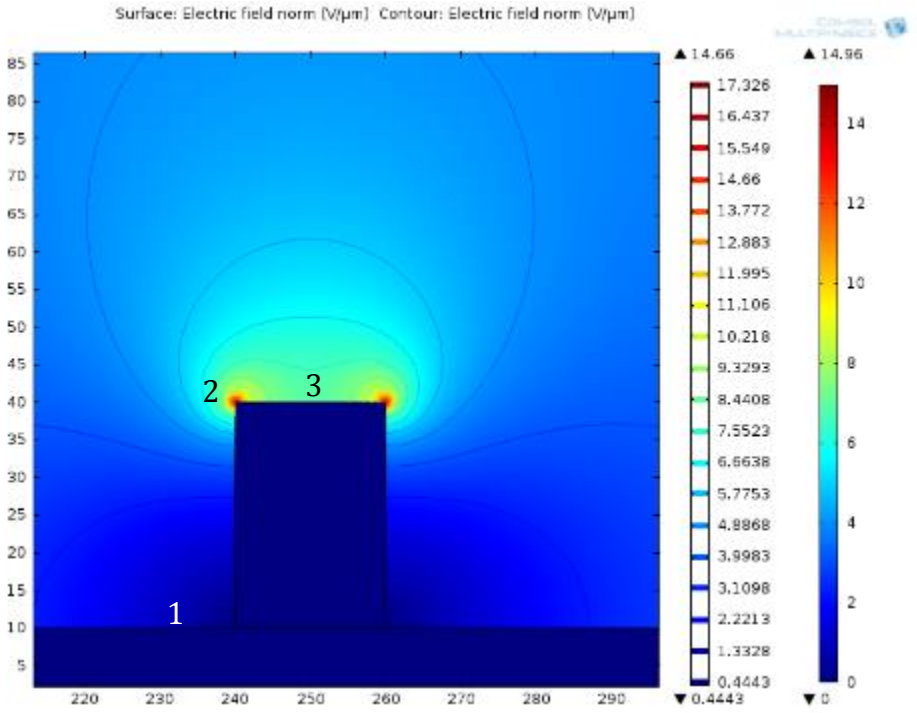

Figure 118. Simulation of the electric field distribution around a tower geometry found on the surface of samples in Table 2. CNTs can be found in and around any part of the tower structure and there are 3 regions of field enhancement. 1) CNTs found in this region will not experience significant field enhancement due to the shielding effect of the nearby tower. CNTs found in region 2) will experience a higher field enhancement compared to CNTs found away from the tower and CNTs found at region 3) will experience the highest field enhancement due to the corner effects.

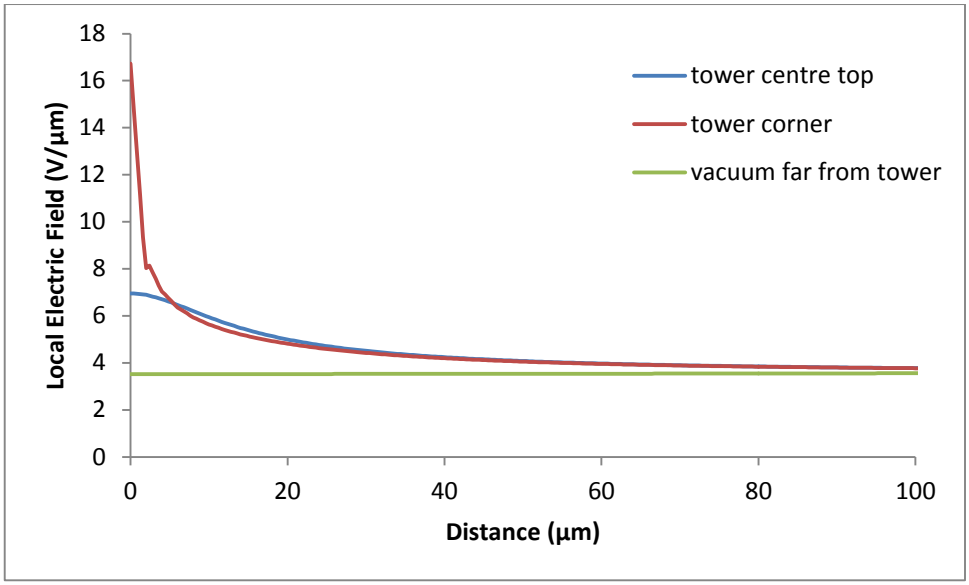

Figure 119. Graph showing the simulated local electric field along a line that extends from the sample surface to the anode, where the line starts at a tower corner, tower centre top and a region far from the tower.

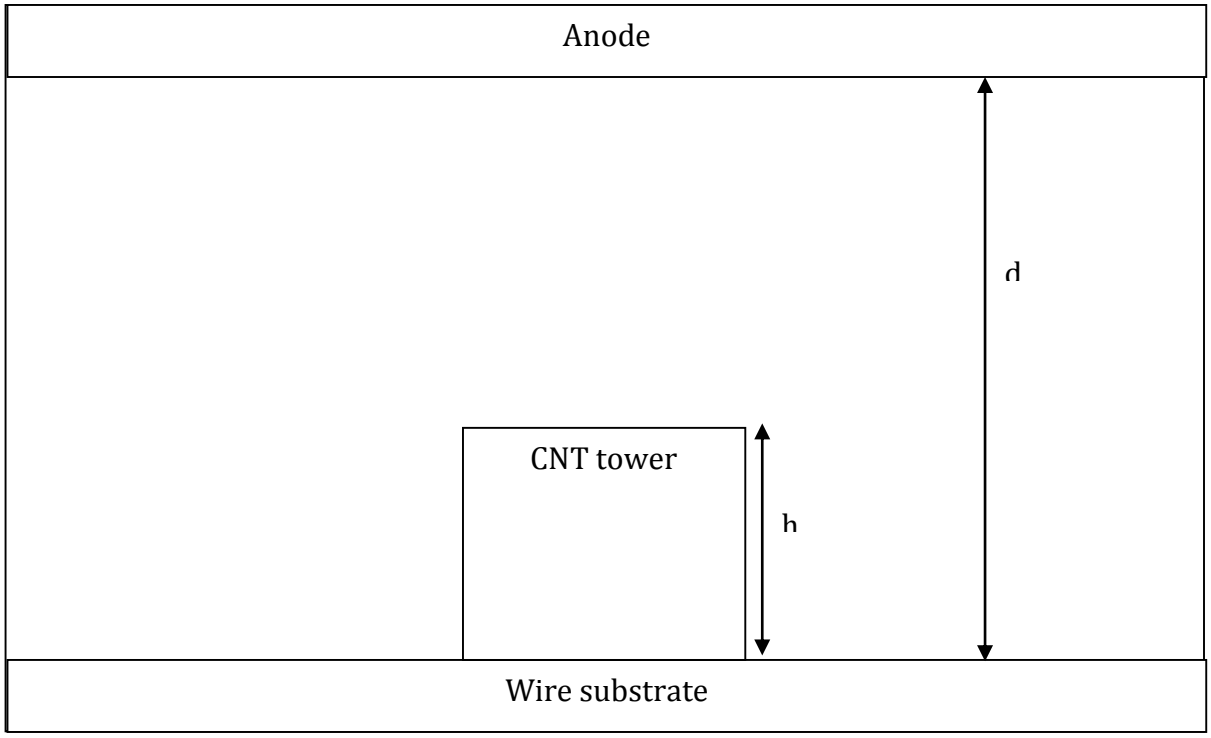

Figure 120. Schematic showing an isolated tower in a planar arrangement which is equivalent to a larger inter-electrode displacement in a cylindrical setup.

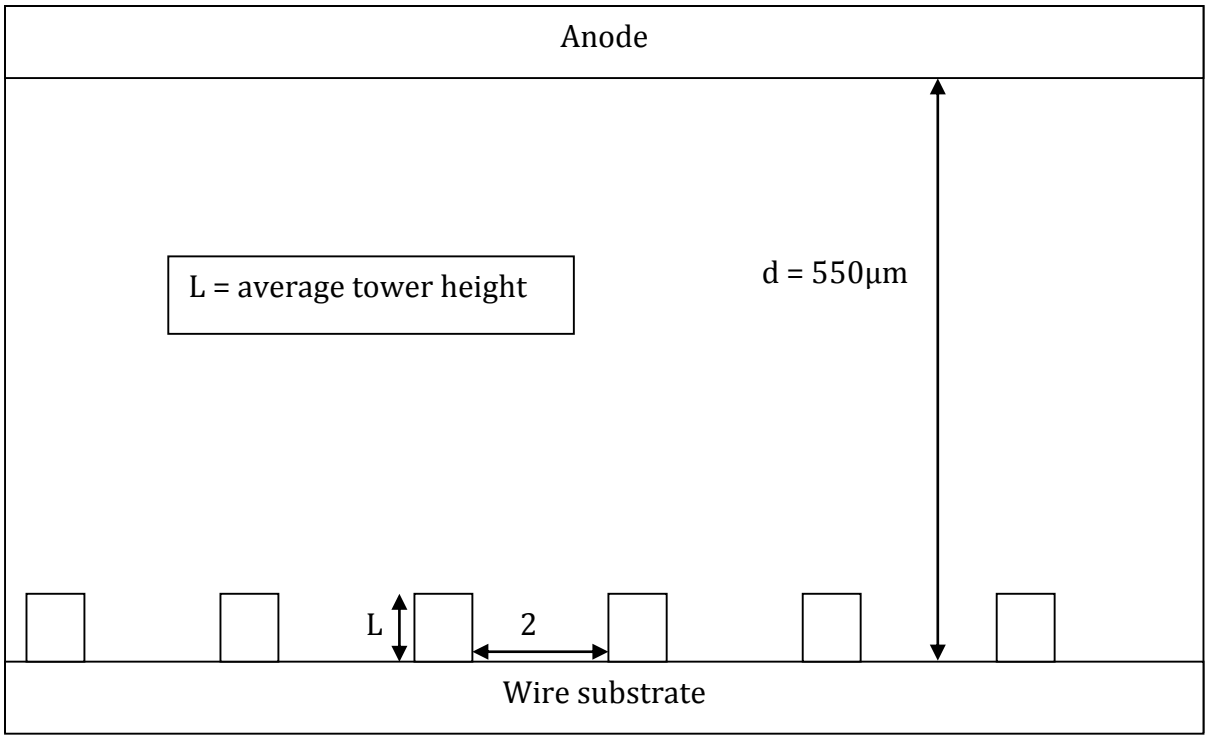

Figure 121. Schematic of the morphology inputted into COMSOL to calculate the relative electric field intensity for CNT towers spaced more than 2L apart.

Figure 124 shows that the measured E_{TO} values vary considerably between 0.9V/µm (in the case of N34) and 2.9Vµm (in the case of N43). It is possible that an unknown contaminant entered the system during the growth of these samples as Table 7 shows that sample N43 was grown under identical processing conditions to N34, except that a longer growth time of 10 minutes was used. Larger clumps would be expected for longer growth times. Possible contamination of the processing environment would hinder growth and this same contamination may be responsible for the higher E_{TO} value. EDX however showed that in addition to carbon; aluminium, iron and chromium were present in smaller quantities. There is no obvious correlation between average clump size and E_{TO} or indeed between clump diameter range and E_{TO} value.

Sample N36a had the lowest E_{TO} value of the clump samples (0.64V/µm). This is not due to the fact that this sample has the largest average clump diameter as it was shown in Section 5.3.1.4 (page 154) that a small change in the inter-electrode distance has little

effect on the E_{TO} value of a sample. It is likely that the average height (or diameter) of clumps is similarly insignificant and this is shown in Figure 124 where there does not seem to be a correlation with E_{TO} value.

In an attempt to understand the field emission properties of clump samples, CNT diameter distributions were calculated by measuring the CNT diameters using TEM micrographs (Figure 125). It was found that there is an inverse relationship between average CNT diameter in a given clump sample, and E_{TO} value (Figure 126). This is counter intuitive as it is expected that, as the diameter of the individual CNTs decreases, then the aspect ratio of the CNTs increases and hence the E_{TO} value is lower.

There is a roughly linear relationship between average CNT diameter and overall thickness of the CNT-Kanthal composite (Figure 127) of clump samples. This is not surprising, as a faster growth rate would be required to grow CNT films that are morphologically thicker, which results in longer, thicker CNTs. As the CNTs grow outwards radially, they become more separated from each other and screening is reduced. This will be explained in more detail in the next section.

5.3.1.6. Comparison between "ridge" samples

As β is related to the aspect ratio of emitters, the growth times of samples were varied in order to examine the relationship between CNT length and E_{TO}. The easiest way to produce long CNTs is to use a longer growth time which inevitably leads to ridge (as defined in Chapter 3) morphologies. Table 9 shows the processing parameters used in the study of these samples.

Sample ID	Precursor	Cat. %	T (°C)	t (mins)	Carrier gas flow (Ar:H_2 SLM)	I_D/I_G	E_{TO} (V/μm)
N28	1% Benzylamine	5	900	2	1:1	0.52	1.87
N34	1% Benzylamine	1	900	2	1:1	0.82	0.94
N35	1% Benzylamine	1	900	10	1:0.2	0.62	1.51
C26	Toluene	5	800	10	1:0	0.71	1.92
C27	Toluene	5	800	10	1:2	0.52	0.94
N36a	1% Benzylamine	5	900	10	1:0.2	0.64	0.73
N45	1% Benzylamine	5	900	2	1:1	0.83	1.84
N40	Benzylamine	5	800	10	1:0	0.88	2.55
N43	1% Benzylamine	1	900	10	1:1	0.68	2.93

Table 8. Table summarising the processing parameters used to grow clumps of entangled CNTs on Kanthal wire.

Samples with thinner CNT films were found to be those that were grown with pure benzylamine precursor because the CNTs grow slower using this precursor compared to toluene due to the nitrogen saturating the surface of the catalyst particles [32]. As the thickness of the carpets increase, E_{TO} decreases and the carpets become increasingly broken along the length of the Kanthal wire (Figure 128, Figure 129, Figure 130 and Figure 131). The length of exposed ridge edges increases and the range in edge length per sample also increases as the carpet thickness increases (Figure 132).

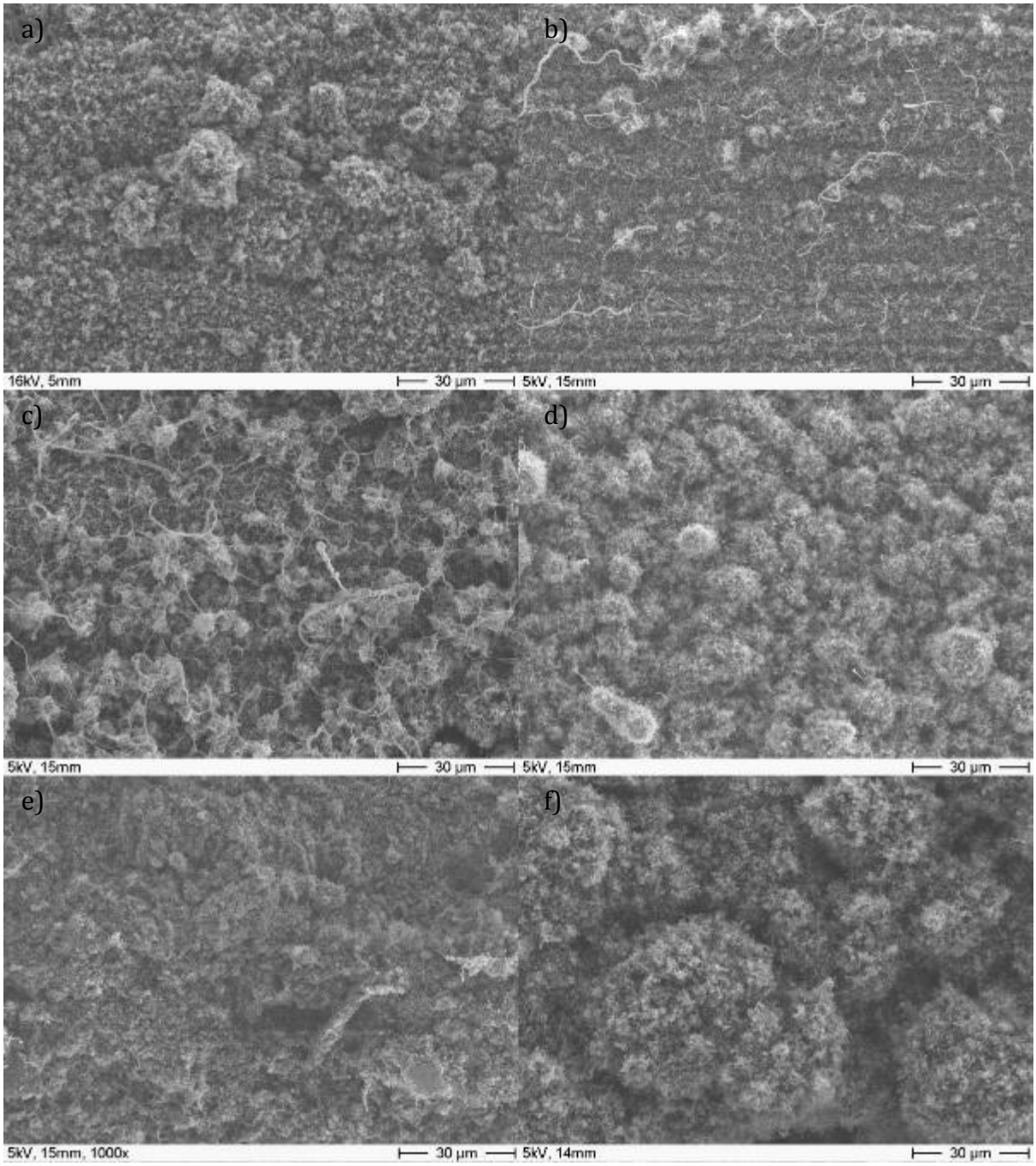

Figure 122. Typical SEM micrographs showing the general morphology of CNT clump samples. Samples N28 (a), N34 (b), N35 (c), C26 (d), C27 (e), N36a (f) are shown, grown by processes summarised in Table 3.

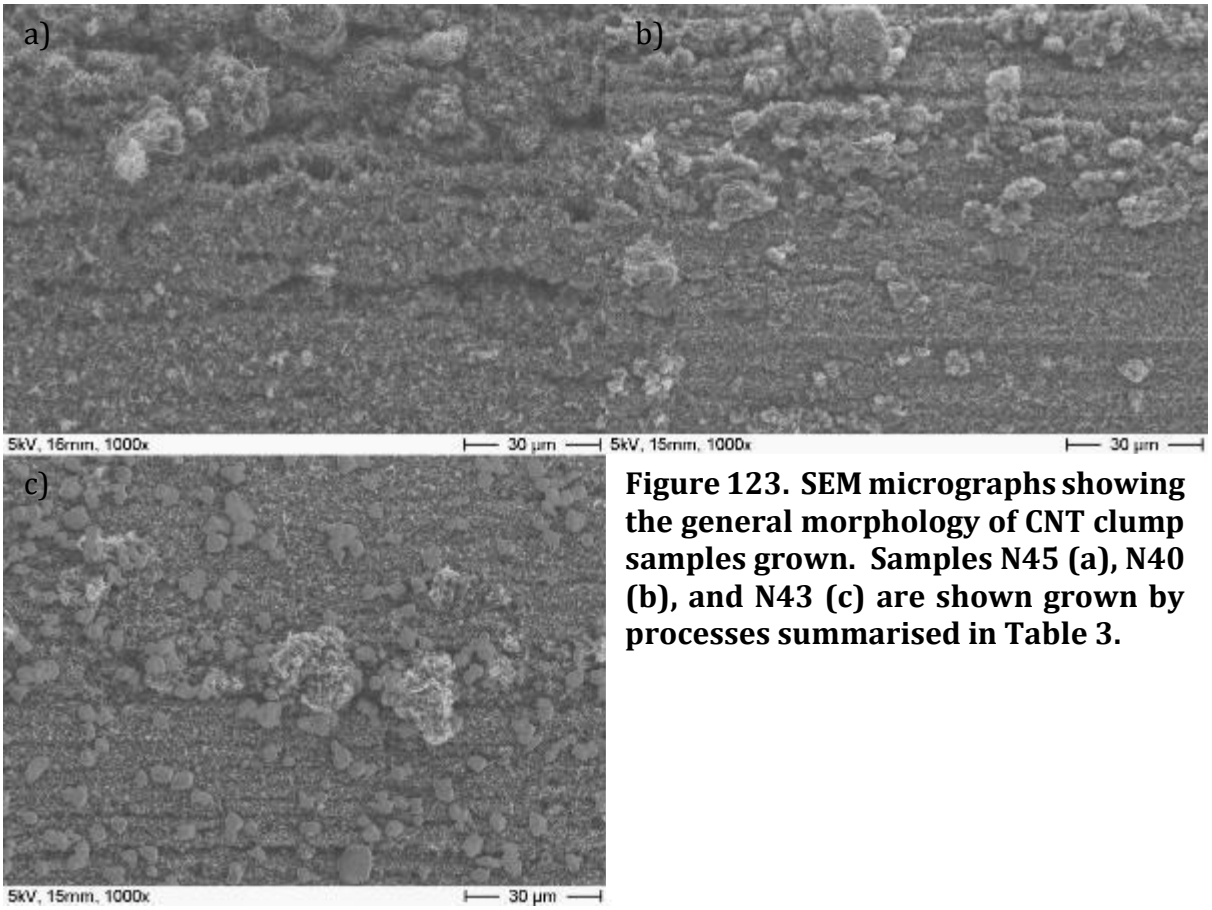

Figure 123. SEM micrographs showing the general morphology of CNT clump samples grown. Samples N45 (a), N40 (b), and N43 (c) are shown grown by processes summarised in Table 3.

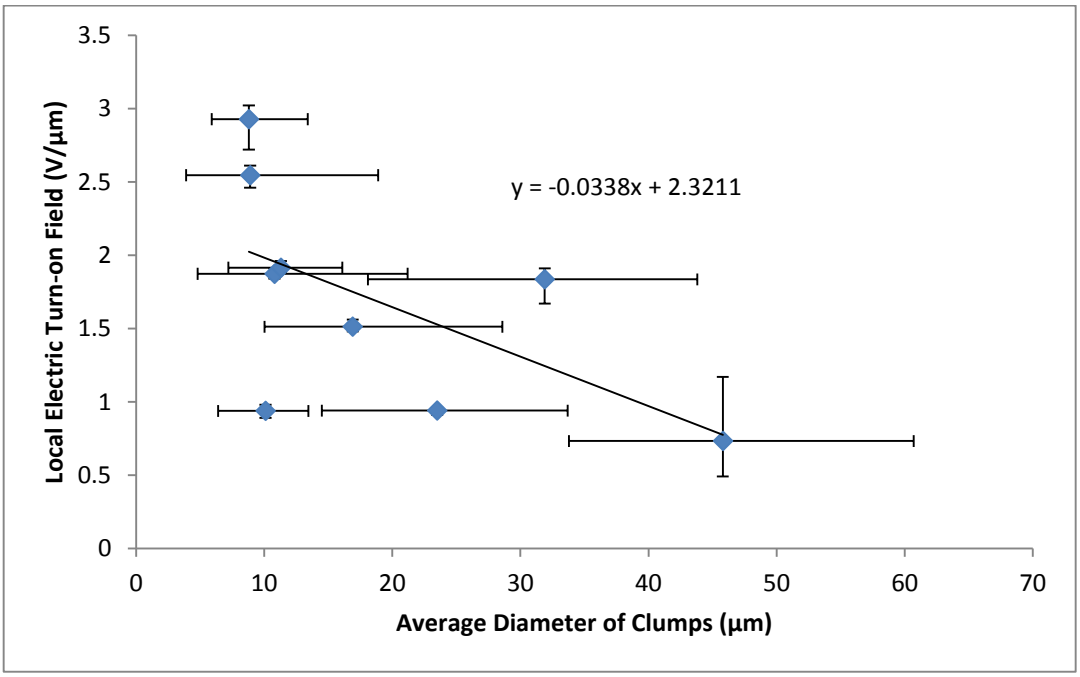

Figure 124. Graph showing no obvious correlation between average clump diameter and E_{TO}.

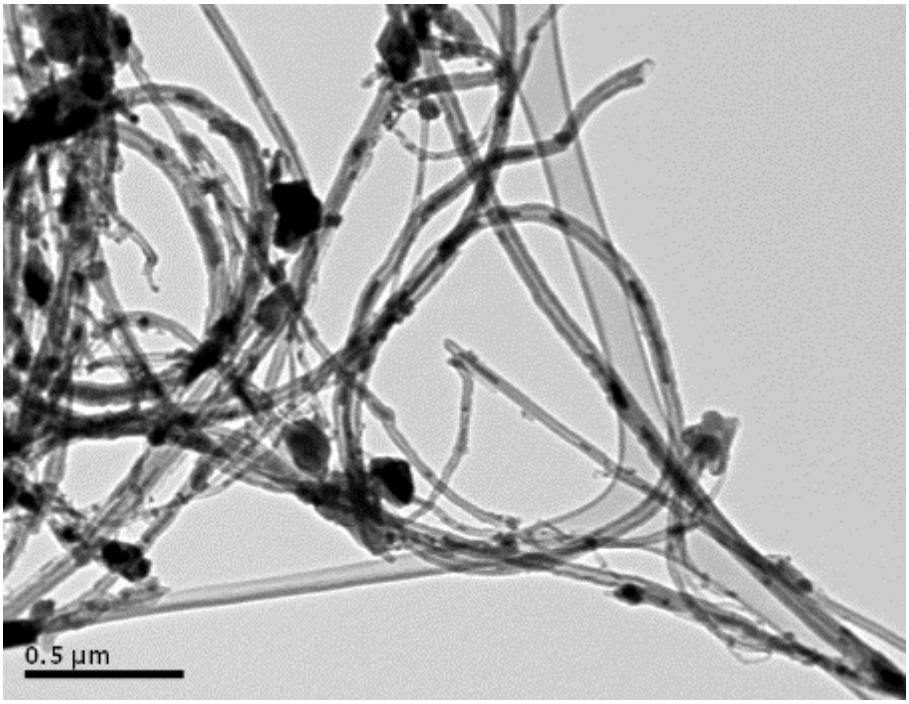

Figure 125. Typical TEM of CNTs found in a clump sample. This particular TEM micrograph is taken from sample C27 and these TEM micrographs are what is used to calculate average diameters of CNTs.

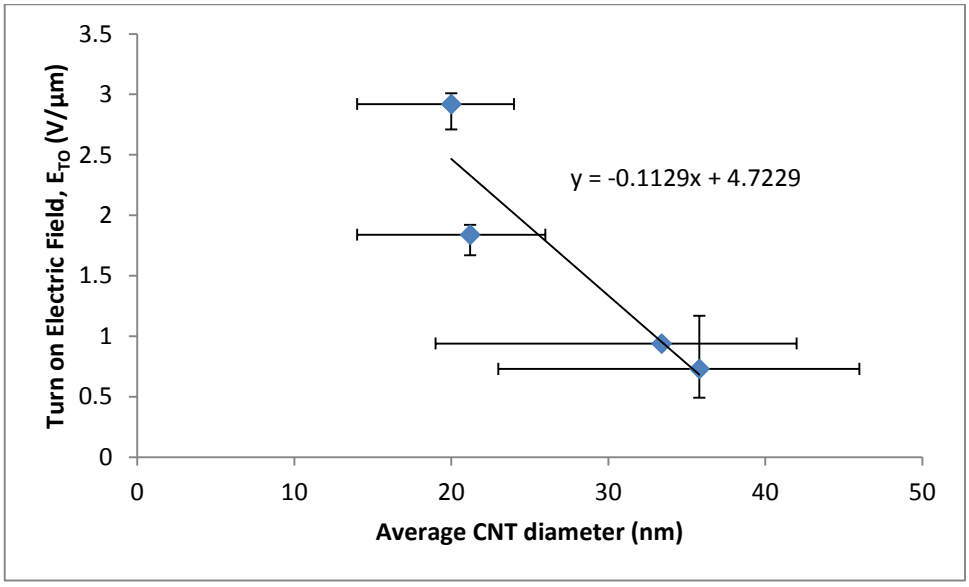

Figure 126. Graph showing the inverse relationship between E_{TO} value and average CNT diameter per clump sample. The error bars in the x-axis correspond to the 2nd and 3rd quartile.

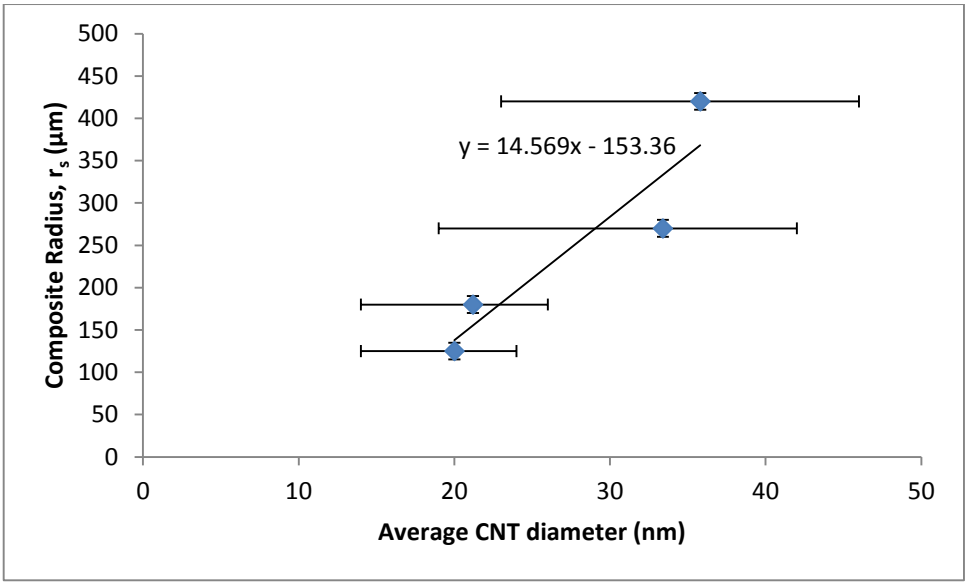

Figure 127. Graph showing a rough linear relationship between composite radius (r_s) and average CNT diameter for a given clump sample. The error bars in the x-axis correspond to the 2nd and 3rd quartile.

There are two competing forces that determine the geometry of the carpets. Firstly, CNTs grow radially from the Kanthal wire surface and this separates them from each other as their tips will be further apart than their bases. Secondly, the nitrogen bonding between neighbouring CNTs forces them into bundles [155]. The result is either a continuous, smooth CNT carpet, several carpet ridges, or something in between. N29 and N21 respectively are examples of the extreme cases (Figure 128c and Figure 130c).

Similar to the results with clump samples, ridge samples also show an inverse relationship between average CNT diameter and E_{TO} values (Figure 133). Figure 134 shows that there is also a roughly linear relationship between r_s and average CNT diameter.

Sample ID	Precursor	Cat. %	T (°C)	t (mins)	Carrier gas flow	I_D/I_G ratio	E_{TO} (V/μm)	r_s (μm)
N30	Benzylamine	1	900	4	1:1	1.23	1.37	160
C28	Toluene	5	900	10	1:0.2	0.54	1.26	170
N29	Benzylamine	1	900	6	1:1	0.99	1.25	180
N26	1% benzylamine 99% toluene	5	900	4	1:0.2	0.62	1.10	200
N39	100% benzylamine	5	900	10	1:0.2	1.01	1.35	240
C27	100% toluene	5	800	10	1:2	0.73	0.94	270
N27	1% benzylamine 99% toluene	5	900	6	1:0.2	0.57	1.25	320
C29	100% toluene	5	900	10	1	0.53	0.98	360
N36a	1% benzylamine 99% toluene	5	900	10	1:0.2	0.64	0.73	420
N21	1% benzylamine 99% toluene	5	900	10	1:0.2	0.54	0.49	450
N37	1% benzylamine 99% toluene	5	900	10	1:0.2	0.96	0.89	485
N36b	1% benzylamine 99% toluene	5	900	10	1:0.2	0.67	0.35	550
N38a	1% benzylamine 99% toluene	5	900	10	1:0.2	0.64	0.48	650

Table 9. Table summarising the various processing parameters used to grow ridge-sample of CNTs on Kanthal wires.

Figure 135 shows that as the composite radius increases, E_{TO} decreases. As composite radius is related to the thickness of the CNT films, as the CNT thickness increases E_{TO} decreases also. E_{TO} is defined in a cylindrical setup and from Equation 2. This is counter-intuitive as Equation 2 shows that as r_s increases, the field enhancement (compared to a planar setup of the same inter-electrode displacement) decreases (Figure 106b). As r_s increases for a smooth cylinder, the shape of the cathode tends towards a flat surface, and hence loses any beneficial field enhancement due to curvature. At small r_s values (for a smooth cylinder), the field enhancement effect of curvature is greatest, and a small increase in r_s results in a significant drop in β value. At large r_s values, the change in β value is small, as the system approximates a planar setup with no field enhancement. Therefore it would be expected that as the CNT film thickness increased, E_{TO} would increase as β would decrease. However, the opposite is true in the experimental data which indicates that β is actually increasing with increasing CNT film thickness.

In Section 5.3.1.4 (page 154) it was discussed how the bundling of CNTs into towers creates edges where CNTs would experience an increased β value. When these towers have a large range in height, screening effects are reduced and the emitting CNTs are spaced more favourably apart and hence E_{TO} values are reduced compared to tower samples with a small range in tower heights. Ridge samples can be thought of as similar to tower samples except the short axis is extended to infinity. Hence it is reasonable to assume that the edges of these ridge structures will also act as regions where field enhancement is experienced.

As r_s increases, the length of CNTs becomes comparable to the radius of the wire substrate (125 μm). At this point, the CNTs behave as though they are on a flat substrate and therefore E_{TO} is related to the aspect ratio of the emitters meaning that with longer CNTs, E_{TO} decreases, which is what is observed. If this experiment was repeated on a flat

substrate however, we would not observe a lower E_{TO} because bundling will mean that CNTs are not spaced apart and will shield each other. It is a combination of the ridge morphology separating CNTs, and the setup approximating a planar setup (so that increased CNT length lowers E_{TO}) that is responsible for the trend seen in Figure 117.

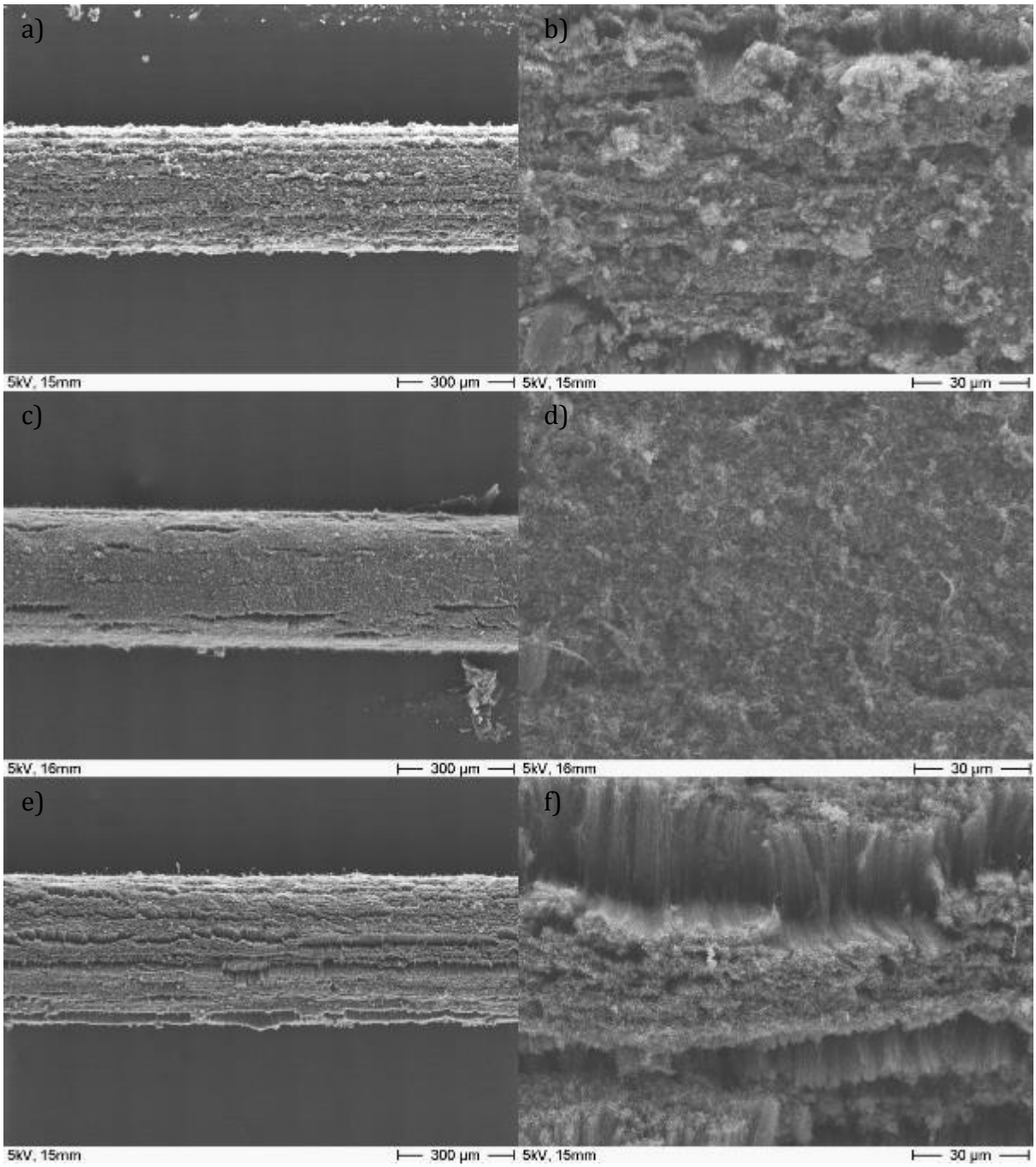

Figure 128. SEM micrographs of ridge samples N30 (a and b), N29 (c and d) and N26 (e and f). The low magnification SEM micrographs (a, c and e) show that as the thickness of the CNT film increases, the structure forms ridges along the length of the wire substrate as the carpets grow radially from the wire substrate.

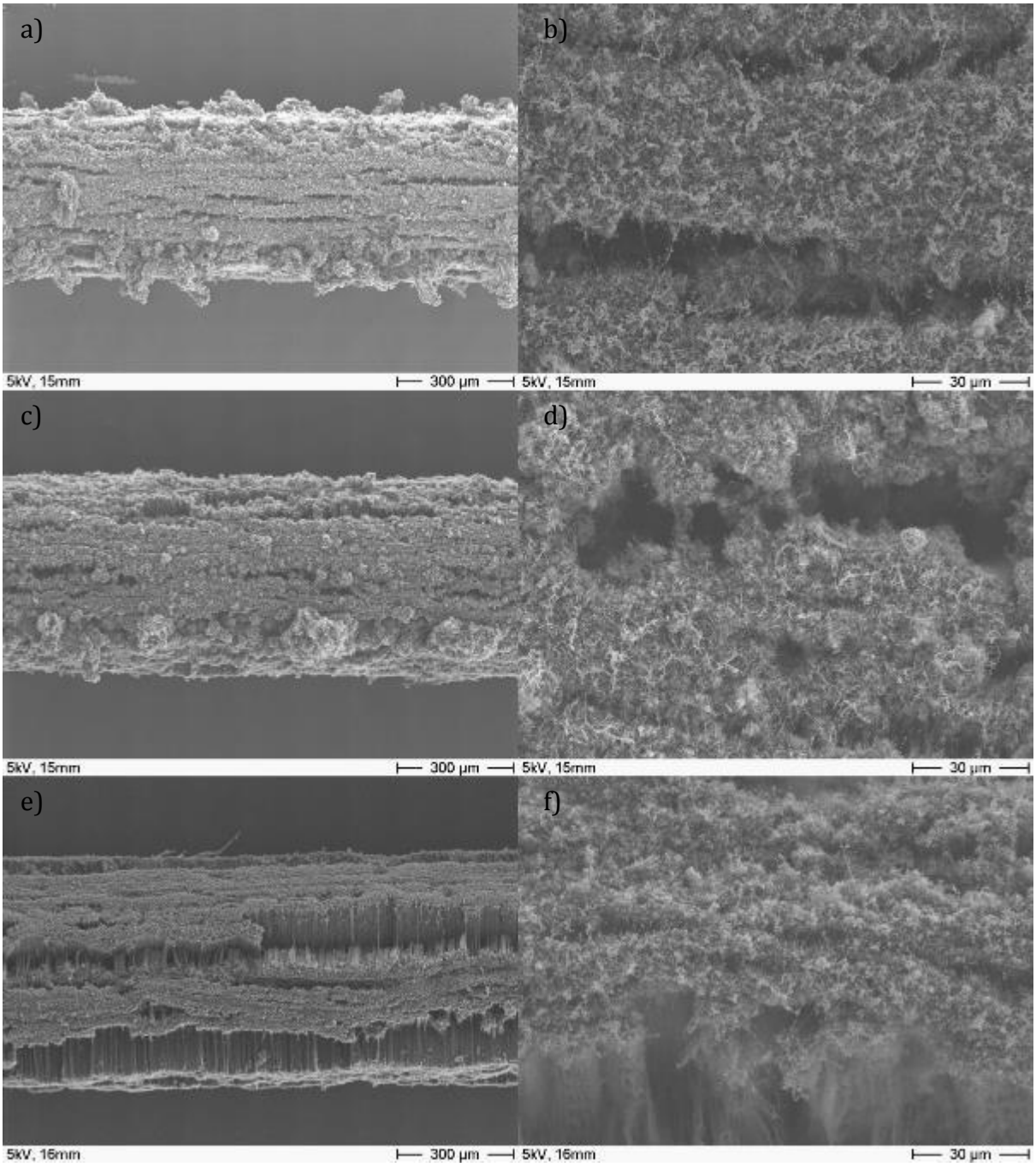

Figure 129. SEM micrographs of ridge samples N39 (a and b), C27 (c and d) and N27 (e and f). The low magnification SEM micrographs (a, c and e) show that as the thickness of the CNT film increases, the structure forms ridges along the length of the wire substrate as the carpets grow radially from the wire substrate.

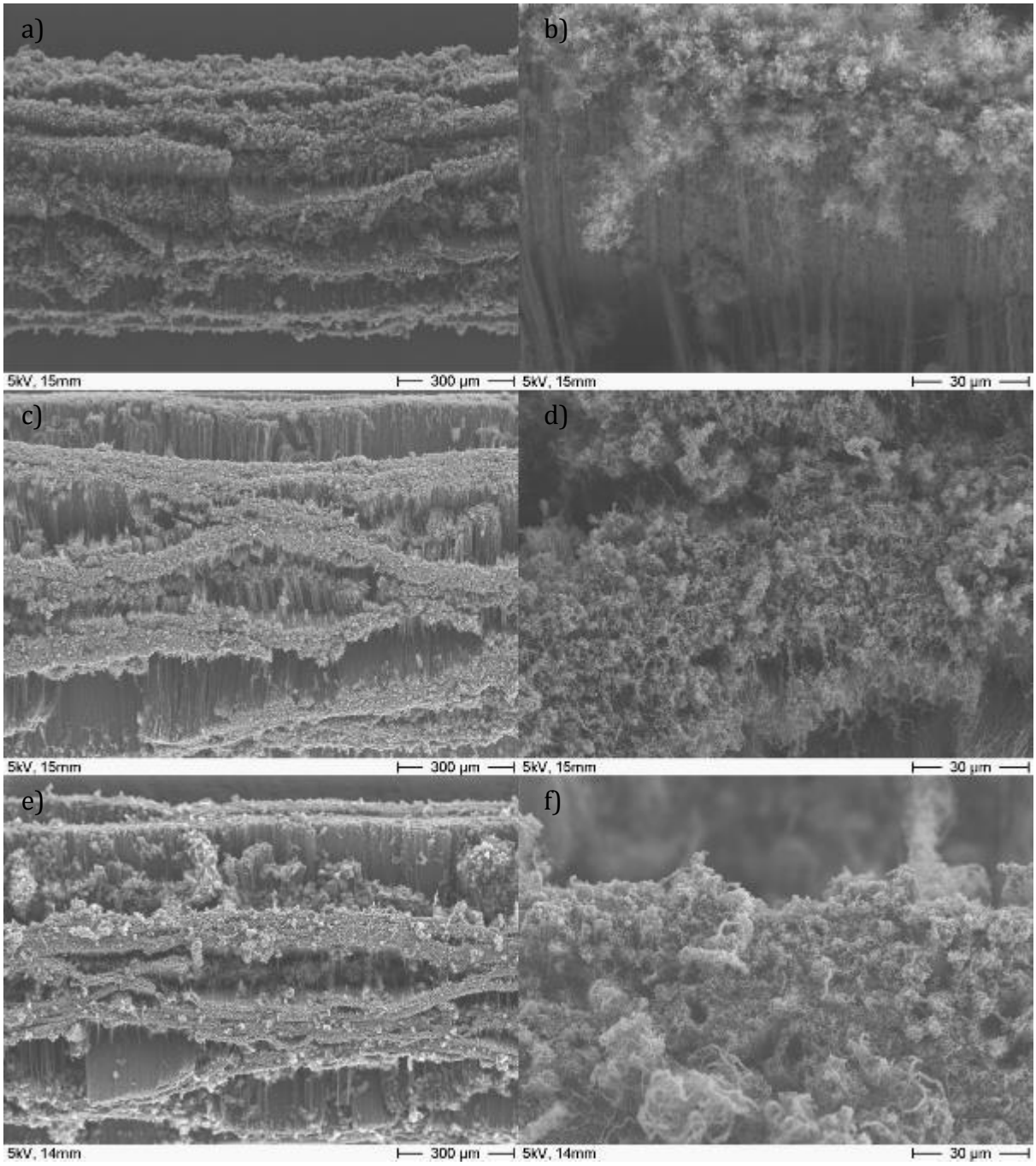

Figure 130. SEM micrographs of ridge samples C29 (a and b), N21 (c and d) and N37 (e and f). The low magnification SEM micrographs (a, c and e) show that as the thickness of the CNT film increases, the structure forms ridges along the length of the wire substrate as the carpets grow radially from the wire substrate.

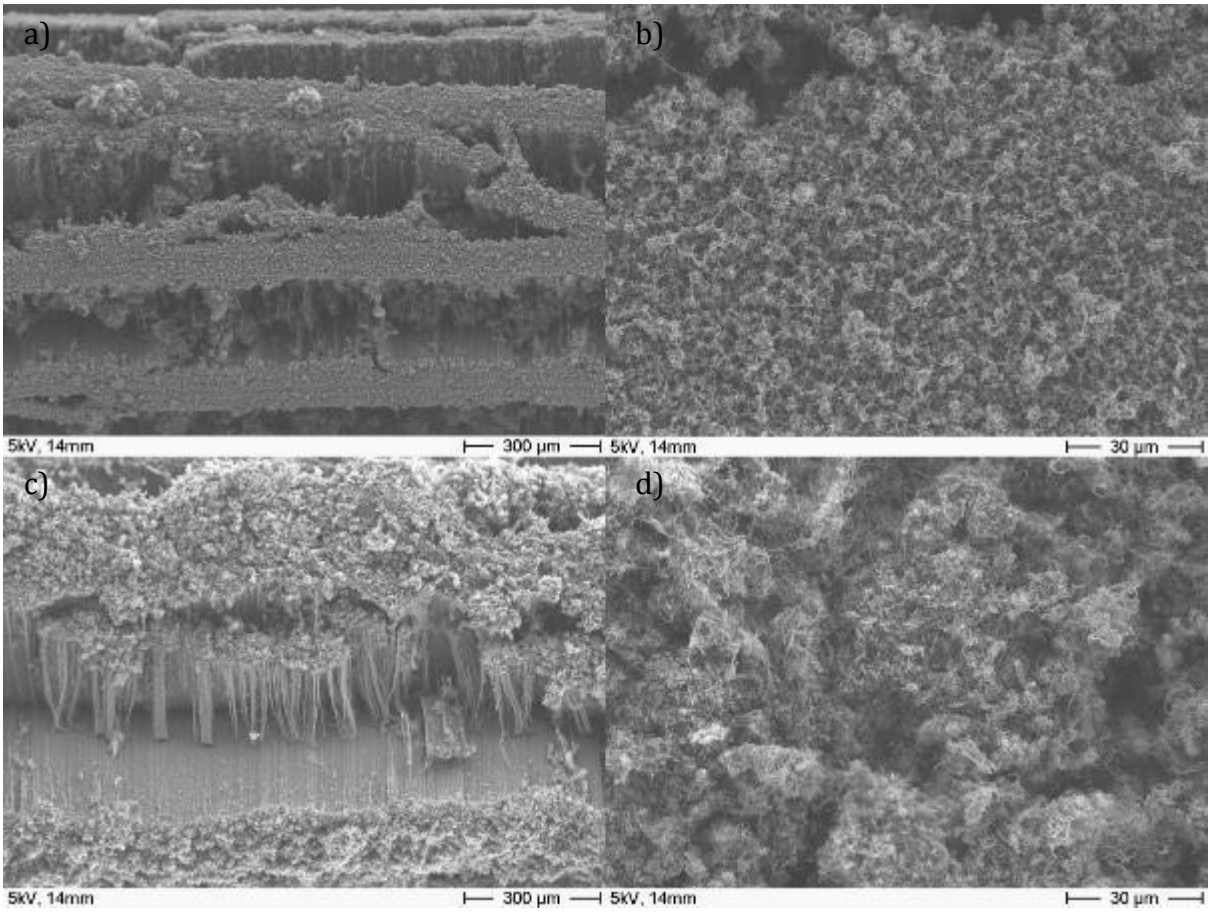

Figure 131. SEM micrographs of N36b (a and b) and N38a (c and d). The low magnification micrographs (a and c) show that as the thickness of the CNT film increases, ridges form along the length of the sample as the carpets grow radially from the wire substrate.

As the thickness of the CNT films increase, the range in length of the opening between ridges also increases (Figure 132). It can also be seen from SEM (Figure 128, Figure 129 and Figure 130) that secondary ridges form as the thickness of the film increases, and above an r_s value of 360µm (~235µm CNT length), are observed as shorter ridges inside the openings of the CNT film and as other forms of CNT agglomerates (Figure 130a, Figure 130c, Figure 130e, Figure 131a and Figure 131c).

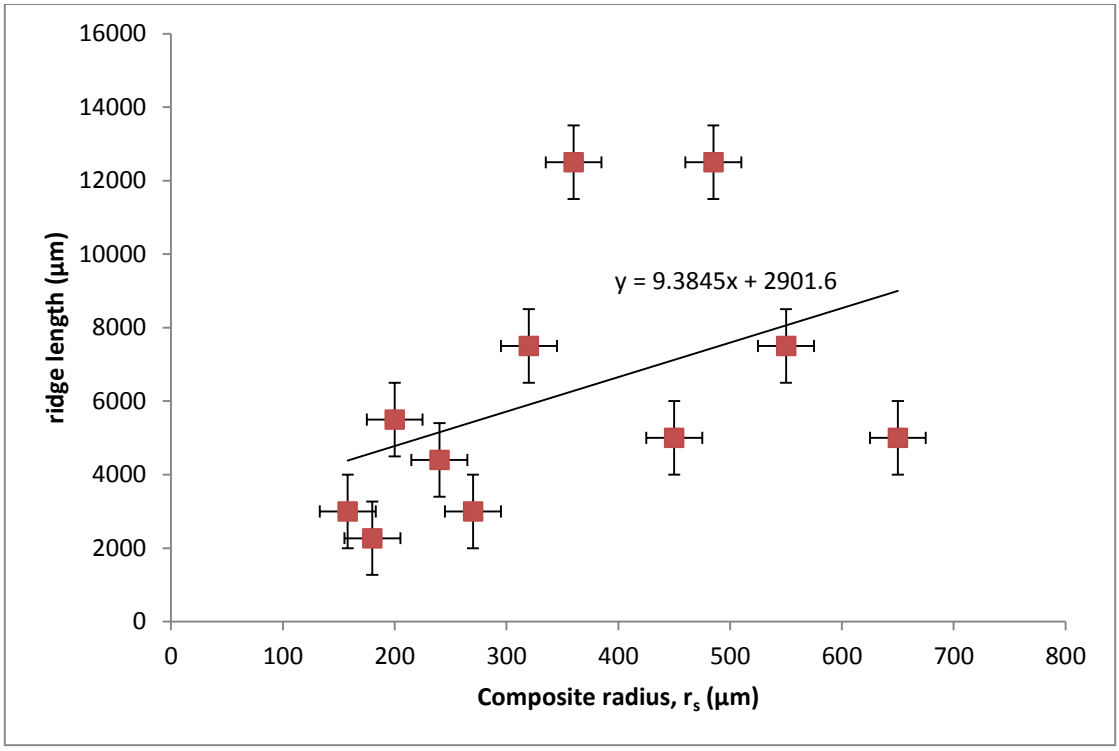

Figure 132. Graph showing the relationship between exposed ridge length per given magnification of SEM micrograph versus the combined length of substrate radius and film thickness. As the thickness of the CNT film increases, the average ridge length for a given area increases as the structure becomes more open and more edges are exposed. The range of ridge length for a given area also increases as the CNT film thickness increases.

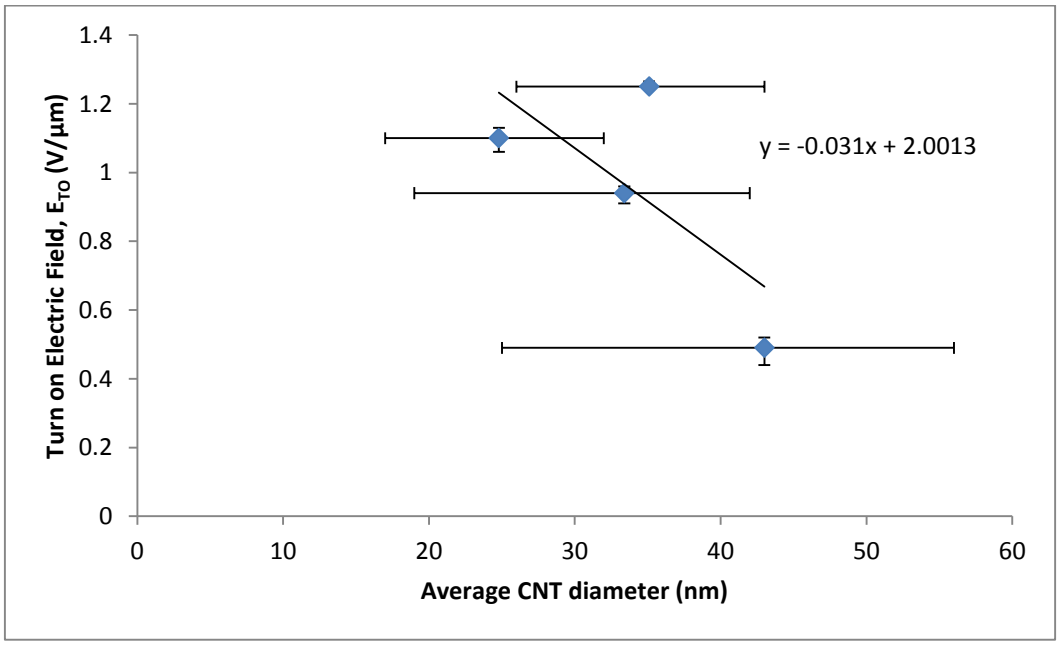

Figure 133. Graph showing the inverse relationship between E_{TO} value and average CNT diameter per ridge sample. This is comparable and consistent with clump samples. The error bars in the x-axis correspond to the 2nd and 3rd quartile.

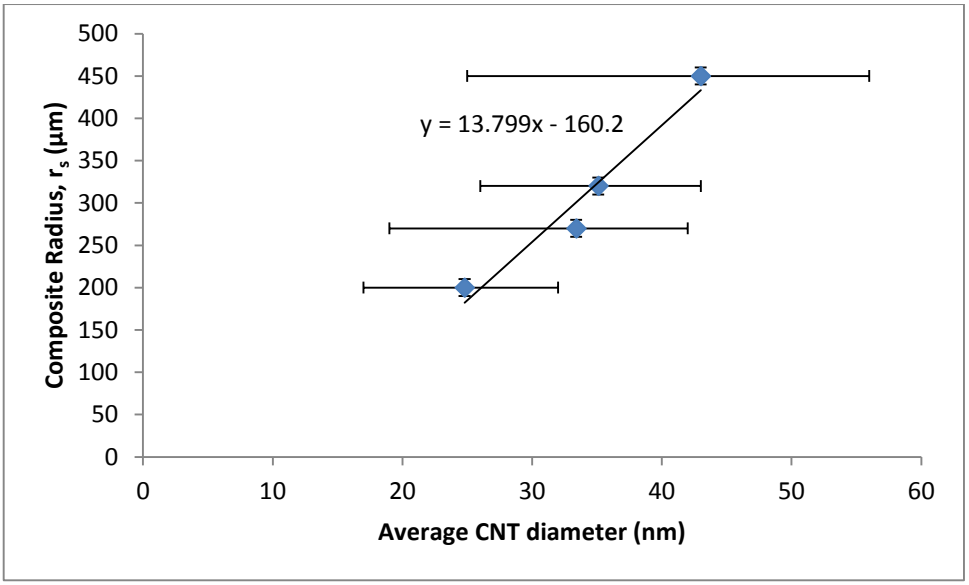

Figure 134. Graph showing the linear relationship between composite radius (r_s) and average CNT diameter for a given ridge sample. This is consistent with what was observed for clump samples. The error bars in the x-axis correspond to the 2nd and 3rd quartile.

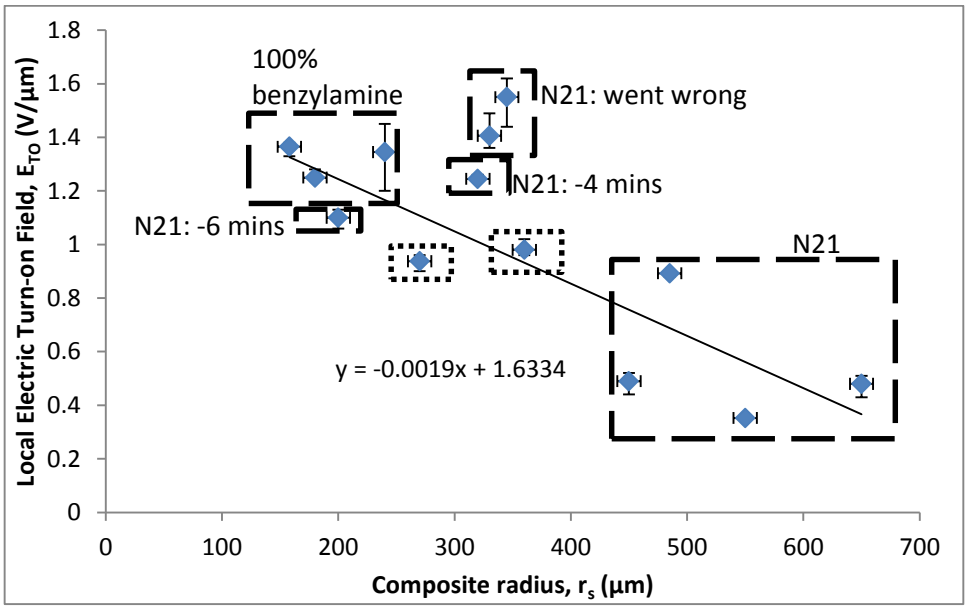

Figure 135. Graph showing ridge-type samples and their relationship to composite radius (r_s) and the local electric turn-on field (E_{TO}). Data points the dashed squares are those that are grown using benzylamine and those inside dotted squares are those grown using toluene.

This would explain the linear trend of decreasing E_{TO} as the CNT film thickness increases above an r_s value of 360µm. Below this value, there is no relationship between CNT film

thickness and E_{TO} value as there is little secondary growth between the ridges and little variation in the height of ridges (Figure 135).

Sample N21 produced the best results in terms of lowest E_{TO}, and the growth experiment was repeated several times to measure the reproducibility of these field emission results. Samples N36b, N37, N38a in Table 9 shows the various N21 experiments repeated. They all produced similar ridge type morphologies except sample N36a, which produced a clump type morphology (Figure 136). Despite the different morphology, this sample achieved an E_{TO} value of 0.73V/μm which is comparable to other ridge samples of this film thickness. This is probably due to the existence of opening in the CNT film, which increases the chance of protruding CNTs being found at the edges.

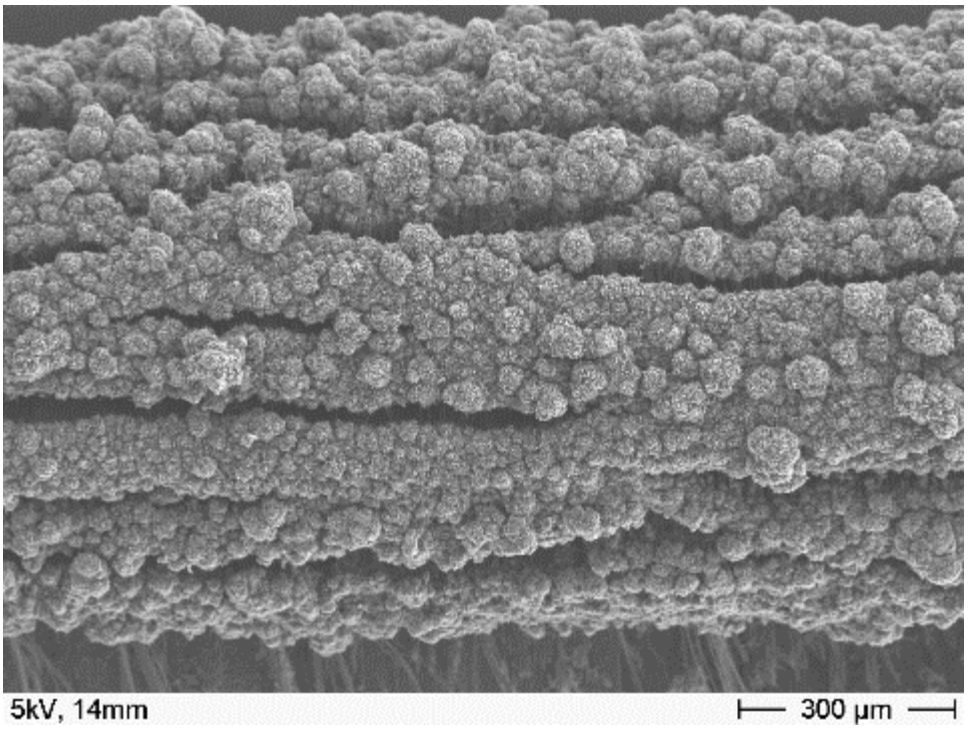

Figure 136. Low magnification SEM micrographs of sample N36a which shows a clump-type morphology despite having identical processing conditions to sample N21.

The E_{TO} of the repeated N21 ridge sample varies between 0.35 V/μm (N36b) and 0.92 V/μm (N37). E_{TO} values were 0.51V/μm for sample N38a and 0.52V/μm for the original N21 sample.

The best sample produced an E_{TO} of 0.35 V/μm and is similar in morphology to the original N21 sample (Figure 131a). However there are more, thinner ridges in N36a compared to N21 and there are many CNTs that bridge between each ridge. This type of morphology is more likely to produce protruding CNTs that could contribute to field emission. Sample N21 has thicker ridges than N36 which means that CNTs are unable to bridge individual ridges which in turn means that there are fewer protruding CNTs.

5.3.1.7. Summary of the Field Emission Properties of CNT Films

Various morphologies of CNT films that were grown in Chapter 3 were investigated with respect to their field emission properties. A simple, planar case was explored first consisting of short CNTS, with increasingly complex geometries investigated subsequently. It is likely that the best film emitters (that is, with the lowest E_{TO} values) have many protruding CNTs aligned perpendicular to the surface. Also, the CNTs with lowest I_D/I_G values tend to have the lowest E_{TO} values.

Films that had towers (*i.e.* vertically aligned bundles) or ridges of CNTs aligned perpendicular to the surface of the wire are favourable in comparison to clumps or short CNTS. The edges inherent to tower and ridge samples create space to facilitate protruding CNTs and act as a way of separating emitters so that shielding is minimised.

Most researchers have tended to focus on the field emission properties of a single sample or single morphology as they tend to be demonstrating the concept of a device, and hence it is difficult to compare results between articles as the experimental setups can vary [112, 161-163, 203]. Bonard *et al* [199] studies the morphology of CNT films and their relation to the field emission properties. They did this by changing the concentration of catalyst in the precursor 'ink' so that the density of CNTs grown changed. If the concentration of CNTs was too low, short CNTs were grown which had a high E_{TO}. If a high density of CNTs grew, E_{TO} was also high because CNTs were vertically aligned but

tightly packed so that few were protruding. They found that a medium concentration of catalyst particles resulted in the most protruding CNTs and therefore lowest E_{TO} value. Work in this thesis differs because it is in a cylindrical arrangement, the morphologies however, are similar as they resemble three dimensional blocks of CNTs. Other work has also shown that it is the presence of protruding CNTs that contributes to field emission properties [62, 75, 157, 198, 199]. Growing CNTs on a cylindrical substrate is beneficial because CNTs are more likely to protrude away from each other as they grow outwards. It has been shown by others that for a given CNT film, only a small proportion of the CNTs actually contribute to the emitted current and emitter density can be $\sim 10^4$ cm^{-2} out of a CNT density of $\sim 10^8$ cm^{-2} [62, 199]. The films consist of entangled carpets of CNTs with some CNTs protruding outwards. De Heer *et al* [75] suggested it is closer to $\sim 10^5$ cm^{-2} for a CNT density of 10^8 cm^{-2}, however no SEM micrographs of the CNT films are presented. It is likely that for the CNT films in this study, the emitter density would be greater, because CNTs grown on a wire protrude out radially. As the CNTs grow longer, they become more separated and hence more emitters become available.

5.3.2. Prolonged emission measurements

The lifetime of the cathode component is important if the final device is to function reliably. Samples were therefore tested to understand how the current decays over a period of time. A voltage was applied so that an emission current of 500μA is measured after the initial I-V curves were obtained. This was the maximum current possible whilst maintaining a constant pressure. The voltage was held at this value for one hour and the current logged with respect to time. In a few samples, the current was unstable below 500μA (*i.e.* the current raised dramatically) and the experiment was discontinued so that no damage occurred to equipment.

Figure 137 shows a typical graph from this experiment showing an exponential decay in the emitted current with respect to time whilst the voltage is kept at a constant value. There was an exponential decay in every sample tested, with most of the current decay occurring in the first 30 minutes after which, 30% to 70% of the initial current had been lost.

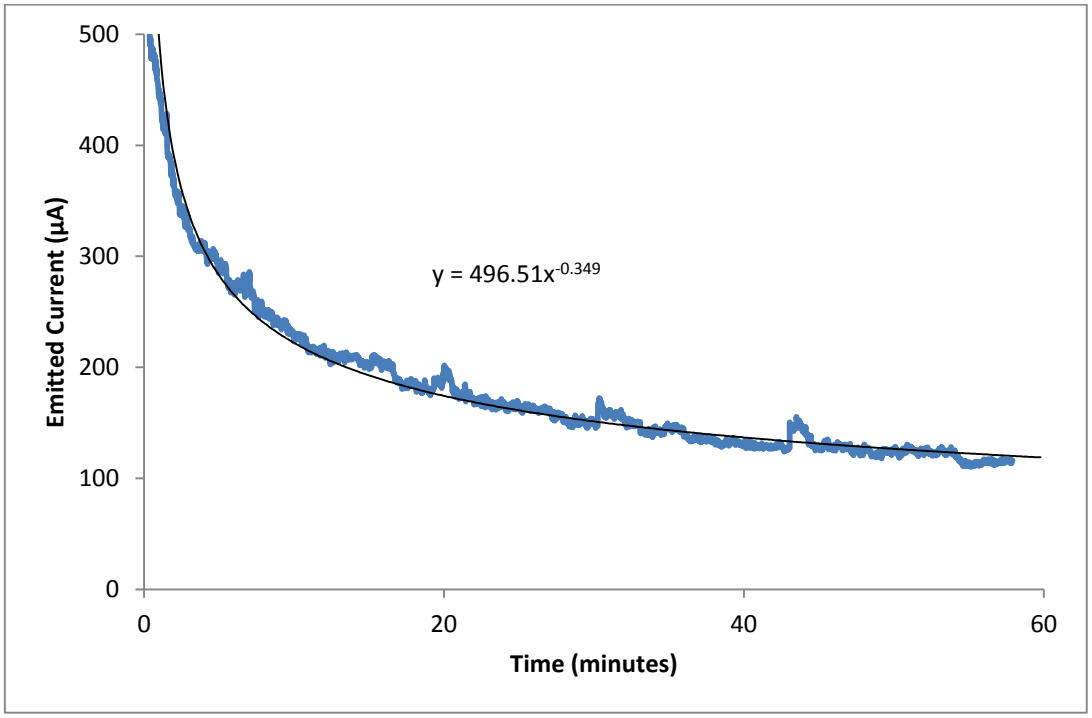

Figure 137. Graph showing the current degradation of a typical sample (in this case sample N28) when an initial current of 500µA was emitted and then held at a constant voltage. Current decays exponentially and fluctuates significantly showing the relatively long term unstable field emission properties of CNTs.

There did not appear to be any correlation between E_{TO} value, I_D/I_G ratio, or overall film morphology and rate of current decay. There was no visible change in SEM micrographs after field emission.

There is an inverse linear relationship between initial current decay rate and the final current recorded after 60 minutes of continuous emission (Figure 138). If a sample experiences rapid current decay in the first few minutes of emission, then a lower end current compared to a sample that experienced only modest initial current decay is to be expected. There is however a considerable spread in the data shown in Figure 138, which

indicates that the long term continuous emission process of CNT films is unstable and erratic.

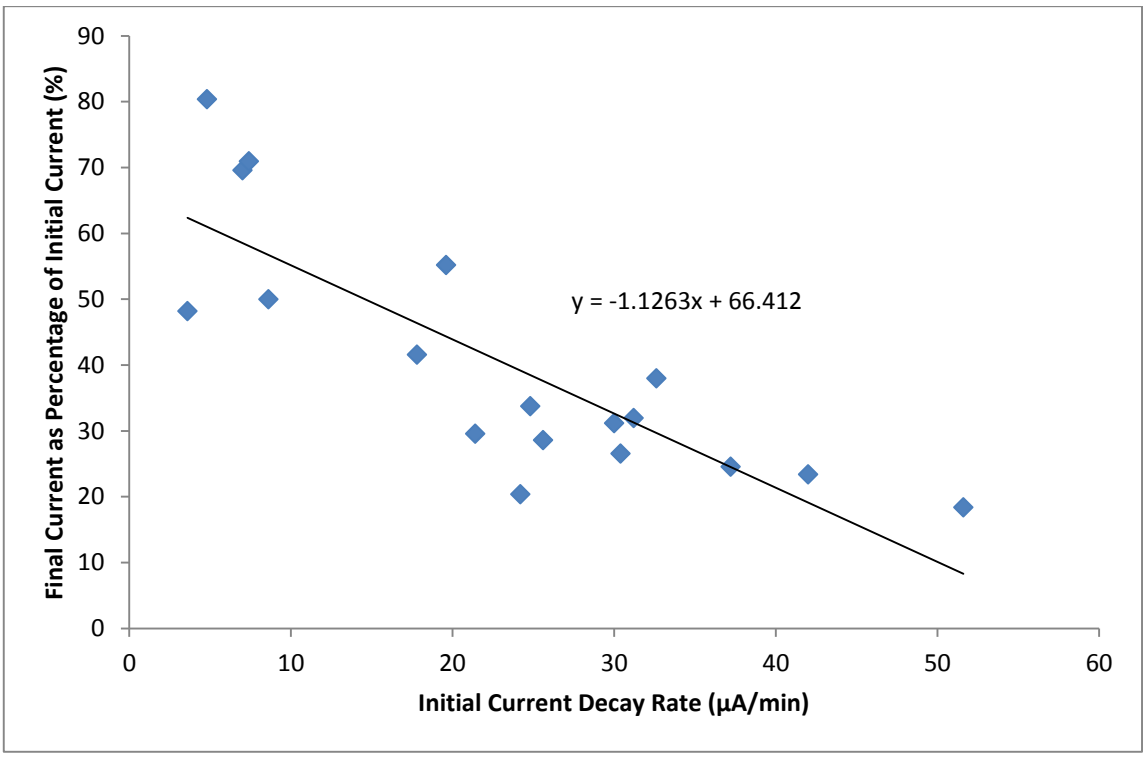

Figure 138. Graph showing the relationship between the current decay rate and final current as percentage of initial current. There is clearly a linear inverse relationship which is to be expected.

The longevity of samples in this study appear to be worse than those found in the literature [45, 75, 204]. The two main parameters that appear to change from article to article is that of the current density at the start of the lifetime experiment, and the pressure of the system. At higher currents, Joule heating means that the tips of the CNTs can become damaged. At higher pressures, the electric field concentrated at CNT tips attracts absorbents from the chamber and at higher electric fields, plasma can form and ion bombardment – all of which degrade CNTs dramatically [189]. Other research groups that use similar pressure to work in this thesis start lifetime experiments at currents less than 100µA/cm^2 [75, 204]. They tend not to see any degradation with time. Nevertheless, lifetime experiments are often used simply as verification that the cathode device

fabricated can operate over long periods of time, rather than for a deeper scientific understanding.

5.4. Emission area measurements using a phosphor tube

The aluminium anode was replaced with a glass tube with a green phosphor coating and an indium tin oxide (ITO) undercoating so that the multilayer structure is glass/ITO/phosphor (Figure 139). The ITO is designed to be transparent and conductive so that light emitted from the phosphor can escape the device, whilst being conductive so that current can flow and measured. A P43 gadolinium oxysulphide: terebium (Gd_2O_2S:Tb) phosphor was chosen as this emits light at a wavelength of 544nm (green). A green phosphor was chosen as these types of phosphors are known for being the most efficient. A white phosphor will have a lower efficiency as it contains red phosphor and it is the red phosphor which limits the efficiency. Whilst the phosphor tube has a higher resistance than the aluminium tube, E_{TO} values can still be compared to those measured with the aluminium tube as the resistance of the system is high at low electric fields (*i.e.* before field emission has begun).

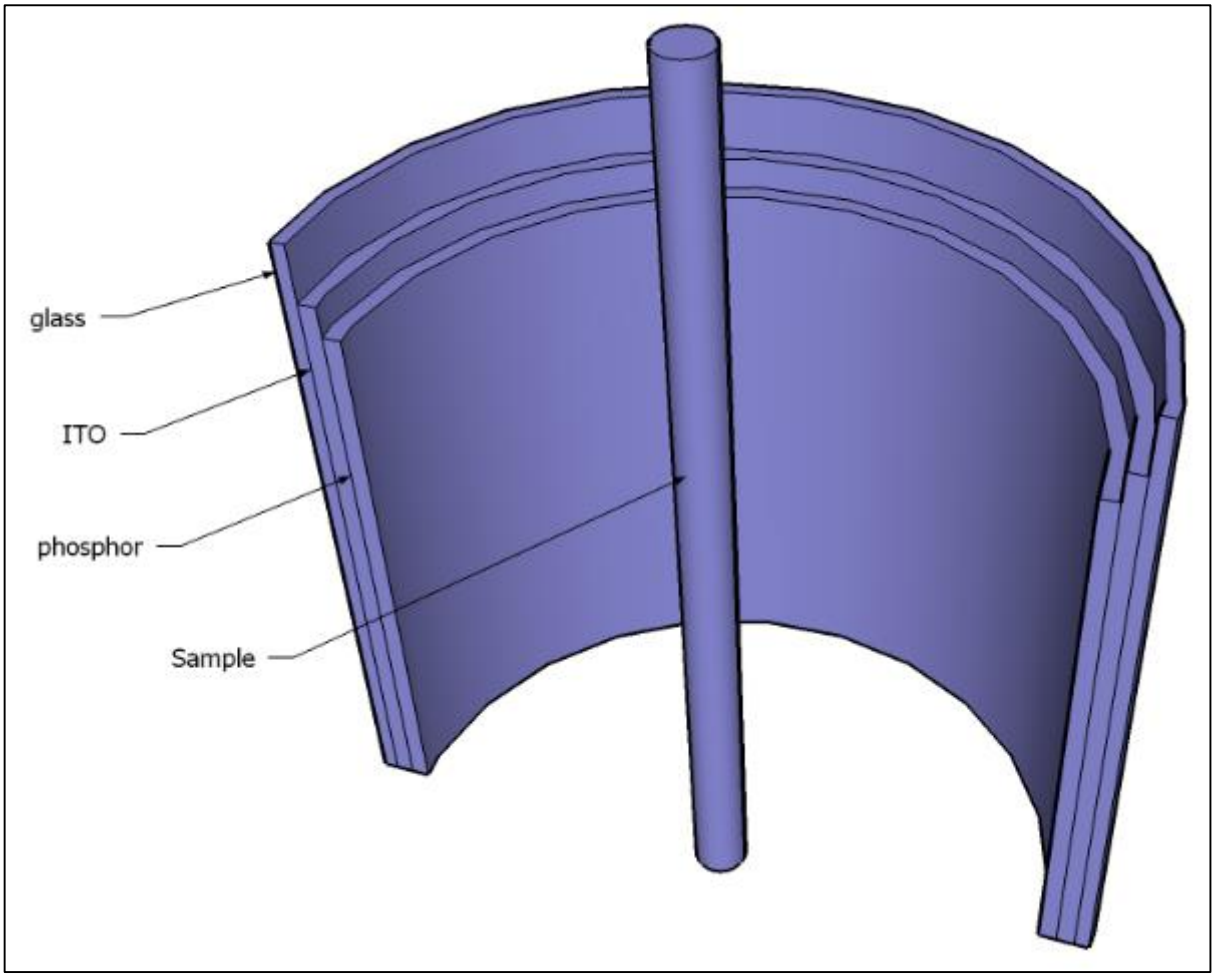

Figure 139. A cross section of the tube described in Figure 105, except the aluminium anode tube has been replaced with a glass/ITO/phosphor multilayer structure so that light emission can be obtained and an indication to emission area explored.

Experiments were conducted in the same way as previously for field emission experiments, and as the voltage applied to the system was increased, a camera was used to record the pattern observed on the phosphor screen. Videos were captured in real time and show how bright spots on the phosphor evolve with increasing current. Snapshots of the video were taken just before the point at which full luminosity occurs (if it does) to show the maximum number of phosphor spots in a particular experiment. Sample N42 shown in Figure 140 was chosen to be tested in the phosphor screen experiment initially, as this morphology closely represents the "flat" type situation described in Section 5.3.1.1 (page 150). Figure 140 shows the morphology of the CNT

film prior to the field emission experiment, and hardly any protruding CNTs were observed. The sample has an E_{TO} value of 3.06V/μm which is poor compared to most samples, but consistent with the fact that there are few, if any, protruding CNTs. As the voltage is increased, a few bright spots are observed (Figure 141a) and as the voltage is increased further, very few additional bright spots are observed (Figure 141b). Maximum luminosity is achieved at an E value of 4.94V/μm and a current density on the cathode of 135μA/cm^2 (Figure 141c).

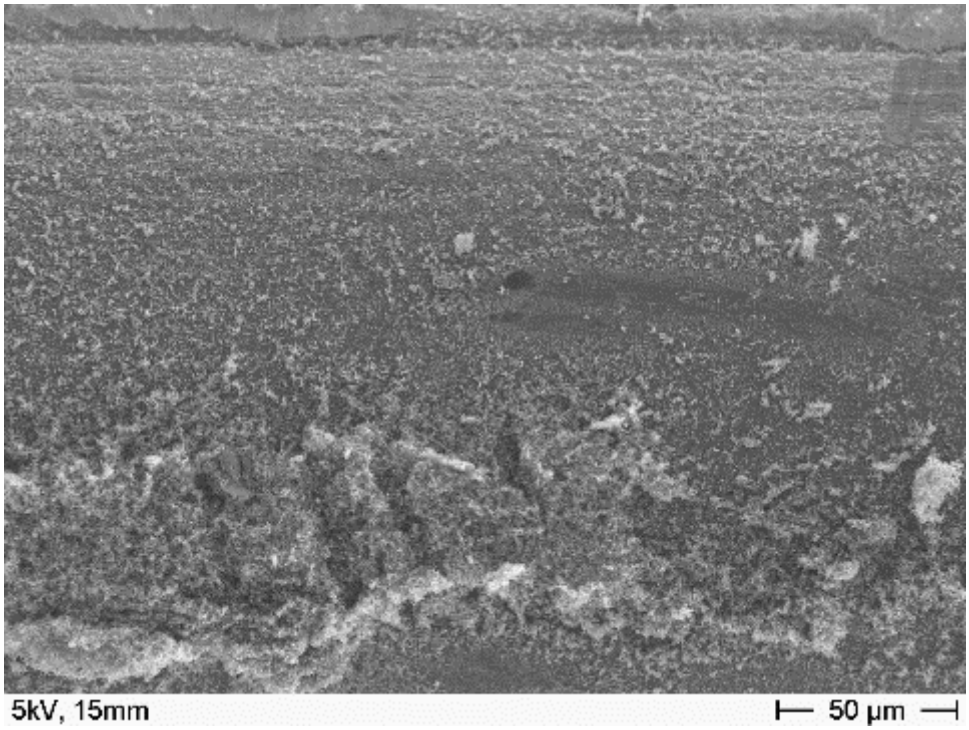

Figure 140. SEM micrograph of sample N42 that shows a flat surface morphology. No protruding CNTs are observed.

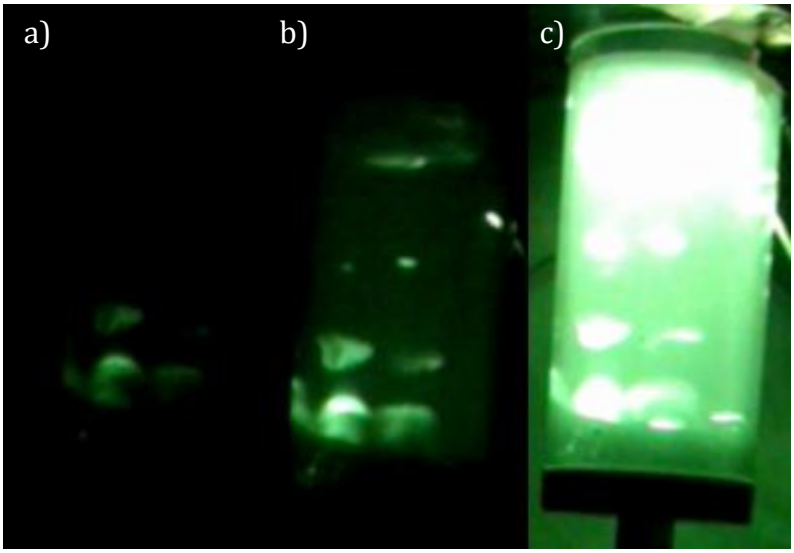

Figure 141. Phosphor screen patterns for sample N42 at "turn on" (a), at ~3.40V/μm and at maximum brightness at ~4.94V/μm (c).

Samples belonging to each morphological category (*i.e.* individual, clump, tower and ridge) were tested in the same manner. Sample N38b contains individually separated CNTs (Figure 142), and the corresponding phosphor patterns observed are shown in Figure 143. The sample has an E_{TO} value of 1.14V/μm which is consistent with the repeated experiments using an aluminium anode, and this relatively low value is due to the aligned protruding CNTs. Few bright spots are observed initially on the phosphor (Figure 143a), which implies that only a few CNTs participate in the field emission process in this particular sample. As the voltage is increased further, these same spots become brighter (Figure 143b). Maximum brightness is achieved at an E value of ~1.80V/μm with a current density on the cathode of 920μA/cm^2 (Figure 143c). As the voltage is reduced from maximum brightness, phosphor circles and lines are observed (Figure 143d). This is due to heating of several thousand degrees near the tip of the CNT [145, 205, 206].

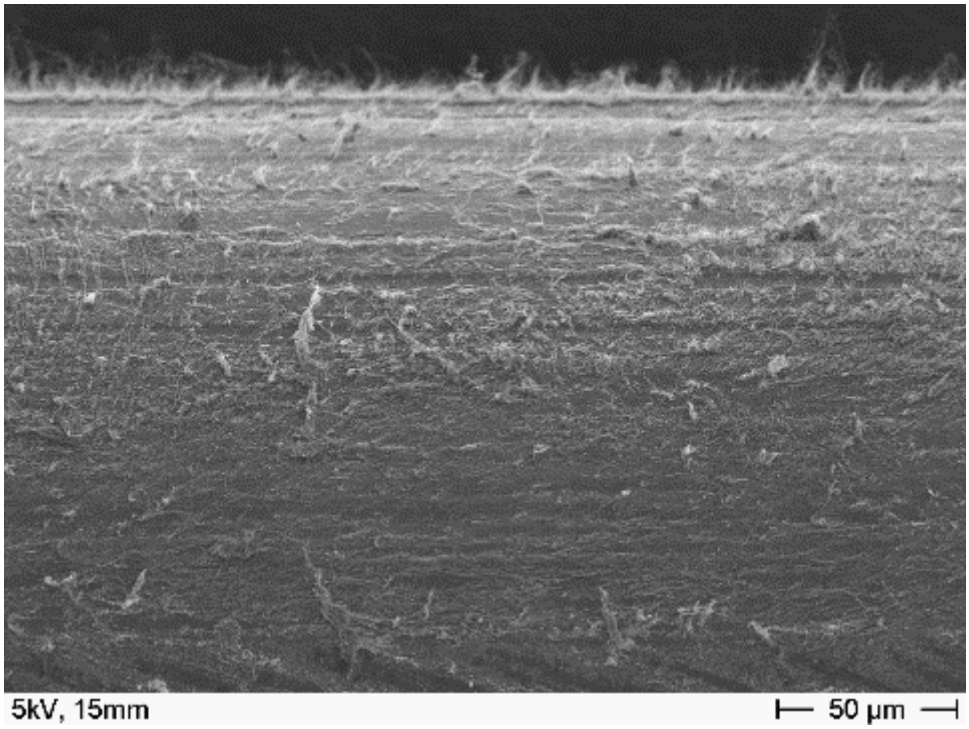

Figure 142. SEM micrograph of sample N38b showing individually separated CNTs aligned perpendicular to the Kanthal wire surface.

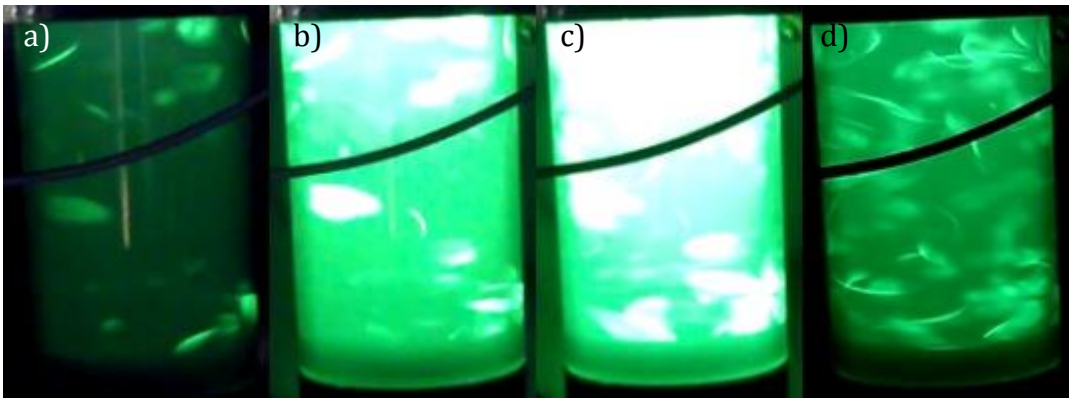

Figure 143. Phosphor patterns for sample N38b at "turn on" (a), at 1.45V/µm the same spots are brighter (b), at maximum brightness at 1.80V/µm with emitted current density on the cathode of 920µA/cm² (c). As the voltage is reduced after maximum brightness, circles and lines are observed (d). The dark line on each image is an artefact of the experimental setup and was removed for subsequent experiments.

Sample N45 was tested in the same manner, and Figure 144 shows the morphology of this clump sample and Figure 145 the corresponding phosphor patterns at various voltages. The density of bright spots has increased compared to earlier samples, and the size of the spots has also decreased (Figure 145a). Full uniform luminosity was achieved

at an E value of 4.16V/μm with a current density of 2.75mA/cm^2 on the cathode (Figure 145b). An E_{TO} value of 1.86V/μm was observed which is not as low as sample N38b. This is unusual as sample N38b produced larger, and fewer bright spots. Figure 145c shows the phosphor pattern immediately after full luminosity as the voltage is decreasing and shows an increase in the number of spots compared to at "turn on". As the voltage is decreased still further, the number of spots decreases, as emitters are turned off (Figure 145d).

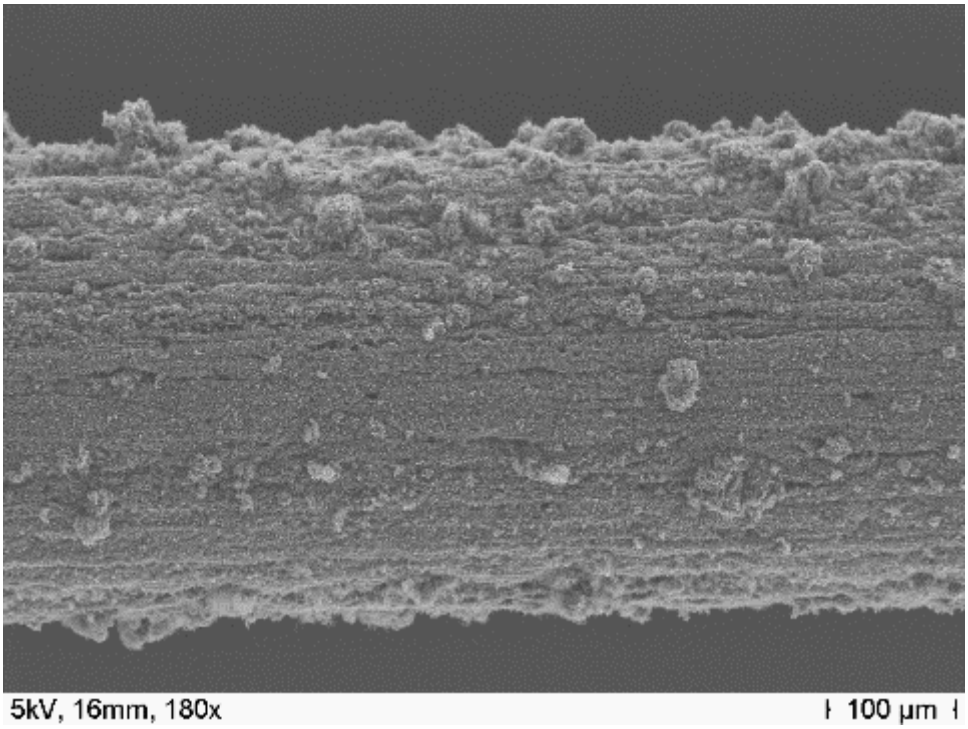

Figure 144. SEM micrograph of sample N45 which represents a clump morphology.

Sample N48 shows a tower type morphology (Figure 146) and the corresponding phosphor patterns can be seen in Figure 147. The bright spots are a similar size to those in sample N45 (Figure 147a). As the voltage is increased further, full luminosity is achieved at an E value of 4.06V/μm at a current density of 3.32mA/cm^2 on the cathode (Figure 147b). As the voltage is decreased from the maximum, no spots are observed (Figure 147c), instead a band of light is observed near the centre of the device. This sample has an E_{TO} value of 2.56V/μm which is higher than for the clump sample.

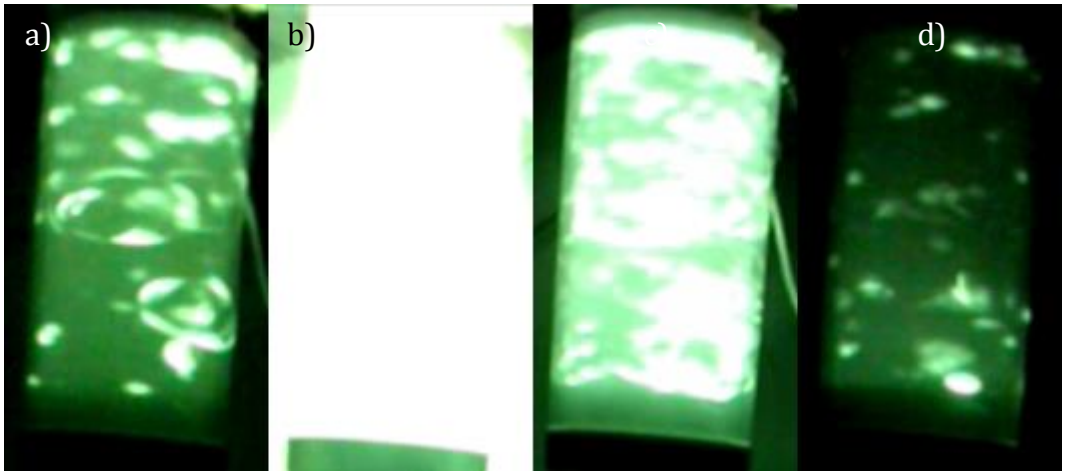

Figure 145. Phosphor patterns for sample N45 immediately after "turn on" which shows more active emission sites compared to previous samples (a). Full luminosity is achieved at an E value of 4.16V/μm and a current density on the cathode of 2.75mA/cm^2 (b). Similar emission sites are present immediately after full luminosity and as the voltage is decreased (c).

When this sample was removed it was observed that a white deposit appeared on the cathode (Figure 148a) and black particles were seen on the inside of the anode phosphor tube (Figure 148b). Faceted particles of the order of several microns were observed by SEM on the surface of the CNT film (Figure 146). EDX reveals that these particles contain elements which were in the phosphor coating (Figure 149). It was discovered that there was a spike in the voltage being delivered to the device during the brightest parts of the experiment, and this corresponded to a spike in the emitted current.

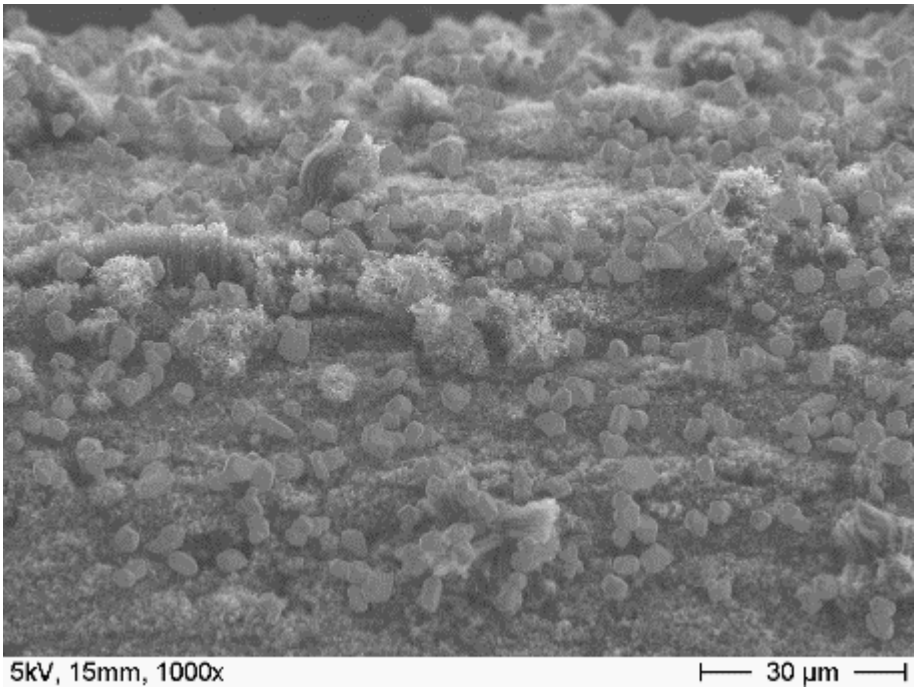

Figure 146. SEM micrograph of sample N48 which represents a tower morphology. Faceted phosphor particles are observed on the surface of the sample after the phosphor tube experiment occurred.

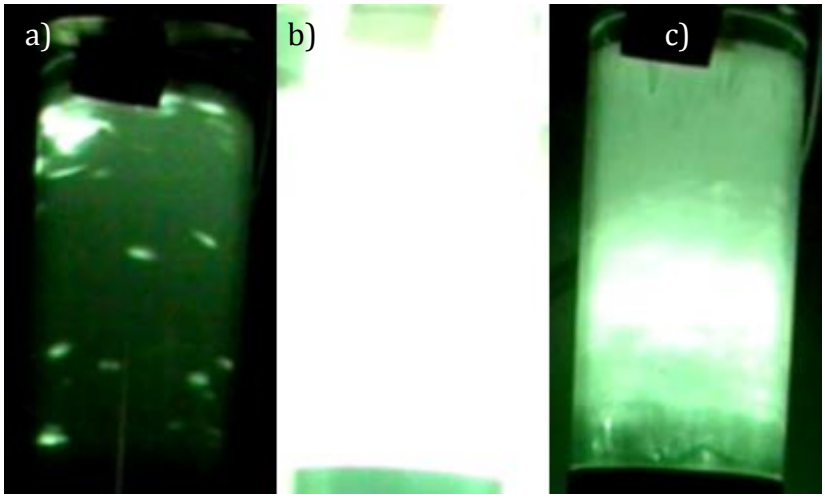

Figure 147. Phosphor patterns for sample N48 which shows spots that are of a similar size and density to sample N45 (a). Full luminosity is achieved at an E value of 3.85V/µm and a current density of 1.73mA/cm^2 on the cathode (b). A band of emission occurs in the centre of the device as the voltage is decreased (c).

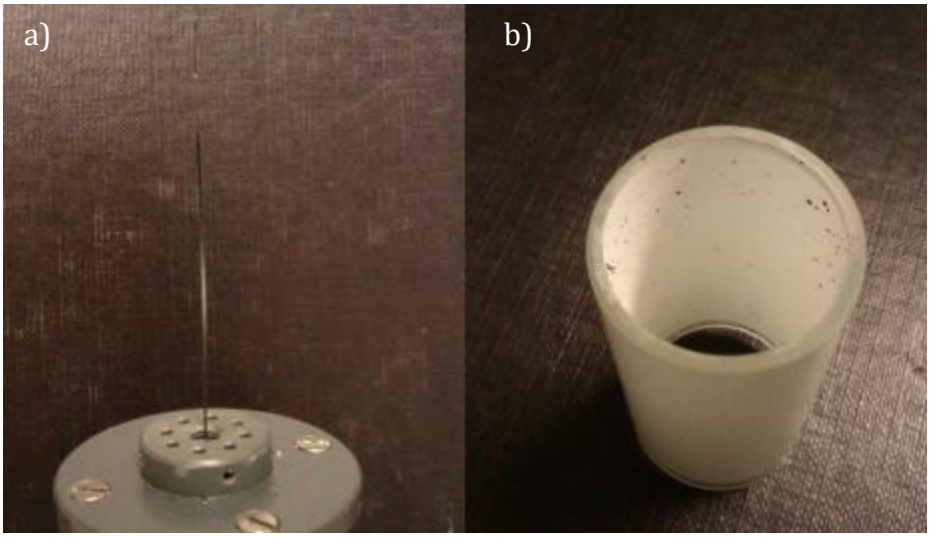

Figure 148. Photographs of sample N48 after a phosphor emission experiment showing the cathode material coated in a white substance (a), and the inside of the anode showing black particles deposited (b).

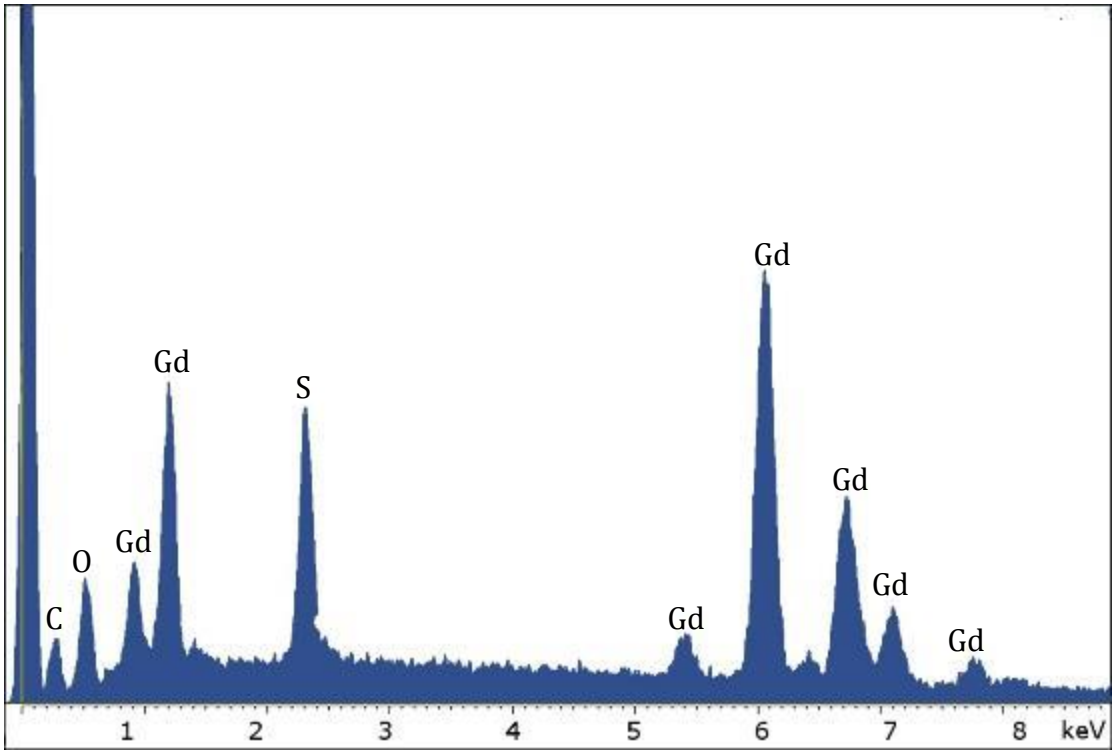

Figure 149. EDX spectrum of the particles found on sample N48 after field emission experiment using a phosphor coated glass tube as the anode. Elements found in these particles match those of the phosphor tube coating and this indicates that the phosphor coating sputtered onto the sample cathode.

The local E value, near the cathode reached ~26V/μm with a peak current density on the cathode surface of ~3.42mA/cm^2. It is likely that during such high electric fields and current, phosphor particles were sputtered onto the surface of the cathode.

Sample N41 exhibits a ridge type morphology (Figure 150) and the corresponding phosphor patterns can be seen in Figure 151. This sample has an E_{TO} value of 1.20V/μm and there are fewer bright spots than previous samples, possibly due to a few CNTs contributing to the field emission current (Figure 151a). Full luminosity is achieved at an E value of 3.32V/μm and at a current density of 2.59mA/cm^2 on the cathode (Figure 151b). Lines appear as the voltage is decreased from maximum brightness (Figure 151c).

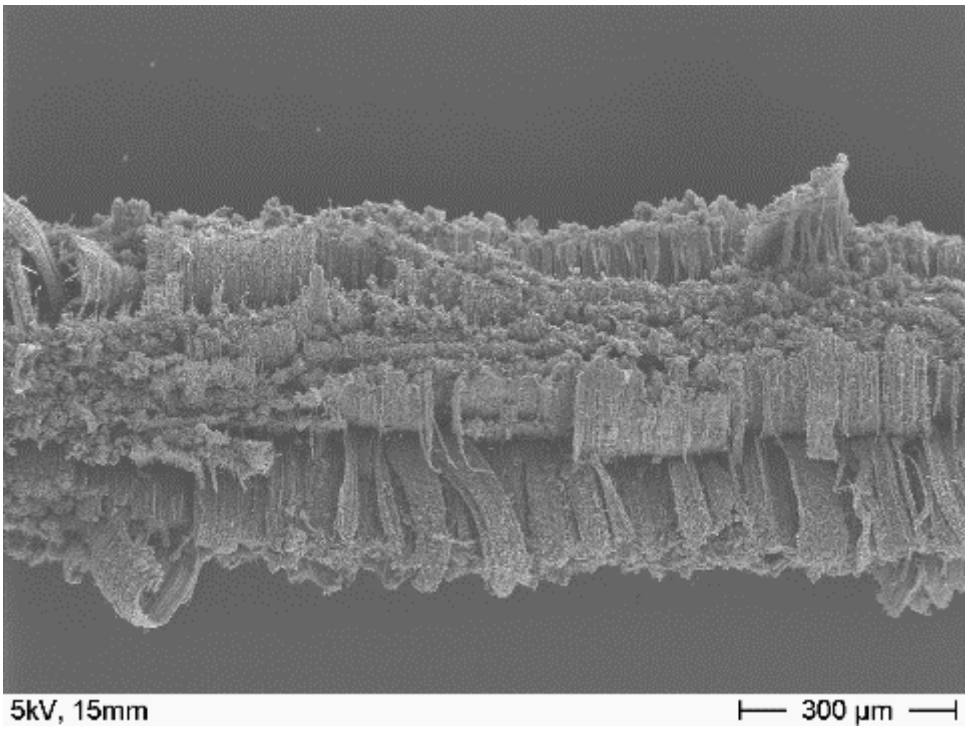

Figure 150. SEM micrograph of sample N41 which represents a ridge morphology.

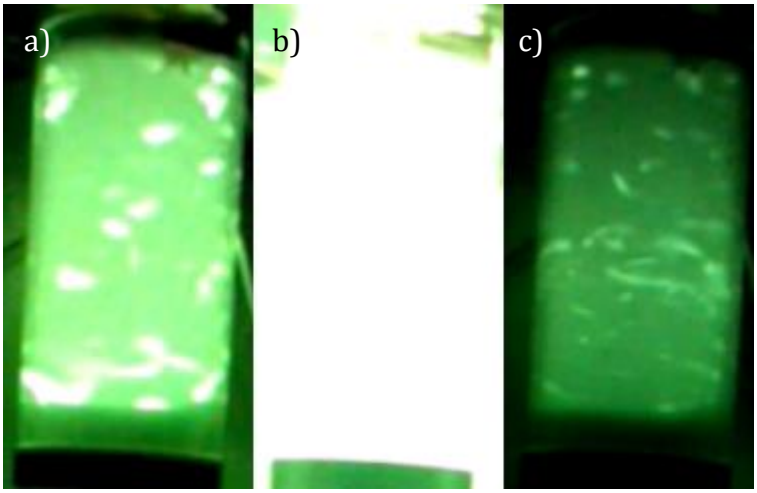

Figure 151. Phosphor patterns for sample N41 shows fewer spots compared to previous samples (a). Full luminosity is achieved at an E value of 3.32V/μm and at a current density of 2.59mA/cm^2 on the cathode (b). Lines appear as the voltage is decreased after maximum brightness (c).

5.4.1. Summary of the Emission Area Measurements Using a Phosphor Tube

A phosphor tube was used as the anode to assess the lighting capabilities of CNT films and lighting homogeneity. A ridge sample achieved the lowest electric field value at full luminosity of 3.32V/μm, followed by a tower sample at 3.85V/μm, and a clump sample at 4.16V/μm. The sample that produced protruding CNTs using a "pull off" technique did not achieve full luminosity, this is likely due to too few CNTs contributing to the emitted current.

Large spots are observed on the phosphor tube that do not correspond to individual CNTs because literature suggests that there should be at least 10^4 emitters per cm^2. Liu *et al* [207] used pixels on a phosphor screen that are 200μm in diameter and conclude that there are tens or even hundreds of emitting CNTs (assuming that a single emission site refers to a single CNT) in a pixel. Therefore a single spot on the phosphor tube in this study is actually more likely to be several CNTs.

It could be that a single spot represents protruding CNTs around a tower or ridge that is taller than surrounding structures. Retrieving more information from each spot is

difficult because the resolution is limited by the grain size of the phosphor and because of the cylindrical geometry, the electron beam from an emitter will spread outwards as it reaches the anode.

5.4. Chapter Conclusions

The morphologies that were identified in the previous chapter were tested for their field emission properties and the results discussed. It was found that more open, rough morphologies resulted in improved field emission properties (lower E_{TO} values) with the lowest E_{TO} value of 0.35 V/μm achieved for a ridge sample of CNT length ~425 μm and I_D/I_G ratio of 0.67. The worst performing sample had E_{TO} value of ~3.69 V/μm which had a very high I_D/I_G ratio of 1.19 and very short CNTs of only a few microns. Microstructures such as towers and ridges help enhance the field enhancement factor of the system by increasing the probability of protruding CNTs at their edges and by spacing these CNTs apart, thereby reducing screening. A combination of long CNTs and ridge type morphologies resulted in the samples with the lowest E_{TO} values.

A quantifiable number for the field enhancement factor is not a useful figure of merit as it is derived from the emitting area, which is difficult (if not impossible) to measure as the emitting area is unknown and there may be different emitted currents from different regions of the sample surface due to the variation in the local electric field. E_{TO} value is a more useful parameter to assess the "quality" of the emitting samples as it is more directly related to the performance of the final device. For example, E_{TO} value could be similar to the 'switch on' of the lighting device.. Also, it is difficult to compare with planar samples as such samples would not contain so many protruding and separated CNTs due to crowding effects and because no CNTs will be growing radially.

CNT films degraded faster than those found in the literature and there was no correlation between degradation of emitted current or CNT properties. It is likely that the starting

current used for longevity tests was too high, and CNTs heated up and evaporated, causing thermal runaway. This resulted in a premature decay compared to if the starting current was lower. Along with E_{TO}, the lifetime of the emitting films is important for the final device and would provide a useful means of comparing emitting samples as a way of choosing which sample would be better for a lighting device.

The aluminium anode tube was replaced with a phosphor tube to study the emission area of samples and to produce a lamp. Full luminosity was achieved and it was revealed that only a few phosphor spots are visible during emission, before full luminosity is achieved. This indicates that clusters of CNTs are emitting for each phosphor spot, potentially around the edge of a tall tower, or along a tall ridge.

Introducing a phosphor screen at the anode is challenging, especially for higher emitted currents as the resistance of the screen becomes significant. It is likely that the heat dissipated during these experiments in the phosphor screen contributed to the increase in pressure of the experiment. This resulted in premature failure of the device. The phosphor screen experiments are only useful as an attempt to produce a working prototype. It is better for the aluminium anode to be used in assessing what CNT films are better emitters as the resistance is low, and it is assumed that the luminosity of the final device is a function of the emitter current.

6. Summary, Conclusions and Future Work

6.1. Summary and Conclusions

In this study, both continuous films of CNTs and individual CNTs were investigated for their use as efficient field emitters for implementation in a direct field emission lamp. Modern compact fluorescent lamps rely heavily on thermionic emission to achieve sufficient current for luminosity. They also rely on a small amount of mercury vapour which produces UV light from the gas discharge, which is then converted to visible light by the phosphor tube. A direct field emission lamp requires no external heating, no mercury and is dimmable.

CNT direct field emission lamps have already been fabricated [161-163, 208], however there appears to be little optimisation of such devices and little understanding how CNT film morphology affects field emission properties, which is important to understand how to improve such devices. Demonstration of "one off" working devices, rather than a comprehensive study of how CNT film morphology affects field emission properties appears to have been the priority in the literature. This is the first study investigating how different "as grown" CNT film morphologies on various wires influence their field emission properties.

It is difficult to compare results for CNT films with those found in the literature because the experimental setup is different. It is uncertain how many emitters are contributing to the measured current, and there are different definitions of the turn-on field. To add to this confusion, when the anode-cathode separation distance is less than 3 times the height of the emitter, the field enhancement factor is no longer a fixed value and actually decreases due the system approximating a planar state [209]. This investigation attempted to overcome these difficulties by comparing the field emission properties of

various “as grown” CNT morphologies and of individual CNTs in one study (*i.e.* keeping the experimental setup the same).

An aerosol CVD technique was utilised to grow CNT films on Kanthal wire as this technique is simple, cheap, and easily scalable [210]. Kanthal wire is used as heating coils in furnaces due to its stability at high temperatures, but has been shown to be a good support for CNT growth due to the inertness of its surface with respect to iron catalyst particles[165]. 5wt% ferrocene dissolved in toluene was atomised in an ultrasonic generator and carried into a furnace using a carrier gas of 1 SLM argon at 800°C for ten minutes as the standard set of growth parameters. Toluene was replaced by benzylamine for the growth of nitrogen doped CNTs and by a 1M trimethylborane (TEB) solution in hexane for the growth of boron doped CNTs. Each growth parameter was changed and the CNT morphology and defect density was characterised with respect to its deposition position inside the furnace; growth temperature; adding hydrogen to the carrier gas; and catalyst concentration. Characterisation was by SEM and Raman scattering spectroscopy. CNT morphology was most sensitive to growth temperature, growth time and precursor used. Defect density was most sensitive to the addition of hydrogen to the carrier gas and the precursor used. Temperature and time is a function of displacement inside the furnace and so these two parameters can be changed by simply changing where the substrate is. CNT morphology will dictate the field enhancement factor of the system whereas the defect density will dictate the work function of the CNT film, both of which are important in the field emission process. When hydrogen is added to the carrier gas when making undoped CNTs, it removes amorphous carbon and defective CNTs due to an etching effect. As these types of carbon are more reactive, these are removed preferentially to graphitic carbon. When hydrogen is added to the carrier gas for the growth of doped CNTs, it has the opposite effect and the defect density increases. It is

suggested that this is due to the hydrogen reacting with the nitrogen in the N-CNTs to produce ammonia. When benzylamine or TEB is used, this introduces nitrogen or boron into CNTs respectively which introduces defects in the CNT structure by changing the coordination number and introducing strain.

Three distinct "as grown" morphological types were identified. They were named as 'clumps', 'towers' and 'ridges'. Clumps were observed when toluene was used and are a result of CNTs entangling with each other. They are most likely formed due to the roughness of the Kanthal wire surface. Catalyst particles nucleate on this rough surface and grow CNTs at different angles to each other, creating an entangled clump. When benzylamine is used as the precursor, clumps are far less likely to form and towers (vertically aligned bundles) form instead, due to the N-N bonding that ensures CNTs adhere to each other while they grow. Ridges of closely packed, vertically aligned CNTs form if the CNTs are sufficiently long (greater than 35μm and up to 525μm) and they have a propensity to adhere to each other. The formation of these structures is a result of the curvature of the wires upon which they are grown. Ridges were seen to grow when the length of the CNTs were as short as 35μm when benzylamine was used.

The field emission properties of CNT films are dominated by the existence of protruding CNTs and the various different CNT film morphologies act to either increase or decrease the existence of such CNTs, and to space them so that screening affects are minimised. Ridges and towers are the best structures for this purpose. A simple model was made in COMSOL where the microscopic tower geometries involved were considered, firstly for a single tower, then for an array of towers. When the height of the towers for an array was kept the same and the inter tower distance was less than twice their height, screening effects meant that the electric field at the corners of the tower was reduced. By adjusting the average height of the towers to match that of a sample, it was shown that the electric

field is enhanced greatly in comparison to when there is no variation in the height of the towers. This means that most of the emitted current is from protruding CNTs found at the corners of the tallest towers.

Varying levels of electron irradiation were inflicted on individual CNTs *in situ* in a TEM to investigate the role of defects on field emission properties. The introduction of a limited number of defects into the existing graphitic structure resulted in a slightly lower work function. EELS reveals that, upon irradiation of the CNT tip, the sp^2 peak reduces significantly implying that the graphitic C-C bonding is disrupted in this region. This is confirmed by TEM showing that the walls of the CNT are distorted. Defects in the CNT structure can result in localised density of states (LDoS) being introduced near the Fermi Level which therefore results in the effective work function decreasing.

High intensity electron irradiation resulted in the entire structure at the tip reassembling resulting in a change in the geometry. It was possible to determine that the effective work function had significantly increased by comparing CNTs before and after high intensity irradiation because the CNT tip had not changed shape. EELS showed that the sp^2 peak had disappeared and it is assumed that the structure had become amorphous as TEM showed no visible walls. This is not certain however, as the TEM did not have a very high resolution. By making the damaged CNT emit electrons for 5 minutes, the turn-on field is enhanced. This is most probably due to recrystallization of the CNT tip as the sp^2 peak reappears. A peak current of 20μA was observed during this process and the recrystallization is due to heating of the CNT tip due to the Nottingham effect [68].

CNT film emitter lifetime was poor compared to the literature [138, 157, 211]. With a starting current of 500μA, there was an exponential decay in every sample tested, with most of the current decay occurring in the first 30 minutes, after which 30% to 70% of the initial current had been lost. This same rate of decay was not observed in the field

emission testing of individual CNTs that were taken from these CNT films indicating that something other than damage to the CNTs themselves is causing this decay. The decay observed for CNT films is either caused by the pressure used for this experiment (10^{-6} mbar) which tended to be an order of magnitude higher than articles which state a long lifetime of several hours [157, 199], or due to a poor CNT-substrate connection (*i.e.* conductivity). Emitter lifetime could be significantly shorted by such high pressures due to ion bombardment. If the CNT-substrate interface has a high resistance, then heat is generated when a current flows. This could result in the destruction of the emitter due to thermal runaway.

The lowest turn-on field in this study was 0.35 V/μm, due to a low defect density (I_D/I_G of 0.67) and long CNTs of length 425μm. This was achieved using a solution of 1% benzylamine and 99% toluene with 5wt% ferrocene at a growth temperature of 900°C for ten minutes using a 1:0.2 SLM ($Ar:H_2$) carrier gas, and is in line with that found in the literature [63, 212]. The highest turn-on field was 3.69 V/μm and was a result of the high defect density (I_D/I_G ratio of 1.19) and short CNTs that were less than a few microns.

6.2. Future Work

Whilst the emphasis in this project has been towards the development of a direct field emission lamp, the work described in this thesis can be translated to other applications that rely on field emitters such as displays, X-ray generators, microwave amplifiers and terahertz oscillators. Microwave amplifiers appear to be the most suitable application of the work presented here as they rely on a cylindrical setup for operation. High currents (of the order of 10mA) are needed for this application. This can be achieved with a higher vacuum and/or a better CNT-substrate connection. The latter can be achieved by using a buffer layer on the substrate prior to CNT deposition which helps increase adhesion with the substrate and increase the conductivity of the connection [212].

Other applications such as displays require a patterning technique to fabricate 'cells'. Future work therefore needs to concentrate on controlling the density and spacing of the tower structures that were grown in this work, so that each tower can be activated when needed, via a triode gate. Perhaps using stainless steel wire instead of Kanthal and treating with sulphuric acid so that towers could be grown in areas where the chromium layer is broken as has been shown by Masarapu *et al* [128] on flat stainless steel.

The formation of ridges with higher mutual separation should be maximised which could be achieved by using a thinner wire as the substrate. A thinner wire would have a smaller curvature of radius and hence would maximise separation between ridges. The carbon fibre ribbon used in this study contained individual fibres that were ~10μm in diameter. An individual carbon fibre could be used and pre-treated in hydrogen at elevated temperatures to remove any surface contaminations. Carbon fibre as thin as ~10μm is difficult to handle and so a method would need to be developed which would address this. The recrystallization of individual CNT tips have important implications for emitting devices. Further work on optimising emission current density needs to be undertaken to see if this effect is up-scalable, so prolonging the life time of the emitters.

References

1. Jacobson, M.Z., *Review of solutions to global warming, air pollution and energy security.* Geochimica Et Cosmochimica Acta, 2009. **73**(13): p. A581-A581.
2. Soutis, C., *Fibre reinforced composites in aircraft construction.* Progress in Aerospace Sciences, 2005. **41**(2): p. 143-151.
3. Forsyth, E.B., *Superconducting Power Transmission-Systems - the Past and Possibly the Future.* Superconductor Science & Technology, 1993. **6**(10): p. 699-714.
4. Zeng, B., et al., *Field emission of silicon nanowires grown on carbon cloth.* Applied Physics Letters, 2007. **90**(3): p. 90.
5. Kroto, H.W., et al., *C-60 - Buckminsterfullerene.* Nature, 1985. **318**(6042): p. 162-163.
6. Iijima, S., *Helical microtubules of graphitic carbon.* Nature, 1991. **354**(6348): p. 56-58.
7. Novoselov, K.S., et al., *Electric field effect in atomically thin carbon films.* Science, 2004. **306**(5696): p. 666-669.
8. Balaban, A.T., D.J. Klein, and X. Liu, *Graphitic Cones.* Carbon, 1994. **32**(2): p. 357-359.
9. Boskovic, B.O., et al., *Large-area synthesis of carbon nanofibres at room temperature.* Nature materials, 2002. **1**(3): p. 165-168.
10. Jadhav, A.D., S.B. Ogale, and B.L.V. Prasad, *Carbon nano horn and bovine serum albumin hierarchical composite: towards bio-friendly superhydrophobic protein film surfaces.* Journal of Materials Chemistry, 2008. **18**(29): p. 3422-3425.
11. Nakada, K., et al., *Edge state in graphene ribbons: Nanometer size effect and edge shape dependence.* Physical Review B - Condensed Matter and Materials Physics, 1996. **54**(24): p. 17954-17961.
12. Zhou, O., et al., *Generation of continuous and pulsed diagnostic imaging x-ray radiation using a carbon-nanotube-based field-emission cathode.* Applied Physics Letters, 2002. **81**(2): p. 355-357.
13. Ramaccia, D., F. Bilotti, and A. Toscano, *Boosting PV cell performances by using horn nano-concentrators.* 2012 Ieee Antennas and Propagation Society International Symposium (Apsursi), 2012.
14. Boskovic, B.O., et al., *Low temperature synthesis of carbon nanofibres on carbon fibre matrices.* Carbon, 2005. **43**(13): p. 2643-2648.
15. Amaratunga, G., *Watching the Nanotube.* IEEE Spectrum, 2003. **40**(9): p. 28-32.
16. Croci, M., et al., *A fully sealed luminescent tube based on carbon nanotube field emission.* Microelectronics Journal, 2004. **35**(4): p. 329-336.
17. Edison, T., *Method of Manufacturing Electric Lamps*, U.S.P. Office, Editor. 1880.
18. Works, H.S. *Light Bulb*. 2002; Available from: http://home.howstuffworks.com/light-bulb1.htm.
19. Yih, S.W.H. and C.T. Wang, *Tungsten: Sources, Metallurgy, Properties, and Applications*. 1979, New York: Plenum Press.
20. Sarangi, D., C. Hierold, and A. Karimi, *Carbon nanotubes over metallic wires and its possible applications.* Fullerenes Nanotubes and Carbon Nanostructures, 2005. **13**: p. 243-254.
21. de Jonge, N. and J.M. Bonard, *Carbon nanotube electron sources and applications.* Philosophical Transactions of the Royal Society of London Series a-Mathematical Physical and Engineering Sciences, 2004. **362**(1823): p. 2239-2266.
22. Gomer, R., *Field Emission and Field Ionization*. 1961: American Institute of Physics.

23. Smith, R.C. and S.R.P. Silva, *Maximizing the electron field emission performance of carbon nanotube arrays.* Applied Physics Letters, 2009. **94**(13): p. -.
24. Wang, X.Q., et al., *Modeling and simulation for the field emission of carbon nanotubes array.* Physica E-Low-Dimensional Systems & Nanostructures, 2005. **30**: p. 101-106.
25. Read, F.H. and N.J. Bowring, *Field enhancement factors of one-dimensional and two-dimensional arrays of nanotubes.* Microelectronic Engineering, 2004. **73-74**: p. 679-685.
26. Bonard, J.M., et al., *Field emission from carbon nanotubes: the first five years.* Solid-State Electronics, 2001. **45**(6): p. 893-914.
27. Loiseau, A., et al., *Understanding Carbon Nanotubes: From Basics to Application*. 2006: Springer.
28. Harris, P.J.F., *Carbon Nanotubes and Related Structures*. 1999: Cambridge University Press.
29. Subramoney, S., *Novel nanocarbons - Structure, properties, and potential applications.* Advanced Materials, 1998. **10**(15): p. 1157-+.
30. ; Available from: http://www.robaid.com/wp-content/gallery/carbon-nanotubes/mwnt_big-1.jpg.
31. Koos, A.A., et al., *Comparison of structural changes in nitrogen and boron-doped multi-walled carbon nanotubes.* Carbon, 2010. **48**(11): p. 3033-3041.
32. Koós, A.A., et al., *Effect of the experimental parameters on the structure of nitrogen-doped carbon nanotubes produced by aerosol chemical vapour deposition.* Carbon, 2009. **47**(1): p. 30-37.
33. Terrones, H., et al., *Graphitic cones in carbon nanofibres.* Molecular Crystals and Liquid Crystals, 2002. **387**: p. 263-274.
34. Ma, X., et al., *Polymerized carbon nanobells and their field-emission properties.* Applied Physics Letters, 1999. **75**(20): p. 3105-3107.
35. Stephan, O., et al., *Doping Graphitic and Carbon Nanotube Structures with Boron and Nitrogen.* Science, 1994. **266**(5191): p. 1683-1685.
36. Blase, X., et al., *Structural and electronic properties of composite BxCyNz nanotubes and heterojunctions.* Applied Physics a-Materials Science & Processing, 1999. **68**(3): p. 293-300.
37. Qiao, L., et al., *First-principles investigation on the field emission properties of B-doped carbon nanotubes.* Diamond and Related Materials, 2009. **18**(4): p. 657-661.
38. Panchalkarla, L.S., A. Govindaraj, and C.N.R. Rao, *Nitrogen- and boron-doped double-walled carbon nanotubes.* Acs Nano, 2007. **1**(5): p. 494-500.
39. Li, Y.L., et al., *The growth of N-doped carbon nanotube arrays on sintered Al2O3 substrates.* Materials Science and Engineering B-Advanced Functional Solid-State Materials, 2009. **158**(1-3): p. 69-74.
40. Saito, Y. and S. Uemura, *Field emission from carbon nanotubes and its application to electron sources.* Carbon, 2000. **38**(2): p. 169-182.
41. Wei, Y., et al., *Cold linear cathodes with carbon nanotube emitters and their application in luminescent tubes.* Nanotechnology, 2007. **18**(32): p. -.
42. Fu, W.Q., et al., *Spherical field emission cathode based on carbon nanotube paste and its application in luminescent bulbs.* Journal of Vacuum Science & Technology B, 2008. **26**(4): p. 1404-1406.

43. Defra. *Climate Change & Energy*. 2008 03/07/2009]; Available from: http://www.defra.gov.uk/enviroment/climatechange/uk/household/products/cfl.htm.
44. Edgcombe, C.J. and U. Valdre, *Experimental and computational study of field emission characteristics from amorphous carbon single nanotips grown by carbon contamination - I. Experiments and computation.* Philosophical Magazine B-Physics of Condensed Matter Statistical Mechanics Electronic Optical and Magnetic Properties, 2002. **82**(9): p. 987-1007.
45. Bonard, J.M., et al., *Field emission from carbon nanotubes: Perspectives for applications and clues to the emission mechanism.* Applied Physics A: Materials Science and Processing, 1999. **69**(3): p. 245-254.
46. Chen, Y., D.T. Shaw, and L.P. Guo, *Field emission of different oriented carbon nanotubes.* Applied Physics Letters, 2000. **76**(17): p. 2469-2471.
47. Chai, G.Y. and L. Chow, *Electron emission from the side wall of an individual multiwall carbon nanotube.* Carbon, 2007. **45**(2): p. 281-284.
48. De Vita, A., et al., *Electronic structure at carbon nanotube tips.* Applied Physics a-Materials Science & Processing, 1999. **68**(3): p. 283-286.
49. Bonard, J.-M., et al., *Field emission from carbon nanotubes: perspectives for applications and clues to the emission mechanism.* Applied Physics a-Materials Science & Processing, 1999. **69**: p. 245-254.
50. Jo, S.H., et al., *Field emission of carbon nanotubes grown on carbon cloth.* Journal of Vacuum Science & Technology B, 2005. **23**(6): p. 2363-2368.
51. Pan, L., et al., *Field emission properties of titanium carbide coated carbon nanotube arrays.* Advanced Engineering Materials, 2007. **9**(7): p. 584-587.
52. Song, J.H., et al., *Field emission from carbon nanotube arrays fabricated by pyrolysis of iron phthalocyanine.* Journal of Physics D-Applied Physics, 2004. **37**(1): p. 5-9.
53. Chen, G.H., et al., *Enhanced field emission properties of vertically aligned double-walled carbon nanotube arrays.* Nanotechnology, 2008. **19**(41): p. -.
54. Somani, S.P., et al., *Field electron emission of multiwalled carbon nanotubes and carbon nanofibers grown from Camphor.* Solid-State Electronics, 2008. **52**(6): p. 941-945.
55. Seelaboyina, R., J. Huang, and W.B. Choi, *Enhanced field emission of thin multiwall carbon nanotubes by electron multiplication from microchannel plate.* Applied Physics Letters, 2006. **88**(19): p. -.
56. Charlier, J.C., et al., *Enhanced Electron Field Emission in B-doped Carbon Nanotubes.* Nano letters, 2002. **2**(11): p. 1191-1195.
57. Bulusheva, L., et al., *Effect of Nitrogen Doping on the Electrochemical and FIeld Emission Characteristics of Carbon Nanotubes*, in *Nanotec09*. 2009: Brussels.
58. Okotrub, A., et al., *Structure and Field Electron Emission Characteristics of Aligned Carbon Nanotubes.* Physics, Chemistry and Application of Nanostructures: Reviews and Short Notes, 2007: p. 585-588
59. Bulusheva, L.G., et al., *Effect of Fe/Ni catalyst composition on nitrogen doping and field emission properties of carbon nanotubes.* Carbon, 2008. **46**(6): p. 864-869.
60. Wang, X., et al., *Controllable Growth, Structure, and Low Field Emission of Well-Aligned CN_x Nanotubes.* Journal of Physical Chemistry B, 2002(106): p. 2186-2190.

61. Lai, Y.H., H.B. Lian, and K.Y. Lee, *Field emission of vertically aligned carbon nanotubes with various content of nitrogen.* Diamond and Related Materials, 2009. **18**(2): p. 544-547.
62. Bonard, J.M., et al., *Field emission of individual carbon nanotubes in the scanning electron microscope.* Physical review letters, 2002. **89**(19): p. 89.
63. Jo, S.H., et al., *Field emission of carbon nanotubes grown on carbon cloth.* Applied Physics Letters, 2004. **85**(5): p. 810-812.
64. Navitski, A., et al. *Efficient high-current field emission from arrays of carbon nanotube columns*. in *Journal of Vacuum Science and Technology B: Microelectronics and Nanometer Structures*. 2010.
65. Kim, J.P., et al., *Long-term stability of various carbon-nanotube-based micro-tip emitters.* Diamond and Related Materials, 2009. **18**(2): p. 486-489.
66. Kumar, M., et al., *Field emission from camphor-pyrolyzed carbon nanotubes.* Chemical Physics Letters, 2004. **385**(3): p. 161-165.
67. Bonard, J.M., et al., *Field emission from carbon nanotubes: The first five years.* Solid-State Electronics, 2001. **45**(6): p. 893-914.
68. Charbonnier, F.M., et al., *Nottingham Effect in Field + T-F Emission - Heating + Cooling Domains + Inversion Temperature.* Physical Review Letters, 1964. **13**(13): p. 397-&.
69. Milne, W.I., et al., *Growth of aligned multiwall carbon nanotubes and the effect of adsorbates on the field emission properties.* Molecular Nanostructures, 2003. **685**: p. 605-611
70. Kyung, S.J., et al., *Improvement of electron field emission from carbon nanotubes by Ar neutral beam treatment.* Carbon, 2008. **46**(10): p. 1316-1321.
71. Zeng, B.Q., et al., *Field emission of silicon nanowires.* Applied Physics Letters, 2006. **88**(21): p. -.
72. Zhang, N., et al., *Patterned growth of ZnO nanorods and their field emission properties.* Current Applied Physics, 2009. **9**(1): p. 34-38.
73. De, H.W.A., A. Châtelain, and D. Ugarte, *A carbon nanotube field-emission electron source.* Science, 1995. **270**(5239): p. 1179-1180.
74. Service, R.F., *Nanotubes show image-display talent.* Science, 1995. **270**(5239): p. 270.
75. de Heer, W.A., et al., *Aligned Carbon Nanotube Films: Production and Opitical and Electronic Properties.* Science, 1995. **268**: p. 845-846.
76. Choi, W.B., et al., *Fully sealed, high-brightness carbon-nanotube field-emission display.* Applied Physics Letters, 1999. **75**(20): p. 3129-3131.
77. Xu, N.S. and S.E. Huq, *Novel cold cathode materials and applications.* Materials Science and Engineering R: Reports, 2005. **48**(2): p. 48.
78. Spindt, C.A., et al., *Field-emitter-array development for microwave applications.* Journal of Vacuum Science & Technology B, 1996. **14**.
79. Han, J.H., et al., *Field emission properties of carbon nanotubes grown on Co/TiN coated Ta substrate for cathode in microwave power amplifier.* Diamond and Related Materials, 2004. **13**(4): p. 987-993.
80. Whaley, D.R., et al., *application of field emitter arrays to microwave power amplifiers.* IEEE Transactions on Plasma Science, 2000. **28**(3).
81. Knipp, J.K. and G.E. Uhlenbeck, *Emission of gamma radiation during the beta decay of nuclei.* Physica, 1936. **3**(6): p. 425-439.

82. Tolt, Z.L., et al., *Carbon nanotube cold cathodes for application in low current x-ray tubes.* Journal of Vacuum Science and Technology B: Microelectronics and Nanometer Structures, 2008. **26**(2): p. 706-710.
83. Kibis, O.V. and M.E. Portnoi, *Carbon Nanotubes: A New Type of Emitter in the Terehartz Range.* Technical Physics Letters, 2005. **31**(8): p. 671/672.
84. Manohara, H., et al., *Field Emission Testing of Carbon Nanotubes for THz Frequency Vacuum Micro-Tube Sources.* SPIE Proceedings, 2004. **5343**.
85. Zhou, Q.L., et al., *Flame synthesis of carbon nanotubes with high density on stainless steel mesh.* Journal of Alloys and Compounds, 2008. **463**(1-2): p. 317-322.
86. Xu, F.S., X.F. Liu, and S.D. Tse, *Synthesis of carbon nanotubes on metal alloy substrates with voltage bias in methane inverse diffusion flames.* Carbon, 2006. **44**(3): p. 570-577.
87. Hsieh, C.C., et al., *Synthesis of Carbon Nanotubes Using a Butane-Air Bunsen Burner and the Resulting Field Emission Characteristics.* Journal of Physical Chemistry C, 2008. **112**(49): p. 19224-19230.
88. Bellucci, S., et al., *Study of field emission of multiwalled C nanotubes synthesized by arc discharge.* Journal of Physics Condensed Matter, 2007. **19**(39): p. 19.
89. Gamaly, E.G. and T.W. Ebbesen, *Mechanism of Carbon Nanotube Formation in the Arc-Discharge.* Physical Review B, 1995. **52**(3): p. 2083-2089.
90. Grobert, N., *Carbon nanotubes - becoming clean.* Materials Today, 2006. **10**(1-2): p. 28-35.
91. Masarapu, C. and B.Q. Wei, *Direct growth of aligned multiwalled carbon nanotubes on treated stainless steel substrates.* Langmuir, 2007. **23**(17): p. 9046-9049.
92. Merkulov, I.A., K.L. Klein, and M.L. Simpson, *A synergetic description of carbon nanofiber growth.* Journal of Applied Physics, 2009. **105**(6): p. -.
93. Hata, K., et al., *Water-assisted highly efficient synthesis of impurity-free single-walled carbon nanotubes.* Abstracts of Papers of the American Chemical Society, 2005. **229**: p. U967-U967.
94. Zeng, B.Q., et al., *Enhancement of field emission of aligned carbon nanotubes by thermal oxidation.* Applied Physics Letters, 2006. **89**(22): p. -.
95. Park, K.H., et al., *Catalyst-assisted hot filament chemical vapor deposition and characterization of carbon nanostructures.* Thin Solid Films, 2006. **501**(1-2): p. 233-237.
96. Musatov, A.L., et al., *Field electron emission from nanotube carbon layers grown by CVD process.* Applied Surface Science, 2001. **183**(1): p. 111-119.
97. Somani, S.P., et al., *Carbon nanofibers and multiwalled carbon nanotubes from camphor and their field electron emission.* Current Applied Physics, 2009. **9**(1): p. 144-150.
98. Terrones, M., et al., *Controlled production of aligned-nanotube bundles.* Nature, 1997. **388**(6637): p. 52-55.
99. Cao, P.J., et al., *The effect of substrate morphology on the diameter distribution of carbon nanotubes grown on silica and ceramic substrates.* Materials Letters, 2007. **61**(8): p. 1899-1903.
100. Tapaszto, L., et al., *Diameter and morphology dependence on experimental conditions of carbon nanotube arrays grown by spray pyrolysis.* Carbon, 2005. **43**(5): p. 970-977.
101. Singh, C., M.S. Shaffer, and A.H. Windle, *Production of controlled architectures of aligned carbon nanotubes by an injection chemical vapour deposition method.* Carbon, 2003. **41**(2): p. 359-368.

102. Chen, J., et al., *The application of carbon nanotubes in high-efficiency low power consumption field-emission luminescent tube.* Ultramicroscopy, 2003. **95**(1-4): p. 153-156.
103. Meyyappan, M., et al., *Carbon nanotube growth by PECVD: a review.* Plasma Sources Science & Technology, 2003. **12**(2): p. 205-216.
104. Ren, Z.F., et al., *Synthesis of large arrays of well-aligned carbon nanotubes on glass.* Science, 1998. **282**(5391): p. 1105-1107.
105. Tu, Y., et al., *Growth of aligned carbon nanotubes with controlled site density.* Applied Physics Letters, 2002. **80**(21): p. 4018-4020.
106. Li, Z.H., et al., *Preparation of parallel arrayed carbon nanotube film and its structure research.* Inorganic Materials, 2007. **43**(7): p. 696-699.
107. Gozzi, D., A. Latini, and M. Tomellini, *Thermodynamics of CVD Synthesis of multiwalled carbon nanotubes: a case study.* The Journal of Physical Chemistry C, 2009. **113**(1): p. 45-53.
108. Ren, Z.F. and Z.P. Huang, *Synthesis of large arrays of well-aligned carbon nanotubes on glass.* Science, 1998. **282**(5391): p. 1105-1107.
109. Kim, Y.K., et al., *Electron-emission properties of titanium carbide-coated carbon nanotubes grown on a nano-sized tungsten tip.* Thin Solid Films, 2008. **517**(3): p. 1156-1160.
110. Kim, H.J., et al., *Growth of carbon nanotube field emitters on single strand carbon fiber: A linear electron source.* Nanotechnology, 2011. **22**(9): p. 22.
111. Geohegan, D.B., et al., *In situ growth rate measurements and length control during chemical vapor deposition of vertically aligned multiwall carbon nanotubes.* Applied Physics Letters, 2003. **83**(9): p. 1851-1853.
112. Noury, O., et al., *Growth of carbon nanotubes on cylindrical wires by thermal chemical vapor deposition.* Chemical Physics Letters, 2001. **346**(5-6): p. 349-355.
113. Seelaboyina, R., J. Huang, and W.B. Choi, *Enhanced field emission of thin multiwall carbon nanotubes by electron multiplication from microchannel plate.* Applied Physics Letters, 2006. **88**(19): p. 88.
114. Chhowalla, M., et al., *Field emission from short and stubby vertically aligned carbon nanotubes.* Applied Physics Letters, 2001. **79**(13): p. 2079-2081.
115. Reyes-Reyes, M., et al., *Efficient encapsulation of gaseous nitrogen inside carbon nanotubes with bamboo-like structure using aerosol thermolysis.* Chemical Physics Letters, 2004. **396**(1-3): p. 167-173.
116. Sinnott, S.B., et al., *Model of carbon nanotube growth through chemical vapor deposition.* Chemical Physics Letters, 1999. **315**(1): p. 25-30.
117. Zakhidov, A.A., et al., *Field emission of electrons by carbon nanotube twist-yarns.* Applied Physics A: Materials Science and Processing, 2007. **88**(4): p. 593-600.
118. Seah, C.M., S.P. Chai, and A.R. Mohamed, *Synthesis of aligned carbon nanotubes.* Carbon, 2011. **49**(14): p. 4613-4635.
119. Grobert, N., *Nanotubes - grow or go?* Materials Today, 2006. **9**(10): p. 64-64.
120. Derbyshire, F.J., A.E.B. Presland, and D.L. Trimm, *Graphite Formation by Dissolution-Precipitation of Carbon in Cobalt, Nickel and Iron.* Carbon, 1975. **13**(2): p. 111-113.
121. Baker, R.T.K., *Catalytic Growth of Carbon Filaments.* Carbon, 1989. **27**(3): p. 315-323.
122. Hofmann, S., et al., *Surface diffusion: The low activation energy path for nanotube growth.* Physical Review Letters, 2005. **95**(3): p. -.

123. Ducati, C., et al., *Temperature selective growth of carbon nanotubes by chemical vapor deposition.* Journal of Applied Physics, 2002. **92**(6): p. 3299-3303.
124. Meyyappan, M., et al., *Carbon nanotube growth by PECVD: A review.* Plasma Sources Science and Technology, 2003. **12**(2): p. 205-216.
125. Talapatra, S., et al., *Direct growth of aligned carbon nanotubes on bulk metals.* Nature nanotechnology, 2006. **1**(2): p. 112-116.
126. Abad, M.D., et al., *Catalytic growth of carbon nanotubes on stainless steel: Characterization and frictional properties.* Diamond and Related Materials, 2008. **17**(11): p. 1853-1857.
127. Baddour, C.E., et al., *A simple thermal CVD method for carbon nanotube synthesis on stainless steel 304 without the addition of an external catalyst.* Carbon, 2009. **47**(1): p. 313-318.
128. Masarapu, C. and B. Wei, *Direct growth of aligned multiwalled carbon nanotubes on treated stainless steel substrates.* Langmuir, 2007. **23**(17): p. 9046-9049.
129. Abad, M.D., et al., *Catalytic growth of carbon nanotubes on stainless steel: Characterization and frictional properties.* Diamond and Related Materials, 2008. **17**(11): p. 1853-1857.
130. Huang, Z.P., et al., *effect of nickel, iron and cobalt on growth of aligned carbon nanotubes.* Applied Physics a-Materials Science & Processing, 2002. **74**(3): p. 387-391.
131. Ma, R.Z., et al., *Syntheses and properties of B-C-N and BN nanostructures.* Philosophical Transactions of the Royal Society of London Series a-Mathematical Physical and Engineering Sciences, 2004. **362**(1823): p. 2161-2186.
132. Sharma, R.B., et al., *Field emission properties of boron and nitrogen doped carbon nanotubes.* Chemical Physics Letters, 2006. **428**(1): p. 102-108.
133. Borowiak-Palen, E., et al., *Efficient production of B-substituted single-wall carbon nanotubes.* Chemical Physics Letters, 2003. **378**(5): p. 516-520.
134. Blase, X., *Properties of composite BxCyNz nanotubes and related heterojunctions.* Computational Materials Science, 2000. **17**(2-4): p. 107-114.
135. Liu, J., S. Webster, and D.L. Carroll, *Temperature and Flow Rate of NH_3 Effects on Nitrogen Content and Doping Enviroments of Carbon Nanotubes Grown by Injection CVD Method.* Journal of Physical Chemistry B, 2005(109): p. 15769-15774.
136. Bormashov, V.S., et al., *Novel method of flat cold cathode formation from carbon-nitrogen nanofibers.* Ultramicroscopy, 2007. **107**(9): p. 857-860.
137. Kudashov, A.G., et al., *Influence of Ni-Co catalyst composition on nitrogen content in carbon nanotubes.* Journal of Physical Chemistry B, 2004. **108**(26): p. 9048-9053.
138. Huang, J.X., et al., *Field-emission fluorescent lamp using carbon nanotubes on a wire-type cold cathode and a reflecting anode.* Journal of Vacuum Science and Technology B: Microelectronics and Nanometer Structures, 2008. **26**(5): p. 1700-1704.
139. Meysami, S.S., et al., *Aerosol-assisted chemical vapour deposition synthesis of multi-wall carbon nanotubes.* 2013.
140. Meysami, S.S., et al., *Aerosol-assisted chemical vapour deposition synthesis of multi-wall carbon nanotubes: I. Mapping the reactor.* Carbon, 2013. **58**: p. 151-158.
141. Maruyama, S., et al., *Low-temperature synthesis of high-purity single-walled carbon nanotubes from alcohol.* Chemical Physics Letters, 2002. **360**(3): p. 229-234.
142. Orlanducci, S., et al., *Nanodiamond-coated carbon nanotubes: Early stage of the CVD growth process.* Chemical Vapor Deposition, 2008. **14**(7): p. 241-246.

143. Dresselhaus, M.S., et al., *Raman spectroscopy on isolated single wall carbon nanotubes.* Carbon, 2002. **40**(12): p. 2043-2061.
144. Guillorn, M.A., et al., *Operation of individual integrally gated carbon nanotube field emitter cells.* Applied Physics Letters, 2002. **81**(15): p. 2860-2862.
145. Zajec, B., et al., *Ring-shaped field emission patterns from carbon nanotube films.* Carbon, 2011. **49**(10): p. 3332-3339.
146. Huang, S., X. Cai, and J. Liu, *Growth of millimeter-long and horizontally aligned single-walled carbon nanotubes on flat substrates.* Journal of the American Chemical Society, 2003. **125**(19): p. 5636-5637.
147. Plata, D.L., et al., *Early evaluation of potential environmental impacts of carbon nanotube synthesis by chemical vapor deposition.* Environmental Science and Technology, 2009. **43**(21): p. 8367-8373.
148. Mayne, M., et al., *Pyrolytic production of aligned carbon nanotubes from homogeneously dispersed benzene-based aerosols.* Chemical Physics Letters, 2001. **338**(2-3): p. 101-107.
149. Piccirillo, C., R. Binions, and I.P. Parkin, *Synthesis and functional properties of vanadium oxides: V(2)O(3), VO(2), and V(2)O(5) deposited on glass by aerosol-assisted CVD.* Chemical Vapor Deposition, 2007. **13**(4): p. 145-151.
150. Glerup, M., et al., *Synthesis of multi-walled carbon nanotubes and nano-fibres using the aerosol method with metal-ions as the catalyst precursors.* Chemical Physics Letters, 2003. **377**(3-4): p. 293-298.
151. Smith, R.C. and S.R.P. Silva, *Maximizing the electron field emission performance of carbon nanotube arrays.* Applied Physics Letters, 2009. **94**(13): p. 94.
152. Veronese, G.P., et al., *High density electron emission source based on carbon nanotubes for industrial applications.* Diamond and Related Materials, 2009. **18**(5): p. 963-966.
153. Dai, H.J., *Carbon nanotubes: opportunities and challenges.* Surface Science, 2002. **500**(1-3): p. 218-241.
154. Wang, C., et al., *First-Principles Calculations on the Emission Properties of Pristine and N-Doped Carbon Nanotubes.* The Journal of Physical Chemistry C, 2009. **113**(3): p. 812-818.
155. Nevidomskyy, A.H., G. Csanyi, and M.C. Payne, *Chemically active substitutional nitrogen impurity in carbon nanotubes.* Physical review letters, 2003. **91**(10).
156. Tawfik, S.A., S.M. El-Sheikh, and N.M. Salem, *First principles calculation of field emission from carbon nanotubes with nitrogen and boron doping.* Physica E-Low-Dimensional Systems & Nanostructures, 2011. **44**(1): p. 111-114.
157. Fan, S.S., et al., *Self-oriented regular arrays of carbon nanotubes and their field emission properties.* Science, 1999. **283**(5401): p. 512-514.
158. Tapasztó, L., et al., *Diameter and morphology dependence on experimental conditions of carbon nanotube arrays grown by spray pyrolysis.* Carbon, 2005. **43**(5): p. 970-977.
159. Hata, K., et al., *Water-assisted highly efficient synthesis of impurity-free single-walled carbon nanotubes.* Science, 2004. **306**(5700): p. 1362-1364.
160. Jo, S.H., et al., *Field emission of carbon nanotubes grown on carbon cloth.* Journal of Vacuum Science and Technology B: Microelectronics and Nanometer Structures, 2005. **23**(6): p. 2363-2368.

161. Agarwal, S., S.B. Yamini, and K.K. Kar, *The fabrication of carbon-nanotube-coated electrodes and a field-emission-based luminescent device.* Nanotechnology, 2010. **21**(6): p. 21.
162. Bonard, J.M., et al., *Field emission from cylindrical carbon nanotube cathodes: Possibilities for luminescent tubes.* Applied Physics Letters, 2001. **78**(18): p. 2775-2777.
163. Croci, M., et al. *A fully sealed luminescent tube based on carbon nanotube field emission*. in *Microelectronics Journal*. 2004.
164. Rahaman, A., N. Patra, and K.K. Kar, *Self catalyzing behavior of kanthal wire for coating of carbon nanotubes.* Fullerenes Nanotubes and Carbon Nanostructures, 2008. **16**(1): p. 78-87.
165. Noury, O., et al., *Growth of carbon nanotubes on cylindrical wires by thermal chemical vapor deposition.* Chemical Physics Letters, 2001. **346**(5): p. 349-355.
166. Chang, W.T., *Selective growth of carbon nanotubes using catalyst poisoning and geometric trench.* Journal of Materials Science-Materials in Electronics, 2010. **21**(1): p. 16-19.
167. Grobert, N., *Carbon nanotubes - becoming clean.* Materials Today, 2007. **10**(1): p. 28-35.
168. Herndon, L. and E. Emmet Reid, *The Decomposition of Organic Compounds at High Temperatures and Pressures*. Vol. 50. 1928, Baltimore, Maryland: Mack Printing Company. 12.
169. Castro, C., et al., *Dynamics of catalyst particle formation and multi-walled carbon nanotube growth in aerosol-assisted catalytic chemical vapor deposition.* Carbon, 2010. **48**: p. 3807-3816.
170. Melechko, A.V., et al., *Vertically aligned carbon nanofibers and related structures: Controlled synthesis and directed assembly.* Journal of Applied Physics, 2005. **97**(4).
171. Meysami, S.S., et al., *Aerosol-assisted chemical vapour deposition synthesis of multi-wall carbon nanotubes: II. An analytical study.* Carbon, 2013. **58**: p. 159-169.
172. Ayala, P., et al., *Influence of the catalyst hydrogen pretreatment on the growth of vertically aligned nitrogen-doped carbon nanotubes.* Chemistry of Materials, 2007. **19**(25): p. 6131-6137.
173. Hsieh, C.C., et al., *Synthesis of carbon nanotubes using a butane-air bunsen burner and the resulting field emission characteristics.* The Journal of Physical Chemistry C, 2008. **112**(49): p. 19224-19230.
174. Zhang, Y., et al., *Integration and characterization of aligned carbon nanotubes on metal/silicon substrates and effects of water.* Applied Surface Science, 2009. **255**(9): p. 5003-5008.
175. Heresanu, V., et al., *Nature of the catalyst particles in CCVD synthesis of multiwalled carbon nanotubes revealed by the cooling step study.* Journal of Physical Chemistry C, 2008. **112**(19): p. 7371-7378.
176. Panchakarla, L.S., A. Govindaraj, and C.N.R. Rao, *Boron- and nitrogen-doped carbon nanotubes and graphene.* Inorganica Chimica Acta, 2010. **363**(15): p. 4163-4174.
177. Yadav, R.M., et al., *Effect of growth temperature on bamboo-shaped carbon-nitrogen (C-N) nanotubes synthesized using ferrocene acetonitrile precursor.* Nanoscale Research Letters, 2009. **4**(3): p. 197-203.
178. Blase, X., et al., *Theory of composite BxCyNz nanotube heteroiunctions.* Applied Physics Letters, 1997. **70**(2): p. 197-199.

179. Ma, R., et al., *Syntheses and properties of B-C-N and BN nanostructures.* Philosophical Transactions of the Royal Society A: Mathematical, Physical and Engineering Sciences, 2004. **362**(1823): p. 2161-2186.
180. Hurd, C. and F. Carnahan, *the action of heat on ethylamine and benzylamine.* Journal of the American Chemical Society, 1930. **52**: p. 4151-4158.
181. Zamudio, A., et al., *Efficient anchoring of silver nanoparticles on N-doped carbon nanotubes.* Small, 2006. **2**(3): p. 346-350.
182. Singh, C., M.S.P. Shaffer, and A.H. Windle, *Production of controlled architectures of aligned carbon nanotubes by an injection chemical vapour deposition method.* Carbon, 2003. **41**(2): p. 359-368.
183. Rümmeli, M.H., et al., *Novel catalysts, room temperature, and the importance of oxygen for the synthesis of single-walled carbon nanotubes.* Nano letters, 2005. **5**(7): p. 1209-1215.
184. Jung, Y.J., et al., *Mechanism of selective growth of carbon nanotubes on SiO2/Si patterns.* Nano letters, 2003. **3**(4): p. 561-564.
185. Li, Y.L., et al., *The growth of N-doped carbon nanotube arrays on sintered Al2O3 substrates.* Materials Science and Engineering B: Solid-State Materials for Advanced Technology, 2009. **158**(1): p. 69-74.
186. Wen, Q., et al., *Synthesis of vertically aligned CNTs with hollow channel on Al 2O3-Al substrate electroplated with Fe nanoparticles.* Journal of the Electrochemical Society, 2008. **155**(10): p. 155.
187. Hou, P.Y., et al., *Thermally grown Al(2)O(3) on a H(2)-annealed Fe(3)Al alloy: Stress evolution and film adhesion.* Acta Materialia, 2007. **55**(16): p. 5601-5613.
188. Peet, M., *Tungsten Filament Lamps: A Case Study*, in *Department of Engineering Materials*. University of Sheffield. p. 21.
189. Bormashov, V.S., et al. *The influence of the ion bombardment on the current stability of field-emission cathodes of carbon nanotubes*. in *Nuclear Instruments and Methods in Physics Research, Section A: Accelerators, Spectrometers, Detectors and Associated Equipment*. 2006.
190. Smith, R.C., D.C. Cox, and S.R.P. Silva, *In situ field emission characterization of multiwalled carbon nanotubes.* Journal of Vacuum Science and Technology B: Microelectronics and Nanometer Structures, 2008. **26**(2): p. 842-846.
191. Liu, P., et al., *Measuring the work function of carbon nanotubes with thermionic method.* Nano Letters, 2008. **8**(2): p. 647-651.
192. Terrones, M., et al., *N-doping and coalescence of carbon nanotubes: synthesis and electronic properties.* Applied Physics a-Materials Science & Processing, 2002. **74**(3): p. 355-361.
193. Zobelli, A., et al., *Electron knock-on cross section of carbon and boron nitride nanotubes.* Physical Review B, 2007. **75**(24).
195. Zou, R., et al., *Enhanced field emission from printed CNTs by hard hairbrush and electrolytic treatment in NaCl solution.* Physica E: Low-Dimensional Systems and Nanostructures, 2008. **41**(2): p. 315-319.
196. Lee, J.A., et al., *Improvement of field-emission properties of screen printed carbon nanotube films via argon plasma treatment.* Journal of the Electrochemical Society, 2006. **153**(6): p. 153.
197. Collins, P.G. and P. Avouris, *Nanotubes for electronics.* Scientific American, 2000. **283**(6): p. 62-69.

198. Connolly, T., et al., *Carbon-nanotube-polymer nanocomposites for field-emission cathodes.* Small, 2009. **5**(7): p. 826-831.
199. Bonard, J.M., et al., *Tuning the field emission properties of patterned carbon nanotube films.* Advanced Materials, 2001. **13**(3): p. 184-188.
200. Dean, K.A., T.P. Burgin, and B.R. Chalamala, *Evaporation of carbon nanotubes during electron field emission.* Applied Physics Letters, 2001. **79**(12): p. 1873-1875.
201. She, J.C., et al., *Vacuum breakdown of carbon-nanotube field emitters on a silicon tip.* Applied Physics Letters, 2003. **83**(13): p. 2671-2673.
202. Ayala, P., et al., *The doping of carbon nanotubes with nitrogen and their potential applications.* Carbon, 2010. **48**(3): p. 575-586.
203. Wei, Y., et al., *Cold linear cathodes with carbon nanotube emitters and their application in luminescent tubes.* Nanotechnology, 2007. **18**(32): p. 18.
204. Darsono, N., et al., *Field emission properties of carbon nanotube pastes examined using design of experiments.* Journal of Materials Science-Materials in Electronics, 2008. **19**(1): p. 17-23.
205. Purcell, S.T., et al., *Hot nanotubes: Stable heating of individual multiwall carbon nanotubes to 2000 K induced by the field-emission current.* Physical review letters, 2002. **88**(10): p. 1055021-1055024.
206. Marchand, M., et al., *Ring patterns in high-current field emission from carbon nanotubes.* Physical Review B, 2009. **80**(24).
207. Liu, W.H., et al., *Turn-on field distribution of field-emitting sites in carbon nanotube film: Study with luminescent image.* Journal of Vacuum Science & Technology B, 2008. **26**(1): p. 32-35.
208. Fu, W., et al., *Spherical field emission cathode based on carbon nanotube paste and its application in luminescent bulbs.* Journal of Vacuum Science and Technology B: Microelectronics and Nanometer Structures, 2008. **26**(4): p. 1404-1406.
209. Smith, R.C. and S.R.P. Silva, *Interpretation of the field enhancement factor for electron emission from carbon nanotubes.* Journal of Applied Physics, 2009. **106**(1): p. 106.
210. Enouz-Vedrenne, S., et al., *Effect of the Synthesis Method on the Distribution of C, B, and N Elements in Multiwall Nanotubes: A Spatially Resolved Electron Energy Loss Spectroscopy Study.* Journal of Physical Chemistry C, 2008. **112**(42): p. 16422-16430.
211. Jung, H.Y., S.M. Jung, and J.S. Suh, *Horizontally aligned single-walled carbon nanotube field emitters fabricated on vertically aligned multi-walled carbon nanotube electrode arrays.* Carbon, 2008. **46**(10): p. 1345-1349.
212. Kumar, M., et al., *The use of camphor-grown carbon nanotube array as an efficient field emitter.* Carbon, 2007. **45**(9): p. 1899-1904.